CRANFIELD UNIVERSITY

Crispin Allison

Flexible Liners for Corrosion Protection of Pipelines

School of Applied Sciences

PhD
Academic Year: 2008 - 2012

Supervisor: Dr. M. J. Robinson
February 2012

CRANFIELD UNIVERSITY

School of Applied Sciences

PhD

Academic Year 2008 - 2012

Crispin Allison

Flexible Liners for Corrosion Protection of pipelines

Supervisor: Dr. M. J. Robinson

February 2012

ABSTRACT

Flexible plastic liners are sometimes installed into new and existing oil and gas pipelines to prevent corrosion of the pipe wall. A practical difficulty of this method is that the plastic liners are permeable to gases, which can collect and form an annular space between the liner and the pipe. If the operating pressure in the pipe decreases then the collected gas can cause the liner to collapse and block the pipe.

One method for overcoming this problem is to insert vents at intervals along the liner to allow the gas to escape into the pipe during depressurisation. However, there is concern that this arrangement might lead to excessive corrosion beneath the vent where the pipe wall is exposed. The rate of corrosion is expected to be controlled by the vent size but this principle needs to be confirmed by experiment. The work described in this thesis is aimed at investigating this corrosion by experiment for a range of conditions typical of oil and gas production.

A novel crevice corrosion cell was designed, consisting of an X100 carbon steel plate and a sheet of transparent Perspex, separated by a thin gasket. A small hole in the Perspex simulated a liner vent and allowed carbon dioxide to reach the steel surface. Tests were carried out in 3.5% NaCl solutions saturated with carbon dioxide at 1 bar partial pressure.

Corrosion rates along the length of the annular space were measured using the Linear Polarisation Resistance (LPR) technique on pairs of insulated X100 electrodes set into the plate. The corrosion rates within the annular space have been shown to be small compared to those in the bulk solution and to diminish rapidly with distance from the vent. Mathematical modelling, based on the transport of carbon dioxide, is described to explain these findings and support the experimental work. The effectiveness of the LinerVent^{TM}, installed over the vent, in a turbulence pipeline was demonstrated. The benefit of applying cathodic protection within the annular space was also demonstrated. The results are discussed in terms of the fundamental corrosion principles and their practical implications

Key words: Flexible liner, pipeline, CO_2 corrosion, annular space, diffusion model, cathodic protection, inhibitor.

This page is intentionally left blank

ACKNOWLEDGEMENTS

I would like to express my gratitude to Dr. M. J. Robinson for his guidance, support and push during this research project. His expertise and contribution have been invaluable for my doctoral studies. I truly appreciate Dr Robinson for his deep theoretical and practical knowledge in corrosion and his organisational abilities. I would also like to thank the Petroleum Technology Development Fund (PTDF) of Nigeria for sponsoring this research; further gratitude to Swagelining Limited UK for providing the materials and technical documentation for this research. My appreciation also goes to the Chief of the Naval Staff for graciously releasing my family and I to pursue this PhD research.

In addition, I would like to mention Andrew Dyer, Colin Matthews, Rukhsana Ormesher and Tony Parker of the School of Applied Science at Cranfield University for their assistance and technical support on numerous occasions. My appreciation also goes to Mr Colin of Wotton Engineering for endlessly grinding my long metal plate.

I would like to specially thank my Pastor, Rev Biyi Ajala, for his prayers, mentoring, counselling and support to my family and I especially during challenging times. I am so grateful to God for His wisdom upon Rev Ajala's life. I also extend my gratitude to all my friends and the members of Cranfield Pentecostal Assembly and Holding Forth the Word Ministry especially Dr Daniel Kamunge, Dr Gareth Davies, Dr Sola, Grp Capt Jemitola, Okereke N., Loveth Uhiah, Lt Col. Allison I. Allison, Masoud and Adnan.

I would like to specially thank the Amayanabo of Nembe Kingdom, HRM Dr. Edmound Daukoru for his support. My sincere gratitude also goes to Dr Silva Opuala-Charles and his wife, Mrs Timi Opuala-Charles, for their immense financial, spiritual and moral support and for sponsoring my wife and I to the United States to attend the NACE Corrosion Conference in 2011.

And finally, my sincere love to my wife Sarah and my princesses Divine and Destiny for their love and support. Sarah, you are just wonderful and a true wife from the Lord. I would like to mention my son Obote who was given birth during my PhD studies.

I dedicate this work to my Lord and Saviour, Jesus Christ.

This page is intentionally left blank

TABLE OF CONTENTS

LIST OF FIGURES

LIST OF TABLES

LIST OF EQUATIONS

LIST OF ABBREVIATIONS

A	Amps
CP	Cathodic Protection
CAPEX	Capital Expenditure
CCS	Critical Crevice Solution
CCST	Critical Crevice Solution Theory
Cl	Chlorine
CE	Counter Electrode
cm	Centimetre
COREL	Corrosion Resistant Liners
CRA	Corrosion Resistant Alloys
E	Corrosion potential
EIS	Electrochemical Impedance Spectroscopy
GNP	Gross National Product
H	Hydrogen
HDPE	High Density Polyethylene
IRDT	Infra-Red Drop Theory
i	Corrosion Rate
JIP	Joint Industry Project
Km	Kilometre
LPR	Linear Polarisation Resistance
MDPE	Medium Density Polyethylene
mm	Millimetres
n	Integer counter
NACE	National Association of Corrosion Engineers
O	Oxygen
OCP	Open Circuit Potential
OPEX	Operating Expenditure
S	Sulphur
SRB	Sulphate Reducing Bacteria
SCE	Saturated Calomel Electrode

SEM	Scanning Electrode Microscopy
US	United States of America
V	Volts
WE	Working Electrode
TM	Trade-Mark
corr	Corrosion

List of Symbols

Symbol	Meaning	Units
C_r	Corrosion rate	mm/y
CO_3^{2-}	Carbonate ions	-
HCO_3^-	Bicarbonate ions	-
T	Absolute temperature	K^0
b_a, b_c	Anodic and cathodic Tafel slope	V/decade
D	Diffusion coefficient	m^2/s
i_a	Anodic current density	A/m^2
i_c	Cathodic current density	A/m^2
P_{CO_2}	Partial pressure of carbon dioxide gas	Bar
£	British Pound Sterling	-

CHAPTER 1
INTRODUCTION

1.1 Background

Corrosion has been known to man since the early days of civilization when the use of metallic materials for construction of working implements became more frequent. Corrosion, coupled with man's limited resources, poses negative economic implications. Therefore, attempts have always been made to overcome it. In recent times this has culminated in greater scientific research into corrosion mechanisms, and inventions of preventive and protective designs to combat corrosion of structural materials.

Knowledge of corrosion science has revealed that the presence of a corroding medium makes it imperative to build-in corrosion protection measures with the aim of protecting materials used in construction. The common methods employed in corrosion protection include a corrosion resistant film on the metal surface and coating (Morgan, 1993). Other methods include controlling flow conditions, use of Corrosion Resistant Alloys (CRA), application of inhibitors and using cathodic protection (Dayalan et al., 1998b).

1.2 Corrosion Issues in the Oil and Gas Industry

The oil and gas industry uses large quantities of carbon and low-alloy steels in the construction of pipelines, offshore rigs and structures (Papavinasam et al., 2005; Lopez et al., 2003). Pipelines are the most economical means of large scale transportation of hydrocarbons including produced water and are a better option than road and railway transportation. This is especially so when large quantities are to be moved on a regular basis (Guo et al., 2005). In addition, pipelines have demonstrated capability to be adapted to different kinds of environments including remote areas and hostile environments.

Global energy needs led to extended searches for oil in offshore environments. By 1897 the first offshore pipeline was installed (Leffler et al., 2003). Since then offshore pipelines have become the unique means of efficiently transporting hydrocarbons from offshore installations. Figure 1-1 presents a schematic of some of the uses of pipelines offshore.

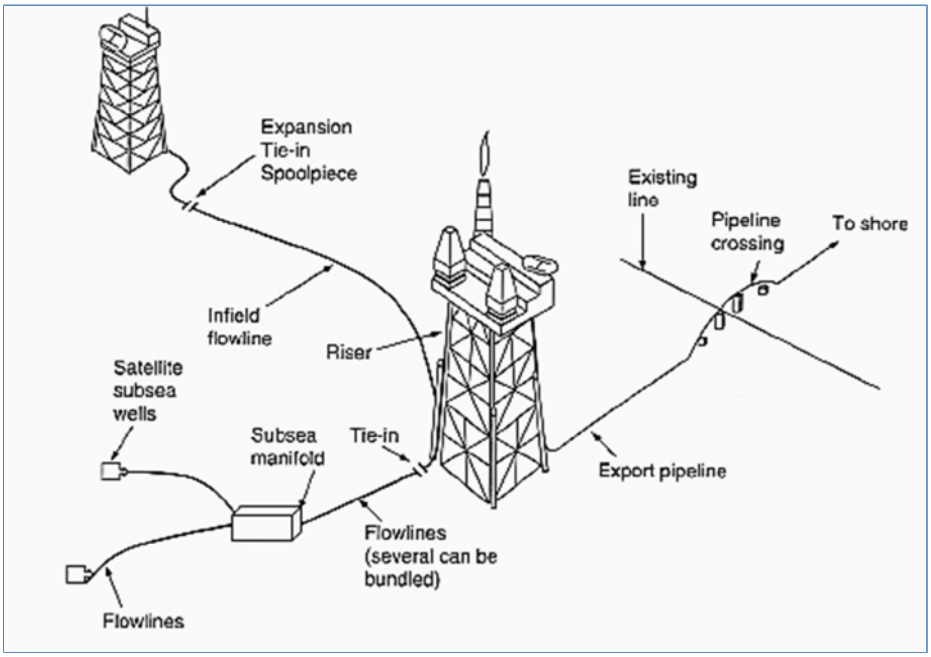

Figure 1-1 Schematic of some of the application of pipelines offshore (Leffler et al., 2003)

Harsh sea environment necessitates the use of highly resilient and high performance materials. Carbon steel is and still remains the primary member in the construction of oil and gas transport pipelines owing to economic reasons, availability and well developed technology (Fosbol et al., 2009; Okafor et al., 2011). However, its downside is the fact that it easily corrodes, changing to its more thermodynamically stable form (iron ore) thus becoming mechanically unreliable.

Corrosion protection is therefore very important because of the large sums of money spent on corrosion mitigation designs, repair of corroded pipes, refurbishment and cleaning of polluted environments.

1.2.1 Cost of Corrosion

Corrosion issues have been costly, worldwide, either directly or indirectly. For instance, a corrosion study conducted in the United States in 1949 showed that the annual cost of corrosion was about $5.5 billion, approximately 2.1% of the gross national product (GNP). Another recent study revealed the cost of corrosion to be about $276 billion; this represented about 3% of the GNP (Thompson and Patrick, 2003). In the United Kingdom, a study conducted in 1970 estimated the annual cost of corrosion to be about 3.5% of the GNP. Current studies show that corrosion costs the offshore sectors an estimated €392.5 million annually (Biezma and San Cristóbal, 2005). Other researches have also shown that the average cost of corrosion for other countries in terms of the GNP clocks an average of about 4.2% (Tems and Al Zahrani, 2006).

In the US pipeline industry, a study revealed that 41% of offshore pipeline failures resulting in leakage between 1985 and 1994 were caused mainly by corrosion. Subsequently corrosion related costs were approximately between $5.4 billion and $8.8 billion annually (Thompson and Patrick, 2003). Another study estimated the cost of corrosion of transmission pipelines to be about $9,860 per kilometre (Tems and Al Zahrani, 2006). A study in Norway attributed 60% of offshore maintenance costs to corrosion (Cavassi and Cornago, 1999).

Unfortunately, work done so far has not proven to be an effective long term corrosion protection strategy as there are still problems of external and internal corrosion resulting in so much loss. A study carried out by Advantica between 1961 and 2000 showed that 19% of leakages were due to external corrosion while 24% were due to internal corrosion (Tems and Al Zahrani, 2006). The study also demonstrated that the overall avoidable cost of corrosion was in the region of about 15% and the automotive industry experienced a 27% reduction based on investments in innovative corrosion prevention technologies. Therefore the drive to improve innovative technology to combat the challenges posed by internal corrosion of pipelines could be the way forward; hence, the need to carry out further research.

1.2.2 Corrosion Protection Measures/Designs

Pipelines are protected against internal corrosion using different design measures. The most common is corrosion allowance, where thicker pipes (extra layers of 3 to 10.0 mm of steel) which take a longer time to corrode are employed (Beunier et al., 2009). This method obviously leads to larger steel quantities, heavier pipes and longer fabrication/welding times and is therefore not cost effective.

Other methods include the use of corrosion resistant alloys which are applied in areas where high corrosion rates are envisaged. This technique is also time-consuming and very expensive because of the alloys employed for their design and the welding process. The other very regularly used method by most operators is chemical inhibitors. These conventional methods lead to excessive cost, installation weight and welding thickness which are not economical for the oil and gas industry (Beunier et al., 2009). The last method and the most innovative technique and which is the focus of this research is the use of flexible plastic liners to protect the internal surface of the carbon steel pipelines and is discussed below.

1.2.3 Flexible Plastic Liners

The use of plastic liners can trace its origin from pipe refurbishment in the onshore industry. These industries have even gone further and replaced lengths of metallic pipelines with plastic pipes.

Plastic lining of pipelines involves the use of flexible plastic material to line/cover the interior (inner surface) of the carbon steel. The idea is to prevent any contact of the carbon steel with the hydrocarbon being transported, thereby preventing corrosion. The plastic is drawn through the carbon steel pipeline by a specialised technique so that it seats neatly on the surface.

These plastic pipes are made from medium and high density polyethylene (MDPE and HDPE) materials (Baker and McIntyre, 2003). Following the success of plastic liners in

these industries, their use has been extended to offshore oil and gas installations for internal corrosion protection of pipelines. Currently plastic lined pipes are deployed offshore for water injection lines to increase reservoir pressure and improve hydrocarbon recovery.

Series of research projects were undertaken to investigate the feasibility of applying plastic lining for offshore pipelines. The results were very encouraging and demonstrated the effectiveness of plastic lined pipelines in preventing internal corrosion of carbon steel pipelines. The succeeding section further presents other additional benefits of plastic lined pipelines.

1.3 Benefits of Plastic Lined Steel Pipelines

As has been discussed previously, plastic liners would allow the use of low cost carbon steel pipelines as opposed to the more expensive conventional corrosion protection methods. This combination of carbon steel pipe and plastic liner affords the dual advantage of the strength of steel and the corrosion resistance of plastics. According to McIntyre (2002) some of the benefits of plastic lining include:

- **Thermal Benefits/Insulation** – The plastic covering on the metal surface brings some form of insulation to the metallic pipelines (Sato et al., 1999). The insulation effect reduces the heat loss due to exchange of heat between the hydrocarbon and the cold pipe surface directly in contact with seawater. It is important to note that despite the external insulation of pipelines, internal insulation by plastic is far better since it is directly in contact with the fluid. Furthermore, it reduces the cost of preheating the hydrocarbon on arriving at the process facility.

- **Low Surface Energy** – This has the advantage of reducing the chances of wax appearance which happens due to drop of the produced hydrocarbon temperature. The flow assurance benefit is achieved when the plastic is

combined with other specialised materials such as silicon and Teflon. Adhesion of hydrates and waxes to the pipeline is minimised and so blockage and flow restriction is overcome.

- **Economic Benefit** – Another major area of the positive effect of plastic lining is economic value in terms of cost reduction. Large sums of money which could have been used for corrosion allowance design, corrosion resistant alloys or/and inhibitors are saved by applying plastic liners. According to Maclachlan and Headford (1996), a life cycle cost savings offered by a plastic lined pipeline compared with the conventional systems were in the order of 30 – 50%. Table 1-1 gives a brief comparison of the cost involved in using a plastic lined pipe and other types of pipes.

Table 1-1: Project cost for different design (cost/length) (McIntyre, 2002)

	Carbon Steel (19 mm thick)	Carbon Steel (14.3mm thick lined with 15mm PE plastic)	Super Duplex (12.7mm thick)
Procurement and fabrication cost (£ k)	1,300.00	1,700.00	5,500.00
Installation (£ k)	5,700.00	5,800.00	5,800.00
Engineering and contingency (£ k)	2,100.00	2,200.00	3,400.00
Total (£ k)	**9,100.00**	**9,700.00**	**14,700.00**
Annual operating cost (inhibitors, transport, storage, maintenance, etc) in £ k	200.00	-	-

Table 1-1 above clearly shows that the capital expenditure (CAPEX) is lowest for the carbon steel followed by the carbon steel lined with the plastic liner; while the super duplex is much higher. However, the total cost of operating the facility designed with carbon steel will take an additional cost of £200,000.00 annually. For example, for an installation designed for 10 years, it will result in an additional cost of £2,000,000.00. Adding this to the cost of construction, the overall cost (CAPEX plus OPEX) for the carbon steel installation would be £11,100,000.00. It can be seen that there is no operating expenditure (OPEX) for the plastic lined carbon steel, and therefore the overall cost still remains at just £9,700,000.00. Despite the risk of rapid corrosion of the unlined carbon steel leading to pitting and consequently out of service, the lined carbon steel will not face corrosion in addition to its low cost.

Despite the fact that the super duplex steel does not have an OPEX, its CAPEX is one and a half times that of lined pipelines. Table 1-1 clearly depicts the economic benefit of the plastic lined carbon steel pipelines over other types. It is generally agreed among subsea contractors and operators that the use of plastic lined pipelines subsea would result in a savings of between 20% and 40% (McIntyre, 2002). The author believes that even a greater reduction in both the capital and operating costs could be derived from the use of plastic lined pipelines and gave an estimated cost savings of between 25 and 50%.

1.4 Plastic Liner Collapse

Associated gases such as CO_2 and H_2S are contained in the hydrocarbons transported by pipelines (Siegmund et al., 2002). Unfortunately, the liner materials used for lining the carbon steel pipelines are slightly permeable to these gases. Over time these gases permeate the liner and accumulate in the micro-annulus. If the pipeline is depressurisation, the gases in the micro-annulus expand and lead to liner collapse. Therefore it was concluded that this was a major threat that would negate the use of plastic liners.

1.5 Plastic Liner Technology

As a result of this challenge, a Joint Industry Project called COREL (COrrosion REsisting Liners) was commissioned to investigate liner collapse and proffer solution with Atkin-Boreas Consultancy Ltd as one of the major participants. The Joint Industry Project (JIP) was also to find ways to overcome this threat. After much research, it was concluded in the phase 1 of project that the challenge facing the use of plastic liners could be resolved through the two most promising venting designs (Figure 1-2):

- Grooved liner design, and
- Perforated liner design

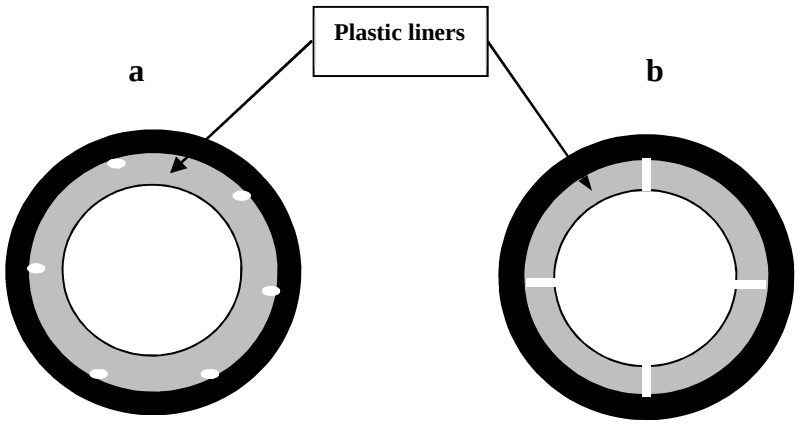

Figure 1-2: Schematics of different liner concepts (a) grooved, (b) perforated

1.5.1 Grooved Liner

The grooved liner design has grooves cut on the outer surface of the plastic running longitudinally through the length of the plastic. All gases trapped in the plastic/steel interface are collected along the grooves and flow to an appropriate point for venting, ensuring the safety of the flexible liner. This design has already been patented and is in use.

1.5.2 Perforated Liners

Perforated plastic liners have holes drilled through the liner walls at intervals to allow the trapped gases to escape into the pipe during depressurisation and so permit venting to prevent liner collapse. However, there is concern that this would lead to excessive corrosion beneath the vent where the pipe wall is exposed. The vent dimension was designed to ensure the corrosion to be self-limiting and would localise corrosion to the area just beneath the vent.

It can be concluded that perforated liners have the advantage over the grooved design because the venting mechanism is self-contained, and therefore a better and preferred option for subsea applications (Baker, 2005).

1.6 Field Research Work on Plastic Liners

Laboratory tests were conducted to look at the issue of the size of the perforation required to vent the annulus and whether it would lead to corrosion of the steel pipe. The partial success of the test proved that the perforated liner is a good solution to the plastic liner collapse, provided the corrosion of the steel does not become a threat. Overall, the results of the laboratory tests gave some confidence but required more laboratory tests to give credence to the design and therefore this research.

During the JIP tests it was discovered that the surface of the control piece did not experience significant corrosion compared to the steel beneath the liner. Another aspect of the research was to test the capabilities of an invention of Atkin-Boreas called a LinerVent^{TM} designed to be used with the liner vent. It was observed that where the LinerVent^{TM} was inserted in the plastic liner, the steel appeared to be free of corrosion attack.

The COREL JIP tests were inconclusive and had some outstanding issues which were the validation of the crevice model by repeating the principle of the COREL tests. Other

areas included a better understanding of the CO_2 corrosion mechanism and the effect of corrosion inhibitor with regard to plastic lined pipelines.

In 2006, an MSc project (Flexible liners for corrosion protection of pipelines) was carried out at Cranfield University in line with the COREL JIP research to measure the corrosion rates along the length of a simulated annular space between a plate of X100 pipeline steel and a plastic liner (Wright, 2006). The project also investigated the possibility of controlling corrosion beneath the liner with a small disk-shaped sacrificial anode located in the annular space adjacent to the vent. Tests were carried out and the results were very promising but further work was required to provide confirmation.

1.7 Aim and Objectives of the Project

This research is therefore aimed at investigating the corrosion under a vented plastic liner and how it can be managed within acceptable limits and the evaluation of the effectiveness of the Atkins-Boreas LinerVent™ based on questions raised in the COREL JIP tests and the MSc project. This will be achieved through firm experimental evidence with a view to making recommendations for use of perforated plastic liners. Therefore to achieve the aim, the following objectives are in focus:

[1] To investigate the rate and distribution of corrosion in the annular space between a flexible liner and a steel pipe wall due to the presence of brine containing carbon dioxide.

[2] To model mass transport of carbon dioxide through a liner vent and predict the metal loss in the annular space.

[3] To control corrosion within the annular space using sacrificial zinc anodes located beneath the liner.

[4] Use laboratory simulations to determine the effect of corrosion inhibitor in the annular space.

CHAPTER 2
LITERATURE REVIEW

2.1 Developmental Stages of Plastic Lined Pipelines

Plastic lining of carbon steel pipelines prevents contact between the pipe and the hydrocarbon or water being transported, thereby preventing corrosion. The use of plastic liners can trace its origin to pipe refurbishment and is now used most notably in the water, gas, chemical and food processing industries (Marais et al., 2002). The water and gas industries have replaced metallic pipelines with plastic pipes in an attempt to reap the various benefits of plastic.

Plastic liner technology is therefore well proven and is presently fully utilised in services involving transportation of water, gas and other substances. For instance in 1995 Durapipe – Stewarts & Lloyds Plastics supplied over 10,000 km of pipe for the manufacture of water and gas pipes (Maclachlan, 1996). The success of this technology in onshore applications has made it imperative for it to be applied in offshore oil and gas installations either initially or as a repair option. However, this is slow and not very much has been achieved with plastic lined pipelines in hydrocarbon transportation except for water injection systems to increase reservoir pressure (Congram, 2009).

Palmer-Jones and Paisley (2000) in their research for reliable methods of repairing internal corrosion defects in pipelines supported the use of internal liners such as High Density Polyethylene (HDPE). Medium Density Polyethylene (MDPE) and HDPE liners are gradually being used for lining the inside surfaces of corroded and ageing pipelines to prevent further interior deterioration and in so doing, restore the fluid transporting capability of pipelines (McIntyre, 2000). De Mul et al. (2000) described plastic liner technology as a fit-and-forget system to avert leakages in aging pipelines. For example, plastic liners have been used by Petroleum Development Oman LLC as retrofits to extend the life of over 150 flowlines and pipelines. In 1992 the Company installed its first plastic lined wet crude flowline in its Yibal oilfield and in 1999 it installed a 34” wet crude plastic lined transmission pipelines (De Mul et al., 2000). The

Company declared that the use of plastic lined pipelines in their oil fields, has led to a considerable reduction in the number of pipeline leakages.

In 1994 the first offshore plastic lined pipeline was commissioned in the North Sea when Shell and Coflexip Stena applied it in the Brent South Project (Maclachlan, 1996). In 1995 McDermont Marine Construction Limited installed another plastic lined water injection pipeline in the North Sea for BP's Foinaven Field (Parjus et al., 1996). Table 2-1 shows a list of plastic lined pipelines installed in the North Sea between 1994 and 1996.

Table 2-1 Plastic lined pipelines installed in the North Sea between 1994 and 1996 (Maclachlan, 1996)

Operator	Field	Year	Length	Diameter
Shell	Brent South	1994	5 km	8"
Shell	Pelican	1995	8 km	8"
BP	Foinaven	1995	35 km 11 km	8" 10"
Shell	Tern and Eider	1996	16 km	16"

The offshore projects presented in Table 2-1 were designed for water injection systems and the pipes were lined from MDPE and HDPE plastic materials (Baker and McIntyre, 2003).

Field and experimental results obtained so far have been very encouraging in as far as demonstrating the effectiveness of plastic lined pipelines in preventing internal corrosion of carbon steel pipelines is concerned. Despite this success story however, application of plastic liners for hydrocarbon transport has its challenges which are discussed in the succeeding section.

2.2 Challenges of Plastic Liners in the Oil and Gas Industry

The delay in the full acceptance of plastic lining technology in offshore applications could be attributed largely to the problem of liner collapse when used for transport of hydrocarbons. The cause of liner collapse was categorised into two, namely longitudinal buckling and circumferential collapse (Groves et al., 2004; Boot and Naqvi, 2000).

According to Groves et al. (2004) longitudinal buckling is due to differential thermal expansion of the liner within the pipe resulting from fluctuation of the temperature and pressure of the hydrocarbon being transported. They attributed this failure to the effect of liners which are loosely fitted. The solution to this was to design tightly fitted liners. Unfortunately, it was discovered that tightly fitted plastic liners suffer from the problem of circumferential liner collapse, which will be discussed in the next subsection.

2.2.1 Plastic liner collapse

Hydrocarbons from oil reservoirs contain CO_2 and H_2S in the fluid stream (Siegmund et al., 2002; De Mul et al., 2000). In addition CO_2 is used to boost the pressure of production wells; therefore, its presence in transmission pipelines is inevitable (Curtis et al., 2002). Unfortunately, the plastic liner materials for lining the internal surfaces of the pipelines used for the hydrocarbon transport are slightly permeable to these gases. As a result the gases pass through the permeable liner and accumulate in the space between the steel and liner known as the micro-annulus.

Over time the micro-annulus becomes a reservoir of gases such that the pressure eventually becomes equal to the pressure within the pipeline bore. Experience gained from the field and experimental work has shown that in the event of pipeline depressurisation (for operational reasons or maintenance), the gas pressure in the annulus can expand and cause the liner to collapse (Boot and Naqvi, 2000). Figure 2-1 is a schematic showing liner collapse due to expansion of the gases within the micro-annular. This circumferential liner collapse causes damage to the plastic liner and also blockage by restricting the flow of the hydrocarbons. The minimum likely pressure

differential to cause collapse when investigated was found to be in the range of about 4 to 5 bar (Baker and McIntyre, 2003).

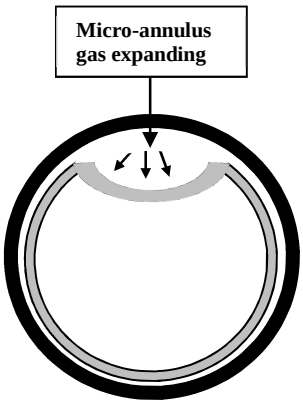

Figure 2-1: Schematic showing liner collapse due to micro-annular gas pressure

2.3 Plastic Liner Technology

As discussed in section 1.4, the major threat against the use of plastic liners for internal corrosion protection of pipelines is liner collapse caused by permeation of gases. There has therefore been an urgent need to investigate ways of preventing liner collapse by other means such as venting (Boot and Naqvi, 2000).

In the mid-1990s the British Gas and Shell Canada instituted the COREL (COrrosion REsisting Liners) Joint Industry Project (JIP) with the aim of investigating liner collapse and provide solutions for a reliable lining system (Frost et al., 2000; Groves et al., 2004). The phase 1 of the COREL joint industry project was aimed at identifying different liner concepts with a view to overcoming liner collapse both for onshore and offshore applications. The result of the investigation demonstrated that plain plastic liners had limited scope and gave the following liner concepts for further research (Frost et al., 2000):

- Impermeable liner (impermeable membrane bonded within liner wall)
- Grooved liners for longitudinal venting
- Perforated liners (internal venting)

2.3.1 Impermeable liner

This liner concept requires the use of an impermeable membrane such as a thin metallic layer within the liner to prevent permeation of gases. The membrane also serves to strengthen the liner so that it becomes less susceptible to collapse (Frost et al., 2000). A schematic of this concept is shown in Figure 2-2. This solution requires the production of special liner materials which are costly.

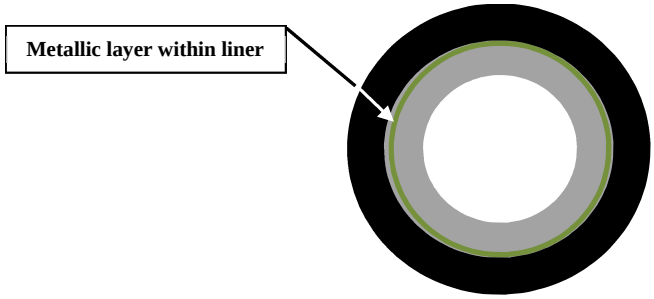

Figure 2-2: Schematics of impermeable liner concept design

With the challenges likely to be encountered with the impermeable liner design, it was decided that the grooved liner and the perforated liner be considered in phase 2 of the COREL project. Phase 2 was aimed at developing a design that was viable for both subsea and onshore, can be installed in long lengths with ease, and with a reliable venting path (Groves et al., 2004). Consequently COREL phase 2 with 9 participants including Boreas Consulting Limited was instituted and commissioned to investigate these two venting designs. The COREL investigation also included tests on the LinerVent^{TM} developed and patented by Atkins-Boreas for use with the perforated liner (Baker and McIntyre, 2003).

2.3.2 Grooved Liner

The grooved liner design has axial grooves cut on the outer surface of the plastic running longitudinally through the length of the plastic. Figure 2-3 is the grooved liner design with the longitudinal channels. All gases trapped in the micro-annulus are collected along the grooves and flow axially to an appropriate point for venting, thus ensuring the safety of the flexible liner. For this design, the gases must be vented at a

convenient point where the external pressure must be close to atmospheric pressure. This design has already been patented and is in use in the onshore industry.

One of the main challenges with the groove liner design is the potential of grooves closing up with time due to the effect of temperature and pressure of the transported hydrocarbons (Frost et al., 2000; Groves et al., 2004). Despite the gradual closing up of the channels, Frost et al. agree that it will still remain open for about 20 years.

The grooved liner has a significant disadvantage if required for subsea pipeline application; the gases collected cannot be evacuated due to the location of subsea pipelines and also due to the effect of hydrostatic pressure. Therefore, either a parallel vent line must be designed or the grooves must be continued throughout the length of the pipeline to a point where it can be safely vented. As a result of these design challenges and cost implications, grooved liner design is therefore not feasible for subsea applications.

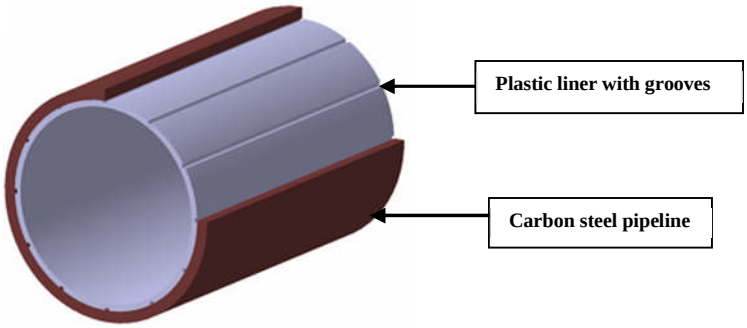

Figure 2-3: Schematic of grooved liner design

2.3.3 Perforated Liners

Perforated plastic liners have holes drilled through the liner walls at intervals to allow the trapped gases in the micro-annulus to escape into the pipeline bore during depressurisation and so permit venting (Figure 2-4). This action ensures pressure-balancing and subsequently prevents collapse. In the design of the liner vent, the holes must be large enough for the trapped gases to escape at a rate sufficient to prevent the collapse of the liner. Theoretical and experimental work carried out by Frost et al.

(2000) demonstrated that a hole with a diameter of 2-3 mm inserted in liners would allow full gas evacuation despite the effect of swelling of the liner and blockage. They also suggested inserting one hole per meter and spaced at 90° intervals around the circumference.

However, there was concern that this vent design concept would lead to excessive corrosion beneath the vent where the pipe wall is exposed. This is because the vent allows transported fluids to come in contact with it. It is therefore important to design the vent size to minimise the corrosion rate beneath the liner. Mathematical modelling carried out with respect to the vent dimension suggests that the corrosion would be controlled if the vent is designed such that the aspect ratio is greater than 3.1 (ratio of depth of hole to diameter (Baker, 2005). This vent size would not only minimise the corrosion rate but also allow rapid depressurisation of the micro-annulus.

This model did not only demonstrate a limited mass transport of aggressive species through the vent to the steel leading to a minimum corrosion rate but also ensured maximum pressure relief (Frost et al., 2000; Groves et al., 2004). However, this conclusion needed to be tested by experimentation for a range of values typical of service conditions. A technical report by Atkins-Boreas stressed the fact that the configuration of the vent size would ensure the corrosion to be self-limiting and therefore can be controlled (Baker, 2005). This possibility was attributed to the fact that the aspect ratio of the vent would localise corrosion to the area just beneath the vent.

It is clearly seen that the perforated liner has an advantage over the grooved liner design, particularly for subsea pipelines, as the trapped gases are directed back into the pipeline. It is due to the self-contained venting mechanism of the perforated liner that it is the preferred option for subsea pipelines when compared with the grooved liner design.

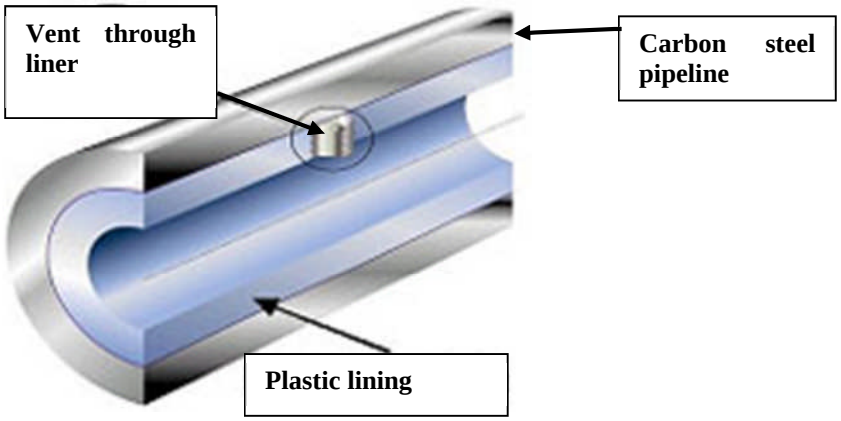

Figure 2-4 Schematic of perforated liner design (Swagelining)

2.3.3.1 Swagelining

One of the very important factors in the successful application of the plastic liner technology is the liner insertion technique. There are different liner insertion techniques such as the roll-down, titeliner, sub-lining and the swagelining (Maclachlan, 1996). This section will discuss briefly the well proven swagelining technique.

Swagelining is a liner insertion technique in which the plastic liner has an outer diameter slightly bigger than the inside diameter of the pipe to be lined. The plastic liner is pulled through a reduction die using a winch, which temporary reduces the liner diameter before it enters the pipe bore. Figure 2-5 shows the swagelining process.

The load on the liner due to the pulling device is maintained such that it is fully elastic. Once the liner is inside the pipe, the tension is relaxed and the liner reverts back to its original size and gives a tight fit within the pipe (Swagelining). This system has been in use since 1987 and was applied for the insertion of the liners in the BP Foinaven project discussed earlier.

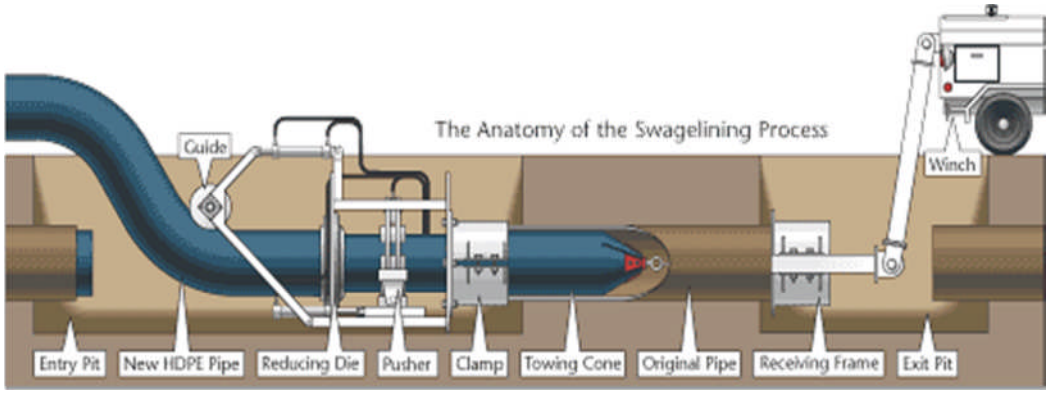

Figure 2-5: Liner insertion process using Swagelining technique (Payton, 2011)

2.4 LinerVent™ Venting Designs for Perforated Plastic Lined Pipelines

The COREL investigation included tests on the LinerVent™, an invention which has already been patented (McIntyre, 2000) for the venting of plastic lined pipelines. The LinerVent™ design has metamorphosed through some stages over the years and the following subsections will briefly discuss these stages.

2.4.1 LinerVent™ Installed within Carbon Steel Pipeline

McIntyre (2000) described the initial concept of the LinerVent™ design which was to be installed on the carbon steel pipeline wall, shown in Figure 2-6. In this design, the LinerVent™ consists of a vent assembly (1) made up of a main body (3) having a small venting hole (4) for gas passage. There is a porous element (5) which fits into an opening (6) in the main body and a non-return valve (7) comprising a ball (8) and spring (9), held in place by a retaining cap (10). The valve assembly is flushed with the pipeline inner surface and so does not obstruct the plastic liner (12).

The vent assembly is designed to be inserted through the wall of the carbon steel pipeline during manufacture. Liner collapse is prevented as gases pass through the vent hole connecting the micro-annulus and exhaust to the external environment through the

non-return valve. The porous element which could be a sintered metal provides a barrier against the liner deforming under pressure and so keeps the unit intact and operational.

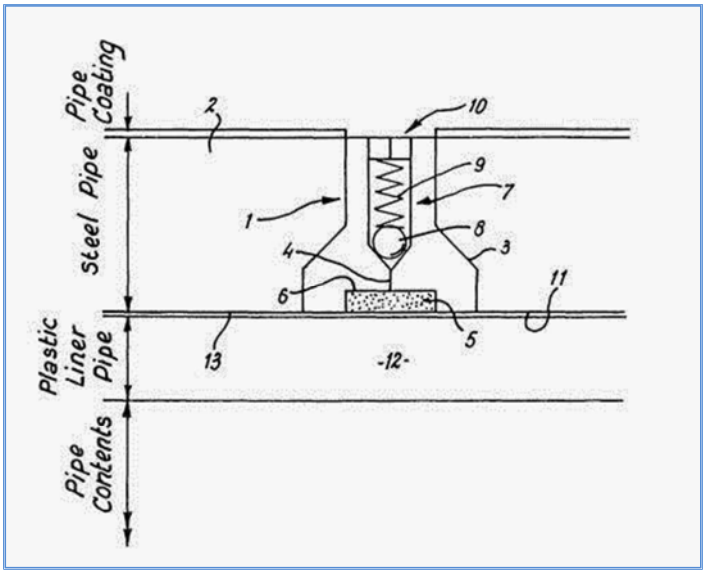

Figure 2-6: LinerVent™ design inserted through pipeline wall (McIntyre, 2000)

2.4.2 LinerVent™ Installed within Plastic Liner

In 2000, Boreas Consultants Ltd invented and patented another LinerVent™ design for installation within the plastic liner (McIntyre, 2006). This invention was an improvement on the earlier venting device discussed above where the vent was fitted on the pipe wall. The new LinerVent™ device is inserted into the perforation in the plastic liner and retained in place by threading, gluing or fusing. Unlike the first design, the current one allows gases that have accumulated within the micro-annulus to escape into the pipeline bore and not to the external environment.

The LinerVent™ is shown schematically in Figure 2-7. The LinerVent™ is inserted into a pre-drilled hole in the wall of the plastic liner. The bottom of the LinerVent™ is exposed to the micro-annulus while the top flushes with the plastic liner exposed to the pipeline bore with the flowing hydrocarbons fluid.

It is pertinent to note that this later invention allows gas flows back into the fluid stream, as opposed to the initial invention which vents gas to the surroundings, which

introduces undesirable contents of the hydrocarbon to the surrounding. In addition, the liner is not exposed to any external pressure which could also lead to corrosion or collapse. It is also worthy of note that the perforation and the LinerVent™ device have been designed to provide the most effective control of corrosion and reduce transport of corrosive medium behind the liner due to fluid turbulence.

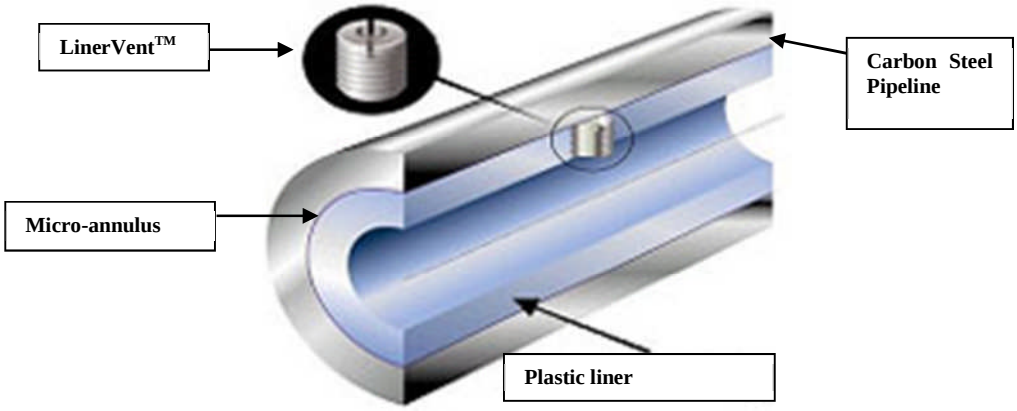

Figure 2-7: Pictorial view of LinerVent™ with inserted within plastic liner (Swagelining)

Finally it is important to note that the plastic liner and the LinerVent™ are all designed to prevent corrosion of the internal surfaces of carbon steel pipelines which is exposed to the harsh CO_2 environment and seawater. Therefore it is important to discuss CO_2 corrosion and the factors that influence this type of corrosion especially in the oil and gas industry**.**

2.5 Corrosion Theory

Corrosion generally is defined as the destruction or deterioration of a substance or its properties because of an adverse reaction with its environment (Fontana, 1986). Almost all metals are affected by their environment because of their inherent tendency to corrode and form a combined state where they are thermodynamically stable (Trethewey and Chamberlain, 1995). In order for corrosion to take place, there must be an anode, a cathode, a reducible reactant, an electrical connection through which the current flows and the electrolyte for ion migration. Metallic atom M undergoes anodic

reaction and is converted into metallic ion after losing n valency electron(s) according to the following reaction:

Anodic Reaction:

$$M \rightarrow M^{+n} + ne^{-}$$ **Equation 2-1**

There are however several cathodic reaction depending on the environment. The most common cathodic reaction are:

Cathodic Reactions:

$$2H^{+} + 2e^{-} \rightarrow H_2$$ **Equation 2-2**

$$O_2 + 4H^{+} + 4e^{-} \rightarrow 2H_2O$$ **Equation 2-3**

$$O_2 + 2H_2O + 4e^{-} \rightarrow 4OH^{-}$$ **Equation 2-4**

It is pertinent to note that Equation 2-2 which is the evolution of hydrogen is a common cathodic reaction because most of the operating environments are acidic. In addition, oxygen reduction, Equation 2-3, is another common cathodic reaction because of the presence of oxygen in the air.

If this corrosion theory in aqueous environment is applied to iron exposed to air, the following anodic and cathodic reactions are obtained:

Anodic Reaction:

$$Fe \rightarrow Fe^{2+} + 2e$$ **Equation 2-5**

Cathodic Reaction:

$$O_2 + 2H_2O + 4e^{-} \rightarrow 4OH^{-}$$ **Equation 2-6**

In the absence of oxygen, hydrogen is liberated and the cathodic reaction becomes:

$$2H_2O + 2e^- \rightarrow H_2 + 2OH^-$$ **Equation 2-7**

These two electrochemical reactions occur at microscopic anodes and cathodes on the corroding metal surface as shown in the schematic diagram in Figure 2-8. Combining the two half-cell reactions, the overall reaction becomes:

Overall Reaction:

$$2Fe + 2H_2O + O_2 \rightarrow 2Fe^{2+} + 4OH^- \rightarrow 2Fe(OH)_2\downarrow$$ **Equation 2-8**

The ferrous hydroxide is unstable and reacts with more oxygen to form a ferric salt called red rust as shown below (Rothwell and Tullmin, 2000):

$$4Fe(OH)_2 + 2H_2O + O_2 \rightarrow 4Fe(OH)_3 \rightarrow 2Fe_2O_3 + 6H_2O$$ **Equation 2-9**

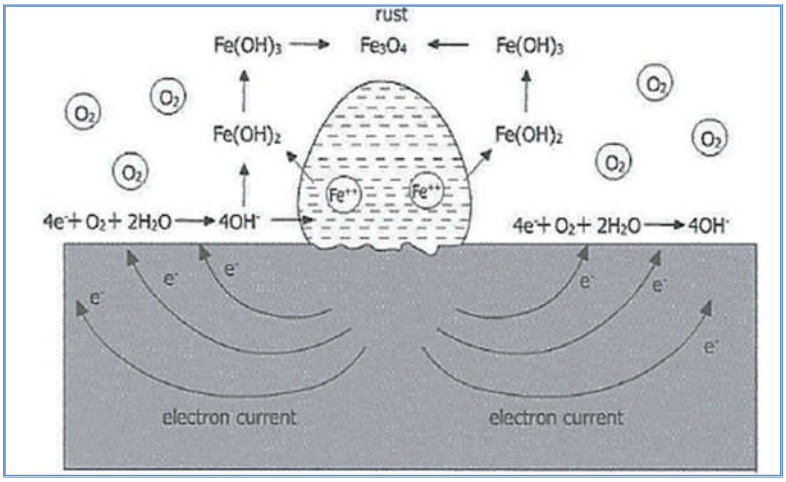

Figure 2-8: Schematic illustration of corrosion reaction of iron (Ahmad, 2006)

For corrosion to take place, the anodic and cathodic reactions must take place at the same rate. The anodic reaction is indicated by an increase in electrons and depletion of the metal forming its own ion, while that of the cathodic reaction is the consumption of electrons. The anode reaction results in a negative charge and corresponds to a negative potential while the cathode reaction in a positive potential.

2.6 Types of Corrosion

There are several types of corrosion depending on the material(s) involved and the environment. It is therefore important to discuss some of the corrosion types that could be encountered in the oil and gas environment. There could be situations where more than one type of corrosion could be observed on a particular material or one type leading to another or a more severe corrosion attack. The following subsections will discuss some of the different types of corrosion which are based on the appearance of the corroding substance.

2.6.1 Uniform Corrosion

Uniform corrosion is one of the commonest forms of corrosion attack of materials. As the name signifies, it is characterised by an electrochemical reaction taking place almost uniformly over the exposed surface of the corroding substance. Uniform corrosion is characterised by a reduction in thickness in a relatively uniform manner over the entire surface (Ahmad, 2006). The surface of the corroding material is gradually eroded until its structural integrity is compromised.

2.6.2 Pitting Corrosion

Pitting corrosion is the leading cause of internal failures in hydrocarbon production and processing equipment in the oil and gas industry (Clark et al., 2007). It is a localised corrosion which is very destructive because of the perforations that are created in the corroding material. In most cases this type of corrosion is not easily noticed because the perforations called pits are small and difficult to detect as they could be covered by some coatings or by the corrosion products (Rothwell and Tullmin, 2000). Figure 2-9 is a picture showing pitting corrosion of a metal surface. Inside the pits very corrosive medium are formed due to the process of hydrolysis. Kvarekval and Dugstad (2005) demonstrated that pitting corrosion attacks have occurred with penetration rates up to 5 mm/y and that the intensity and penetration rate of this type of corrosion is a function of the pH of the environment.

Pitting corrosion is particularly dangerous because the localized pits which are hidden could lead to degradation of structures resulting in sudden failures (Papavinasam et al., 2005). It predominantly occurs in stainless steel structures where the passivity has been broken and on other systems where corrosion inhibitors passivate the steel surface (Ijesseling, 2000).

Figure 2-9: Picture showing pitting corrosion of a metal surface (Clark et al., 2007)

2.6.3 Erosion Corrosion

As the name signifies, erosion corrosion is the deterioration of a material due to the relative movement between the corrosive medium and the material surface. In case of metallic substances, the rapid movement of the fluid mechanically erodes the metal to form ions and in the case where corrosion products are formed, they are removed leading to increased corrosion. Serious erosion problems have been encountered by many offshore field operators in CO_2 fields because of high fluid velocity (Crolet and Bonis, 1986).

This type of corrosion is characterised physically by the presence of grooves, waves, gullies, holes, and valleys showing the direction of the eroding medium (Fontana, 1986). Impingement resulting from impact of liquid particle can be categorised as a special form of erosion corrosion which can lead to serious material damage (Rothwell and Tullmin, 2000).

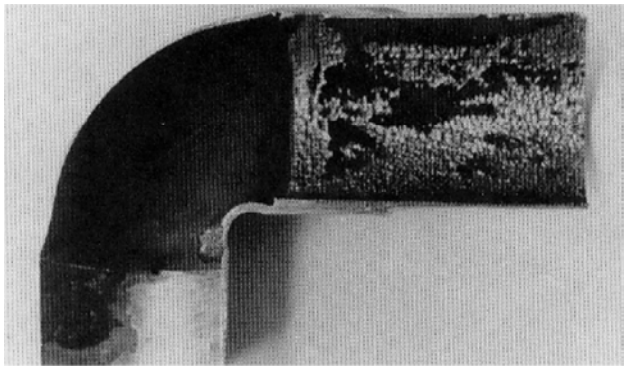

Figure 2-10: Erosion corrosion of pipeline (Postlethwaite and Nesic, 2000)

2.6.4 Crevice corrosion

This is a localised corrosion mechanism that occurs mostly within crevices or covered areas on metal surfaces exposed to corrosive substances. Abdulsalam and Pickering (1998, pg 1336) defined *crevice corrosion as a dangerous form of localised corrosion, which occurs as a result of the occluded cell that forms under a crevice on the metal surface*. According to the author, crevice corrosion is more pronounced on systems which rely on the formation of passive films for corrosion resistance. Crevice corrosion is caused by a change of the crevice environment with respect to the bulk solution and was described by some researchers as resulting from the effect of differential aeration (Shreir et al., 1994). For instance, any difference in the oxygen concentration between the external environment and the crevice will lead to accelerated corrosion within the crevice area.

This type of corrosion attack is predominantly seen where very small volumes of stagnant corrosive solution are trapped in places like lap joints, gasket surfaces, spaces under bolts, under rivet heads and surface deposits (Fontana, 1986). The combination of metallic material and non-metallic material such as gaskets, concrete, plastics, glass and asbestos (used either for construction or protection) can cause crevice corrosion. Other causes include cracks, cavities, barnacles, bio-fouling organisms, dirt or deposits on the metal surface.

Corrosion within Annular Space

It is important at this stage to mention that the crevice corrosion model treated in this research is actually corrosion within an annular space rather than the conventional crevice corrosion. This corrosion model is not driven by an external cathode. Both the anode and cathode are located within the annular space and therefore the pH is not expected to change. However, crevice corrosion in brine containing CO_2 would be possible in the correct material configuration. The carbonic acid would be reduced at the exposed external cathode and anodic metal loss would occur in the crevice.

2.6.4.1 Factors affecting Crevice Corrosion

Lee et al. (1984) categorised the factors that affect the prediction of crevice corrosion into three categories: geometrical, metallurgical and environmental. The geometrical factors include crevice gap, crevice depth, area ratio of creviced area to exposed cathode area, number of crevices and crevice type (Oldfield and Sutton, 1978b). The metallurgical factors include the alloy composition and level of impurity in the steel. Finally the environmental factors include, among others, the temperature, pH, concentration of chloride ion and oxygen. Figure 2-11 is a schematic of the factors that affect crevice corrosion.

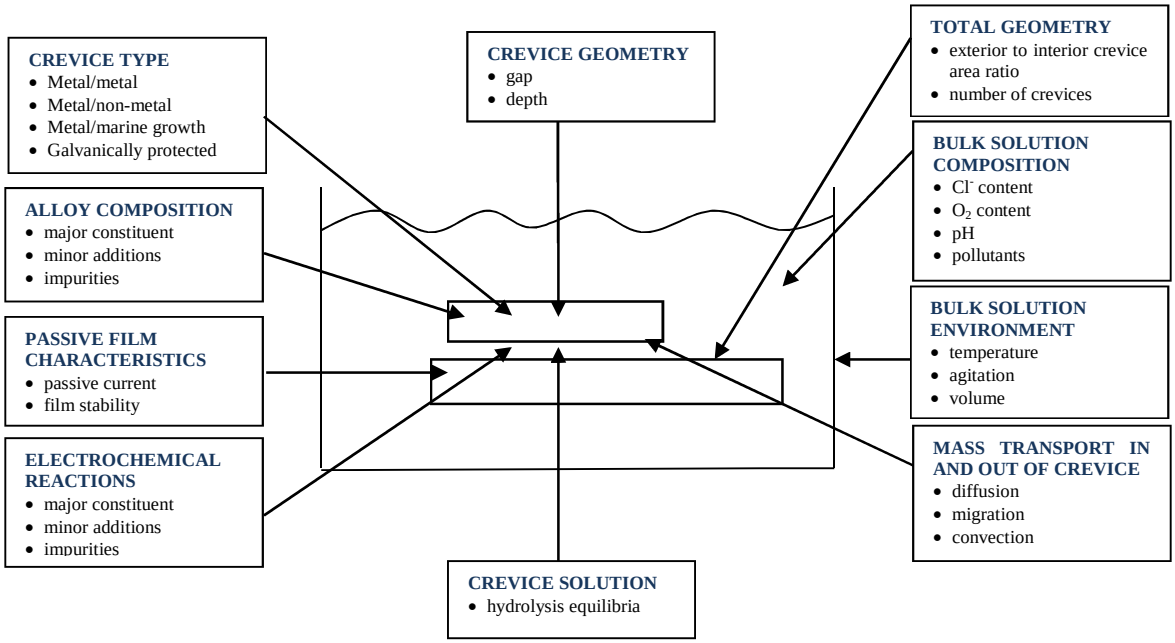

Figure 2-11: Schematic of factors that affect crevice corrosion (Oldfield and Sutton, 1978b)

Crevice Geometry

Crevice geometry is an important factor because it influences the potential distribution and the polarization curve and therefore the corrosion rate within a crevice (Abdulsalam and Pickering, 1998; Heppner et al., 2004; Kennell et al., 2008). The crevice gap influences the onset of crevice corrosion as it controls the mass transport of corrosive species and the potential gradient within the crevice (Mohammed, 2005). This is supported by Shreir et al. (1994) who demonstrated that a steep concentration gradient of the corrosive species are created with narrow crevices gaps and so are more prone to rapid crevice corrosion. According to the authors, crevices with large gaps are not affected so much by the mass transport of oxygen from the bulk solution. They concluded that if crevices cannot be avoided, then decreasing the aspect ratio between the crevice depth and crevice gap can reduce the severity of crevice corrosion.

In their study on the effect of crevice gap on the initiation of crevice corrosion in passive metals, Heppner et al. (2004) demonstrated that as the crevice gap decreases in size, the current density flowing within the crevice and the rate of migration of Cl^- increases, thus shortening the time required for the formation of a CCS. Conversely, for

larger crevices, they showed that the crevice solution was milder with higher pH, lower passive current and reduced Cl^- concentration and therefore a longer time was required to attain steady-state conditions.

The crevice depth, like the crevice gap, also affects the mass transport of corrosive species within the crevice. In addition, as the crevice depth decreases, the potential becomes more positive (Abdulsalam and Pickering, 1998) .

Crevice Type

Crevice type relates to the configuration of the crevice, that is, whether it is the union of two metals (metal-to-metal), metal-to-nonmetal or biofouling organisms covering the surface. Crevices formed between metal and nonmetals are of significant concern because the crevice gap is typically smaller in geometry compared to metal-to-metal. As such a tighter crevice geometry is formed which facilitates capillary action leading to severe crevice corrosion.

Passive Film Characteristics

This is very important as will be discussed later. The nature of the passive film determines the ease with which the breakdown of the passive film results when there is crevice corrosion attack.

Bulk Solution Composition and Environment

The bulk solution includes the solution composition and the environmental effects. The very important environmental factors that affect crevice corrosion include the temperature, agitation and volume. In general, the initiation of crevice corrosion of stainless steel is not very much affected by increase in temperature. However, its rate of propagation is decreased when the temperature is between ambient and 70 °C (Ahmad, 2006).

The solution composition is determined by the presence of corrosive species like Cl^- ion and oxygen; and other factors like the pH. The presence of aggressive species within the solution results in the severity of crevice corrosion attack.

Tan et al. (2001) in their work on mapping non-uniform corrosion using the wire beam electrode investigated crevice corrosion by measuring the corrosion rate of steel in CO_2 and O_2 environments. It was shown that the crevice corrosion behaviour under O_2 environments was more aggressive compared to that of the CO_2. In addition, in the O_2 environment, the corrosion potential was about 300 mV more negative than outside the crevice (bold surface).

Mass Transfer into Crevice

Mass transport of species from the bulk solution into the crevice is mainly by diffusion, migration and convection (Ahmad, 2006). As corrosive species are transported into the crevice, their concentration increases very fast thereby increasing the activity within the crevice.

2.6.4.2 Mechanism of Crevice Corrosion

There are two main theories which are commonly used by most researchers to explain the mechanism of crevice corrosion in materials. These are namely the Critical Crevice Solution Theory (CCST) and the IR Drop Theory (IRDT) (Kennell et al., 2008). Both theories are similar in explaining the low levels of crevice corrosion at initial stages in terms of the generation of a passive current and oxygen depletion within the crevice. This action results in making the crevice wall an anodic site and the exterior surface a cathodic site.

Critical Crevice Solution Theory

The critical crevice solution theory (CCST) is based on the attainment of certain chemical and electrochemical changes in the crevice solution in terms of the pH and chloride ion concentration (Sharland, 1992). According to the CCST, at the start of crevice corrosion, oxygen is depleted within the crevice and the passive current generated causes anions, Cl^- ions in particular, to migrate into the crevice causing the pH to drop. Increase in the concentration of Cl^- ions coupled with the decrease in pH makes the crevice solution very corrosive. Anodic reactions may increase causing a further reduction in pH and an increase in the rate of transport of anions into the crevice

space. The corrosive crevice solution attacks the passive film with a consequent destruction of the crevice wall.

Oldfield and Sutton (1978a) studied crevice corrosion of stainless steel experimentally and confirmed the high concentration of $Cr^{3+,}$ Fe^{2+} and Cl^- ions within the crevice solution and a high activity of H^+ ions (low pH values). They demonstrated that when these values reach a critical concentration, there is a corresponding breakdown of the passive film, characterised by a sudden drop in the E_{corr} to the active region. In their work the critical crevice solution composition was taken as that which gave an active peak current of 10 $\mu A/cm^2$, representing the onset of significant crevice corrosion. They concluded that the corrosion potentials (E_{corr}) inside the crevice are lower than the potentials outside and this fall is accompanied by an increase in the corrosion current.

IR Drop Theory

According to the IR drop theory, crevice corrosion will start immediately the potential difference between the crevice and the outside surface reaches a critical value that the anodic potential becomes active (Kennell et al., 2008). The potential drop is affected by the concentration gradient of corrosive species, composition and the geometry of crevice. The effect of IR drop for steel is shown in Figure 2-12 below.

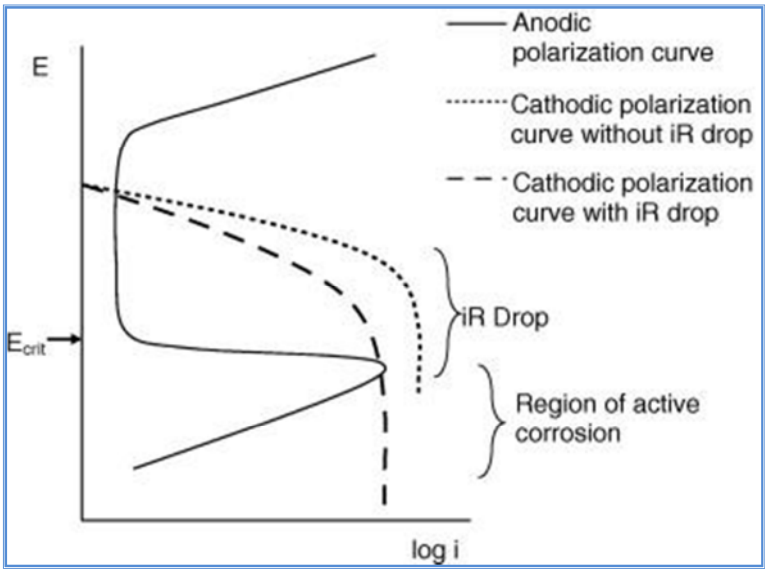

Figure 2-12: Polarization diagram showing the effect of IR drop for a passive metal (Kennell et al., 2008)

The figure shows the effect of IR drop on the polarization curve. The cathodic curve cuts the anodic curve at the passive region with a very low corrosion rate when there is no IR drop effect. However, the effect of IR drop moves the anodic curve to cut the cathodic curve below the critical potential resulting in a large corrosion current/rate.

Oldfield and Sutton (1978b) in their work on the mathematical modelling of crevice corrosion developed a crevice corrosion model that could be used to predict corrosion susceptibility of stainless steel material. They demonstrated that the mechanism of crevice corrosion involves the four steps below:

Depletion of oxygen within the crevice solution. First as dissolved oxygen is consumed at cathodic sites close to exterior (bold) surface of the crevice, they are replaced from the bulk solution. However, within the restricted crevice area, transport of oxygen is limited leading to depletion of supply and the eventual polarisation of the metal surface to a negative potential. The E_{corr} also rises due to the restoration of the passive film (Oldfield and Sutton, 1978a).

Decrease in pH and Increase in Cl^- ion in the crevice solution. In this stage, the pH in the crevice falls as a result of the hydrolysis of the metal ions which generates hydrogen ions. Hydrolysis of metal ions also results in an increase in the concentration of the Cl^- within the crevice due to migration.

De-passivation and onset of rapid corrosion. During this stage, the pH falls to a very low level and the concentration of Cl^- rises to a very high level, leading to the break-down of the passive film. There is also a relatively rapid fall in E_{corr} from the passive region to about -300 mV (SCE). Figure 2-13 shows the changes in the potential within the crevice for type 316 stainless steel. This crevice solution composition is critical crevice solution (CCS). Sharland (1992) agrees that rapid crevice corrosion is preceded by the formation of the critical crevice solution. For most stainless steels, the passive film breaks down between pH 1 and 2 (Oldfield and Sutton, 1978b).

Propagation of crevice corrosion. This stage begins with the complete breakdown of passivation and rapid dissolution of the alloy inside the crevice (propagation). During this stage, the E_{corr} remains at a low value, indicative of active corrosion inside the crevice.

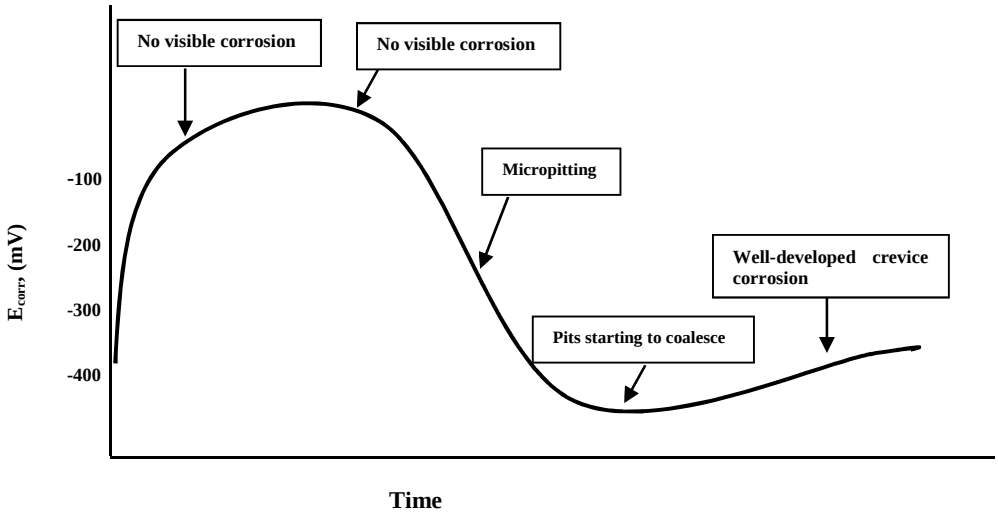

Figure 2-13: Schematic Ecorr/time curve showing the development of crevice corrosion of type 316 crevices (Oldfield and Sutton, 1978a)

It is pertinent to note that the Oldfield and Sutton model does not take into account the concentration gradient of the corrosive species within the crevice but only mass transport of the species.

Kennell et al. (2008) in their work on critical crevice solution and IR drop crevice corrosion model categorised the stages of crevice corrosion into three: incubation, initiation and propagation. They believe that crevice corrosion can move into an initiation stage characterised by high corrosion rate or remain in the incubation stage without corrosion. As such their model tries to factor the influence of the critical crevice solution theory (CCST) and the IR drop theory (IRDT) to explaining crevice corrosion.

They demonstrated that the incubation period is followed by an increase in the concentration gradient and passive current causes the crevice solution potential to fall below a critical value (especially at the tip) leading to active corrosion. The propagation stage is associated with more diffusion of corrosive species into the crevice coupled

with hydrolysis of metal ions within the crevice. As a result the crevice becomes active with the highest level of corrosion occurring around the crevice mouth because of the higher surface over-potential.

Oldfield and Sutton (1996) in their work on the prediction of initiation and propagation of crevice corrosion on aluminium alloys in seawater investigated crevice corrosion of aluminium, which relies on its protective film for corrosion protection. They demonstrated that as the pH drops, the potential within the crevice increases to the pitting potential leading to the initiation of severe crevice corrosion (Figure 2-14).

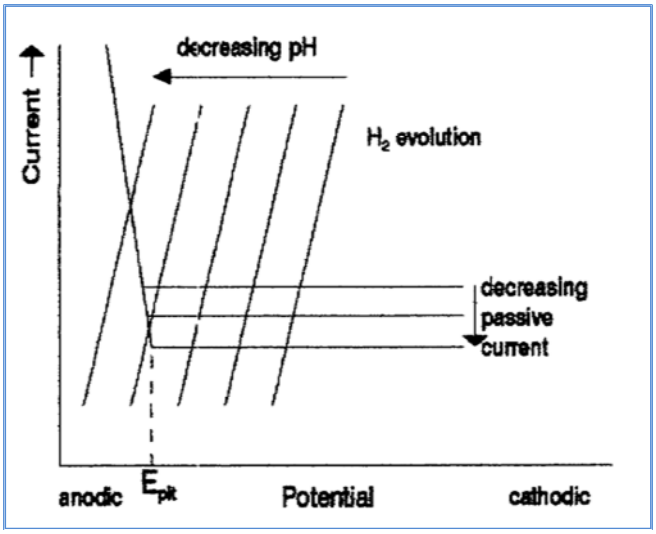

Figure 2-14: Schematic of crevice corrosion mechanism of Al-alloys (Oldfield and Sutton, 1996)

It can be seen from the figure that as the pH decreases, the corrosion potential increases and eventually exceeds the pitting potential. Also as the passive current decreases, the pH at which the pitting potential is attained increases. The pH drop within the crevice was predicted to be above 2.9. According to Alavi and Cottis (1987) the pH of part of the crevice formed by the aluminium alloy was slightly acidic (pH 3 – 4) while deeper into the crevice, the solution is alkaline (pH 8). They concluded that the pH within the crevice can never fall below pH 2.9 because at that point, the solubility product of aluminium chloride is reached (aluminium chloride dissolves to yield its ions).

2.6.5 Hydrogen Embrittlement

Hydrogen embrittlement is strictly not a type of corrosion but is all the same, one of the problems associated with corrosion attack of metallic substances. It occurs on a steel structure and may be caused by the evolution of hydrogen from cathodic reactions, over application of cathodic protection (CP) and by sulphate-reducing bacteria (SRB). The problem occurs when some of the H generated are absorbed into the steel structure and eventually leads to sudden brittle failures (Robinson and Kilgallon, 1994). Figure 2-15 is a picture of a carbon steel failure due to hydrogen embrittlement.

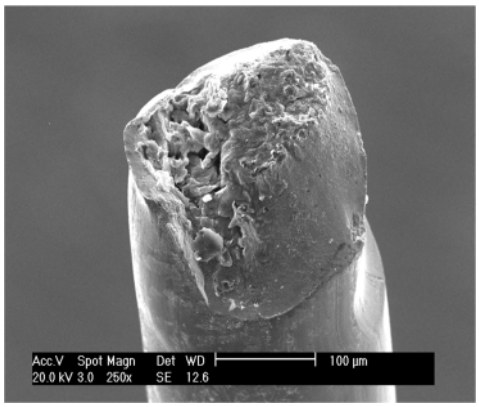

Figure 2-15: SEM picture of a carbon steel failure due to hydrogen embrittlement (Allison, 2004)

2.7 Corrosion in the Oil and Gas Industry

Corrosion attack to pipeline systems could either be external and/or internal due to the transported hydrocarbon (Duan et al., 2008). Corrosion of exterior surfaces is often tackled by coatings that prevent contact with the external environment and/or by cathodic protection. Internal corrosion is due to the presence of corrosive gases within the transported hydrocarbon and Figure 2-16 is an example of internal corrosion.

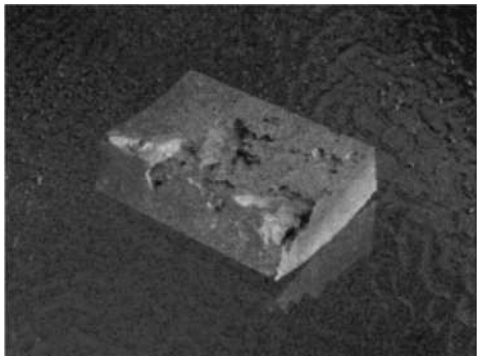

Figure 2-16: Pipeline for transporting CO_2-containing hydrocarbon fluids showing internal corrosion (Kermani and Morshed, 2003)

2.7.1 External and Internal Corrosion of Oil and Gas Pipelines

According to Teevens et al. (2008) internal and external corrosion are the leading causes of failures in petroleum pipeline operation. Of these two types of corrosion, internal corrosion is the most costly because of the challenges involved in controlling the same (López et al., 2003). Depending on the main corrosive agent, most internal corrosion problems could be sweet (CO_2 corrosion) or sour corrosion (H_2S corrosion) (Palmer-Jones and Paisley, 2000). Sweet corrosion is the most common type of internal corrosion and responsible for about 60% of oilfield failures (López et al., 2003). It is manifested in the form of uniform corrosion, pitting corrosion, mesa attack, erosion corrosion, corrosion fatigue, among others (Kermani and Smith, 1997).

2.8 CO_2 Corrosion Mechanism

The presence of CO_2 in hydrocarbons causes severe internal corrosion problems in oil and gas pipelines and is mostly influenced by the materials, medium and interphase-related (Schmitt and Horstemeier, 2006). Sweet corrosion is initiated by the dissolution of CO_2 gas in water and the subsequent formation of carbonic acid (H_2CO_3), which also lowers the bulk solution pH. The strong corrosive nature of the acid combined with the low pH increases the corrosion rate of transmission pipelines.

In order to control sweet corrosion in pipelines, it is important to understand the underlying mechanisms and thus be in a position to predict whether corrosion will be

initiated. This is because an understanding of the mechanism leads to a better corrosion protection design and therefore a good economic impact. The difficulty in the corrosion mechanism involving the cathodic and anodic processes makes it very challenging to predict the corrosiveness of carbonic acid. In addition the effect of formation water, reservoir high temperatures and pressures have made it even more difficult to simulate tests to come up with totally dependable predictive models.

De Waard and Milliams (1975) were among the first researchers of sweet corrosion to propose a mechanism for the prediction of corrosion process. This initial research was focussed on the corrosion rate as it relates to temperature and carbon dioxide partial pressures. The experiments were carried out at various temperatures up to 80 ˚C and the corrosion rates were monitored using the linear polarisation technique. The first most successful attempt at predicting the rate of sweet corrosion was achieved by using the 'De Waard-Milliams Equation (1993) shown below:

Equation 2-10

$$\text{Log}(v) = 7.96 - \frac{2320}{(t+273)} - 0.00555t + 0.67\log(P_{CO_2})$$

Where,

- v is the corrosion rate (mm/y)
- t is the temperature (ºC)
- P_{CO_2} is the carbon dioxide partial pressure (bars)

Another outcome of this work was the publication of the De Waard and Milliams nomogram, which is a simple and useful tool for quick estimation of the CO_2 corrosion rate. It is pertinent to note that despite the fact that this model did not take into account the presence of contaminants and the environment, theoretically calculated values of corrosion rate had good correlation with field data.

Crolet and Bonis (1986) developed a corrosion chart after studying the water chemistry and the acidity of field data from about 40 oil and gas wells. They concluded that the key factor in CO_2 corrosion is the chemical composition of the water. The work showed that there was no correlation between a single parameter of the corrosive medium and

the corrosive nature of oil wells. The parameters investigated included CO_2 partial pressure, temperature, ionic strength, among others. In addition, their work showed some relationship between corrosivity of oil wells and in situ pH; there were however some few exceptions.

Further work by De Waard and Milliams gave rise to a modern version of the equation which uses a different temperature dependent function based on Henry's constant and is presented below (Wang and Postlethwaite, 2001).

$$\text{Log (Vcor)} = 5.8 - \frac{1710}{(273+t)} + 0.67 \log(P_{CO_2}) \qquad \textbf{Equation 2-11}$$

Further work in this field showed that the use of Equation 2-11 will give a 'worst case' situation and that there are other factors that affected the corrosion rate. A more recent study by De Waard and Lot (1993) demonstrated the need for a review of the previous work. This work took into consideration the effects of protective corrosion product layers, partial dissociation of carbonic acid, corrosion products contamination, flow rate and operational conditions of the different oil wells and therefore the application of a correction factor. Addition of this correction factor has resulted in a modified nomogram (Figure 2-17) which gives a more reliable corrosion prediction.

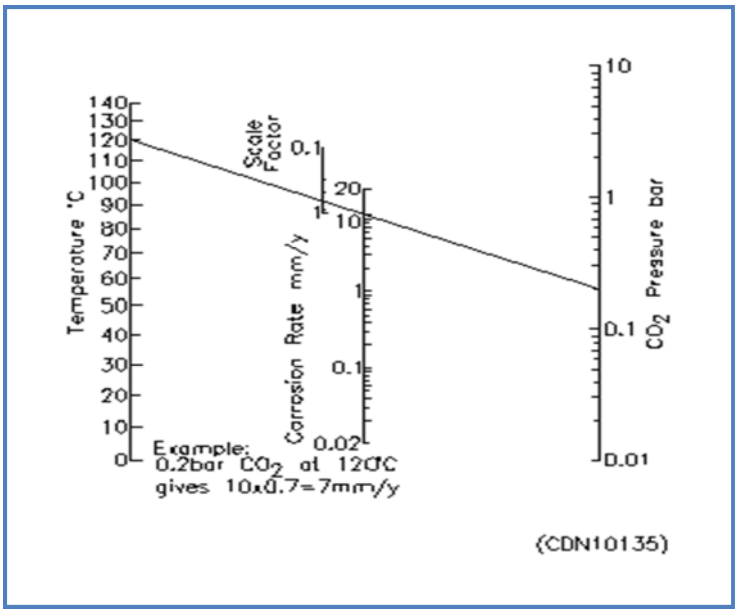

Figure 2-17: Modified De Waard-Milliams nomograph for predicting CO_2 corrosion rate (De Waard and Lotz, 1993)

2.8.1 Electrochemistry of CO_2 Reaction

The corrosion of carbon steel pipelines in CO_2 containing environments is principally associated with the dissolution of CO_2 in water (H_2O). The CO_2 reacts with H_2O to form carbonic acid (H_2CO_3). Three species are known to be present in the aqueous solution as shown in the equations below:

$$CO_2\,(g) + H_2O\,(l) \rightarrow H_2CO_3\,(l) \qquad \textbf{Equation 2-12}$$

$$H_2CO_3 \rightarrow H^+ + HCO_3^- \text{ [bicarbonate]} \qquad \textbf{Equation 2-13}$$

$$HCO_3^- \rightarrow H^+ + CO_3^{2-} \qquad \textbf{Equation 2-14}$$

Carbonic acid is classified as a weak acid with a low dissociation constant. Surprisingly, corrosion rates in carbon dioxide saturated solutions are greater than some known strong acids at similar pH values (Kermani and Smith, 1997). It has also been observed that carbonic acid causes serious corrosion when it comes in contact with carbon steel materials and the corrosion rates can reach very high levels. It is proposed that the

carbonic acid supplies a reservoir of H^+ ions. The electrochemical reactions occurring at the metal surface are shown below:

Cathodic reaction

$$2H_2CO_3 + 2e^- \rightarrow H_2 + 2HCO_3^- \quad \text{(Reduction)} \qquad \textbf{Equation 2-15}$$

$$HCO_3^- + H^+ \rightarrow H_2CO_3 \quad \text{(Regeneration)} \qquad \textbf{Equation 2-16}$$

$$2H^+ + 2e^- \rightarrow H_2 \quad \text{(Overall Reaction)} \qquad \textbf{Equation 2-17}$$

Anodic reaction:

$$Fe \rightarrow Fe^{2+} + 2e^- \qquad \textbf{Equation 2-18}$$

De Waard and Lotz (1993) believe that the high corrosion rate cannot be as a result of H^+ alone, as in the case of strong acids, because of the very limited number of H^+ ions generated. Therefore the high corrosion rate is thought to be caused by the direct reduction of carbonic acid in the corrosion process shown in Equation 2-15.

The above processes result in the formation of $FeCO_3$ corrosion product film on the metal surface. It is pertinent to note that $FeCO_3$ is a precipitate with low solubility which decreases with temperature. It forms only a partially protective film on the steel surface based on the environmental condition. Other researchers believe that most of the dissolved species are not just $FeCO_3$ but $Fe(HCO_3)_2$ according to the equation below (De Waard and Lotz, 1993):

$$Fe^{2+} + CO_3^{2-} \rightarrow FeCO_3 \qquad \textbf{Equation 2-19}$$

$$Fe^{2+} + 2HCO_3^- \rightarrow Fe(HCO_3)_2 \qquad \textbf{Equation 2-20}$$

$$Fe(HCO_3)_2 \rightarrow FeCO_3 + CO_3 + H_2O \qquad \textbf{Equation 2-21}$$

This mechanism is similar with a recent work by Dayalan, et al. (1998b). They simplified the CO_2 corrosion mechanism into four steps with the same three species (H^+, H_2CO_3 and HCO_3^-) discussed above as the major contributors in the sweet corrosion process.

The quantity of CO_2 dissolved in solution at the given CO_2 partial pressure and temperature can be calculated using Henry's law (Shayegani et al., 2008).

$$P_{CO_2} = K_H[CO_2] \qquad \textbf{Equation 2-22}$$

Where,

- P - partial pressure of CO_2 (in bars)
- C - concentration (in mol/L)
- K_H - Henry's constant (L.bar/mol)

Due to these electrochemical processes, corrosion products are formed on the corroding metal surface. Depending on the concentration of the corrosion product ($FeCO_3$) formed and other factors, the steel surface could be protective or not.

2.8.2 CO_2 Corrosion Products

The formation of CO_2 corrosion products is complex and influenced by many factors such as the supersaturation of $FeCO_3$ in solution and its precipitation rate (Gao et al., 2011). As corrosion product layers play a very important role in CO_2 corrosion, many studies have been carried out to study the corrosion product. Some researchers have suggested that the corrosion product formed on the steel surface are made up of an insoluble part ($FeCO_3$) and undissolved part from the steel called cementite (Fe_3C) (Hong et al., 2000). Gao et al. (2011) went further to demonstrate that the protectiveness of the corrosion product films are affected by many factors such as the pressure, temperature, flow rate and pH, with temperature and pressure been the most critical.

The nature and protectiveness of the corrosion product determines the corrosion rate of the metal. Studies have shown that the formation of $FeCO_3$ tends to decrease the

corrosion rate (Hong et al., 2000) while that of Fe_3C could result in high corrosion rates especially at the beginning of the CO_2 corrosion process (Gao et al., 2011).

However, De Waard and Lot (1993) demonstrated that generally the presence of corrosion products in a solution saturated with CO_2 will reduce the corrosion rate and that without some of these corrosion products, much higher corrosion rates are possible.

2.8.2.1 Iron Carbonate ($FeCO_3$) Corrosion Product

The most common type of corrosion product encountered in CO_2 corrosion is iron carbonate and is formed when the concentration of Fe^{2+} and CO_3^{2-} exceeds the solubility limit, as shown in Equation 2-19. When the rate at which the corrosion product precipitates on the surface exceeds the rate of corrosion, thick protective scales are formed. However, when the corrosion rate exceeds the rate at which the corrosion product precipitates, a porous and unprotective scale is formed (Nesic, 2007). It is important to note that at room temperature, the precipitation process is slow and unprotective scales are formed while at high temperatures precipitation proceeds faster with the formation of protective scales (Nesic, 2007).

According to Schmitt and Horstemeier (2006) the precipitation rate of $FeCO_3$ is slow but is influenced by temperature and that even under supersaturated situations, the corrosion rate could be high until a protective layer was formed. They therefore suggested that the kinetics of $FeCO_3$ precipitate could be the controlling factor for the protectiveness of the corrosion product. They however agreed that at higher pH values (6.5 and above), protective iron carbonate films could be formed at room temperature. Hong et al. (2000) demonstrated that the protectiveness of $FeCO_3$ depended on the extent of surface coverage and the property of the film. They went further to state that the tendency to form the $FeCO_3$ film is a function of the saturation factor (Fsat) which is given as:

$$\text{Saturation Factor (Fsat)} = \frac{[Fe^{2+}]s\,[CO_3^{2-}]s}{K_{sp}} \qquad \textbf{Equation 2-23}$$

Where,

- $[Fe^{2+}]$ – surface concentration of Fe^{2+}
- $[CO_3^{2-}]$ – surface concentration of CO_3^{2-}
- Ksp – solubility product of $FeCO_3$ in a saturated solution at given temperature

Wang and Postlethwaite (2001) demonstrated in their experiments that corrosion product films could be formed at low temperatures (below 60 °C) and CO_2 partial pressure of 1 bar while films do form are not protective.

2.8.2.2 Iron Carbide (Fe_3C) Corrosion Residue

Schmitt and Horstemeier (2006) demonstrated that at temperatures below 40°C, the steel surface consisted mainly of Fe_3C with some $FeCO_3$ and carbonates of alloying metals. They mentioned that the Fe_3C was part of the original steel microstructure and suggested that they could serve as sites for cathodic reaction.

A current work by Martinez et al. (2011) is also in agreement with the work of Schmitt and Horstemeier (2006). In their work, they demonstrated that the corrosion product consisted predominantly of Fe_3C residue with smaller quantities of $FeCO_3$. Their SEM results showed that the corrosion that had taken place in the carbonic acid environment had selectively removed the ferrite phase, leaving behind Fe_3C with a resultant porous and non-protective structure. They attributed this to be the reason for the initial limited corrosion protection observed and concluded that for $FeCO_3$ films to be formed, Fe^{2+} ions must be in sufficient quantity.

2.9 Factors affecting CO_2 Corrosion

The overall process of CO_2 corrosion is complex and is influenced by a number of factors such as temperature, fluid characteristics (CO_2 partial pressure, gas/liquid ratio, formation water composition, water-to-oil ratio, pH), flow characteristics, and material characteristics (Dayalan et al., 1998b). These parameters are mainly dependent on the reservoir characteristics and on enhanced oil recovery techniques which introduces additional variables (Wang and Postlethwaite, 2001). It is therefore imperative to briefly

discuss some of these parameters and the extent to which they affect the sweet corrosion process.

2.9.1 Effect of Gas Pressure

The partial pressure of CO_2 in the hydrocarbon stream is an important parameter in CO_2 corrosion because the corrosion rate of a CO_2 saturated solution is generally dependent on the CO_2 partial pressure. This is because the CO_2 partial pressure is directly related to the carbonic acid concentration. Assuming other conditions are constant, the corrosion rate of carbon steel increases when the partial pressure of CO_2 increases. Studies have also shown that there was an increase both in the solubility of CO_2 and the acidity of the produced fluids with increasing CO_2 partial pressure (De Waard and Milliams, 1975).

The De Waard-Lotz equation presented in Equation 2-11 indicated that if other conditions in a CO_2 corrosion environment are constant, the corrosion rate [log(Vcor)] is proportional to the CO_2 partial pressure [$\log(P_{CO_2})$] with a proportionality factor of 0.67. Other researchers found out experimentally that this value is between 0.5 to 0.8, which agrees well with the de Waard-Lotz equation (Wang and Postlethwaite, 2001).

Since natural gas is not completely an ideal gas, increase in the system pressure will affect the CO_2 partial pressure and so De Waard and Lot recommended the use of CO_2 fugacity (fCO_2) which takes account of the system pressure. The corrosion rate is therefore given as (De Waard and Lotz, 1993):

Equation 2-24

$$\text{Log } V_{nomo} = 5.8 - \frac{1710}{T} + 0.67\log(f_{CO_2})$$

Where,

- $f_{CO_2} = a \times P_{CO_2}$
- a – fugacity coefficient
- T - temperature

2.9.2 Effect of Temperature

Corrosion rates generally increase with increasing temperatures when no protective surface films are present on the corroding surface (Wang and Postlethwaite, 2001). As discussed earlier, the precipitation of $FeCO_3$ does not necessarily result in a protective film formed over the metal surface. At temperatures below 60 ˚C, the corrosion product film, if formed on the surface of the metal, is porous, weak and easily removed by flowing liquids. However, most of the research work on the effect of temperature on the corrosion rate shows that the corrosion rate increases until it gets to a maximum value at about 70 ˚C – 80 ˚C. After this point, the corrosion rate decreases due to the formation of a more protective $FeCO_3$ film (De Waard and Lotz, 1993).

Their work further demonstrated that at temperatures above 80 ˚C, the corrosion product film formed is different from the one formed at temperatures below 60 ˚C because it is stronger, non-porous, protective and not easily removed by flowing liquid. This maximum temperature preceding the drop in corrosion rate is called the *Scaling Temperature* (De Waard et al., 1991) and is given as:

$$T_{scale}\,(K) = \frac{2400}{[6.7+0.6\log(fCO2)}$$ **Equation 2-25**

Increasing the CO_2 partial pressure and the pH of the bulk solution tends to lower the scaling temperature and so a protective corrosion film forms earlier with a drop in the corrosion rate. On the other hand, a higher flow rate increases the scaling temperature so that a protective corrosion film forms at a much higher temperature. Therefore for temperatures above 60 ˚C, it was necessary for a correction factor F_{scale} to be introduced into the corrosion rate equation (Equation 2-25) to account for the corrosion product formed (De Waard et al., 1991).

Under the right conditions and temperatures above 80 ºC, $FeCO_3$ corrosion product formed are impervious and reliable to protect the steel surface. Because of the protective nature of the $FeCO_3$ scales formed on the steel surface, the corrosion rate at temperatures exceeding scaling temperature decreases to values close to zero (Dayalan

et al., 1998b). However, it is important to note that the protection offered by the corrosion product film cannot be completely relied upon as it depends on other factors. These factors include the nature of the film, solution pH, and fluid velocity among others. It has been reported that at high temperatures protective scales have been eroded by high-speed liquids (De Waard et al., 1991).

2.9.3 Effect of Flow Velocity

Flow induced corrosion of low carbon steels is commonly encountered in oil and gas production and has been extensively studied over the past decades because of the effects of flow velocity in CO_2 corrosion system. It has been demonstrated that fluid flow has a major influence in the prediction of corrosion rate of carbon steel (Fosbol et al., 2009; Filbo and Orazem, 2001). It is accepted commonly that hydrodynamics and mass transport influence the corrosion process in flowing fluid environments. This is because high velocity flow can result in high shear stress near the pipeline wall and high mass transfer in the diffusion boundary layer (Meng and Jovancicevic, 2008). According to Lopez et al. (2003) the corrosion rate usually increases with flow velocity because the fluid flow prevents the formation of $FeCO_3$ corrosion films, remove the existing films or retard its growth.

This is also in line with the work of Nesic (2007) who gave two main ways in which flow affects CO_2 corrosion. The first case is when no protective film is formed. In this case fluid flow enhances the transport of corrosive species towards the carbon steel surface and so leads to an increase in the corrosion rate. The second case is when a protective film is formed. Here the flow interferes with the formation of the protective film by eroding it and so increase the corrosion rate. This is also in agreement with the work of Olsen et al. (2005).

Turbulence in a pipeline is an important factor in pushing a sweet corrosion system into a corrosive regime. According to Nesic (2007) high fluid velocity could lead to serious localized attack in wells containing CO_2 provided other conditions are favourable. De Waard and Lotz (1993) demonstrated that high flow velocities could double the corrosion rate.

Van et al. (1996) also supported the fact that the adherence of a protective scale on a corroding steel surface is a function of many parameters including the flow rate of the medium. They went further to state that in the repair process of damaged protective $FeCO_3$ scale, flow velocity is most critical as it influences both the mass transfer and PH. Therefore it can be concluded that generally the corrosion rate of carbon steels generally increases with increasing flow velocity (Hara et al., 2000).

2.9.4 Effect of pH

The solution pH of a corroding medium is an important factor because of its strong influence on the corrosion rate especially at lower CO_2 partial pressures. Its effect is somehow indirect because it changes the conditions for the formation of iron carbonate and other scales (Nesic, 2007). Basically, the higher the pH of a medium, the lower the corrosion rate due to decrease in the solubility of $FeCO_3$ and subsequent scaling tendency. Also when the pH increases, the cathodic reduction of H^+ slows down with a resultant decrease of the anodic dissolution of iron (Schmitt and Horstemeier, 2006).

As discussed earlier, at temperatures above 80ºC reliable protective corrosion films are formed on the metal surface. However, below this temperature some protective film could be formed if the pH of corrosive medium is at least 6. When the pH is increased from about 3.5 to 5.5, the corrosion rate decreases by a factor of about 3 (Schmitt and Horstemeier, 2006), but could be affected by the flow velocity. De Waard and Lot (1993) demonstrated that at constant temperature and CO_2 pressure, an increase in pH will result in a decrease in the corrosion rate.

2.10 CO_2 Corrosion Modelling

Modelling the rate of sweet corrosion on carbon steel structures is very important as it will help corrosion design engineers to design oil and gas installations that will not fail outside the design life. Basically a mathematical model is a set of equations that establish relationships between system variables. In addition to predicting what could happen in a pipeline, modelling assists corrosion engineers in making correct decisions in relation to design, operation and control (Nesic, 2007).

There are three different approaches used for CO_2 Corrosion modelling: mechanistic, semi-empirical and empirical (Nesic, 2007). These models have been developed by owners of oil fields, researchers, designers, contractors and operators, for the purpose of corrosion rate prediction of pipelines and flowlines due to the presence of CO_2 in the hydrocarbon (Kapusta and Pots, 2004).

The early CO_2 corrosion models such as the De Waard and Milliams model were comparatively simple as only two parameters (CO_2 partial pressure and temperature) were considered (Papavinasam et al., 2005). However, with better understanding of the CO_2 corrosion process, the models grew in complexity as other important parameters such as protective scales, organic acids, flow velocity, pH among others were taken into account. It is therefore important to briefly discuss these model types.

2.10.1 Empirical Models

Empirical models are developed from little or no theoretical background (Nesic, 2007). They could be linear or non-linear mathematical correlation derived from measured corrosion rate data (Fosbol et al., 2009). The model developed by Dugstad et al. is one of the commonly used empirical models; other empirical models included the linear multiple regression model by Adams et al. and the recent non-linear model of Nesi*c* (2007).

2.10.2 Semi-empirical Models

The semi-empirical models are similar to the empirical models in that they are developed from measured corrosion rate data but differ with respect to the equations used for their derivation (Fosbol et al., 2009). One of the advantages of these models is their simplicity and requires less work in determining the corrosion rate. Unfortunately, like the empirical models they require large datasets and do not easily extrapolate to other systems (Fosbol et al., 2009). They are generally more popular in the oil and gas industry compared to other models because of their successful application. Examples of semi-empirical models include the popular De Waard and collaborators (Nesic, 2007)

and the recent models of Smith and De Waard, and Teevens et al. (2008), which included a software program.

2.10.3 Mechanistic Models

Mechanistic models have a strong theoretical background and the constants in the models have a physical meaning (Nesic, 2007). They take into consideration the chemical, electrochemical, transport processes and engineering principles and not just measured corrosion rate data (Olsen et al., 2005; Kapusta and Pots, 2004). Within their theoretical limits, they can be extrapolated to conditions outside of the database used to develop them with a good level of reliability (Fosbol et al., 2009). However, the main challenge with the mechanistic models is the fact that they are time consuming, difficult to develop and require more work to adapt them to new systems and are therefore not so popular with operators.

2.11 Corrosion Control Strategy

Corrosion being an electrochemical phenomenon can be controlled by altering the electrochemical condition of the corroding interface. Some metals form a corrosion product called a passive film which inhibits further corrosion thereby acting as a natural protective system, e.g. aluminium. For other metals, the corrosion product film formed is unable to protect further corrosion attack and therefore special corrosion protection designs are imperative to ensure material integrity. This is particularly true in the case of carbon steels used for pipeline production. The following subsections will be discussing two of these methods; namely cathodic protection and corrosion inhibitors.

2.11.1 Cathodic Protection

As discussed earlier (section 2.8.1), corrosion as an electrochemical reaction involves the transfer of electron between the anode and the cathode. The anodic reaction results in the metal dissolution with loss of electrons which is required for the reaction at the cathodic. Therefore if these electrons can be provided from an external source, the anodic reaction would be slowed down or stopped. This is the principle behind cathodic protection and is represented on the Evans diagram shown in Figure 2-18.

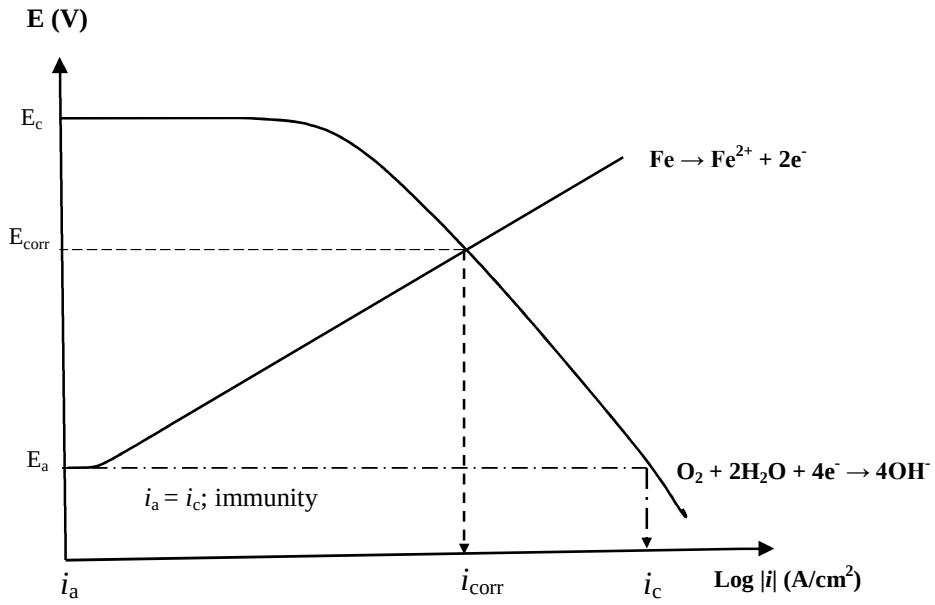

Figure 2-18: Evans diagram showing corrosion and principle of cathodic protection

The figure shows the reaction rates of the anode and cathode expressed in current density *i*. The current density (log *i*) (which is proportional to the corrosion rate) changes with respect to the electrode potential E. The two reaction rates are electrically balanced at the corrosion potential E_{corr}, which corresponds to the current density i_{corr}. Therefore to hold the metal at a potential below E_{corr}, electrons must be supplied.

At E_a, the anodic reaction rate is zero and therefore there is no metal dissolution. At this potential, a cathodic current equal to i_c must be available from an external source to maintain the metal at this potential and zero reaction of the anode. Imperatively if the potential can be held below E_a, the metal dissolution can be maintained at zero (i_a), but a cathodic current greater than i_c must be supplied.

Therefore cathodic protection brings the potential of the cathodic structure to values lower than corrosion/equilibrium potential so that the driving force to move electrons becomes zero or very small corrosion rate (Pedeferri, 1996). The reduction in the potential brings the metal from the corrosion zone to the immunity zone as shown in the Pourbaix diagram in Figure 2-19.

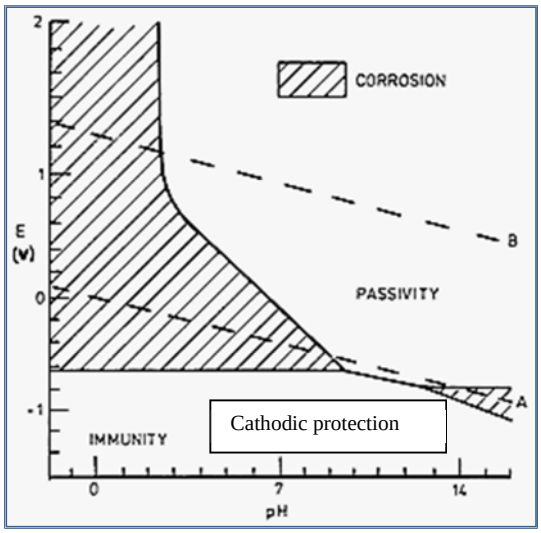

Figure 2-19: Pourbaix diagram for the iron-water system (Trethewey and Chamberlain, 1995)

Figure 2-19 is the Pourbaix diagram for iron-water system showing the regions of immunity, corrosion and passivity, and gives a guide to the stability of the metal in a specific environment. The immunity zone (below the corrosion potential) is required for the protection of iron (Kim, 2001) and it is the region sought for CP design.

There are two methods of applying CP namely impressed current and sacrificial anode. Impressed current is an electrically controlled design while a sacrificial anode uses a less noble metal which corrodes in preference to the material to be protected.

2.11.1.1 Impressed Current Cathodic Protection

Impressed current CP system (Figure 2-20) uses anodes which are connected to the positive terminal of an external direct current power source while the carbon steel structure to be protected is connected to the negative terminal of the dc power source. This design is to deliver relatively large currents from a limited number of anodes and is applied to large structures like ships, offshore rigs, etc.

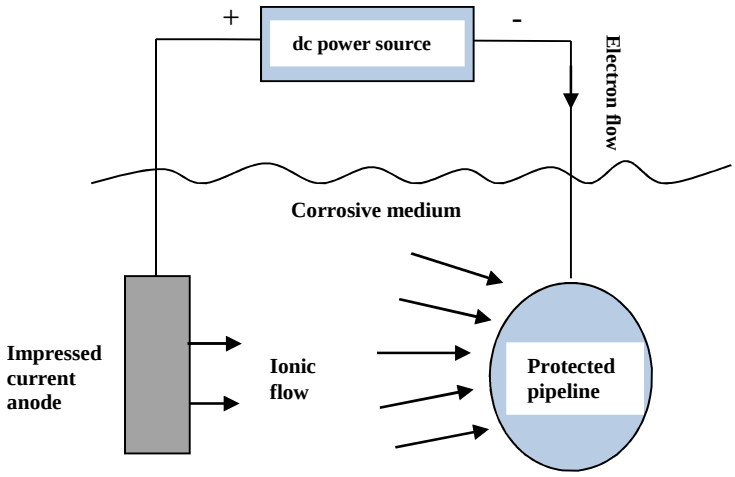

Figure 2-20: Schematic of impressed current CP system

2.11.1.2 Sacrificial Anode Cathodic Protection

The second cathodic protection method makes use of sacrificial anode materials that are more electronegative to the carbon steel structure to be protected (cathode). Electrical current flows from the more active anode to the carbon steel pipeline and in the process the anode corrodes while the carbon steel pipeline is protected from corrosion attack. Cathodic protection is achieved when the change in potential is sufficient to arrest corrosion. Figure 2-21 is a schematic of the sacrificial anode design. Typical sacrificial anode materials connected directly to the carbon steel pipeline structure for cathodic protection include zinc and magnesium (Thompson, 2006).

For design purposes Song (2010) demonstrated that the applied CP decreases the corrosion rate of carbon steel most effectively around the free corrosion potential and this decrease becomes less effective as the steel potential shifts in the more negative direction. It is therefore recommended that the potential for protection is best maintained between the free corrosion potential and the equilibrium potential in order to avoid energy waste and other negative effects of over protection (Song et al., 2004). A widely used industrial criterion for adequate corrosion protection is a value less negative than -850 mV with respect to the SCE (Rothwell and Tullmin, 2000).

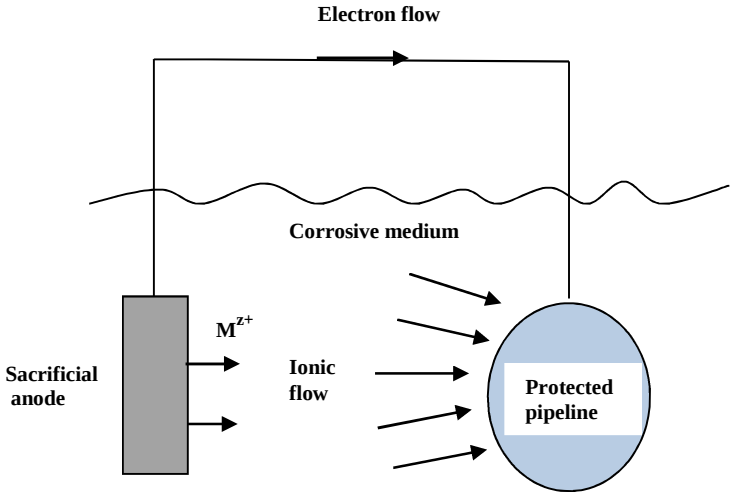

Figure 2-21: Schematic of sacrificial anode CP design

2.11.2 Cathodic Protection Design against Crevices Corrosion

Onshore pipelines are protected against external corrosion by the application of coating such as polyethylene tapes and cathodic protection. Crevice corrosion occurs beneath openings (holidays) of a disbonded steel pipelines when water flows through the holiday into the crevice on the metal surface as depicted in Figure 2-22.

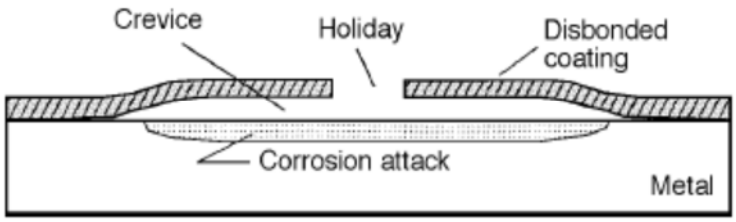

Figure 2-22: Schematic of disbonded coating on metal surface showing crevice, holiday opening, and crevice corrosion (Chin and Sabde, 2000a)

It is generally agreed that cathodic protection (CP) is not applied for the protection of the internal surfaces of pipelines (Song, 2010) but research have shown that it can be effective in preventing corrosion within crevices. Some researchers have demonstrated that cathodic protection has not been able to mitigate the corrosion properly because the

coating acts as a shield, blocking the flow of cathodic current to the pipe surface. However, Chin and Sabde (2000a) in their work on modelling transport process and current distribution in a cathodically protected crevice showed that cathodic protection changes the chemical environment inside a crevice. These changes occurred as a result of the production of OH^- from O_2 reduction reaction, and increase in the solution pH inside the crevice which result in protection. Therefore the principle of cathodic protection can be applied for protection of the crevice corrosion created from the plastic lining of carbon steel pipelines.

Crevice corrosion within disbonded coating has been a major challenge due to the fact that for some systems even applied CP fails to pass sufficient protective current to stop the corrosion in the affected locations. This is especially true for disbonded coatings without a holiday (opening). Gan et al. (1994) conducted a study to determine the feasibility of cathodically protecting the steel surface beneath disbonded coating with a holiday (opening). They demonstrated that crevice corrosion especially around the opening could be mitigated by cathodic protection. They arrived at two possible mechanisms for cathodic protection of steel within a crevice namely O_2 depletion mechanism and pH increase and passivation mechanism. These effects are depicted in the Evan's diagram in Figure 2-23.

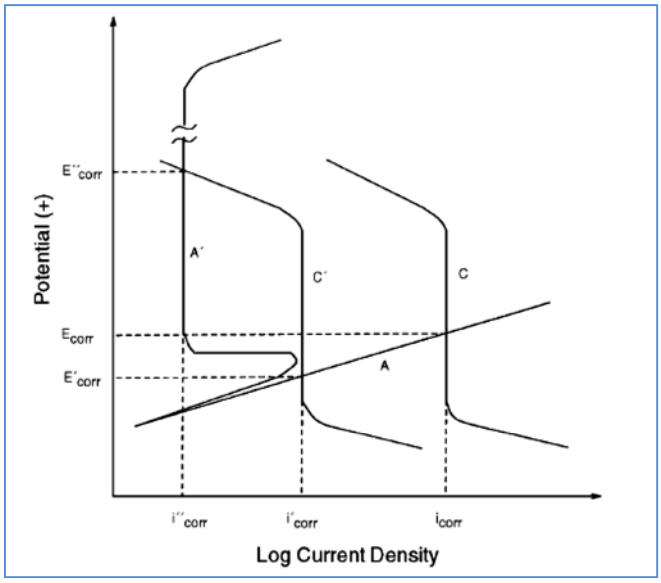

Figure 2-23: Schematic of a potential-current diagram showing effect of cathodic protection inside a crevice (Gan et al., 1994)

‘A’ represents the anodic polarization curve in a neutral solution while C represents the O_2 reduction curve at the initial stage of corrosion. After applying CP, the curve C moves to C´ with a resultant current smaller than C because of the decrease of O_2 within the crevice. This action corresponds to a reduction in the corrosion rate from the high initial value of i_{corr} to a lower corrosion rate of $i´_{corr}$. The corrosion potential in the crevice also moved from E_{corr} to a more negative value of $E´_{corr}$.

They also demonstrated that the potential within the crevice had a steady state value of -760 mV to -780 mV (SCE) while for the cathodically protected systems; the potential at the mouth of the crevice was more negative than -1000 mV (SCE). The potential at other locations were more positive than at the mouth of the crevice but more negative than the value advised by NACE. In agreement with the work of Song et al. (2005), the authors demonstrated that CP reduced the corrosion rate by the reduction of O_2 to hydroxyl (OH^-) or caused an increase in the pH. When the crevice solution becomes adequately alkaline, the steel passivates and the anodic polarization curve moves from A to A´. The corrosion rate decreased to a low value of $i´´_{corr}$, while the corrosion potential shifted to a positive value of $E´´_{corr}$.

Toncre and Ahmad (1980) in their work on cathodic protection against crevice corrosion of mild steel under a disbonded pipeline coating showed that CP could be achieved if the potential at the crevice opening was more negative than -1000 mV (SCE). They concluded that crevice corrosion within the disbonded coating could be mitigated with a sufficiently negative potential that would reduce the dissolved oxygen. However, Fessler et al. (1983) agrees that proper protection could be achieved at the potential of -1,000 mV but with the challenge of hydrogen evolution within the crevice at a more negative potential. This agrees with the work of Gan et al. (1994) who demonstrated the evolution of hydrogen within the crevice at a potential of -1,530 mV (SCE).

Baptista et al. (1995) in their work on CP against crevice corrosion of high-alloy steel in seawater demonstrated that type 316 SS prone to severe crevice corrosion performed without failure because of cathodic protection design. In their work they used a plastic material to create a crevice on the SS material in order to simulate crevice corrosion. They showed that CP prevented crevice corrosion by inhibiting the anodic polarisation of the SS and polarising the SS to a greater cathodic potential. They gave the nominal protection against crevice corrosion to be about -600 mV (Ag/AgCl).

Song et al. (2003a) in their work on "A new pipeline crevice corrosion model with O_2 and CP" simulated crevice corrosion on a pipeline surface using a HDPE as shown in Figure 2-24. Like most researchers, they agreed that O_2 was the cause of the crevice corrosion as it migrates through the holiday by diffusion. They demonstrated also that CP reduced the crevice corrosion by reduction of the O_2 beneath the crevice. They however acknowledged that the CP could not penetrate deep into the crevice and that corrosion deeper within the crevice is influenced by O_2 and the local pH.

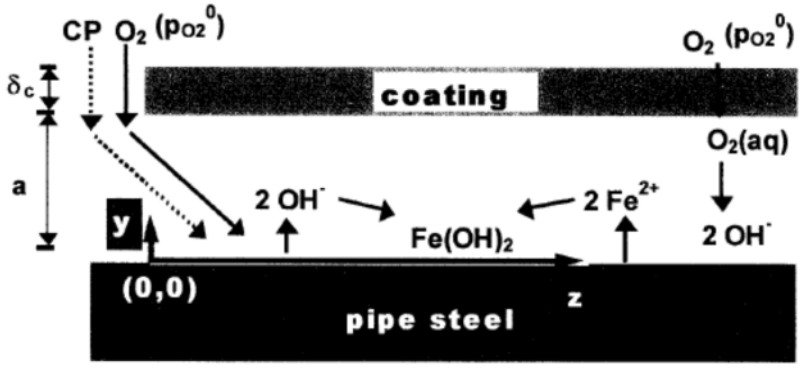

Figure 2-24: Schematic of crevice corrosion cell showing reactions (Song et al., 2003b)

They also demonstrated that for a deaerated system, the CP potential becomes more positive further into the crevice as shown in Figure 2-25. This could be attributed to the effect of "throwing power" limitation.

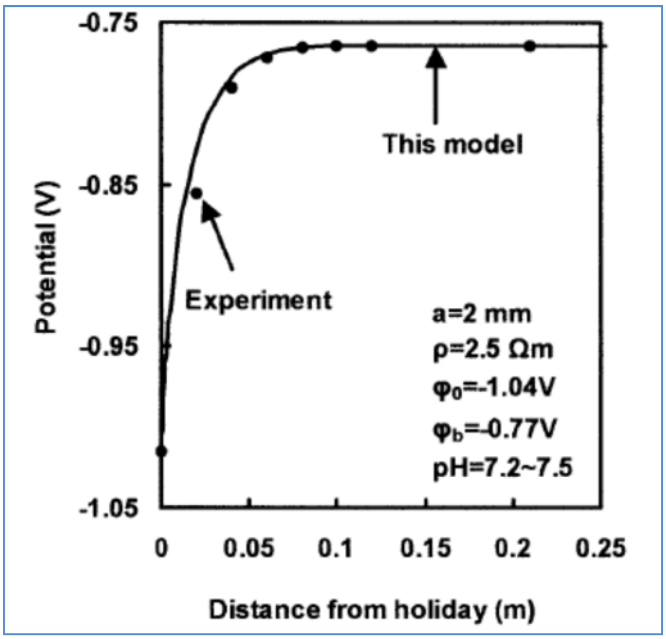

Figure 2-25: Graph of potential against distance from holiday under CP (Song et al., 2003a)

In their work they also demonstrated that as the CP current within the crevice increases, the corrosion rate decreases as shown in Figure 2-26. The values on the graph are the potentials beneath the crevice (holiday). At a potential of -870 mV ($Cu/CuSO_4$), the corrosion current is very small and when the value is further reduced to -900 mV, the corrosion current decreased slightly but was accompanied with H_2O reduction.

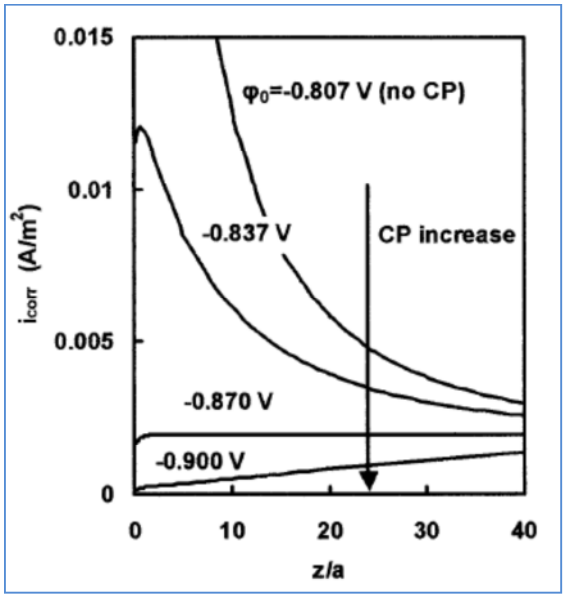

Figure 2-26: Effect of cathodic protection on crevice corrosion current (Song et al., 2003a)

These results/findings indicate that it is possible to mitigate corrosion within the crevice space of a metal and to generate the required protection polarization potential. However, it is important to note that at high applied potentials, hydrogen is generated and at low applied potentials, corrosion protection within the crevice cannot be achieved.

2.11.3 Inhibitor

One option available for mitigating internal corrosion is chemical treatment of the hydrocarbon being transported by the application of corrosion inhibitors (Thompson, 2006). Addition of corrosion inhibitors to reduce the effect of corrosion of carbon steel structures is one of the most practical methods in the oil and gas industry (Bentiss et al., 1999). According to Lopez et al. (2005), when the corrosive environment is extremely aggressive or the scales formed on the steel are non-protective, then the application of corrosion inhibitors is preferred. Corrosion inhibitors have therefore proven to be an effective method for mitigating corrosion, and in many cases, reducing the corrosion rates to acceptable values (Dave et al., 2008). In the case of pipelines, corrosion inhibitors can be applied when a new pipeline is commissioned or at any other time within the operation of the pipeline.

Inhibitors can therefore be defined simply as chemical compounds added in small quantities in order to reduce the corrosion rate of a metal exposed to a corroding medium (López et al., 2005). According to Cruz et al. (2004), the use of corrosion inhibitors is one of the most effective methods to protect metal surfaces against internal corrosion. Inhibitors have been successfully used to protect internal corrosion but the mechanism of operation has not been fully understood.

Other researchers agree with the fact that there is no known mechanism of the inhibition process but that protection is achieved by surface coverage due to the formation of a protective film (Palmer-Jones and Paisley, 2000; Nesic, 2007). They believe that the inhibitor adsorbs onto the steel surface preventing any water or corrosive agents from having direct contact with the metal and so slows down one or more electrochemical reactions. According to Fontana (1986), the action of slowing down the corrosion rate is achieved by the following processes:

- Increasing the anodic or cathodic polarisation behaviour
- Reducing the movement or diffusion of ions to the metallic surface
- Increasing the electrical resistance of the metallic surface

The corrosion inhibitor adsorption ability depends on the metal surface, the corrosion environment and the chemical structure of the inhibitor (Bentiss et al., 1999). Meng and Jovancicevic (2008) demonstrated that inhibitor effectiveness depended on a number of factors such as steel composition, water chemistry, pH, organic acids, water/oil ratio, temperature, CO_2 and H_2S partial pressure, flow regimes and flow geometry.

2.11.3.1 Types of Inhibitors

Inhibitors can generally be classified according to their mechanism and composition. Figure 2-27 shows the classification of corrosion inhibitors. The following subsections will briefly discuss some of these corrosion inhibitors.

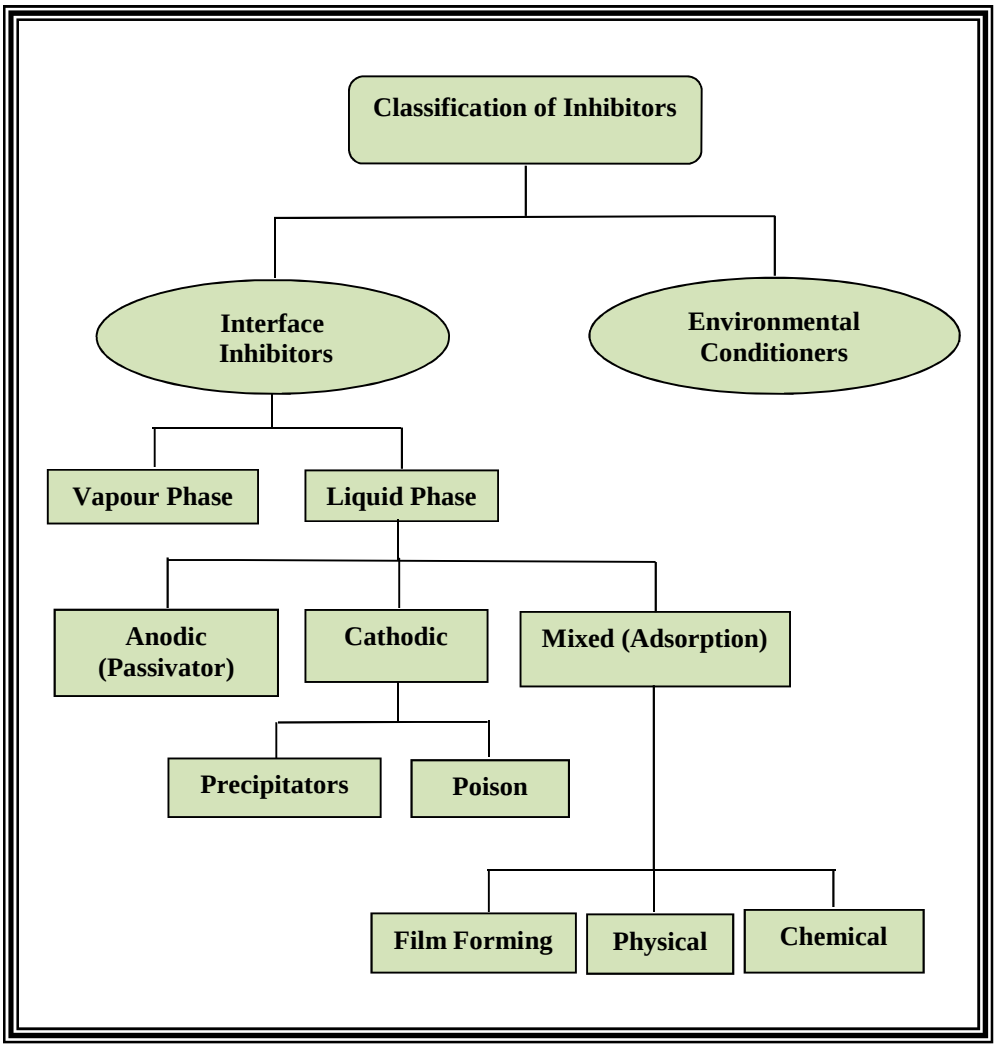

Figure 2-27: Classification of corrosion inhibitors (Revie, 2011)

Environmental Conditioners

Environmental conditioners also called scavengers are corrosion inhibitors which act by removing corrosive species from the corrosive environment. Examples of scavengers include sodium sulphite which removes dissolved oxygen from solutions as represented in the equation below:

$$2Na_2SO_3 + O_2 \rightarrow 2Na_2SO_4$$ **Equation 2-26**

Anodic Inhibitors

Anodic inhibitors also called passivating inhibitors work by causing a large anodic shift in the corrosion potential in the noble direction thereby bringing the metallic surface into the passivation range. There are two types of anodic inhibitors namely:

- Oxidizing anions, such as chromate, nitrite and nitrate that passivates the steel surface in the absence of oxygen.
- Non-oxidizing ions such as phosphate, tungstate and molybdate that requires the presence of oxygen to passivate the steel surface.

Figure 2-28 is an Evans diagram showing the effect of anodic inhibitor.

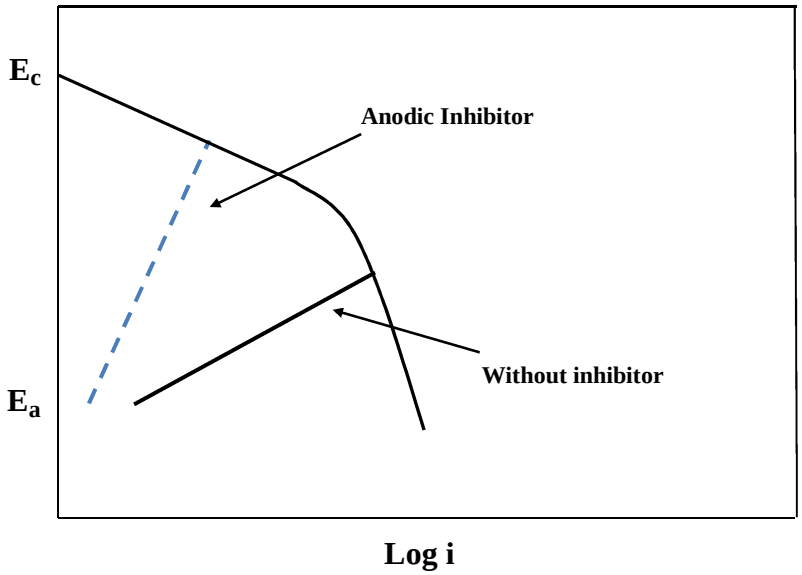

Figure 2-28: Evans diagram showing effect of anodic inhibitor adapted from (Wranglen, 1985)

From the figure it can be seen that the anodic inhibitor caused a large change of the potential in the noble direction with a resultant current change thereby reducing the corrosion rate.

Cathodic Inhibitors

Cathodic inhibitors operate by either slowing the cathodic reaction process or by selectively precipitating on the cathodic areas to increase the surface impedance and so

limit the diffusion of cathodic species to these sites. Cathodic inhibitors can provide inhibition by making the recombination and discharge of hydrogen more difficult or by catalysing cathodic ions such as zinc, calcium to precipitates as oxides on the metal surface. Figure 2-29 is an Evans diagram by Revie (2011) showing the operation of cathodic inhibitor in reducing the corrosion rate. However, it is important to note that the curves depict a change in the anodic polarisation as against the claim of the author. Therefore the graph with no change in the anodic polarisation will be the curve in red and not the second set of curves below.

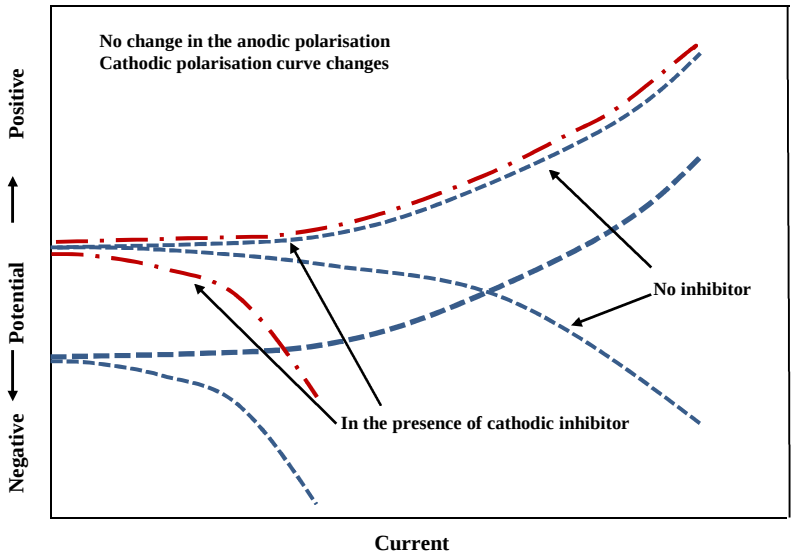

Figure 2-29: Polarisation curve showing effect of cathodic inhibitor (Revie, 2011)

It can be seen that the inhibitor caused the corrosion potential to shift in the more negative direction with a resultant decrease in the current density (corrosion rate).

Organic/Mixed Inhibitors

As the name signifies, organic (mixed) inhibitor affects both cathodic and anodic reactions and therefore the entire surface of the corroding material and must be present in sufficient concentration to function properly. Organic inhibitors form a protective film as a result of adsorption of the organic molecules on the corroding surface and so retard the corrosion process (Shreir et al., 1994). They suppress the anodic and/or the cathodic reactions involved in the corrosion process by adsorbing on the metal surface.

In their study on the corrosion inhibition of mild steel in acidic media by triazole derivative, Bentiss et al. (1999) showed that the effectiveness of the organic inhibitor depends on the ionic charge, type of electrolyte, and the nature of the metal. They also demonstrated that majority of these inhibitors contain heteratoms (example O, N, S) and multiple bonds, which enables the process of adsorption.

Badr (2009) demonstrated the effect of mixed inhibitors when he showed that thiosemicarbazide and its derivatives decreased both the anodic and cathodic current densities (Figure 2-30). He went further to show that the inhibitor retarded both the cathodic (hydrogen evolution) and the anodic reaction with a shift of the corrosion potential to the more negative value compared to the OCP. Like other researchers, it was concluded that the inhibitor molecules function by adsorption on the metal/solution interface thereby blocking the surface and retarding the corrosion process.

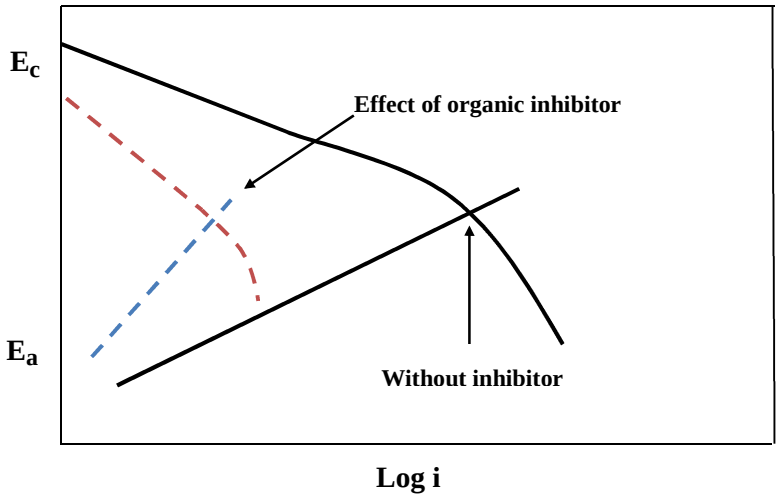

Figure 2-30: Evans diagram showing corrosion kinetics of organic inhibitor adapted from (Wranglen, 1985)

2.11.3.2 Factors Affecting Corrosion Inhibitor Performance

The following factors influence the corrosion protection of chemical inhibitors:

- **The Nature of the Metal**

As discussed earlier, most of the inhibitors are definite in their action towards the protection of particular metals, and so an inhibitor that works well with a certain metal

may have adverse effect when in contact with another type of material. For example, sulphates can inhibit chloride-induced pitting of stainless steel materials but are aggressive towards mild steel (Shreir et al., 1994).

Apart from the nature of the metal surface, the surface finish of the metal (smoothness and cleanliness) can also affect the protection ability of the inhibitor. For instance, clean and smooth surfaces usually require a lower concentration of inhibitor for a good protection compared to dirty or rough surfaces. In addition, the presence of oil, wax, grease or corrosion products on metal surfaces will influence the concentration of inhibitor required for protecting a metal surface and therefore it is important to consider these effects so as prevent localised corrosion attack.

- **Inhibitor Concentration**

For corrosion inhibitors to be most effective in the protection of metals, it is required that the inhibitors are present in sufficient concentration or above a minimum value. This minimum concentration is required to be maintained both for the initial operation and also during the service life so that inhibitor depletion will not lead to localised corrosion attack. Research has shown that insufficient inhibitor can lead to corrosion that is more severe than if no inhibitor was in place (Revie, 2011). Inhibitor concentration is determined by factors such as economics, disposal problems and availability of devices for monitoring inhibitor concentration (Shreir et al., 1994).

- **Presence of Crevices**

Effective protection by corrosion inhibitors where crevices are involved is a function of the continued access of the inhibitor to all the corroding parts within the crevice (under the gasket). Therefore accessibility to restricted areas or crevices is the main challenge for the use of inhibitors. As long as they can penetrate the crevice, corrosion attack can be retarded.

- **Temperature of System**

Temperature is an important factor that influences inhibitor performance due to its affects not only on the inhibitor but also the medium, and the corroding material. Temperature affects the physical as well as the chemical structure of inhibitors. A study carried out by Badr (2009) to investigate the performance of the organic inhibitor thiosemicarbazide, showed that the corrosion rate increased with temperature almost like in the uninhibited state.

Tao et al. (2009) in their investigation on the corrosion inhibition of mild steel in acidic solution by oxo-triazole derivatives showed that inhibitor efficiency decrease with temperature. They attributed the temperature effect to the higher dissolution of mild steel at higher temperatures.

Inhibitor Efficiency

Determination of the type of corrosion inhibitor to be employed in any system is generally based on their efficiency. Cruz et al. (2004) on their work on experimental and theoretical study of 1-(2-ethylamino)-2-methlimidazoline as an inhibitor of carbon steel corrosion in acid media demonstrated that corrosion inhibitor efficiency of organic compounds is directly proportional to the amount of inhibitor adsorbed, or the surface coverage. The authors agree with the work of Bouklah et al. (2006) that inhibitor efficiency depends on the structure and chemical properties of the species formed under the operating condition.

Each molecule of the inhibitor adsorbed on the metal surface may or may not desorb later on and therefore the degree of metal surface coverage and inhibitor efficiency can never be 100%. This is demonstrated with the Langmuir's isotherm (Figure 2-31) which can be used to explain the interaction between the inhibitor and the carbon steel. As the concentration of the inhibitor increases, the surface coverage/efficiency never reaches the 100% value.

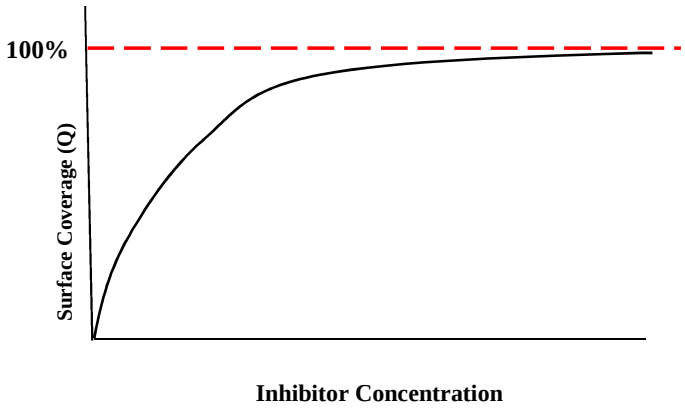

Figure 2-31: Langmuir's isotherm (surface coverage vs inhibitor concentration)

Like other researchers, Meng and Jovancicevic (2008) in their work on electrochemical evaluation of CO_2 corrosion in high turbulence multiphase fluid flow demonstrated that inhibitor efficiency increases with increase in concentration and is shown in Figure 2-32.

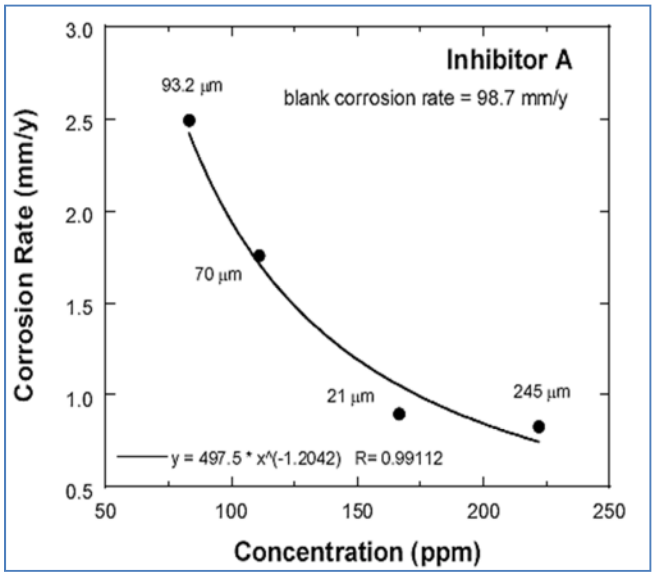

Figure 2-32: Relationship between inhibitor efficiency (corrosion rate reduction) and inhibitor concentration (Meng and Jovancicevic, 2008)

It was shown that a high concentration (110 ppm) of the test inhibitor gave a high surface coverage with a protection efficiency of 99.8%. According to the author, inhibitor efficiency can be calculated using the equation:

Equation 2-27

$$\text{Inhibitor efficiency (\%)} = 1 - \frac{\text{inhibited corrosion rate}}{\text{uninhibited corrosion rate}} \times 100\%$$

CHAPTER 3
ELECTROCHEMICAL TECHNIQUES FOR CORROSION MEASUREMENT

3.1 Introduction

Corrosion monitoring covers measurement techniques to assess the behaviour and condition of a material being tested under different environmental conditions. It is important to note that without corrosion monitoring effective corrosion control cannot be possible. Basically corrosion monitoring techniques can be classified into two types namely electrochemical and non-electrochemical techniques (Stefan and Anders, 2010). This chapter aims to look at the LPR electrochemical measuring technique used for the corrosion monitoring within the bulk solution and the annular space.

3.2 Electrochemical Technique

The electrochemical technique gives information about the corrosion rate and in some cases, the corrosion mechanism. Electrochemical methods are sensitive to the surface state of the material and generally provide very consistent results when used for electrochemical corrosion measurement (Abayarathna and Naraghi, 2001). They include among others the linear polarisation resistance (LPR), electrochemical impedance spectroscopy (EIS), zero resistance ammeter (Rothwell and Tullmin, 2000).

However, the LPR method has been chosen for conducting experiments in this project because of its effectiveness in aqueous solutions and the ease with which instantaneous corrosion rates are measured (Kouril et al., 2006).

3.3 Linear Polarization Resistance (LPR) Technique

Linear polarisation resistance (LPR) is the most commonly used electrochemical technique for measuring corrosion (Stefan and Anders, 2010). This technique requires

an electrolyte with relatively high conductivity and a stable free corrosion potential for excellent results. However, it does not provide information on the corrosion mechanism.

3.3.1 Principle of the Linear Polarization Resistance (LPR) Technique

An electrochemical reaction on the surface of an electrode can occur by two limiting mechanisms: the reaction is controlled by kinetics or by the diffusion of the electroactive species.

The Butler-Volmer equation describes how the electrical current on an electrode depends on the electrode potential. It is valid when the electrode reaction is controlled by electrical charge transfer at the electrode (and not by the mass transfer). Nevertheless, its application in electrochemistry is wide. At high overpotential the equation simplifies to the Tafel equation, and at low overpotential to the Stern Geary equation.

The Stern Geary Equation from which the LPR equipment operates is applicable in the linear region of the Butler-Volmer equation, at low potentials. It is therefore valid to use the LPR equipment to approximately measure the corrosion rate under diffusion controlled experiment.

In this technique, a corroding system is polarised over a small potential range of 10 to 15 mV around the corrosion potential, and the current generated is measured. Figure 3-1 is a schematic LPR scan showing how the polarisation resistance is determined from the gradient of the potential/current curve. This small potential is applied gradually, starting below the open circuit potential, through the open circuit potential, and finally terminating at the start potential. Because of the small potential applied the natural corrosion process of the system is not affected and so the experiment can be repeated without seriously affecting the behaviour of the material (Martinez et al., 2011).

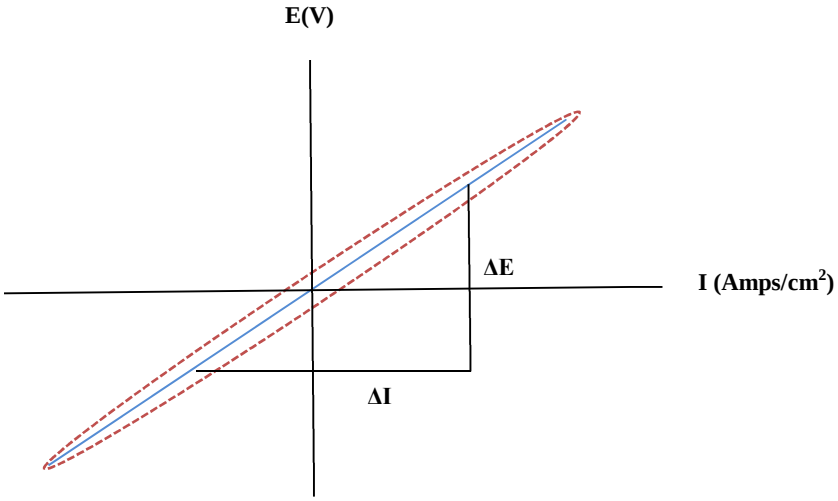

Figure 3-1: Schematic diagram of LPR scan

By monitoring the linear relationship of the applied potential and current between the electrodes, the corrosion rate can be accurately determined from the slope of the $\frac{dE}{di}$ graph, called the polarisation resistance (Rp) (Equation 3-1). The current density, which is approximately linear to the applied potential, is proportional to the inverse of the polarization resistance and provides instantaneous corrosion rate of the electrode under investigation (Enos and Scribner, 1997).

Equation 3-1

$$R_p = \frac{\Delta E}{\Delta i}$$

where,

- R_p is the polarization resistance
- *i* is the current density
- E is the potential

If the polarisation resistance (R_p) is estimated, the corrosion rate can be calculated with the Stern-Geary equation in the following way (ASTM, 1999):

$$i_{corr} = \frac{\boldsymbol{b}_a \boldsymbol{b}_c}{2.303(\boldsymbol{b}_a + \boldsymbol{b}_c)} \; x \; \frac{1}{R_p}$$ **Equation 3-2**

$$i_{corr} = \frac{B}{R_p}$$ **Equation 3-3**

where,

- B [Stern-Geary coefficient] (mV) $= \frac{\boldsymbol{b}_a \boldsymbol{b}_c}{2.303\,(\boldsymbol{b}_a + \boldsymbol{b}_c)}$
- i_{corr} is the corrosion density ($\frac{A}{cm^2}$)
- Rp is the polarisation resistance (Ωcm^2)
- $\mathbf{b}_a$ is the anodic Tafel slope ($\frac{V}{decade}$)
- $\mathbf{b}_c$ is the cathodic Tafel slopes $\frac{V}{decade}$

The LPR equipment incorporates software that converts the measured current densities into corrosion rates based on the material under investigation. The corrosion rate is determined automatically by the *1281* Solartron LPR measuring equipment using inputted values and the linear polarisation resistance (R_p) obtained from the experiments carried out.

Figure 3-2 shows an LPR plot obtained from the Solartron LPR equipment during one of the experiments. The Stern–Geary coefficients B are available for different materials and corrosion environments (Rothwell and Tullmin, 2000). For carbon steel in CO_2 environment, the value of B is taken from the NACE *Corrosion Engineer's Reference Book* as 26 mV/decade (Treseder et al., 1980). By approximating the gradient of the cathodic Tafel slope (b_c) to infinity and the gradient of the anodic Tafel slope (b_a) as 60.0 V/decade (Figure 10-13), the value of B can be calculated from Equation 3-2 as 26 (i.e. B approximates to $\boldsymbol{b}_a/2.303$). The density and equivalent weight of carbon steel used are 7.9 g/cm^2 and 27.9 amu respectively.

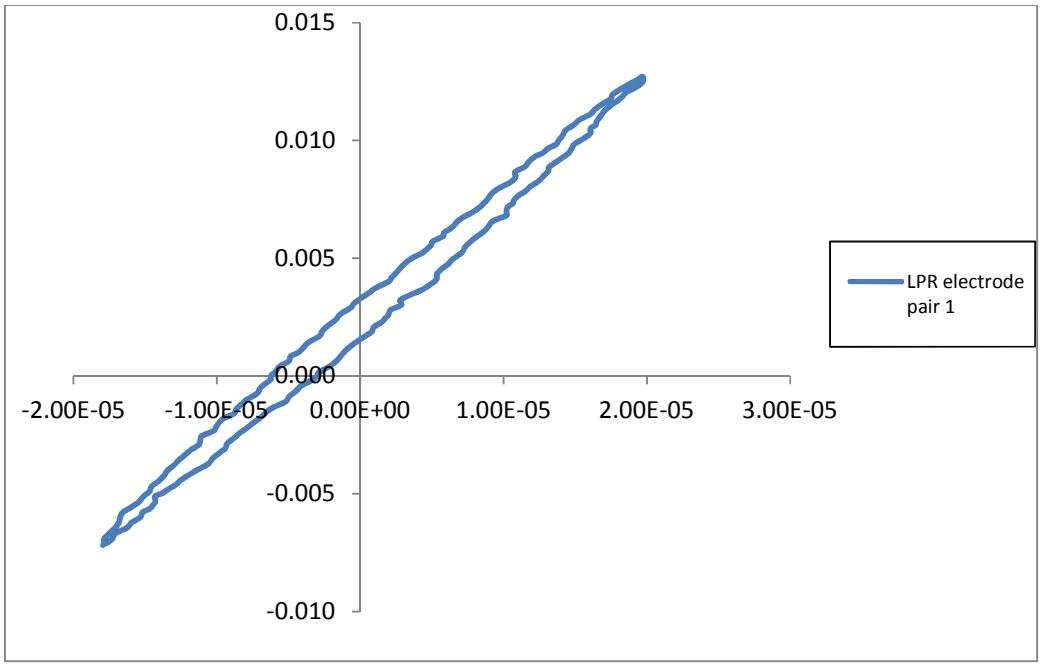

Figure 3-2: LPR plot obtained from the Solartron LPR equipment

The LPR plot above is displaced from the zero point of the graph. This could be attributed to the fact that the system did not completely stabilise before the start of the polarisation experiment. As a result the system was not at the corrosion potential where the cathodic and anodic reactions were equal. It may be preferable to programme the LPR equipment to run the system under open circuit potential for up to 60 seconds.

CHAPTER 4
EXPERIMENTAL

4.1 Introduction

The experimental work was carried out with the aim of investigating the effectiveness of a carbon steel pipeline, internally protected with a perforated plastic liner and in a sweet corrosion environment. As such this chapter explained the materials, method, techniques, equipment and procedures used to examine the corrosion protection abilities of this design in brine saturated with CO_2 at 1 bar pressure.

One of the sections covered some of the chemical and physical properties of the X100 carbon steel used in the design of the control and test electrodes. Other sections focused on the design, construction and assembly of the corrosion cell (perforated plastic lined pipeline). Construction of the component parts were carried out at the Cranfield University Workshop.

The experiments were carried out in the corrosion cell for static and flow conditions within the annular space. The final part of this chapter presents a discussion of the design of a heat exchanger unit which was required for removal of gas bubbles within the annular space.

4.2 Specimen Characteristics

The test and control electrodes were machined from an X100 carbon steel plate. The number 100 is the yield strength, and means 100 kilograms per square inch. These grades of carbon steel are produced by means of thermo mechanical rolling followed by accelerated cooling. In addition to the normal micro-alloys such as Niobium (Nb) and Vanadium (V) used in the manufacture of high strength steels, Molybdenum (Mo), Copper (Cu) and Nickel (Ni) were added to further increase the strength level (Table 4-1). The X100 carbon steel has an average hardness of 254 – 260 Hv and Charpy impact energy value of 235J, measured at -20°C (Hillenbrand et al., 1995).

4.2.1 Chemical Composition

A small sample of the plate was sent to *Exova Teesside Laboratory* for chemical analysis. Table 4-1 presents the chemical composition of the X100 carbon steel plate from the chemical analysis result. From the table, it may be observed that the reduced carbon content of 0.06% combined with the 0.17% Mo, 0.28% Cu and 0.13% Ni and the other micro-alloys (processed by thermo mechanical rolling and accelerated cooling) is responsible for the increase in the strength level to the grade X100. It is worth noting that this carbon steel is suitable for manufacture of hydrocarbon pipelines.

Table 4-1: Chemical composition of X-100 plate (wt %)

C	Mn	Ni	Cr	Mo	Si	Cu	Nb	V	P	S
0.06	**1.78**	**0.13**	**0.03**	**0.17**	**0.25**	**0.28**	**0.03**	**0.05**	**0.016**	**<0.003**

Microstructure

The microstructure was banded with grains elongated parallel to the rolling direction of the plate. It consisted of fine grained, equaxed ferrite with a mean grain size of 5 – 10 microns, which was produced by the thermomechanical treatment. In addition, there was an elongated phase between the ferrite grains that was more deeply etched and possessed an acicular substructure with the appearance of bainite or acicular ferrite (Wright, 2006).

4.3 Test Rig Design

4.3.1 General

A corrosion cell was constructed to simulate the conditions on the inner surface of a steel pipe in close contact with a plastic liner [Figure 4-1]. A plate of clear Perspex, 12.7 mm thick, was used to represent the liner; this was secured by bolts to a plate of ground X100 steel, 500 mm long and 150 mm wide. A gasket with a thickness of 1.6 mm was fitted between the Perspex and steel to define the annular space gap. A liner vent with an aspect ratio of 3.3:1 was produced by drilling a 3.8 mm diameter hole near one end of the Perspex plate. The test solution was held in the Perspex tank (about 6 litres) located above the plate and entered the annular space by passing through the liner vent. Figure 4-2 shows the dimensions of the major components of the test rig.

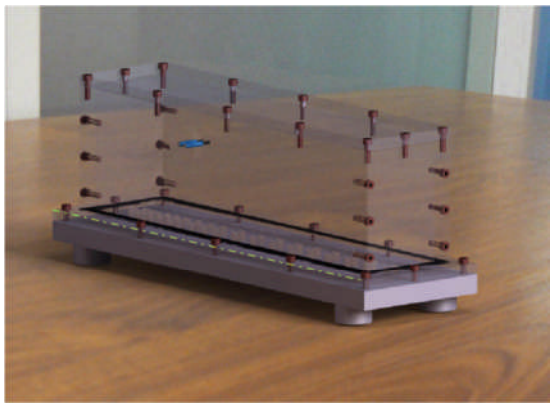

Figure 4-1: Corrosion cell to simulate pipeline lined with a perforated plastic liner

The test rig was designed based on the following design criteria (Wright, 2006):

- Provision to contain the electrolyte.
- Provision to hold all the necessary instrumentation and connecting tubes/pipes.
- Ease of carrying out corrosion rate measurements using the LPR technique, high resolution within the vicinity of the perforation and also along the length of the steel plate.
- Provision to change the size of the annular gap.
- Provision for conducting fluid flow test through the annular space.

The chosen design made it possible to hold and simulate the required test solutions, make necessary connections and also effectively record all electrochemical measurements. Figure 4-3 shows the various views of the test rig. The succeeding sub-sections will discuss the different parts of the assembly.

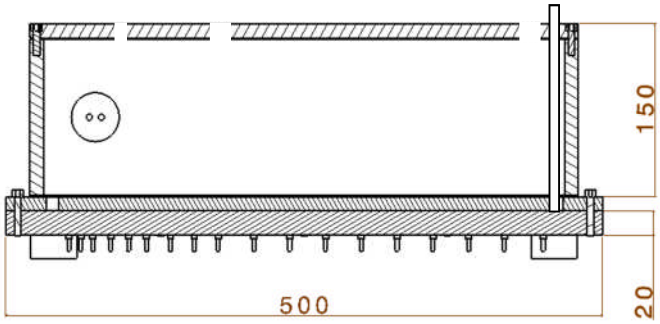

Figure 4-2: Dimensions of major components of test rig

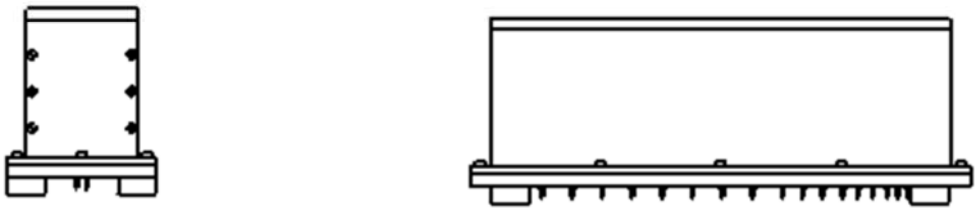

Side views

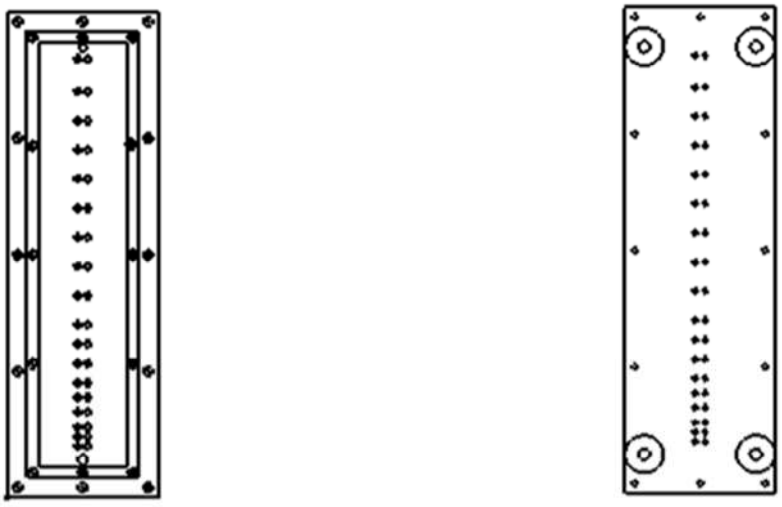

Top view **Bottom view**

Figure 4-3: Different views of test rig

4.3.2 The Steel Plate

The X-100 carbon steel plate provided the surface that housed the test electrodes, made of the same material, and forms one wall of the annular space when coupled to the Perspex tank. Positioned in pairs along the full length of the plate were test electrodes enveloped round with heat shrink insulator to prevent them from direct contact with the plate. The distribution of the test electrodes were such that they were more closely positioned around the vent area for high resolution.

This design made it possible for the closely positioned test electrode (at the vent area) to measure, at a high accuracy, the corrosion rate where CO_2 first entered the annular space. On the other hand the test electrodes which were positioned further apart covered the full length of the plate and measured accurately the corrosion rate where CO_2 had been transported along the annular space. Figures 4-4 and 4-5 show the drawings and a picture of the steel plate.

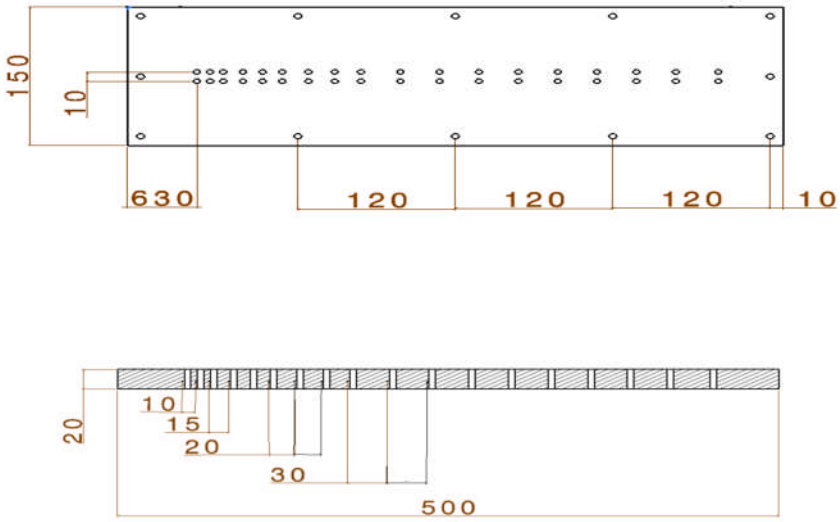

Figure 4-4: Dimensions of carbon steel plate

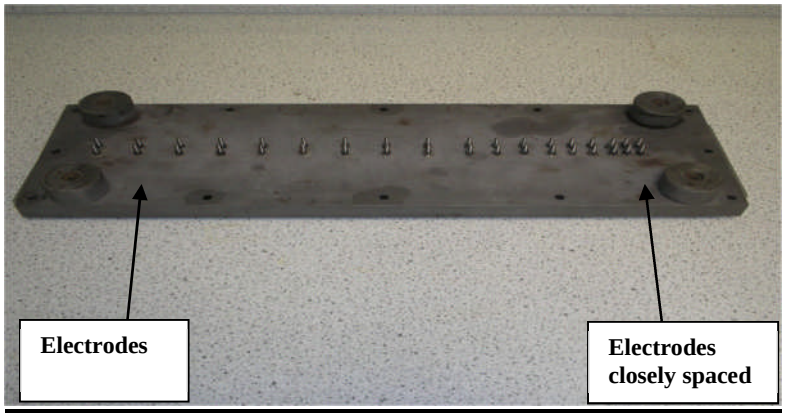

Figure 4-5: Test plate bottom showing test electrodes and connection points for LPR measurement

4.3.2 Annular Space Design

The annular space served as the micro-annulus of a perforated plastic lined pipeline. The annular space was controlled by positioning a gasket material between the steel plate and the Perspex tank.

A plastic gasket material of length 500 mm, breath 150 mm and thickness 1.6 mm was obtained for the construction of the gasket. A rectangular shaped gasket was made from this piece by cutting out from the centre a 460 mm by 110 mm rectangle. A gasket punch was then used to create holes around the circumference of the rectangular shaped gasket to correspond with the holes on the Perspex tank and the steel plate. By positioning the rectangular shaped gasket (Figure 4-6) between the Perspex tank and the steel plate, a annular space was created.

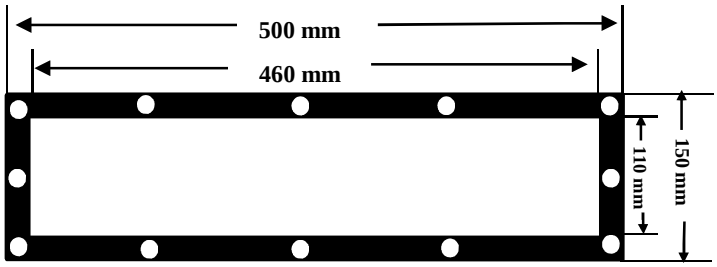

Figure 4-6: Schematic of gasket for creating annular space

4.3.3 Electrode Design

The electrodes were machined from the same material as the carbon steel plate (X-100). The electrodes were machined to form two sections. The larger cylindrical section with length of 23.0 mm and diameter 5.0 mm fits into the steel plate. The smaller cylindrical section of length 10.0 mm and diameter 3.0 mm protrudes through the bottom of the steel plate. This part was threaded for connection of the Solartron LPR measuring equipment cables with screws. Figure 4-7 shows the electrode design.

The electrodes were designed and coupled in pairs such that one was the working electrode and the other the counter electrode. They were spaced 10 mm apart from the test plate centre line. The plate was drilled to size and the test electrodes insulated from the plate with heat shrink plastic and secured using slow-setting araldite.

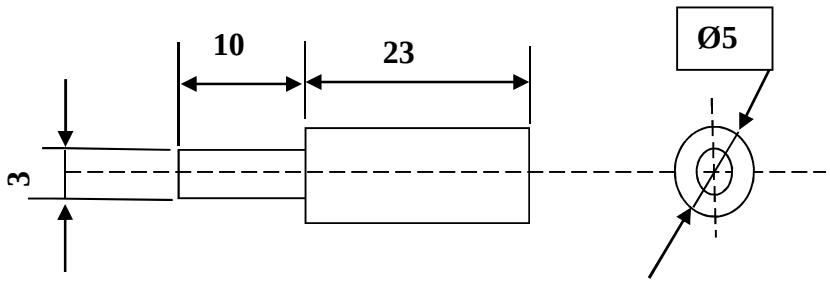

Figure 4-7: Electrodes design

4.3.4 Control Sample

The control sample was constructed from two electrodes machined like the test electrodes, in the succeeding section, and mounted in resin (the electrodes being made from the same material as the test electrodes). The unit (resin/control electrodes) was then mounted on the Perspex tank wall such that the face of the larger cylindrical section was inside the Perspex tank while the smaller threaded part was outside. Sealant was used to secure this unit to prevent electrolyte leakage when in operation.

This design made it possible for the control sample to be fully immersed in the electrolyte when the tank was filled. The threaded end of the control sample which

protruded outside the Perspex tank served as the point of connection to the LPR measuring equipment. Figure 4-8 is the schematics and Figure 4-9 shows the pictorial view.

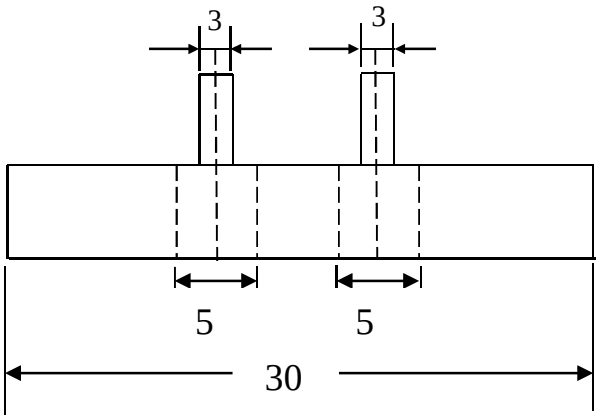

Figure 4-8: Schematics of control sample design

Figure 4-9: Control sample set in disc resin

It is important to mention at this point that crevice corrosion could develop between the control electrodes and the resin, and the test electrodes and the steel plate. However, there was no observed crevice corrosion between the control electrodes and the resin. In the case of the test electrodes and the steel plate, crevice corrosion was successfully avoided by use of heat shrink sleeving which ensured that no liquid was present at the electrode/plate interface.

4.3.5 Tank

A plate of Perspex, 12.7 mm thick acted as a flexible liner on the steel plate surface. It was built up as a tank to hold the electrolyte for the simulation of sweet corrosion in static and flowing conditions. Testing in these environments require a test cell in which the steel plate and the inserted test electrodes were visible for good visual observations while the experiment was running. Therefore the corrosion cell tank unit was made with a clear Perspex material. On one side of the larger surfaces of the tank wall was the control sample, which acted as unprotected carbon steel pipeline, was directly exposed to the electrolyte.

The cover was designed with openings as access for the instrumentation, gas bubbler for the different gases, electrolyte suction and return. The instrumentation included the thermometers, thermostat regulated heater, reference electrode (saturated calomel electrode) and Luggin capillary. It is pertinent to mention that the bubbler in addition to supplying the gases helped in ensuring a constant temperature and uniform concentration of the CO_2 within the tank. Figure 4-10 shows the drawing of the tank.

The tank and plate were coupled together using Allen bolts and four specially designed steel rods acting as flanges. The use of the flanges was to ensure uniform pressure around the tank foot to prevent leakage and damage due to excessive bolting pressure during assembly.

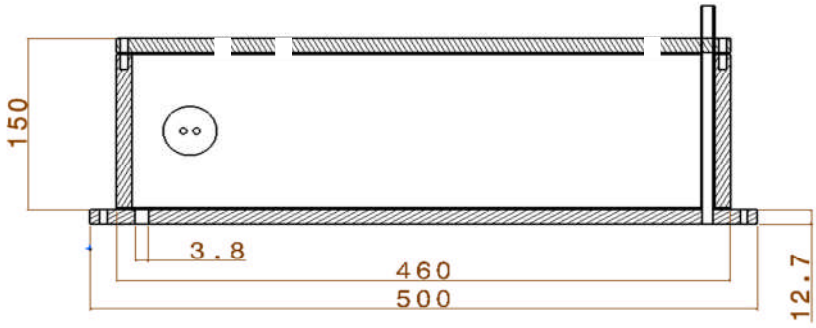

Figure 4-10: Perspex tank design

4.4 Heat Exchanger

A major challenge encountered in preliminary tests carried out was the formation of large gas bubbles within the annular space as shown in Figure 4-11. Initially, the nature/type of the gas could not be ascertained. However, it was suspected to be CO_2 gas. This suggestion was arrived at because of the short time it took for the gas to be formed within the annular space, which was not long enough for hydrogen gas to form from the corrosion reaction. In addition, it was reasoned that as the compressed CO_2 gas stored in the cylinder escaped, cooling occurred due to expansion. This expansion is endothermic; thus the electrolyte temperature drops below room temperature.

This second opinion appeared logical as it was expected that after running the test for some time, the solution in the tank became saturated with CO_2. When this saturated solution entered the annular space, it became supersaturated because of the higher temperature of the steel plate which was at room temperature. Supersaturation is the condition when a solution at a given temperature and pressure contains more gas than it would hold normally if the solution were in equilibrium. When cold saturated solution was heated, the gas solubility decreases with the increasing temperature and the solution became supersaturated. As a result gas bubbles are formed at the plate surface, as it is warmer than the electrolyte contained in the tank.

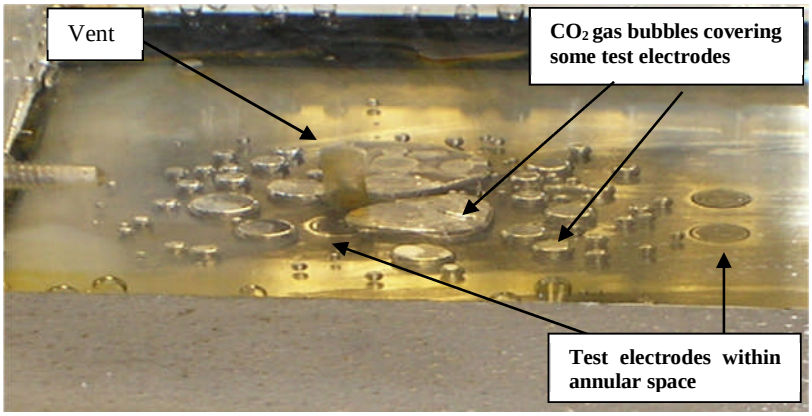

Figure 4-11: Test cell showing gas bubbles within annular space

As a result of this supersaturation of the CO_2 gas, some of it comes out of the solution as gas bubbles. These gas bubbles physically cover most of test electrodes on the plate surface within the annular space and therefore affect the results. Therefore regulating the temperature, especially of the electrolyte entering the annular space and coming in contact with the plate surface, would be a possible solution to the problem. Therefore to eliminate the CO_2 gas bubbles, there was need to design a heat exchanger, described in the following section.

4.4.1 Heat Exchanger Design

Based on the above discussion, the CO_2 bubble formation could be prevented by not allowing saturated CO_2 solution coming into the annular space to become supersaturated. To control this problem of super-saturation in the test rig, two options were considered:

a. Insulation of the steel plate to avoid temperature fluctuation.
b. Increase the temperature of the CO_2 gas coming into the tank and use a thermostat regulated heater to heat up the saturated solution in the tank above the steel plate temperature before it enters the annular space.

The schematic of the corrosion cell showing the different temperatures is shown in Figure 4-12.

Figure 4-12: Schematics showing test rig and the effect of temperature change

Where,

- T_1 – temperature of the CO_2 gas
- T_2 – temperature of electrolyte in tank
- T_3 – temperature of steel plate carrying test electrode (fluctuates with surrounding temperature)
- T_{Atmos} – atmospheric temperature

The temperature of the electrolyte in the tank (T_2), which was originally at room temperature began to decrease gradually as the CO_2, at temperature T_1 (about 15 ºC), was bubbled into the tank to simulate sweet corrosion. Normally $T_2 = T_3$ (which was equal to the atmospheric temperature, T_{Atmos}). The problem of bubble formation arose when $T_2 < T_3$ due to the cooling effect of the cold CO_2 gas. The temperature of the plate (T_3) is measured with a thermometer connected to it and insulated from the environment. It is pertinent to note that T_3 is influenced by the atmospheric temperature (T_{Atmos}) and the temperature of the electrolyte inside the tank (T_2) and so as the cooler saturated solution entered the annular space, there was temperature difference.

It was decided to employ the second option because insulating the plate would only prevent temperature fluctuation and not prevent the temperature drop experienced in the tank.

First approach: warm the CO_2 gas as it leaves the gas cylinder. This was achieved by a heat exchanger unit designed with a water bath and copper coil and hoses. As the CO_2 gas passed through spirally wound copper coil immersed in a water bath. The temperature of the bath was set at 30 ºC to heat up the CO_2 gas as it passed through the copper coil into the tank. The heat exchanger unit with the copper tubing/hoses, thermometers and gas connections are shown in Figure 4-13.

Figure 4-13: Heat exchanger unit showing water bath, thermometers copper coil and hose connection to CO_2 gas supply

This design helped to increase the temperature of the electrolyte within the tank. As such, the tank temperature (T_2) became higher than the atmospheric temperature (T_{Atmos}); $T_2 > T_{Atmos}$. This approach proved fairly successful as the CO_2 gas that came out of solution within the annular space area was reduced considerably. However, some CO_2 gas still came out of the solution, especially around the vent area and the bubbles increased as the experiment progressed. This was attributed to the fact that the plate warms up during the day and so warms the solution that came in contact with it. As a result the saturated CO_2 solution again became supersaturated.

The idea was not to have any gas bubbles as this would compromise the integrity of the results and so a second approach was considered.

Second approach: The electrolyte was heated up in the tank a few degrees above room temperature so that the temperature of the plate (T_3) was always lower than that of the saturated solution (T_2); that is, $T_3 < T_2$. This was achieved by using a submersible thermostat regulated heater to heat up the electrolyte within the tank. This arrangement is shown in Figure 4-14.

Figure 4-14: Submersible thermostat regulated heater in tank

4.5 Solartron Multiplexer 1281 Equipment

Electrochemical measurements were carried out with a Solartron Multiplexer model 1281 equipment interfaced to a laptop computer using the "CorrWare" software for data acquisition and analysis. It is made up of the 1281 Multiplexer unit which is a computer controlled 8-channelled Multiplexer capable of controlling the Solartron 1280 potentiostat from 1 cell to 8 cells. There are 8 channels which gave this specialised equipment the capability to simultaneously record 8 tests pre-programmed using the SCANNER drive with CorrWare software. Thus it is possible to run multiple experiments such as OCP, potentiostatic and LPR sequentially.

The CorrWare software allows a dynamic automatic switching of the potentiostat from one cell to another at specified times. Recorded results including graphs could be viewed on the laptop with the aid of the Corrview software. Figure 4-15 is a schematic of the Solartron Multiplexer unit.

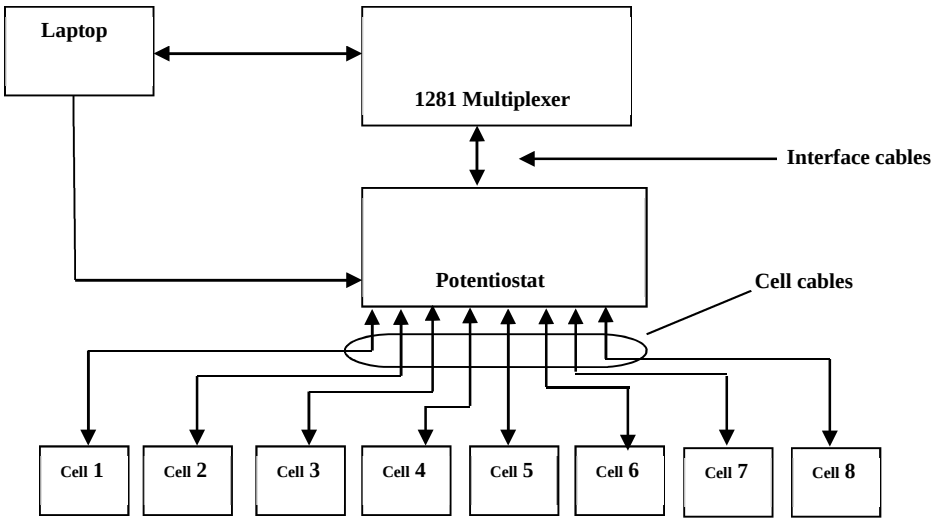

Figure 4-15: Schematic of Solartron Multiplexer 1281 Equipment

Figure 4-16 shows the pictorial view of the Solartron equipment showing the interface (4 cables) connecting the 1281 Multiplexer to the 1280 potentiostat.

Figure 4-16: Solartron Multiplexer 1281 Equipment

Each of the 8 channels is made up of four coloured cable leads to form the connection points to the corrosion cell. Two of the cable leads coloured green (WE) and yellow (RE 1) were connected to the working electrode (WE) of the test cell. The other cable leads

coloured red (CE) and white (RE 2) were connected to the counter electrode of the test cell.

Figure 4-17 gives a schematic diagram of the four cable leads with the colour codes. Polarisation and measurement of the current densities were performed by employing the two electrode connection method.

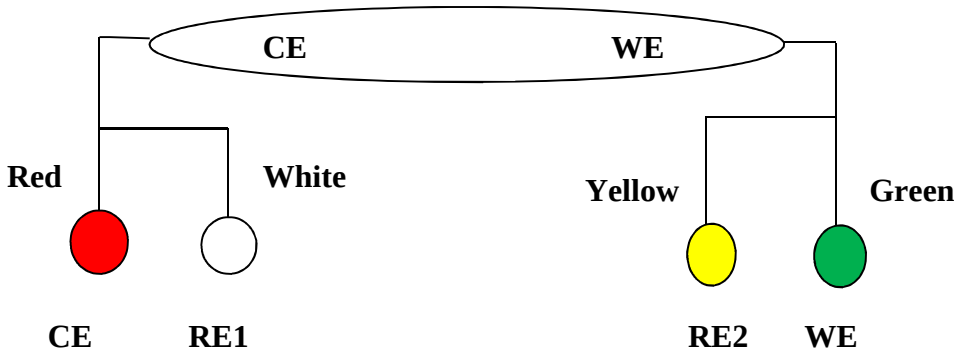

Figure 4-17: Two electrode connection method

Programming Solartron Equipment for LPR Measurement

As discussed earlier, the linear polarisation resistance measurement was employed in this research using the Solartron equipment. During introductory experiments it was observed that there was a jump at the first point of the cathodic scan. This skip which occurred during the cathodic scans resulted in a distorted curve with a resultant error in the determination of the corrosion rate. The skip was believed to be a switching transient and was overcome by programming the Solartron equipment to include a potentiostatic scan at -0.01 V for 5 seconds before the actual LPR scan kicked in. Also an OCP was pre-programmed to stabilise the system before each series of test.

The LPR equipment was programmed to generate a small sweep from -10 mV to +10 mV at a scan rate of 10 mV/min around the rest potential for each electrode. This was repeated at 5.2 minutes interval. The CorrWare software was also programmed to determine the corrosion rate in mm/y. This was done by inputting the carbon steel test electrode information into the Solartron equipment as shown below:

- Surface Area (cm^2) - 0.196
- Density (g/cm^3) - 7.9
- Equivalent Weight (g) - 27.9
- Stern-Geary Coef. (mV) - 26.0
- Reference Electrode Type – SCE (Hg/Hg_2Cl_2 – Sat KCl)

4.6 Experimental Procedure

This section deals with the detailed systematic order in which the experiments were generally carried out and included the various stages of material preparation, test rig set-up, electrical connections and testing.

4.6.1 General Material Preparation

Prior to each test, the steel plate carrying the test electrodes were ground to remove every trace of rust, or impurities. The control sample surface was polished with silicon carbide papers. The control sample was polished first with a size 240 grit silicon carbide paper horizontally from left to right. After this process, a finer carbide paper (size 800) was used to polish the surface vertically from up to down. These processes were to ensure that neither pits nor rough surfaces were left on the control sample or the test electrodes.

Before assembling the corrosion cell, the control sample surface, the steel plate with the inserted test electrodes and the tank were cleaned with cotton soaked in iso-propanol solution to ensure that any remaining surface impurities such as grease were removed. It is worthy of note that traces of grease or oil could affect the corrosion process and subsequently the results. Figure 4-18 shows the steel plate with the test electrodes properly cleaned with iso-propanol ready for assembly.

Figure 4-18: Steel plate cleaned ready for assembly

4.6.2 Electrical Connections for LPR Measurement

After the surface cleaning, the individual test electrodes were tested for any short circuiting with respect to the plate, using a multimeter. This was necessary to prevent error from the onset of the experiment. It is important to note that in the event of a short circuit, it would not only be the small surface area of the test electrodes that would be polarised but the entire steel plate. The next stage was the connection of the threaded portions of the test electrodes 1 to 6, reference electrodes and the control sample to the Solartron equipment.

As discussed earlier, the green and yellow coloured leads were connected to the threaded part of one of the electrodes while the white and red leads were connected to the threaded part of the second pair of electrodes. One of the electrode pairs provided the surface for reduction-oxidation reaction to balance the reaction occurring at the surface of the working electrodes. It is pertinent to note that because of the limited lengths of the lead cables, some wires and clips were used as extension cables for ease of connection.

Figures 4-19 and 4-20 show the test electrodes numbering and some test electrodes already connected to the Solartron equipment. It is worthy of note that channel 3 was connected to electrode pair 1, directly beneath the vent.

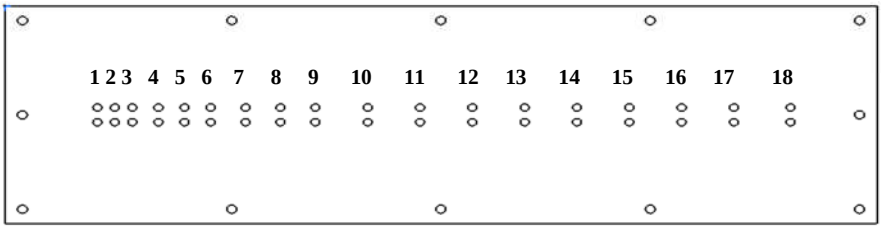

Figure 4-19: Steel plate showing positions of test electrodes

Figure 4-20: Steel plate showing test electrode connection to Solartron lead cables

4.6.3 Test Rig Set-up

After the electrical connection, the surface of the steel plate was again lightly wiped with a cotton wool soaked with iso-propanol to remove any dirt that might be on the surface. The rectangular gasket was also cleaned with iso-propanol and then placed on the surface of the plate. The Perspex tank was then mounted on the plate and the four steel flanges were then placed around the tank and bolted to the steel plate using Allen bolts. The flanges were very important as they applied uniform pressure round the Perspex thus preventing electrolyte leakage from the corrosion cell.

The Perspex cover was secured using Allen bolts and the other items such as the saturated calomel reference electrode with the Luggin capillary, thermometer, and gas bubbler (for CO_2 and N_2) were fed through the holes on the top. The reference electrode and the thermometer were held in position close to the test rig by a clamp stand. The thermostat controlled heater was connected to the cover for ease of connection to power supply. Figure 4-21 shows the schematic diagram of the experimental set up.

Table 4-2: Distances of test electrodes from vent

Test Electrodes	Distances from Vent (mm)
Electrode pair 1	0.0
Electrode pair 2	10.0
Electrode pair 3	20.0
Electrode pair 4	35.0
Electrode pair 5	50.0
Electrode pair 6	65.0
Electrode pair 7	85.0
Electrode pair 8	105.0
Electrode pair 9	125.0
Electrode pair 10	155.0
Electrode pair 11	185.0
Electrode pair 12	215.0
Electrode pair 13	245.0
Electrode pair 14	275.0
Electrode pair 15	305.0
Electrode pair 16	335.0
Electrode pair 17	365.0

Nitrogen gas was bubbled through a plastic container containing about 10 litres of 3.5% NaCl electrolyte for about 2 hours. This was done to deaerate it before transferring into the corrosion cell. Four litres of the deaerated NaCl solution was then gradually siphoned into the Perspex tank using a clean rubber hose. Deaeration with the nitrogen gas was continued in the tank with the electrolyte for some hours to remove any oxygen left and so prepare the environment for sweet corrosion monitoring. Table 4-3 gives a brief summary of the experimental conditions.

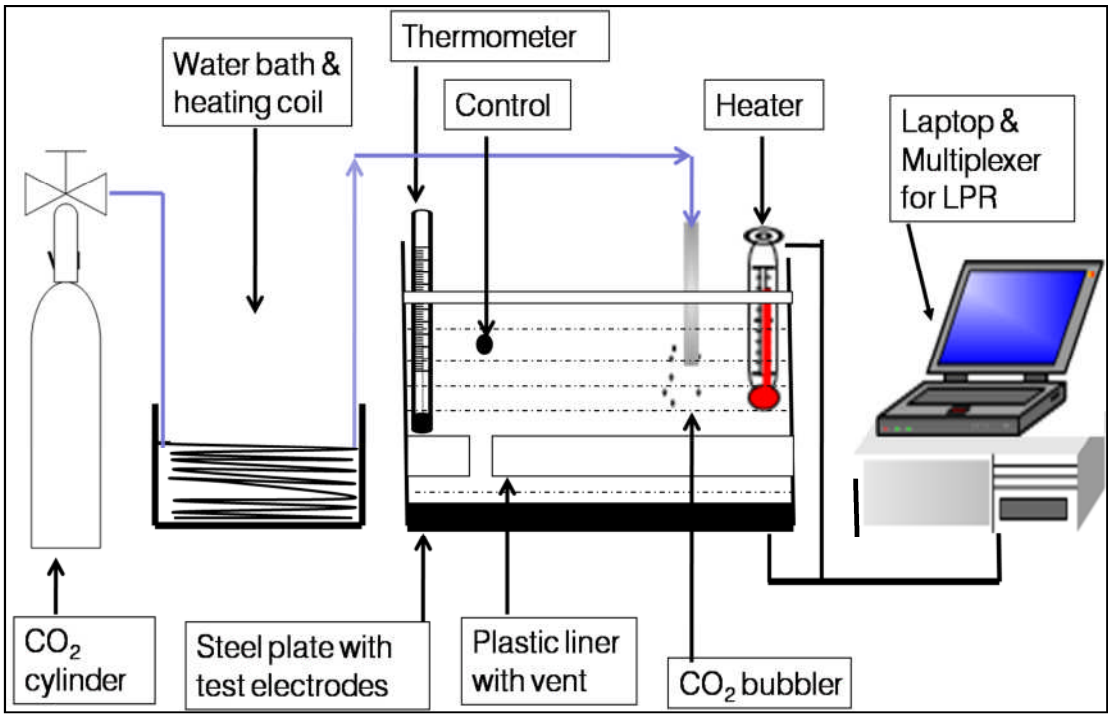

Figure 4-21: Schematics of experimental set up showing the different components

Table 4-3: Experimental Conditions

Test solution	3.5 % NaCl
Test material	Carbon steel: X-100
Gas pressure	CO_2 = 1 bar
Polarisation resistance	From -10 to 10 mV vs OCP
Gasket (thickness)	1.6 mm
Sample area of electrodes	0.196 cm^2
Diameter of vent	0.38 cm
Thickness of flexible plastic liner	1.27 cm

CHAPTER 5
STATIC TEST

5.1 Introduction

Static experiments, in which there were no circulations of the electrolyte through the annular space and with no mixing of the electrolyte within the tank of the corrosion cell, were performed. The experiments were aimed at studying the rate of the transport of the carbon dioxide through the vent into the annular space without an intentionally induced means like mixing. The tests were designed for better resolution of corrosion around the vent area and to obtain as much information as possible with regard to the performance of the perforated liner when there was no flow.

The chapter discusses the material preparation, assembly, de-aeration of the electrolyte and cell and performance of the tests in a sweet corrosion environment. In addition, the LPR monitoring was discussed and the results analysed and presented. The aforementioned static tests were carried out a number of times with the aim of establishing consistency in the results obtained; the best results are presented.

Each test cycle connected to a channel ran for about 5.2 minutes. During the course of the experiment, the Solartron equipment periodically measured the linear polarization resistance (R_p) automatically. The applied potential and corresponding current densities were recorded on the computer for all the tests. Subsequently, the CorrWare software automatically calculated the corrosion rates and recorded them in text files for further analysis.

5.2 Material Preparation

As discussed earlier, prior to each experiment the steel plate with all the inserted test electrodes were ground and surfaces cleaned with iso-propanol. In addition, the control sample was polished with carbide papers of grit sizes 240 and 800 to give a clean surface. The control sample and all components including the gasket were cleaned with iso-propanol prior to assembly and coupling with Allen screws.

5.3 Corrosion Cell Set-up

This section focuses on the set-up of the corrosion cell for the static experiments and includes surface preparation of the test electrodes, coupling of the units, de-aeration, simulation of CO_2 corrosion and connection to the LPR instrument. The test electrodes were tested with a multimeter to ensure that there was no connection between them and the steel plate; which would have introduced error to the results. A total of seven experiments were performed in static conditions and after each experiment, the metal plate with the test electrodes and the control sample on the Perspex tank was reground, cleaned and assembled.

5.3.1 Assembly and Deaeration with Nitrogen Gas

The open end of a saturated calomel reference electrode was connected to a Luggin capillary while the cable end to the LPR measuring equipment together with the red lid of the voltmeter. The control sample was connected to channel 2 of the LPR equipment and the test electrodes (pairs 1, 2, 3, 4, 5 and 6) to channels 3 to 8 of the LPR equipment. After the electrical connections, the corrosion cell was assembled and immediately nitrogen gas was supplied to the unit to keep it free from oxygen and the cell sealed with silicon sealant to prevent leakages.

About 4 litres of deaerated NaCl (3.5%) electrolyte was siphoned from a rubber container into the corrosion cell which was also being deaerated with nitrogen gas. The Perspex cover and the instrumentation secured on it before switching the LPR equipment. N_2 was bubbled continuously in the corrosion cell for 1.5 hours to ensure proper deaeration.

5.3.2 Simulation of CO_2 Corrosion

After the deaeration process was completed, the nitrogen gas supply was replaced with carbon dioxide (CO_2) gas set at 1 bar pressure. The gas supply pipe was channelled from the cylinder through the heat exchanger (operated at 30 ºC) into the gas bubbler in the tank. The gas supply control knob on the gas pressure regulator was gradually opened to prevent vigorous mixing within the bulk solution. The supply of CO_2 was

maintained throughout the duration of the experiment to simulate sweet corrosion and prevent oxygen from entering the cell that could result in oxygen corrosion.

One of the electrodes of the control sample was connected in parallel with the saturated calomel reference electrode in order to measure its potential with reference to the SCE. The Corrview software of the LPR measuring equipment enabled continuous monitoring of the data recording process on the text file for channels 1 to 8 and the nature of the graphs generated. Figure 5-1 shows the pictorial view of the experimental set up.

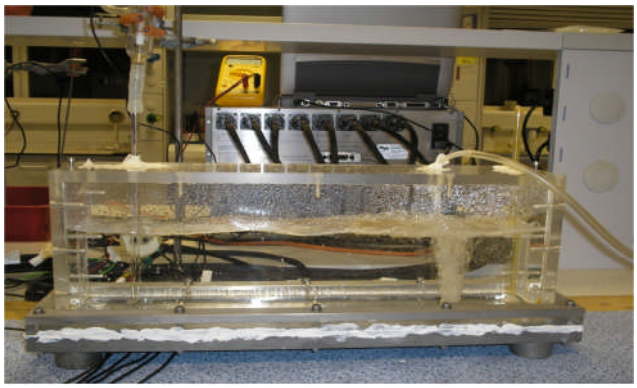

Figure 5-1: Static test showing simulation of CO_2 corrosion

5.4 Results and Discussion

5.4.1 Introduction

This subsection deals with the results and the discussion concerning some of the observations. The data from the LPR equipment were recorded and saved in text files in the laptop and later downloaded on an Excel Spreadsheet for analysis. These results were represented in graphical forms and some results supported with pictures, for more emphasis. It is pertinent to mention that all voltage readings are with respect to the saturated calomel reference electrode (SCE).

It took an average time of about 42 minutes to obtain the result for a complete cycle starting from the measurement of the OCP through to the measurement of the corrosion rates of the control sample and the six test electrodes.

5.4.2 Effect of Deaeration and CO_2 Introduction on the Carbon Steel Potential

Figure 5-2(a) shows the change of the potential from the time nitrogen gas was bubbled into the NaCl solution, for deaeration, up to when it was replaced with CO_2 gas (to simulate sweet corrosion). Nitrogen gas was allowed to bubble through the test solution for a longer time in order to get a well deaerated environment in order to obtain better results without the influence of oxygen corrosion.

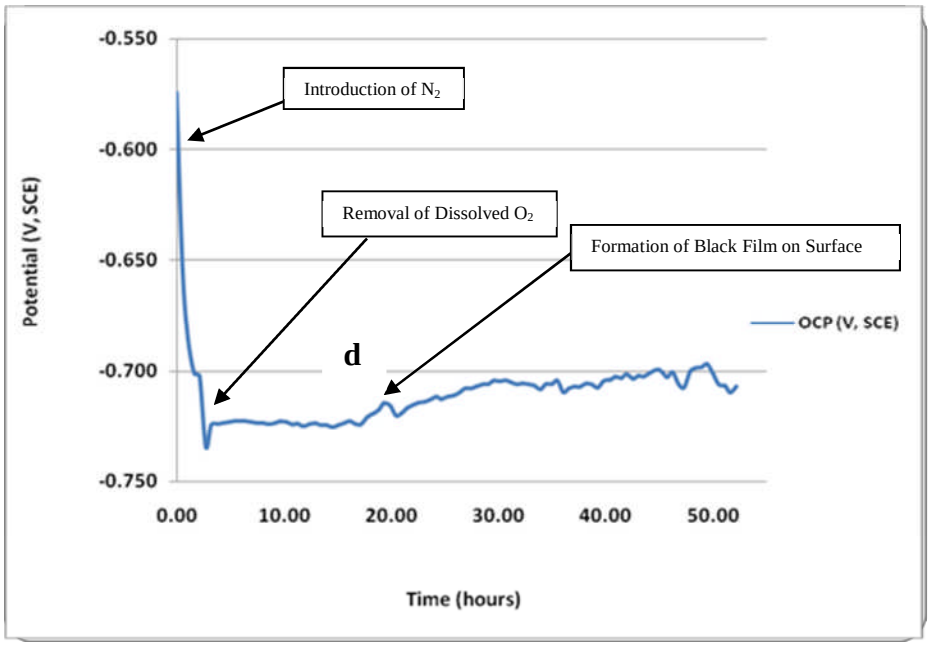

Figure 5-2(a): Graph of open circuit potential of the control sample for Nitrogen purging and carbon dioxide introduction

At the start of the experiment, the open circuit potential reading from the voltmeter was -0.570V (SCE); this corresponded to the recorded value in the LPR text file. This value gradually decreased to -0.734V as a result of the removal of dissolved oxygen from the solution (deaeration). Nitrogen purging was necessary for the removal of as much oxygen as possible from the test solution so that the corrosion rate determining factor would be the carbonic acid. An enlarged portion of the figure above showing the changes in the potential is shown in Figure 5-2(b).

Effect of Nitrogen and Carbon Dioxide (Enlarged Portion)

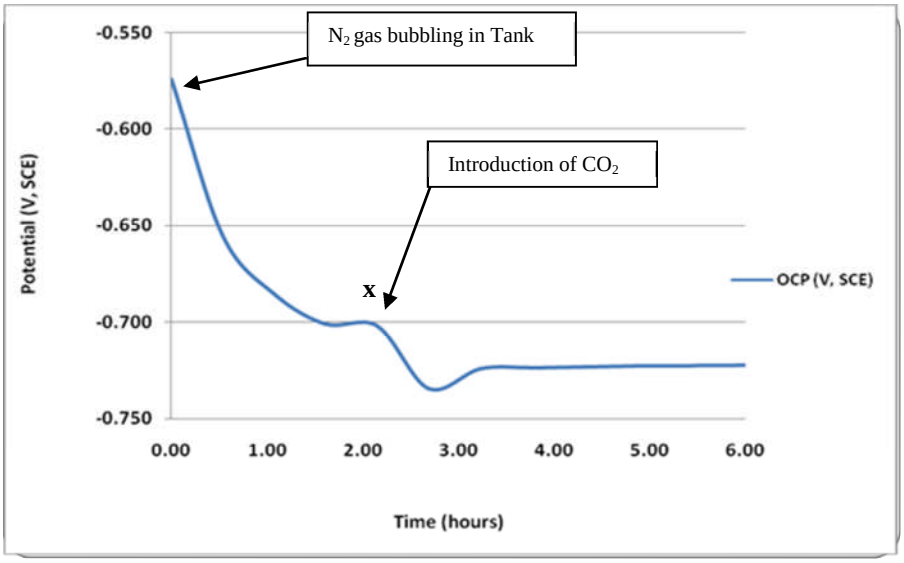

Figure 5-2 (b): Graph showing changes in potential during nitrogen purging and carbon dioxide introduction

Figure 5-2 (b) is an enlarged portion of Figure 5-2 (a) and shows clearly how the potential dropped to -0.702V as a result of the nitrogen purging (point **x**). The introduction of carbon dioxide witnessed a slight drop in the potential before increasing and remaining almost stable. The stable potential is because of the saturation of the NaCl electrolyte with carbon dioxide gas which forms carbonic acid as discussed in the literature review. The slight drop in the potential when CO_2 was initially bubbled into the electrolyte could be attributed to further removal of oxygen or CO_2 corrosion leading to a more active surface.

Using the Evans Diagram to Explain the Graph of the Open Circuit Potential

The results obtained and presented in figures 5-2(a) and 5-2(b) could be explained using the Evans diagrams (graph of electrical potential against the logarithm of the current density) presented in Figure 5-3.

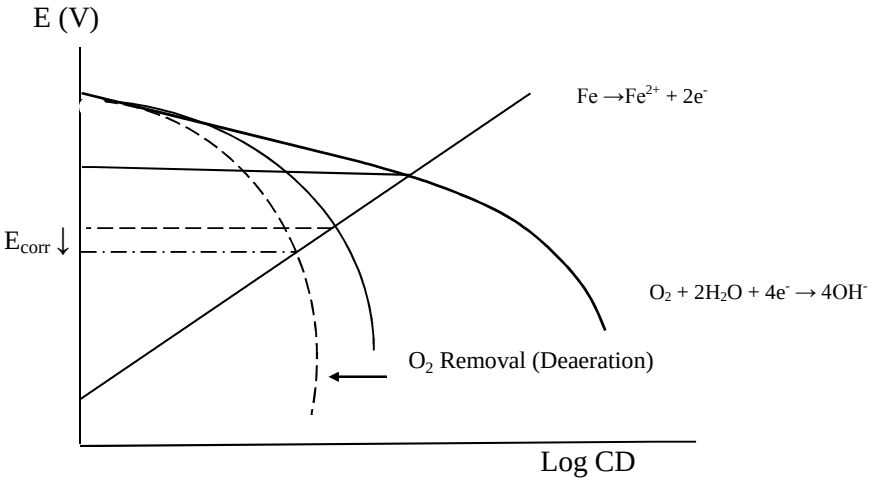

Figure 5-3: Evans diagram displacement of the cathodic curve from right to left showing deaeration

Figure 5-3 shows the movement of the cathodic curve from right to left (bold to dotted line) showing deaeration. This corresponds to point **x** on the potential/time graph in Figure 5-2(b) [drop in the potential from the initial recorded value of -0.574V to -0.702V].

5.4.3 Effect of Carbon Dioxide on Control Sample and Test Electrodes

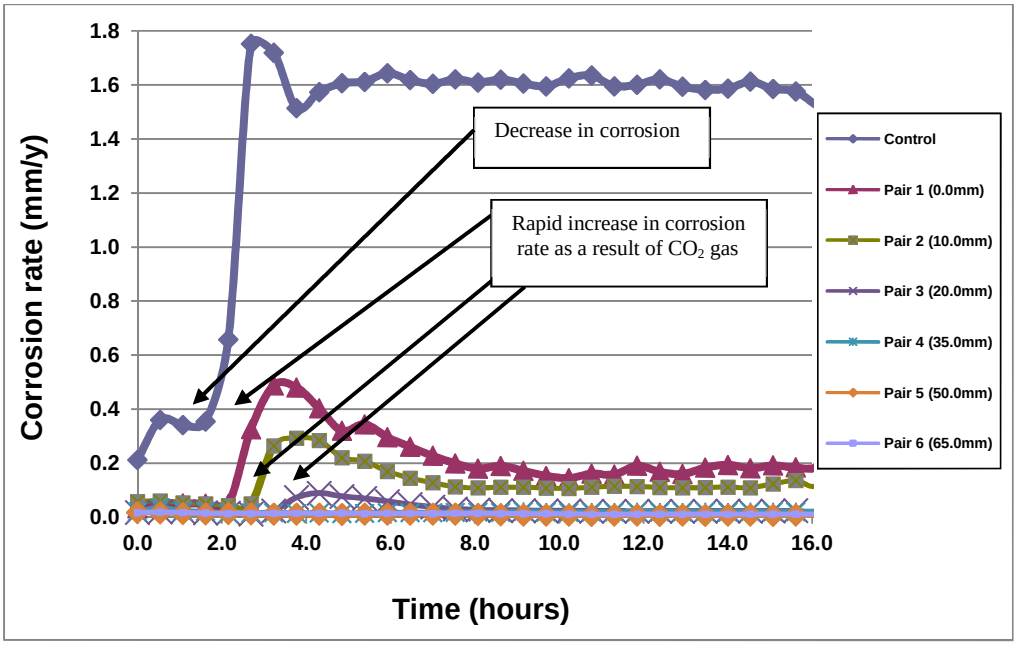

Figure 5-4: Graph of corrosion rate for control sample and test electrodes 1 to 6

Figure 5-4 is the graph of corrosion rate against time for the control sample in the bulk solution and electrode pairs 1 to 6 within the annular space, with pair 1 directly under the vent. The graph shows the corrosion rate of the working electrodes from the period of deaeration, which took about 1 hour 30 minutes, to when it was replaced with CO_2. This length of time for deaeration was necessary to clearly see the changes in the potential and corrosion rate immediately the CO_2 was bubbled into the tank.

There was an initial increase in the corrosion rate from 0.213 mm/y to 0.360 mm/y, at the start of the experiment, possibly due to the effect of some dissolved oxygen still remaining in the electrolyte. This value decreased to 0.342 mm/y due to the continuous deaeration process with the nitrogen gas. Thereafter, the control sample witnessed a sudden increase in the corrosion rate from 0.342 to 1.768 mm/y as soon as CO_2 was bubbled into the electrolyte. This value later displayed a gradual decrease due to the formation of corrosion product and stabilised at an average value of about 1.60 mm/y.

The corrosion rate of test electrode pair 1, within the annular space, increased to a value of 0.49 mm/y because of the initial effect of the CO_2. This corrosion rate dropped to about 0.18 mm/y due to corrosion product formation.

5.4.4 Corrosion Rate within Annular Space

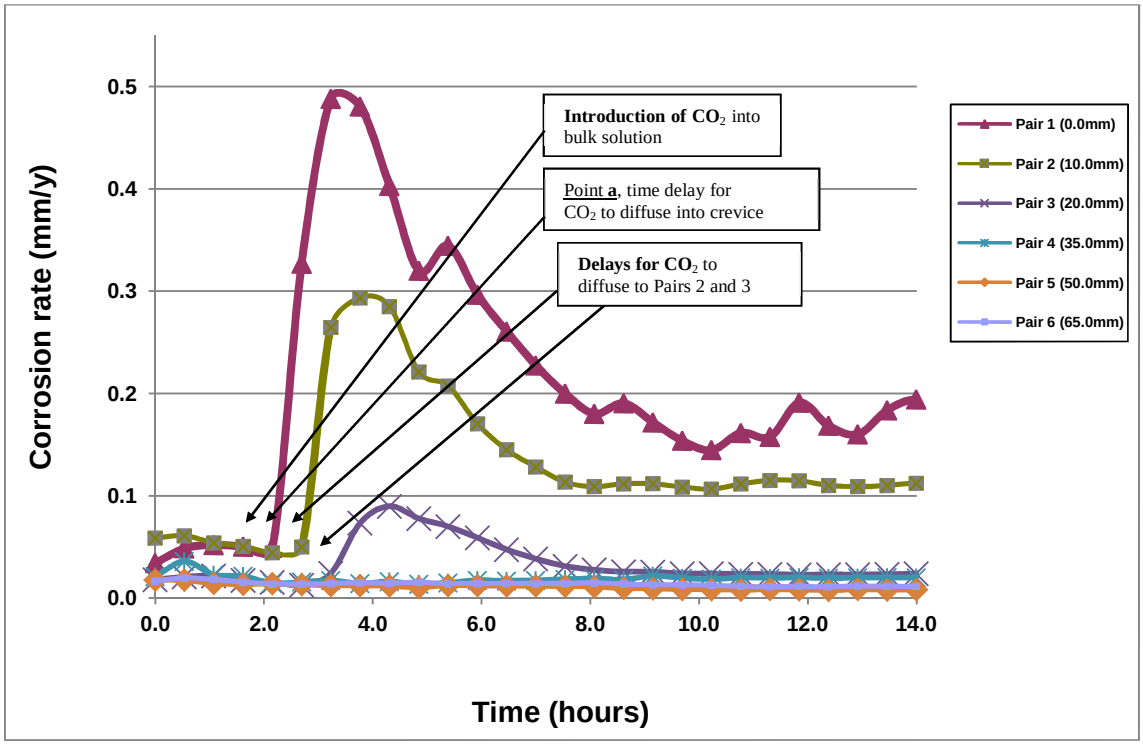

Figure 5-5(a): Graph of corrosion rate within annular space from when nitrogen was bubbled to the introduction of carbon dioxide

The importance of carbon dioxide transport in controlling the corrosion rate is supported by the results in Figure 5-5(a), which shows a progressive delay in the transients measured at each electrode pair, due to the time taken for carbon dioxide to pass from the reservoir, through the vent and into the annular space.

Delay in the Onset of Corrosion in the Annular Space (Diffusion Process)

The effect of CO_2 on the corrosion rate on the test electrodes can be clearly seen for electrode pairs 1 to 3 [Figure 5-5(a)] as it diffuses through the vent. There was an initial delay from the point when CO_2 gas was introduced into the tank to the time it diffused into the annular space. It can de deduced from the shape of the graph (point **a**) that there was a time delay for the gas to diffuse through the vent into the annular space. In other experiments, LPR measurements were carried out using only the control electrode and electrode pair 1, to reduce the interval between readings and improve the accuracy of

the result. The graph of the corrosion rate of test electrode pair 1 is shown in Figure 5-5(b). It can be seen that the corrosion rate increased suddenly to 0.22 mm/y due to the initial effect of CO_2 and then dropped to about 0.12 mm/y.

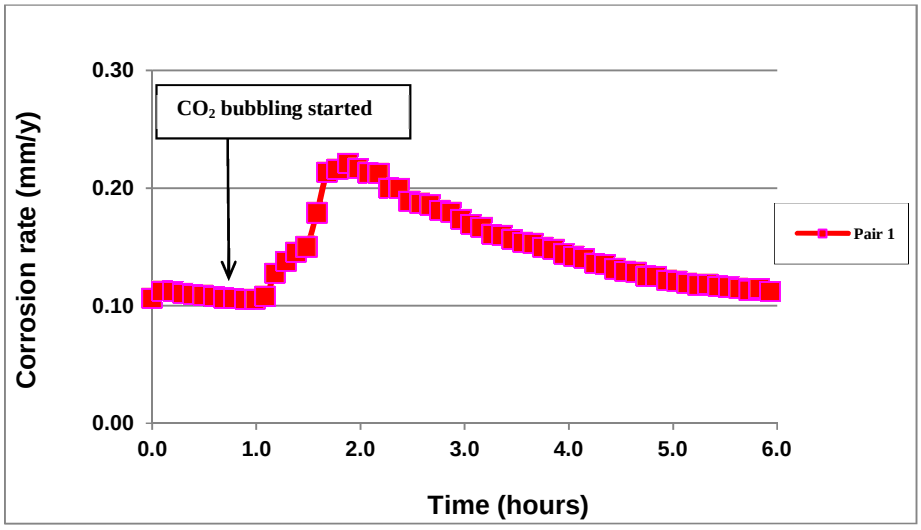

Figure 5-5 (b): Corrosion rate measurement of electrode pair 1

The average value of the stable corrosion rate of electrode pair 1 shown in Figure 5.5(a) and Figure 5.5(b) was taken to be 0.15 mm/y.

Oxygen Removal (Deaeration) Process and CO_2 Effect

At the onset of the experiment shown in Figure 5-4, despite the nitrogen gas being bubbled into the NaCl solution, there was still an increase in the corrosion rate, as seen at the initial part of the graph. This was then followed by a section of reduced corrosion rate due to the effect of the nitrogen gas displacing some of the dissolved oxygen. It is impossible to have a completely deaerated solution but the system was deaerated to a level that the little quantity of oxygen remaining did not affect the CO_2 corrosion process. It can therefore be concluded that the sharp increase in the corrosion rate as can be seen in Figure 5-4 is as a result of the introduction of carbon dioxide gas. The CO_2 gas reacts with water forming carbonic acid which was responsible for the increase in corrosion rate as discussed in the literature review (Kermani and Smith, 1997; De Waard and Lotz, 1993).

As discussed earlier using the Evans diagram, removal of oxygen reduced the corrosion potential by pushing the cathodic curve to the left and in so doing, intercepts the anodic curve at a lower point. This resulted in the downward movement of the potential which corresponds to a reduction of the corrosion rate since the system is under cathodic control. On the other hand the carbonic acid caused corrosion products (Fe_3C and $FeCO_3$), in agreement with the work of Martinez et al. (2011) to form on the electrode surface which shifted the anodic curve upward. This resulted in increase in the potential with a corresponding reduction in the corrosion rate.

5.4.5 Effect of Mass Transport of CO_2 through Vent caused by Mixing in Tank

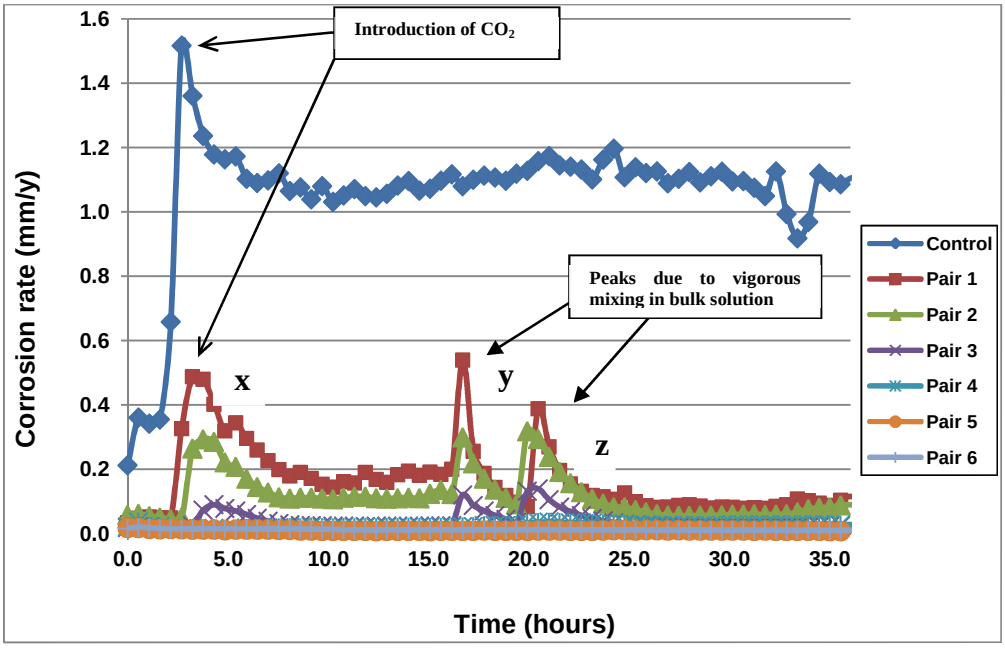

Figure 5-6: Graph of corrosion rate for control sample and test electrode 1 to 6

It was found that vigorous agitation of the solution in the reservoir, using the gas bubbler, could reduce the time for the onset of corrosion due to mixing of the liquid in the liner vent. After the experiment ran for some days, artificial mixing was done inside the tank at two different times to observe the effect on the control sample and test electrodes under the vented liner. Figure 5-6 is the result showing the corrosion rate of the control sample and test electrodes. The first set of sudden increases in the corrosion

rate (point x) was due to the introduction of CO2, as discussed earlier. The corrosion rate of the control sample increased to about 1.58 mm/y. Of the test electrodes within the annular space, electrode pair 1 had the highest corrosion rate of 0.49 mm/y. This is due to the fact that electrode pair 1 first witnessed the carbon dioxide through the vent as a result of diffusion caused by a concentration gradient.

The second sets of sudden increases (points **y** and **z**) are due to the effect of the mixing. The control sample did not show any change in the corrosion rate as a result of the mixing. However, the corrosion rates of the test electrodes around the vent area were affected. This is shown clearly and explained with the enlarged graph in Figure 5-7.

Effect of Mass Transport of CO_2 within the Annular Space due to Mixing

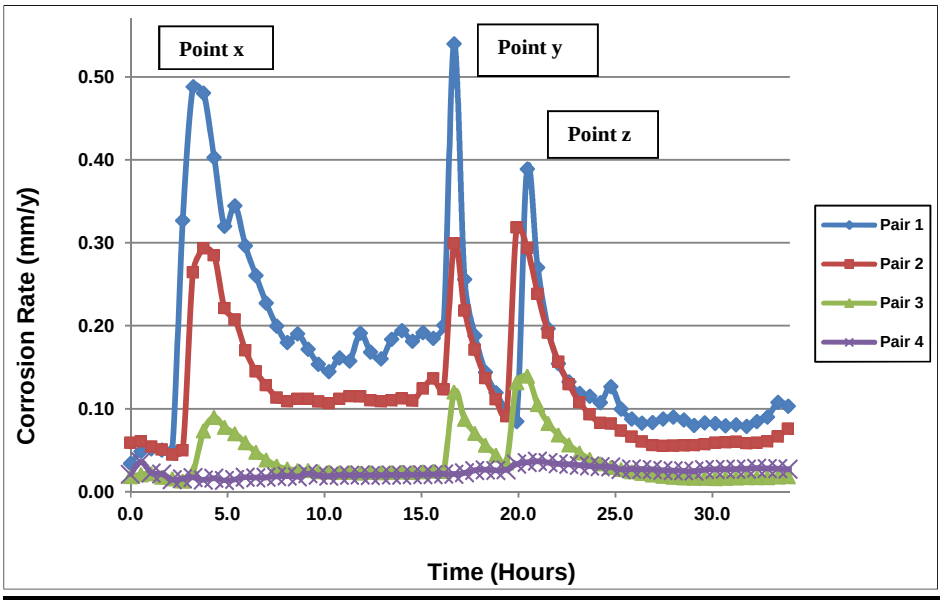

Figure 5-7: Graph of corrosion rate within annular space for test electrode pairs 1 to 4

Figure 5-7 shows the corrosion rate of electrodes pairs 1 to 4, within the annular space, with peaks of high corrosion points. The corrosion rates shown as peak **y** for electrode pair 1 increased from below 0.200 mm/y to 0.540 mm/y. Likewise, the corrosion rates of electrode pairs 2 and 3 increased from 0.100 mm/y and 0.021 mm/y to 0.300 mm/y and 0.12 mm/y respectively. The corrosion rates then dropped because of corrosion film formation. The high corrosion rates labelled **z** are also due to mixing in the bulk

solution. The corrosion rates of electrode pairs 1 and 2 increased from below 0.100 mm/y to 0.399 mm/y and 0.318 mm/y respectively and later dropped to 0.059 mm/y. The corrosion rate of electrode pair 3 also increased from 0.021 mm/y to 0.090 mm/y and then dropped to 0.014 mm/y. In these conditions, transport of CO_2 through the vent was aided by flow, as well as the diffusion caused by a concentration gradient.

Electrode pairs 5 and 6 were really not affected by the CO_2 that diffused into the annular space as they were used up for corrosion process and so their corrosion rates remained low (0.011 mm/y). Generally there is a trend of decrease in the corrosion rate as we move further away from the vent area except where mixing within the bulk solution was performed.

Practical Implication of Mixing within Pipelines with Vented Liners

The sudden increases in the corrosion rates seen within the annular space due to the mixing are very important because they clearly demonstrate that mixing or turbulence within a vented plastic pipeline transports more corrosive species into the annular space. This increase in the mass transport of CO_2 into the annular space consequently increases the corrosion rate. For this particular instance the corrosion rate for pair 1, directly below the vent, reached values as high as 0.540 mm/y. It increased from an average value of about 0.150 mm/y to 0.540 mm/y; over 250%. The corrosion rate of pair 2 which is about 10.0 mm away from the vent, reached a value of about 0.318 mm/y; over 200%.

5.4.6 Comparison of Corrosion Rate along Steel Plate

Having looked at the corrosion rates of the control sample and the test electrodes with respect to time, it is also important to analyse the corrosion distribution along the length of the plate from the vent area. These set of results are important because they help in analysing the extent of the CO_2 attack long the plate length as it diffuses through the vent into the annular space.

The change of the corrosion rate along the metal plate can be analysed by plotting a graph of the corrosion rate against electrode distance from vent. Table 4-2 in Chapter 4 shows the distances of the six test electrodes within the annular space.

Corrosion Cycles for Nitrogen Purging and Carbon Dioxide Introduction

A corrosion cycle is a complete measurement cycle of the LPR equipment from the control sample to all the test electrodes within the annular space (electrode pair 1 to 8). Cycle 1 to cycle 3 represent the period of nitrogen purging while Cycle 4 and beyond were the period when carbon dioxide was bubbled into the solution. Cycles 1 to 6 are labelled clearly as nitrogen cycles 1 to 3 and carbon dioxide cycles 1 to 3 for ease of comparison.

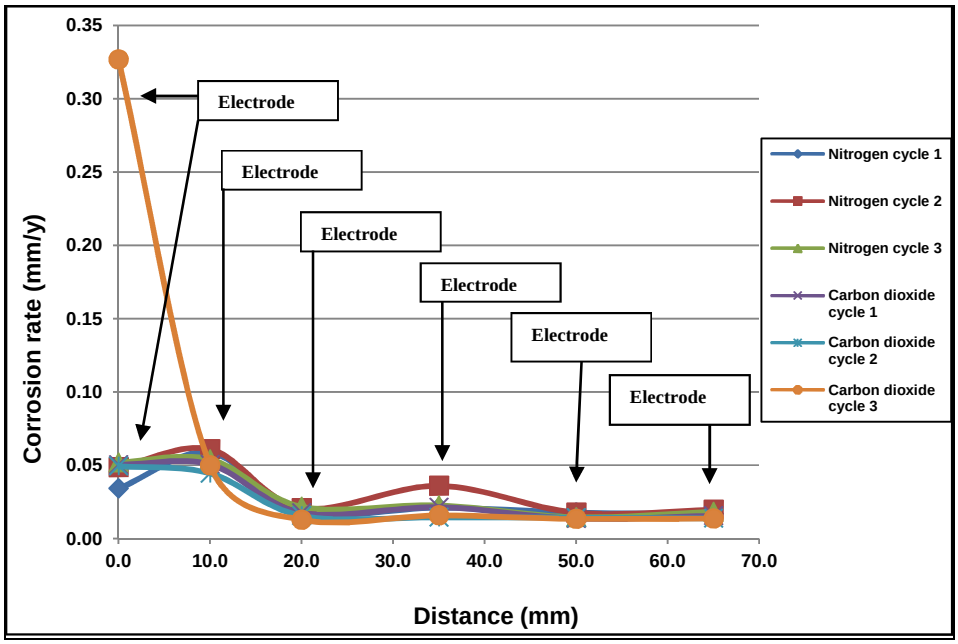

Figure 5-8: Graph of corrosion rate vs distance for nitrogen purging and carbon dioxide introduction

It can be seen from Figure 5-8 that the nitrogen cycles showed a lower corrosion rates which decreased with distance. On the other hand the carbon dioxide cycles showed increased corrosion rates for cycle 2 especially for electrode pair 1; and a decrease for the succeeding electrodes. It is worthy of note that the very high corrosion rate of the

carbon dioxide cyles compared to the nitrogen cycle was due to the corrosive effect of the carbonic acid. A reduction in the corrosion is seen as we move further away from the vent which showed that the CO_2 was used up before it got further down the annular space.

Corrosion Rates for Carbon Dioxide Cycles

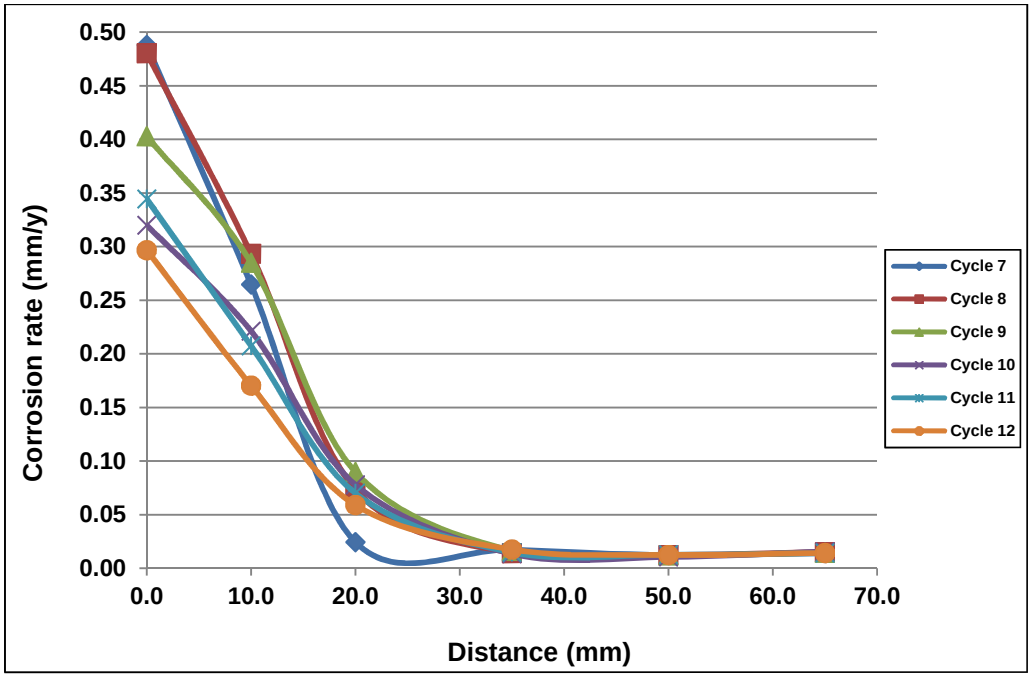

Figure 5-9: Graph of corrosion rate vs distance for CO_2 cycle 4 to 9 (approx 2 hrs 20 mins to 5 hrs 15 mins)

Figure 5-9 shows the graph for the corrosion rates for cycles 7 to 12. These cycles showed a reduction in the corrosion rate with distance from the vent area (0.00 mm) and these rates dropped gradually as the cycles increased. For example the corrosion rate for pair 1 during cycle 7 was 0.481 mm/y and by cycle 12 it has decreased to 0.297 mm/y. It was the same observation made for each point along the annular space further away from the vent; the corrosion rates decreased from a relatively high value as the cycles increased. For all the cycles, the corrosion rate decreased to about 0.018 mm/y by the time it got to pair 4 (35 mm from vent).

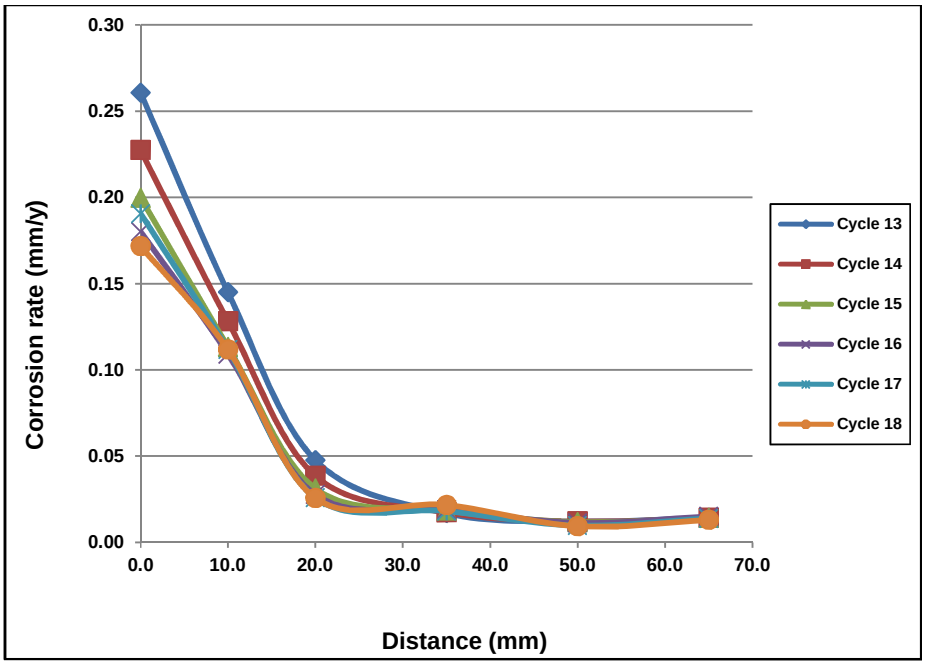

Figure 5-10: Graph of corrosion rate vs distance for CO_2 cycle 4 to 9 (approx 5 hrs 50 mins to 8 hrs 45 mins)

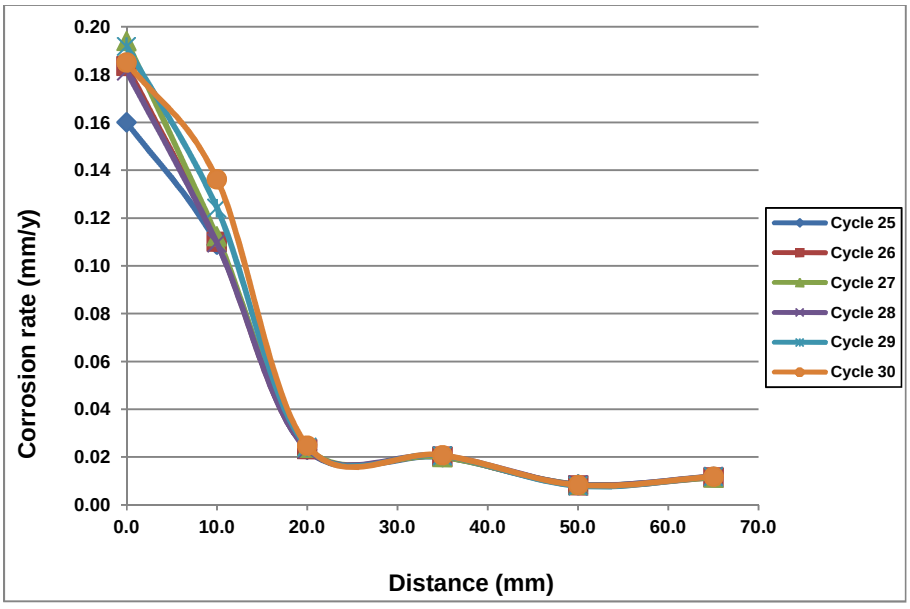

Figure 5-11: Graph of corrosion rate vs distance for CO_2 cycle 4 to 9 (approx 13 hrs 45 mins to 15 hrs 25 mins)

Figures 5-10 and 5-11 show a general decrease in the corrosion rate from electrode pair 1 directly under the vent to pair 6, which is 65.0 mm away from the vent. As the cycle

increased, the corrosion rate decreased straight through pairs 1 to 6. For instance, the corrosion rate of pair 1 in Figure 5-10 decreased from 0.261mm/y to 0.172mm/y; while in Figure 5-11 it decreased from 0.192mm/y to 0.160mm/y.

Generally it can be seen that for all the cycles, the corrosion rate decreased from maximum values occurring at pair 1 (0.0 mm), directly beneath the vent, to the minimum at electrode pair 6; 65.0 mm further away from the vent.

5.5 Summary of Discussions

The deaeration process with nitrogen gas before the experiments confirmed that dissolved oxygen was removed to a level that the CO_2 corrosion process was not affected. This was shown by the drop in the potential (-0.702 mV) and the corrosion rate due to dissolved oxygen. Introduction of CO_2 into the corrosion cell witnessed a rapid increase in the corrosion rate to about 1.768 mm/y (control) and 0.480 mm/y for the test electrode directly beneath the vent within the annular space and then a drop in the corrosion rate. The corrosion rate of the control sample then dropped to about 1.60 mm/y while that of the test electrode directly under the vent dropped to an average value of 0.15 mm/y. These results with the observed surface changes, agree with published results of high corrosion rates when bare steel comes in contact with carbonic acid. And also a reduction in the corrosion rate as soon as corrosion product layers begin to form on the metal surface (Palmer-Jones and Paisley, 2000). This increase happened after some time delay, supporting a diffusion mechanism for the CO_2 transport through the vent. The diffusion mechanism was also observed for the other test electrodes, provided there were no mixing and mass transport was mainly by diffusion due to the concentration gradient of the CO_2.

Another point of interest was the sudden increase in the corrosion rates within the annular space whenever there was mixing in the tank (bulk solution). The practical implication of these results is that vigorous mixing or turbulence in pipeline with vented plastic liners could lead to greater mass transport of corrosive species through the liner vent and greatly affect the extent of corrosion occurring beneath.

The results on the corrosion distribution and the corrosion cycles showed how the corrosion rates decreases with distance from the vent, for the two gas regimes. The nitrogen purging showed a drop in the OCP and the corrosion rates. The CO_2 cycles also showed the gradual drop of the corrosion rate at different point within the annular space, after the initial sudden increase when CO_2 was bubbled into the bulk solution. The graphs showed that there was a progressive reduction in corrosion rate over time, accompanied by the formation of a surface film. The corrosion had not extended significantly more than 35.0 mm from the liner vent. Beyond this point, the corrosion rate was generally low (0.02 mm/y) because the CO_2 that diffused into the annular space had been depleted by corroding the steel surface.

Generally the results clearly supported the fact that the vent design with the aspect ratio of 3.3:1 restricted the mass transport of CO_2 into the annular space. Provided no flow occurred beneath the liner, corrosion only took place locally and its rate was limited by the slow transport of carbon dioxide through the liner vent. The corrosion rates were typically 20% of those of the control (unlined pipe) and diminished with distance from the vent. However, the main challenge was the issue of mixing which always suddenly increased the corrosion rates.

CHAPTER 6
MATHEMATICAL MODELLING OF CO_2 TRANSPORT IN THE LINER VENT LEADING TO CORROSION IN THE ANNULAR SPACE

6.1 Introduction

Mathematical models are essentially predictive tools that estimate the response of a system to changes in system variables. In corrosion science, mathematical models aid in understanding the effect of different variables on the corrosion rates and also prediction of corrosion rates of metals (Kennell et al., 2008).

It is pertinent to note that modelling has helped in understanding and mitigating the corrosion problem especially in predicting the internal corrosion of the oil and gas transport pipelines due to corrosive species like CO_2 (Song, 2010; Walton, 1990). It was therefore imperative to develop a mathematical model for CO_2 transport through the liner vent as this CO_2 was responsible for controlling the corrosion rate in the annular space.

This Chapter briefly looks at one of the CO_2 corrosion models discussed in the literature review and the results obtained in Chapter 5 to describe a corrosion model for transport of CO_2 through vented plastic lined pipelines. CO_2 concentration profiles for the liner vent were obtained and the metal loss under the liner was estimated using diffusion and mass balance equations.

6.2 Development of CO_2 Corrosion Model for Plastic Lined Pipelines

The focus of this sub-section is to provide an understanding of the systematic development of this CO_2 corrosion model using a mechanistic approach based on diffusion mechanism and Fick's laws. The model was intended to serve as a guidance tool for the determination of the metal loss under the plastic liner in a system where

CO_2 is the dominant corrosive species. The corrosion model was simply based on electrochemical reactions and CO_2 transport by diffusion (Papavinasam et al., 2005; Dayalan et al., 1998a).

6.2.1 CO_2 Transport Process

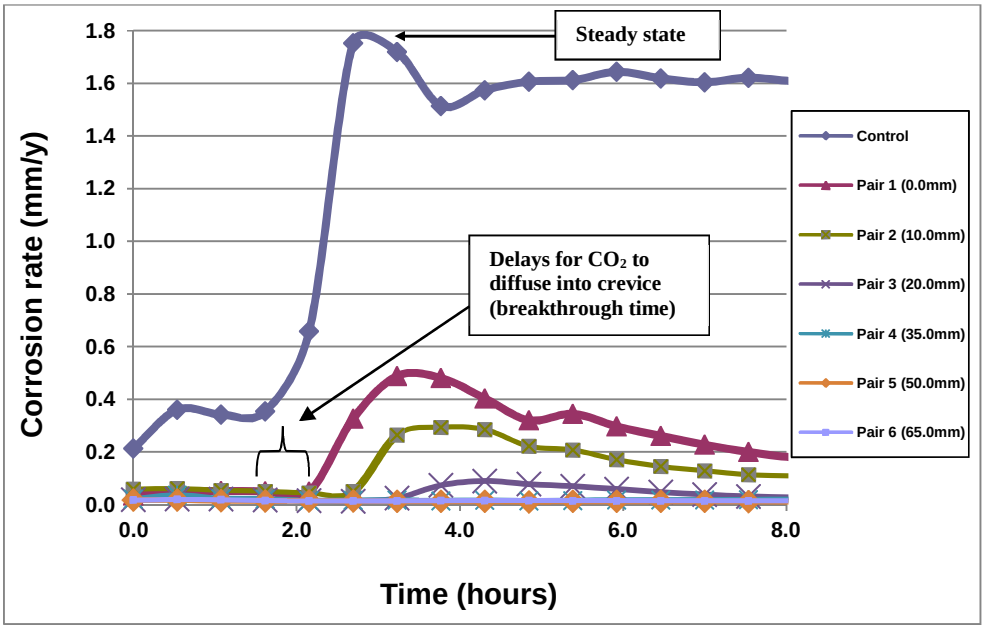

Figure 6-1: Graph of corrosion rate for control sample and test electrodes within annular space

Figure 6-1 is taken from Chapter 5 (Figure 5-4) and shows the delay in the transport of CO_2 into the annular space. In Figure 6-2 only the control electrode and electrode pair 1 were measured to reduce the interval between readings and improve the accuracy of the breakthrough time. The CO_2 transport supports a diffusion process as demonstrated by the progressive delay in the transients measured at each electrode pair (Figure 6-1) and electrode pair 1 (Figure 6-2).

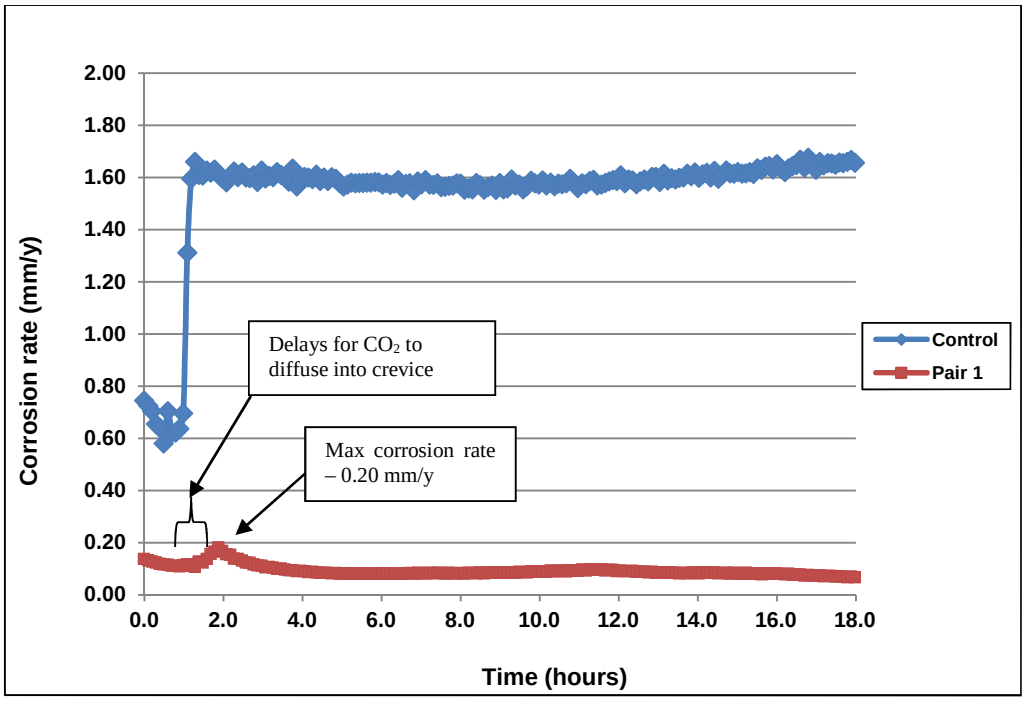

Figure 6-2: Graph of corrosion rate for control sample and test electrodes under vent

Due to the electrochemical reaction on the carbon steel surface within the annular space, Fe^{2+} ions were produced while H^{+}, are reduced at the cathode. Consequently, a concentration gradient was established which resulted in further transport of the CO_2 by diffusion through the vent into the annular space. Therefore the corrosion process was modelled as following a diffusion process.

Shayegani et al. (2008) in their work supported the fact that corrosive species are transported to corrosion sites by diffusion and the one-dimensional form of the mass balance equation may be used to describe the transport process. Therefore in this study, Fick's one-dimensional diffusion equation which describes transport of species through a plane sheet was applied (Chen and Rizvi, 2006).

6.3 Mathematical Theory and Equations of Diffusion

The mathematical theory of diffusion in isotropic substances is based on the hypothesis that the rate of transfer of a diffusing substance through a unit area of a section is proportional to the concentration gradient measured normal to the section (Crank, 1975, pg 2). This definition is expressed as Equation 6-1 (Fick's first law of diffusion):

Equation 6-1

$$F = -D\frac{\partial C}{\partial x}$$

Where,

- F – rate of transfer per unit area of section (in mol/cm^{2}s)
- D - diffusion coefficient (in cm^2/s)
- C - concentration of diffusing substance (in mol/cm^3)
- x – distance on a plane normal to section (in cm)

Equation 6-1 gives the diffusive flux or amount of material diffusing through the unit area. The diffusion partial differential equation for one-dimensional diffusion, also called Fick's second law of diffusion, is derived from the first law (Equation 6-1) and is given as (Melchers, 2003):

Equation 6-2

$$\frac{\partial C}{\partial t} = D\frac{\partial^2 C}{\partial x^2}$$

Where,

- D - diffusion coefficient (in cm^2/s)
- C - concentration (in mol/cm^3)
- x – distance along the plane sheet (in cm)
- t - time (in seconds)

6.4 Diffusion through Plastic Liner Vent (Plane Sheet)

The model is intended to describe diffusion through a plane sheet formed by a plastic liner vent which gives access to a annular space. The annular space was formed between the carbon steel plate and plastic liner. Figure 6-3 is the schematic which presents the vent in the plastic liner with the NaCl electrolyte medium bounded by two parallel planes formed by the vent. This volume of electrolyte forms the plane sheet through which the diffusing substance (CO_2) leaves the bulk solution and enters the annular space through the vent. The planes are formed by the liner surfaces $x = 0$ (top), and $x = l$ (bottom).

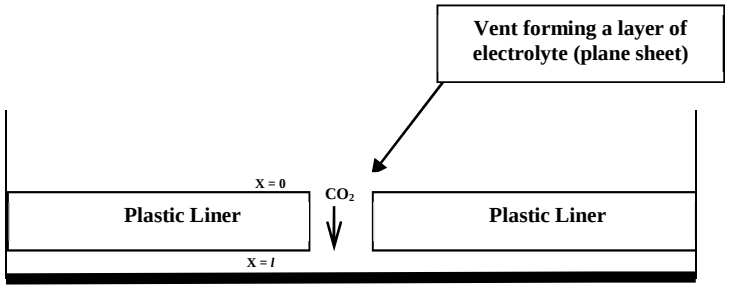

Figure 6-3: Schematic showing plane sheet formed by layer of electrolyte within the vent

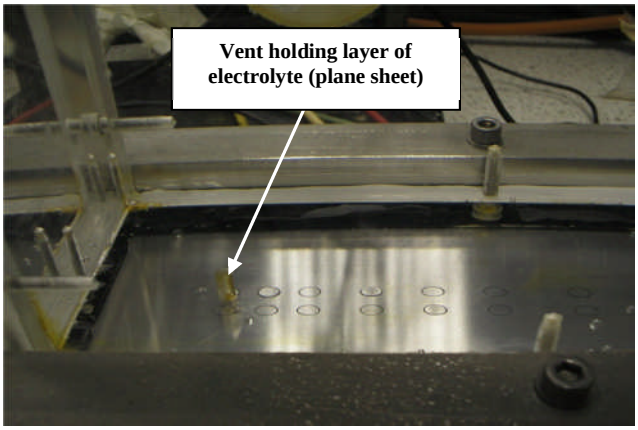

Figure 6-4: Pictorial view of vent with electrolyte layer through which CO_2 diffuses into the annular space

Assumptions

Assumptions were necessary to define the mathematical model used for this study. This approach (of making simplifying assumptions) has been used in past studies such as that by Chin and Sabde (2000a). The following were the assumptions made for the mathematical modelling:

- The brine solution in the liner vent was stationary such that dissolved CO_2 was transported through the vent entirely by diffusion and convection did not play a part.

- Diffusion was uni-directional in the medium with all the CO_2 entering through the face of the electrolyte medium in the vent plane.

- The concentration of CO_2 is highest at the top of the vent ($x = 0$) in the vent solution and the coefficient of diffusion D is constant.

- At the start of the experiment, the solution in the tank was quickly saturated with CO_2 and the concentration at the open end of the liner vent remained constant ($C = 1$). The CO_2 concentration at the vent bottom was zero ($C=0$); that is, all the carbon dioxide that diffused through the vent were immediately removed from the solution by the corrosion reaction directly beneath the vent.

This last assumption was only reasonable in the early stages of the experiment, as the steel surface was active and unfilmed. It was less so in the later stages when a partially protective film had formed on the metal surface and it was evident that corrosion was developing away from the vent and along the annular space.

It is pertinent to mention that the diffusion equation in this model is intended for an infinite, thin sheet, rather than a relatively long, thin vent. However, the equation is still valid in this case as diffusion of CO_2 is restricted to one direction by the walls of the vent and radial diffusion is not possible. As the boundary conditions define that the CO_2

concentration is uniform and constant at the top of the vent, the transport of CO_2 from the tank to the vent need not be considered.

6.4.1 Steady State Condition in Vent

Flux, F, could be determined from the diffusion through the electrolyte medium (plane sheet) as shown in Figure 6-3, with vent length *l* and coefficient of diffusion D. The vent surfaces x = 0 (entrance) and x = 1 (exit) were assumed to correspond to constant concentrations C_1 and C_2 respectively. After a time interval, steady state condition was attained in which the concentration within the vent remained constant. The diffusion equation (Equation 6-2) would then become (Crank, 1975):

Equation 6-3

$$\frac{d^2C}{dx^2} = 0$$

On integrating Equation 6-3 and substituting it into Equation 6-1 the rate of transfer of diffusing substance (CO_2) becomes:

Equation 6-4

$$F = -D\frac{dC}{dx} = \frac{D(C_1 - C_2)}{l}$$

It is pertinent to note that if the length of the vent *l* is substituted as 1.27 cm, the surface concentration C_1 determined from Henry's Law and C_2 assumed to be zero, the flux F can be determined from a known value of the diffusion coefficient D. This equation would be used later to calculate the diffusive flux F of CO_2 that enters the annular space.

6.4.2 Non-steady State Condition in Vent

Due to the gradual process of diffusion of the CO_2 from the tank into the vent, non-steady state (transient) conditions are prevalent. During this transient period the concentration within the vent changes according to Equation 6-5 (Chen and Rizvi, 2006; Crank, 1975).

Equation 6-5

$$C = C_1 + (C_2 - C_1)\frac{x}{l} + \frac{2}{\pi}\sum\frac{C_2\cos n\pi - C_1}{n}\sin\frac{n\pi x}{l}\exp(-Dn^2\pi^2 t/l^2)$$

$$+\frac{4C_0}{\pi}\sum_{m=0}^{\infty}\frac{1}{2m+1}\sin\frac{(2m+1)\pi x}{l}\exp\{-D(2m+1)^2\pi^2 t/l^2\}$$

Where,

- $C_{1,2}$ - concentrations at the entrance and exit points (in mol/cm^3)
- C_o - concentration at the surface of the plane sheet (in mol/cm^3)
- m, n - integers
- D - coefficient of diffusion (in cm^2/s)
- x - depth of diffusant along the plane sheet (in cm)
- l - length of the vent, plane sheet, (in cm)
- t - time (in s)

It is pertinent to note that as t approaches infinity (steady state), the exponential terms become zero and the linear concentration equation (Equation 6-4) is obtained. This implies that the non-steady state condition develops into a steady state condition with time.

6.4.3 Solution of Differential Equation for Diffusion through Plane Sheet

Archer and Grant (1984) in their work on the permeability of metallic membranes (plane sheet) by hydrogen presented the solution for a constant concentration condition at the membrane entrance in dimensionless variables. Therefore the solution to the one-dimensional equation of Equation 6-2 becomes:

Equation 6-6

$$\frac{\partial\sigma(X)}{\partial\tau} = \frac{\partial^2\sigma(X)}{\partial X^2} \quad \text{(Fick's law)}$$

Where the dimensionless variables are:

- $\tau = \frac{Dt}{l^2}$

- X = $\frac{x}{l}$ (dimensionless distance)
- $\sigma(x,\tau) = \frac{c(x,t)}{c_o}$ (dimensionless concentration)

Equation 6-6 was solved for diffusion into a plane sheet for the boundary conditions defined below (Sato et al., 1999; Chen and Rizvi, 2006):

$t = 0 \qquad 0<x<l \qquad C = 0$ **Equation 6-7**

$t > 0 \qquad x = l \qquad C = 0$ **Equation 6-8**

$t = 0 \qquad x = 0 \qquad C = C_\circ$ **Equation 6-9**

Equation 6-7 implied that CO_2 was initially absent in the electrolyte medium in the vent column. Equation 6-8 implied absence of CO_2 at the bottom of the vent; in this case it was used for the corrosion process just outside the bottom of the vent. Equation 6-9 defined the change in the concentration of CO_2 within the vent; the concentration is represented by C.

Taking the boundary conditions,

- $\sigma\ (0, \tau) = 1$ at the entrance and
- $\sigma\ (1, \tau) = 0$ at exit.

The concentration C at any time t and position X (x/*l*) within the vent can be calculated as a proportion of $C_\circ$ from the expression for one dimensional diffusion in a plane sheet (Equation 6-10), derived from Fick's Second Law of diffusion. $C/C_\circ$ $[\sigma(X,\tau)]$ was enumerated from Equation 6-10 (Archer and Grant, 1984) for different times and a range of values of X (x/*l*) by taking the first 20 terms in the converging series.

Equation 6-10

$$\sigma(X,\tau) = (1-X) - \frac{2}{\pi}\sum_{1}^{\infty}\frac{1}{n}\sin n\pi x \exp - n^2\pi^2\tau$$

6.4.4 Predicted CO_2 Concentration Profile

To investigate the concentration changes inside the vent when the electrolyte in the tank was saturated with CO_2, the concentration profiles of the CO_2 within the vent needed to be determined. If Equation 6-10 is plotted on a graph, involving the dimensionless variables τ and X, the coefficient of diffusion D could be determined from the value of τ at breakthrough and the breakthrough times obtained from the experimental results. Plotting this equation on an Excel Spreadsheet, a series of curves were produced (shown below) for different values of τ representing different concentration profiles.

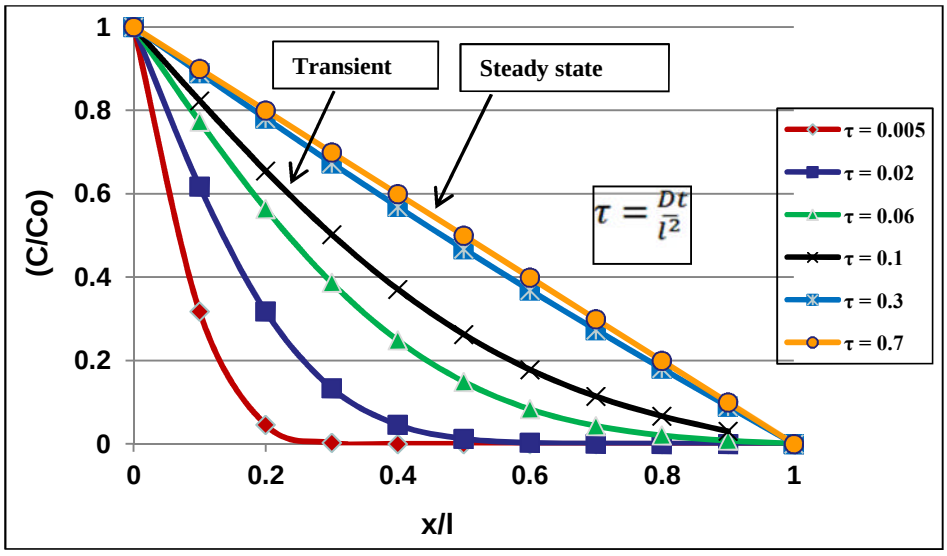

Figure 6-5: Graph of dimensionless concentration of dissolved CO_2 against dimensionless distance of vent

Figure 6-5 is the plot of the concentration profile of diffusing substance through a plane sheet. It demonstrates the variation of CO_2 concentration along the length of the liner vent, at different times from the start of the experiment. The graph indicates a constant concentration ($C/C_\circ = 1$) at the open end of the vent and zero concentration at the vent side open to the annular space. The individual plots are for different values of the non-dimensional term τ. The x axis corresponds to the dimensionless distance X (x/l) while the y axis represents the dimensionless concentration.

The results indicate that the CO_2 concentration in the vent was a function of the perpendicular distance from the top of the vent. It can be seen also that for τ values below 0.5, curves in the CO_2 distribution are evident; this curve indicates a transient or non-steady state condition.

Above this value of 0.5, steady state conditions gradually set in and are fully attained at a τ value of about 0.7. For a τ value of 0.06, a breakthrough case is evident (Archer and Grant, 1984). In the corrosion cell, this is the point where the CO_2 just reaches the surface of the steel plate in the annular space. It is the instance where the corrosion rate of electrode pair 1 rapidly increased (figures 6-1 and 6-2). For a smaller value of τ, for example 0.005, the CO_2 has not diffused through the length of the vent; instead, it has travelled only 30% through it. In the same vein, when τ equals 0.02, the CO_2 has travelled just above 50% through the vent.

6.4.5 Determination of Coefficient of Diffusion

The breakthrough time (t_b) is the time t when the diffusing species (carbon dioxide, in this case) just reaches the far side of the medium (brine) through which it is diffusing. The breakthrough time (t_b) is obtained directly from the graphs as the difference in time between when the corrosion rate of the control sample suddenly increased and when that of electrode pair 1 also suddenly increased. Referring to the graphs in figures 6-1 and 6-2 discussed earlier, a mean breakthrough time of 29 minutes was obtained.

If the coefficient of diffusion D is assumed constant, its value can be calculated from the breakthrough time (t_b) (Marais et al., 2002). The determination of the coefficient of diffusion of the CO_2 in the electrolyte is important because it is required in estimating the quantity of CO_2 that was transported into the annular space through the vent. As discussed earlier, the dimensionless variable τ is expressed as:

$$\tau = \frac{Dt}{l^2}$$ **Equation 6-11**

Where,

- D = coefficient of diffusion (in cm^2/s)
- τ = dimensionless variable
- l = length of vent (in cm)
- t = time (in s)

The dimensionless variable τ is directly proportional to time t at constant D. This implied a longer time to attain steady state which is the condition when the flux of CO_2 in the bulk solution is the same as that at the vent bottom. From Figure 6-5 (concentration profile curves), the breakthrough situation exists at the point when a particular transient curve (in this case the green curve) just meets the dimensionless distance x/l at 1. This transient curve is equivalent to $\tau = 0.06$.

It follows that for the breakthrough situation, $\tau = 0.06$, t = 1740 sec (29 minutes), l = 1.27 cm, and therefore the expression in Equation 6-11 which equals to 0.06 can be used to obtain the value of the diffusion coefficient D. This gives a diffusion coefficient D for carbon dioxide in brine as **$5.6 \times 10^{-5} cm^2 s^{-1}$** at 25°C. This compares quite favourably with a value of $1.96 \times 10^{-5} cm^2 s^{-1}$ at 25°C reported by Nesic et al. (1996) in their work on rotating disc electrode cited by Song (2010). Taking this latter value, the breakthrough time for static conditions in the vent would be expected to be 82 minutes. This implies that despite the precautions taken, the rather shorter time measured in these experiments suggest that a limited amount of mixing did occur and the temperature might have increased above 25°C.

At longer times ($0.7 \leq Dt/l^2 \leq 1.0$), the concentration profiles approach a straight line corresponding to the steady state condition as shown in Figure 6-6. The figure shows the concentration of CO_2 at the bottom of the vent to be zero while the flux is the same. All the CO_2 that diffused into the annular space is therefore used up for corrosion. Taking the steady state, $\tau = 0.7$, the average time t (when corrosion rates are maximum) = 8400 sec (2 hours 20 minutes), and l = 1.27 cm. The coefficient of diffusion D, from Equation 6-11, therefore equals to **1.3×10^{-4} $cm^2 s^{-1}$** at 25°C. It is pertinent to note that using this method is less accurate compared to the breakthrough method, due to the difficulty in correctly identifying when steady state has been reached.

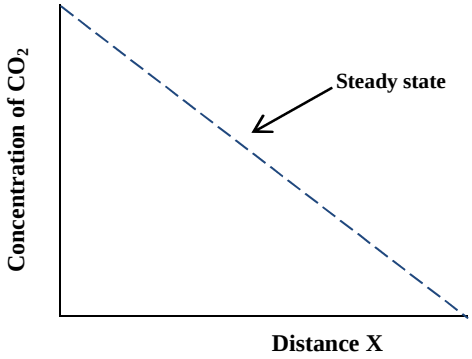

Figure 6-6: Schematic diagram of changes in the concentration in the vent

Therefore the values of D obtained for the breakthrough (5.6 x $10^{-5}cm^2s^{-1}$) and the steady state (**1.3 x 10^{-4} cm^2s^{-1}**) conditions differ greatly. This was not expected since D was assumed constant. If D is taken as 5.6 x $10^{-5}cm^2s^{-1}$, the time to attain steady state will be about 5.0 hours 36 minutes. This disparity could be attributed to the filming of the metal surface with corrosion product therefore causing the corrosion rate to drop before steady state was actually attained. The value of D (**5.6 x $10^{-5}cm^2s^{-1}$** at 25°C) obtained using the breakthrough time is considered to be more reliable.

6.4.6 Prediction of CO_2 Corrosion Rate using Model and Mass Balance Equation

Based on the assumption that all the CO_2 was used up during the corrosion process in the annular space, the diffusion equation could be used to estimate the amount of steel corroded. Referring to Equation 6-4, the flux can be calculated if the concentration of the CO_2 in the bulk solution (C_1) and the coefficient of diffusion are known.

The concentration of CO_2 that dissolved in the bulk solution can be calculated from Henry's law given in Equation 2-23 (stated below again).

$$P_{CO_2} = K_H[CO_2] \qquad \textit{(Equation 2-23)}$$

Taking Henry's constant K_H as 29.5 bar.L/mol (Song, 2010) and the partial pressure of the CO_2 as 1 bar, the concentration becomes 0.034 mol/L.

From Equation 6-4 the diffusive flux F is obtained below (noting that concentration at exit $C_2 = 0$).

$$F = \frac{D\ (C_1)}{l} = \frac{5.6\ x\ 10^{-5}\ (0.034)}{1.27} = 1.49 \text{ x } 10^{-6} \text{ mol cm/L.s} = \frac{1.49\ x\ 10^{-6}}{1000 cm^3}\ \frac{mol\ cm}{s}$$

$$= 1.49 \text{ x } 10^{-9} \text{ mol/cm}^2\text{s}$$

Therefore the flux or rate of transfer of CO_2 through the vent into the annular space is $1.49 \text{ x } 10^{-9}$ mol/cm^{2}s. Since the area of the vent can be calculated from the known vent diameter (Table 4-3), the steady state flux of CO_2 through the vent area is given as:

$$\frac{1.49\ x\ 10^{-9}\ mol}{cm^2\ x\ s}\ x\left[\pi\ \left(\frac{0.38\ cm}{2}\right)^2\right] = 1.69 \text{ x } 10^{-10} \text{ mol/s}$$

Therefore, quantity of CO_2 that diffused into the annular space at steady state = rate of diffusion of CO_2 (flux) x time (27.7 hours).

$$= 1.69 \text{ x } 10^{-10} \text{ x } (27.7 \text{ x } 3600) \text{ mol} = 1.69 \text{ x } 10^{-5} \text{ mol}$$

Since it was assumed that all the CO_2 that diffused into the annular space was used up in the corrosion process, the amount in moles of the Fe that will react with the CO_2 is obtained from Equation 6-12.

$$Fe + [CO_2 + H_2O] \rightarrow FeCO_3 + H_2 \qquad \textbf{Equation 6-12}$$

Equation 6-12 implies that 1 mole of CO_2 (44g) will react with 1 mole of Fe (55.8g) to produce 1 mole of $FeCO_3$ (115.8g); that is, a mole ratio of 1:1. Therefore $1.69 \text{ x } 10^{-5}$ moles of Fe reacted with $1.69 \text{ x } 10^{-5}$ moles of CO_2.

But 1 mole of Fe = 55.8g. Therefore mass of Fe that reacted with CO_2 (metal loss) is **$9.40 \text{ x } 10^{-4}$ g or 0.94 mg** ($55.8 \text{ x } 1.69 \text{ x } 10^{-5}$).

6.4.7 Metal Loss from Corrosion Rate obtained from Experimental Results

Figure 6-7 is the schematic arrangement of the carbon steel surface showing the test electrodes and the portion of the plate exposed to CO_2 corrosion. The corrosion rate decreased as we moved further away from the vent and was very low at about the 35.0 mm from the vent. Figure 6-8 presents the schematic of the corrosion distribution along the steel plate based on Figure 5-10. Since the corrosion rate was obtained from the Solartron LPR equipment, the metal loss can be calculated and compared with that obtained from the mass balance equation.

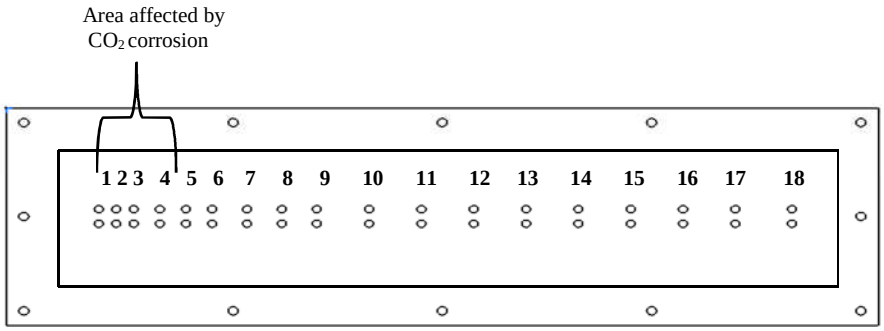

Figure 6-7: Schematic of steel surface in annular space exposed to corrosion

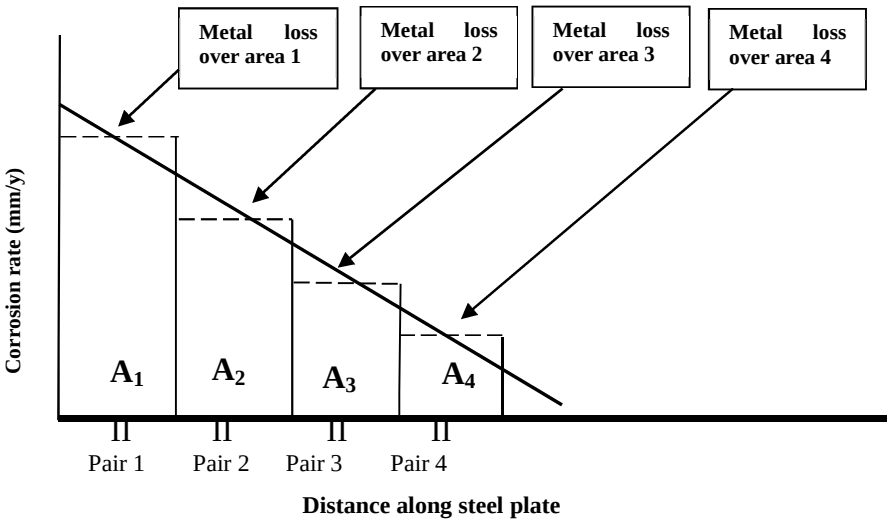

Figure 6-8: Schematic of corrosion rate distribution along steel plate within annular space

The metal loss around the vent area (electrode pairs 1 - 4) can be calculated from the known corrosion rate using the following equation (Fouda et al., 2011; Song et al., 2009):

$$CR = 87.6 \times (W/DAT) \quad \textbf{Equation 6-13}$$

Where,

- CR – corrosion rate (in mm/y)
- W – weight loss (in mg)
- D – density (in g/cm^3)
- A – area of sample (in cm^2)
- T – time of exposure of the metal sample (in hours)

Therefore, metal loss $W = \frac{CR \times DAT}{87.6}$

The plate is divided into the four sections where there is some corrosion. Referring to Figure 5-4, the stable corrosion rates of electrode pairs 1 to 4 are obtained and the total metal loss computed from the equation above and presented in Table 6-1:

Table 6-1: Area under corrosion rate-distance curve

Carbon plate section	Width (cm)	Length (cm)	Area (cm^2)	Corrosion rate (mm/y)	Metal loss (mg)
A_1	8.50	0.10	0.85	0.261	0.550
A_2	8.50	0.10	0.85	0.144	0.303
A_3	8.50	1.25	10.63	0.048	1.264
A_4	8.50	1.50	12.75	0.021	0.664
Total metal loss					**2.781**

The computation of the metal loss is shown in Appendix A.

Therefore the estimated total metal loss obtained using the model is 0.94 mg while that obtained using the measured corrosion rates and corroding area under the liner is 2.78 mg.

6.5 Summary of Discussion

The corrosion model described was based on the diffusion of carbon dioxide based on Fick's laws and was intended to serve as a guidance tool for the determination of the corrosion rate under a plastic lined pipeline where CO_2 is the dominant corrosive species. Due to the electrochemical reaction between the CO_2 and the carbon steel in the annular space, a concentration gradient was established which resulted in more CO_2 being transported through the vent. Fick's one-dimensional diffusion equation which describes transport of species through a plane sheet was therefore applied to obtain a concentration profile of the CO_2 through the electrolyte medium in the vent.

From the experiments performed, a mean breakthrough time of 29 minutes was obtained and a diffusion coefficient for carbon dioxide in brine was calculated to be **$5.6 \times 10^{-5} cm^2 s^{-1}$** at 25°C. This compares quite favourably with a value of $1.96 \times 10^{-5} cm^2 s^{-1}$ at 25°C reported in the literature (Song, 2010). Taking this latter value, the breakthrough time for static conditions in the vent would be expected to be 82 minutes. This implies that despite the precautions taken, the rather shorter time measured in these experiments suggest that a limited amount of mixing did occur and the temperature might have increased above 25°C. It is important to mention that temperature fluctuation within the laboratory could have caused the temperature of the corrosion cell especially the carbon steel plate to be around 25ºC ± 2°C.

For the steady state situation, a mean time t of 2 hours 20 minutes was obtained from the experiment and the coefficient of diffusion was calculated as **1.3×10^{-4} cm^2/s** at 25°C. This value of D obtained differed from the one obtained for the breakthrough situation. If D is taken as $5.6 \times 10^{-5} cm^2 s^{-1}$ the time to attain steady state would be 5.6 hours. This disparity could be attributed to filming of the metal surface by the corrosion

product, which caused the corrosion rate to drop even when steady state had not been attained, and increase in the system temperature. Therefore the coefficient of diffusion D for CO_2 diffusing through a plane sheet of brine is taken to be 5.6 x $10^{-5}cm^2s^{-1}$ at 25°C.

The diffusion model and the mass balance equation were used to estimate the amount of steel corroded. The estimated total metal loss obtained using the model was 0.94 mg compared to 2.78 mg obtained from direct calculation using the corrosion rate and corroding area under the liner. The small difference in the values obtained could be connected to the assumptions made in modelling the CO_2 transport through the liner vent.

Simplifications

The under estimated value of the metal loss resulting from the model is due to the following simplification in the mathematical modelling:

1. The figure at the left-hand side of Figure 6-9 is a schematic of the corrosion cell showing the vent with the concentration profile of the diffusing CO_2. At steady state, the CO_2 flux at the top of the vent will be equal to that at the bottom as shown by the schematic on the right-hand side of the figure. At the bottom, all the CO_2 is assumed to be used up for corrosion process.

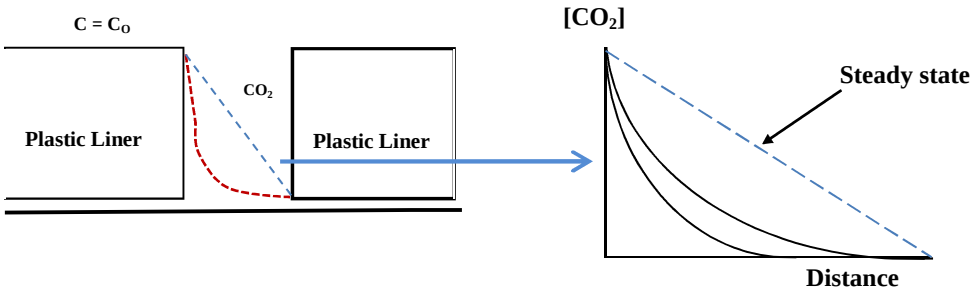

Figure 6-9: Schematic diagram showing vent and concentration gradient at steady state

The experiment ran for a total time t_r of 27.7 hours and the breakthrough time t_b was 27 minutes. The steady state was attained after about 5.6 hours (t_{ss}).

Therefore t_r » t_{ss} » t_b, and it can be assumed that steady state conditions existed for the majority of the experiment. However, as CO_2 was clearly diffusing along the plate and causing corrosion at successive electrode pairs, it is evident that the CO_2 concentration at the bottom of the vent was greater than zero. This situation is shown in Figure 6-10. A reduced concentration gradient would result and this would lower the flux of CO_2 through the vent.

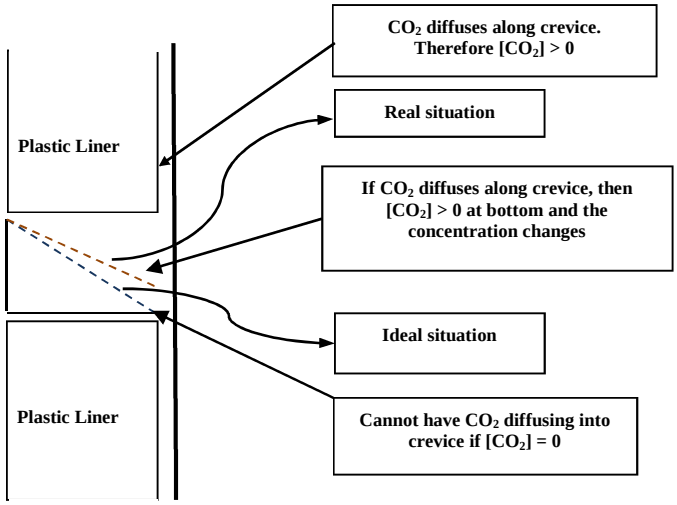

Figure 6-10: Schematic showing changes in the concentration profile of CO_2 within the vent under ideal and real situations

2. In addition the metal loss was an over estimated value because the CO_2 concentration was not uniform across each section of the plate. The electrode pairs, where corrosion was simulated and recorded, were located on the centre-line of the plate, and these experienced a higher CO_2 concentration than at the edges. Figure 6-11 shows a schematic diagram of the diffusion of CO_2 along the annular space on an enlarged portion of the carbon steel plate where corrosion is of concern. This effect will lead to an over estimated value for the metal loss.

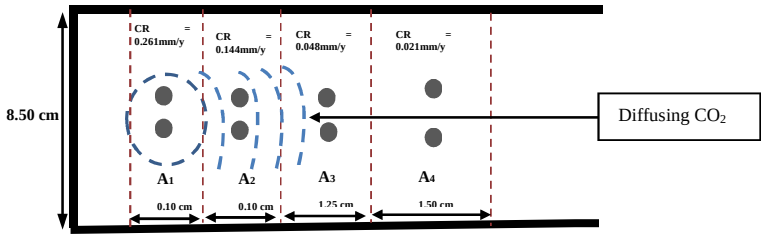

Figure 6-11: Enlarged portion of corroding carbon steel plate near vent area of liner

Possible Challenges of the Experiment

As discussed in the literature review (section 2.6.4.1), transport of species into the annular space is mainly by diffusion and convection (Ahmad, 2006). However, it was assumed that for the static tests, there will not be convection effect in the corrosion cell and mass transport of CO_2 will only be by diffusion. It was a necessary condition for the mathematical modelling, but in fact not strictly correct. It was observed that during the process of introducing the CO_2 bubbler some mixing occurred and mass transport of CO_2 by convection must have taken place. In addition, there was some variation of the corrosion cell temperature due to the effect of the thermostat regulated heater used in heating the corrosion cell.

The effect of temperature fluctuation and convection current will inevitably affect the mass transport of the CO_2 and as a result it was not possible to obtain the same breakthrough times for similar experiments. That was the reason why a mean breakthrough time (t_b) was used in calculating the D (coefficient of diffusion) values.

The mean breakthrough time of 29 minutes was obtained from the average of two breakthrough times of 27 minutes and 31 minutes. Therefore the scatter of the D value can be calculated as follows:

- D value for breakthrough time of 27 minutes = $6.0 \times 10^{-5} cm^2 s^{-1}$
- D value for breakthrough time of 31 minutes = $5.2 \times 10^{-5} cm^2 s^{-1}$

Therefore D can be expressed as $(5.6 \pm 0.4 \times 10^{-5})\ cm^2 s^{-1}$.

From the experiment in Figure 6-2, where only the control sample and test electrode pair 1 where used, one complete cycle of the LPR equipment took an average time of 6 minutes. Therefore the mean breakthrough time of 29 minutes could be approximated to 29 minutes ± 6 minutes, that is, 21% variation. Therefore the coefficient of diffusion can be expressed as ($5.6 \pm 1.1 \times 10^{-5}$) cm^2s^{-1}.

Accuracy of Coefficient of Diffusion Value – Effect of the Annular Gap

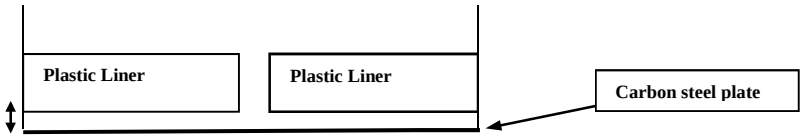

Figure 6-12: Schematic of corrosion cell showing annular gap

It is important to mention other limitations of the model and its effect on the coefficient of diffusion. The length of the liner vent through which the CO_2 travelled before corroding the metal plate is not only the thickness of the plastic liner but also the annular gap. Therefore the total distance becomes 14.3 mm (12.7 mm + 1.6 mm). Including the annular gap has the effect of increasing the calculated D value.

Estimate of the Difference in Calculated D Values

$$D_1 = \frac{0.06\ x\ l_1^2}{t_b}$$

$$D_2 = \frac{0.06\ x\ l_2^2}{t_b}$$

Therefore, $\frac{D_2}{D_1} = \frac{(14.3)^2}{(12.7)^2} = 1.27$

Including the annular gap in the calculation would increase the D value by 27%.

Achieving the Boundary Condition at the Top of the Vent

It was assumed that the CO_2 concentration at the top of the vent would reach a constant value immediately that the gas was bubbled into the tank. However, this is unrealistic and it would have taken a few minutes for CO_2 to saturate the brine in the tank. Evidence for this is seen in the rising corrosion rate of the control electrodes (Figure 5-4). The consequence of this effect is that the breakthrough time measured for the electrode pairs in the annular space would have been longer than if the constant CO_2 concentration had indeed been achieved immediately. The measured D value would have been slightly low as a result.

CHAPTER 7
SWAGELINING LINERVENT™

7.1 Introduction

In Chapter 5, the problem of sudden increases in the corrosion rate within the annular space due to vigorous mixing in the Perspex tank was discussed. There was an increase in the mass transport of CO_2 into the annular space whenever there was mixing in the tank. This problem needed to be resolved if plastic lined pipelines are to be suitable for hydrocarbon transport. It was expected that transport of carbon dioxide into the vent would be restricted further by positioning a porous frit (LinerVent™) over the liner vent and this was investigated experimentally.

The frit was based on a commercially available design (Swagelining) and consisted of a disk of sintered titanium held in a plastic insert. The LinerVent™ was originally an invention of Atkin-Boreas and is now being developed by *Swagelining Limited*. The LinerVent™ with its assembly was designed with screw threads to allow it to be screwed into the vent so that it fits flush with the plastic liner (Figure 7-1).

This chapter presents the design, technical details and the experiments performed to test the effectiveness of the LinerVent™ and a discussion on its effect on the mass transport of CO_2 when installed over the vent. The results section will include the determination of the coefficient of diffusion of the CO_2 through the LinerVent™ based on the mathematical diffusion model discussed in Chapter 6.

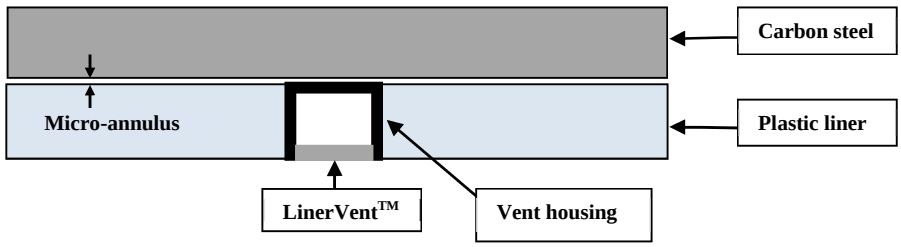

Figure 7-1: Cross-section of LinerVent™ installed in a vented plastic lined pipe

The LinerVent™ was intended to provide additional reduction in the mass transport of corrosive species into the micro-annulus of vented pipelines especially during high velocity fluid flow. It was also intended to reduce the effect of turbulence and improve the stability of the vent geometry of perforated plastic lined pipelines (McIntyre, 2002).

The LinerVent™ is encased in a composite plastic casing. The length and outer diameter of the composite plastic assembly, made from PEEK (Polyether ether ketone) containing Teflon (Figure 7-2), are 8.98 mm and 6.28 mm respectively. The dimensions of the LinerVent™ alone are given in the technical design sub-section below.

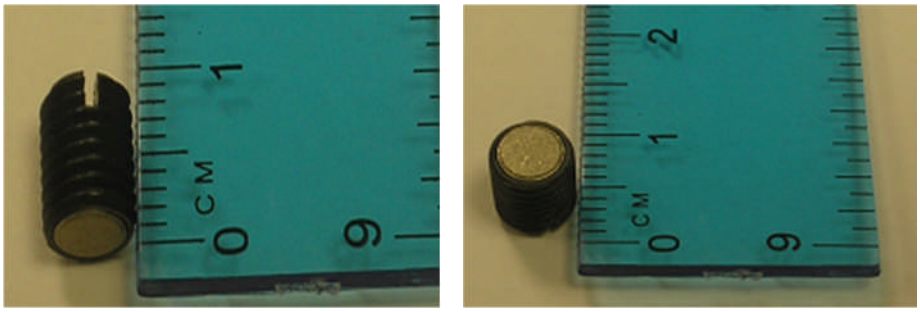

Figure 7-2: LinerVent™ and plastic assembly

7.2 Technical Details and Design of LinerVent™

The LinerVent™ was made from sintered titanium metal and therefore has a pore structure which allows passage of fluids. The use of titanium was primarily dictated by the need for corrosion resistance. Figure 7-3 is a schematic showing how the complete unit could be installed in a vented plastic lined pipe.

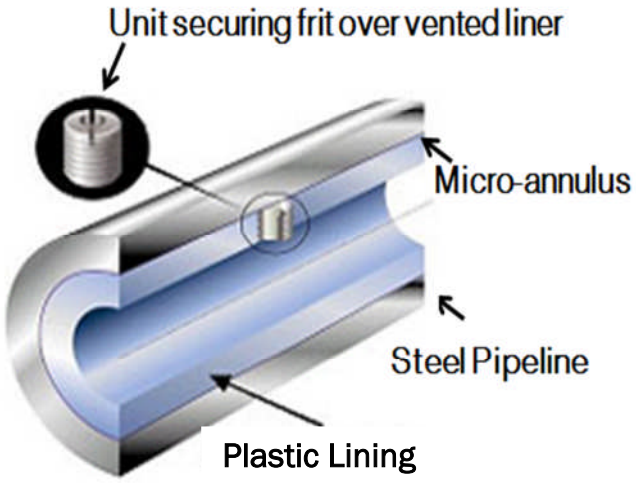

Figure 7-3: Schematic showing LinerVent™ installation in a vented plastic lined pipe (Swagelining)

The technical details of the LinerVent™ are presented below:

- Material – Titanium
- Nominal Porosity – 5 µm
- Dimensions of LinerVent™ disc: diameter – 4.81 mm; thickness – 1.56 mm

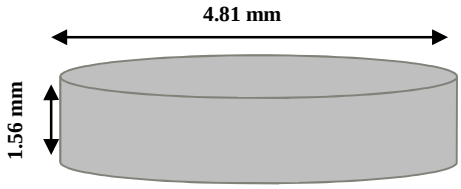

Figure 7-4: Schematic showing dimensions of LinerVent™

7.3 Installation of LinerVent™

In order to carry out the experiments to determine the effectiveness of the LinerVent™ in the corrosion cell, a special disk made from Perspex was designed on which the LinerVent™ could be held. The disk has dimensions of height and inner diameter of 1.56 mm and 4.71 mm respectively, thus securing the LinerVent™ by press-fitting.

The LinerVent™ was carefully removed from its composite plastic assembly and secured inside the specially designed Perspex disk presented schematically in Figure 7-5 (a). Figure 7-5 (b) presents the LinerVent™ and the transparent Perspex disk.

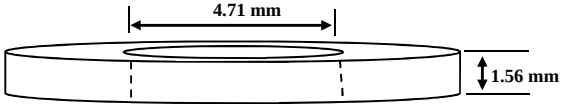

Figure 7-5(a): Specially designed Perspex unit

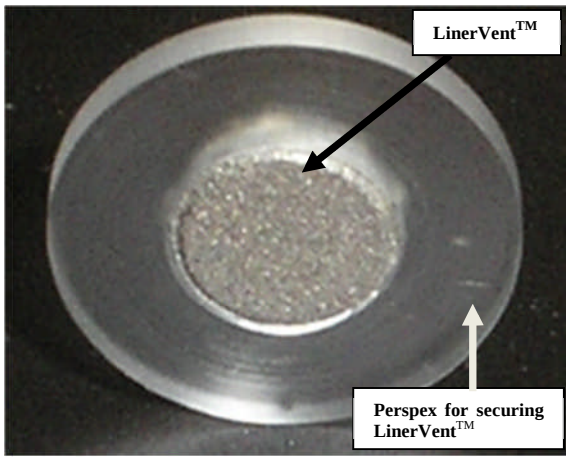

Figure 7-5 (b): Pictorial view of LinerVent™ with transparent Perspex mount

After the LinerVent™ was tightly fitted within the Perspex mount, it was secured above the vent of the liner as presented in the schematics below (Figure 7-6).

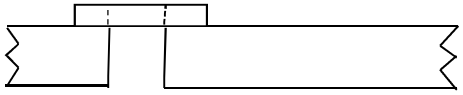

Figure 7-6: Schematic of LinerVent™ in Perspex mount over the liner vent

7.4 Corrosion Cell Set-up

The steel plate with the inserted pairs of test electrodes was ground to remove rust and surface impurities. The control sample on the wall of Perspex tank was polished with

silicon carbide abrasive paper to give a clean surface. The steel plate, Perspex tank and gasket were cleaned with iso-propanol with emphasis on the vent area of the tank to prevent any blockage of the vent. Seven different experiments with the LinerVent^{TM} were performed and after each experiment, the metal plate with the test electrodes and the control sample were reground and cleaned before assembly.

7.4.1 Assembly and Deaeration with Nitrogen Gas

The saturated calomel reference electrode was secured on a clamp. The open end was then connected to a Luggin capillary and the other end with the cable connected to channel 1 of the LPR measuring equipment in parallel with the red lid of the voltmeter. The working and counter electrodes (WE and CE) of the control sample were connected to channel 2 while those of the test electrodes for pairs 1, 2, 3, 4, 5 and 6 were connected to channels 3 to 8 of the LPR measuring equipment.

After the connections, the Perspex tank was placed on top of the steel plate, with the gasket in between. The LinerVent^{TM} which had been press-fit in the thin disk of Perspex mount was placed over the vent with a film of sealant as shown in Figure 7-7. The adhesive sealant was carefully applied around the outer circumference of the Perspex holding unit before mounting. A clean tong was used to apply slight pressure over the unit. Care was taken to avoid the wet sealant either coming in contact with the LinerVent^{TM} or covering the vent hole.

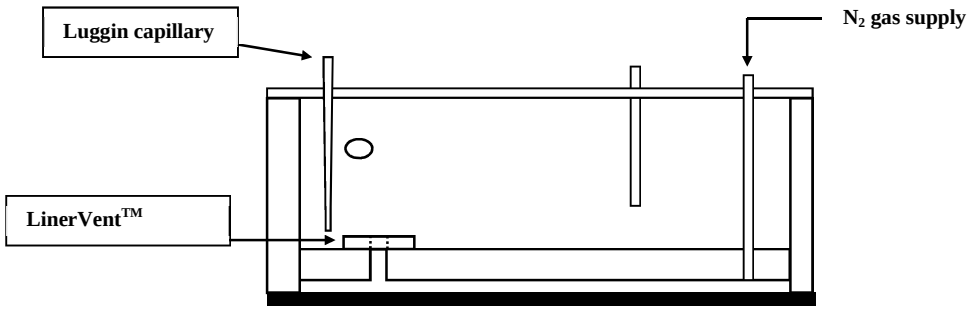

Figure 7-7: Schematic showing LinerVent^{TM} installed over liner vent

The four steel flanges were then placed round the foot of the Perspex tank and secured with Allen bolts and screws. After the coupling of the tank, nitrogen gas was bubbled into the tank. Sealant was applied round the cell and 4 litres of deaerated 3.5% NaCl solution was transferred into the tank. The Perspex cover was then placed over the tank and the Luggin capillary, thermostat, thermometer, gas bubbler secured on it. The LPR measuring equipment was then switched on after ensuring that there were no leakages. Nitrogen gas was bubbled continuously into the corrosion cell for 1.5 hours for complete deaeration.

7.4.2 Simulation of CO_2 Corrosion

Immediately after the deaeration process, the nitrogen gas supply was replaced with carbon dioxide (CO_2) gas set at 1 bar pressure. The gas supply pipe was channelled from the gas cylinder through the heat exchanger into the gas bubbler in the tank. The gas supply was opened and maintained throughout the period of the test to simulate sweet corrosion and prevent oxygen from entering the corrosion cell. Figure 7-8 is a pictorial view of the corrosion cell showing the installed LinerVent™ ready for the test.

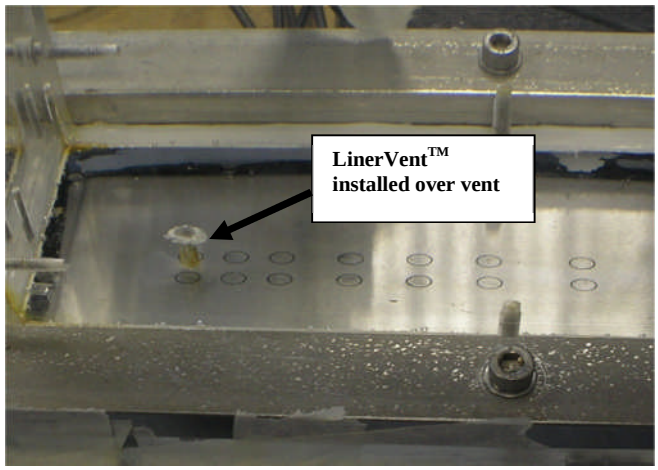

Figure 7-8: LinerVent™ mounted over vent and tank filled with electrolyte ready for test

7.5 Results and Discussion

This section focuses on the results ranging from the Scanning Electron Microscope (SEM) and Energy Dispersive x-ray Spectroscopy (EDS) of the LinerVent™ to the graphical results of the corrosion rate when the LinerVent™ was positioned over the vent. Other areas covered include discussion of results.

7.5.1 Scanning Electron Microscope Result of LinerVent™

Figure 7-9 is the SEM result of the LinerVent™ with different magnifications.

Sintered LinerVent™ showing Pores

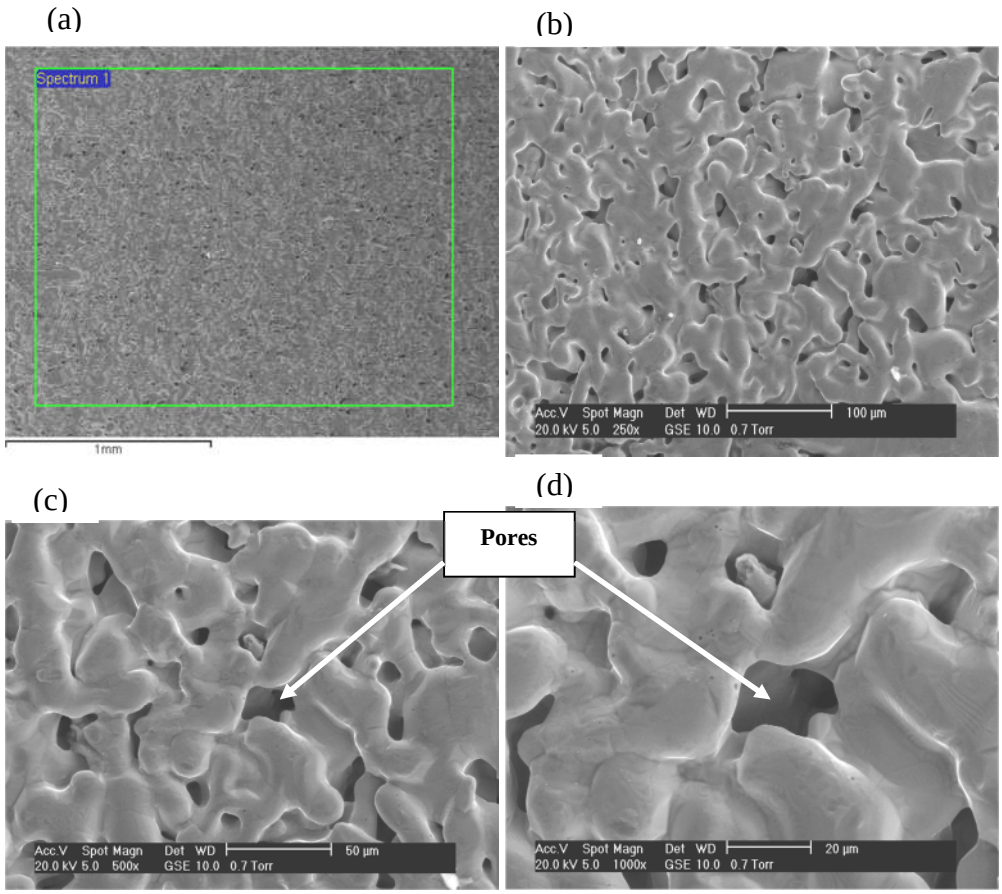

Figure 7-9: SEM result (a) 50 x magnification, 500µm; (b) 250 x magnification, 100 µm (c) 500 x magnification, 50µm; (d) 1000 x magnification, 20 µm

As the magnification increases, the pores within the LinerVent™ appear clearer; this confirmed the fact that the LinerVent™ was made from sintered titanium (McIntyre, 2000). The physical presence of the LinerVent™ installed over the vent would likely delay the rate of mass transport of corrosive species through the pores and so increase the breakthrough time (t_b) of CO_2 into the annular space. It is pertinent to note that the pores also allow gases that could be trapped within the annular space to freely escape back into the pipeline without restriction.

Composition of LinerVent™

Figure 7-10 is the SEM energy-dispersive X-ray spectroscopy showing the composition of the LinerVent™.

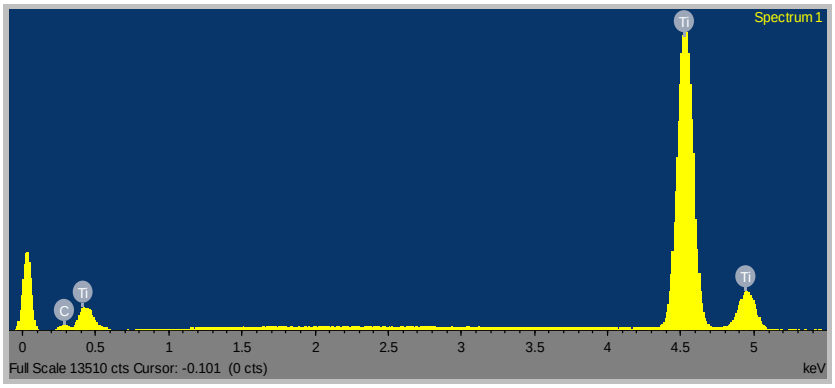

Figure 7-10: SEM Energy-dispersive X-ray Spectroscopy (ESD) spectrum of LinerVent™

The analysis showed that the LinerVent™ is made from pure titanium metal. The observed low traces of carbon are likely to be contaminants like grease on the carbon steel plate.

7.5.2 Diffusion of CO_2 into Annular Space through the LinerVent™

Control Sample and 6 Test Electrodes (*with* LinerVent™)

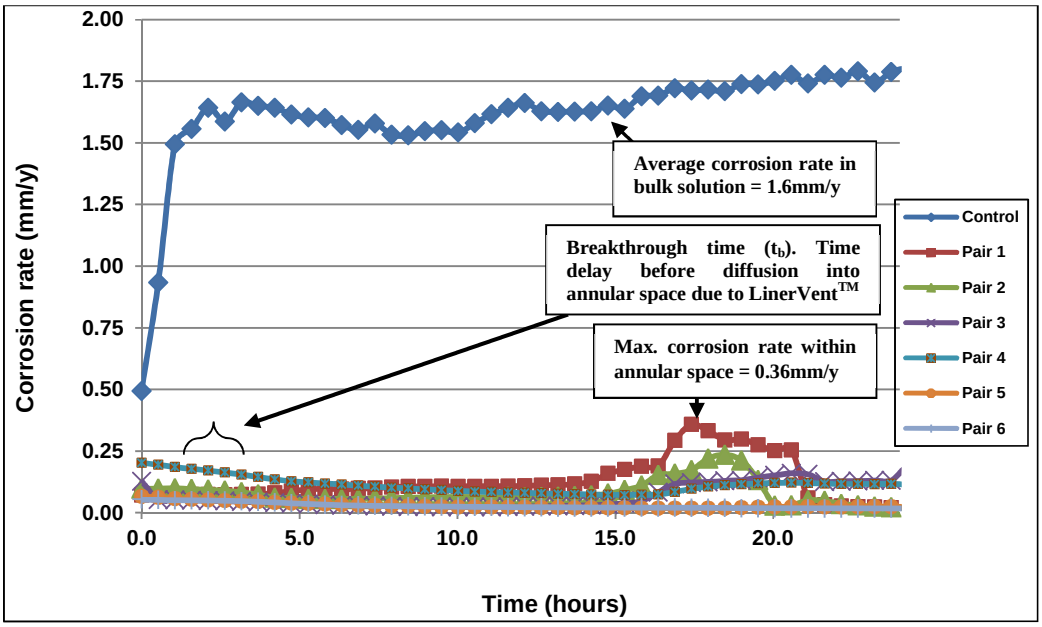

Figure 7-11: Corrosion rate against time *with* LinerVent™ over the plastic liner vent

The corrosion rate of the control sample in the bulk solution increased rapidly to an average value of 1.60 mm/y, when CO_2 was introduced into the bulk solution as in the earlier experiments. However, this was not the case with the test electrodes within the annular space. The corrosion rates of the test electrodes remained low at 0.12 mm/y for about 6 hours from when the CO_2 was introduced into the bulk solution.

The corrosion rate of pair 1 started increasing after about 2 hours from 0.12 mm/y to a maximum value of 0.36 mm/y. Similarly the corrosion rate of pair 2, 10.0 mm from the vent, increased to a maximum value of 0.25 mm/y. The breakthrough time of 1 hour 15 minutes could be attributed to the effect of the LinerVent™ installed over the vent because it delayed the diffusion process of CO_2 through the vent.

Result *without* LinerVent™ over Vent – Control Sample and 6 Test Electrodes

Referring to Figure 6-1 where there was no LinerVent™ over the liner vent, it can be seen that the breakthrough time (t_b) was very short, about 31 minutes. The diffusion rate

through the vent into the annular space was faster compared to the case in Figure 7-11. This could only be attributed to the presence of the LinerVent™ which delayed the diffusion of CO_2 into the annular space. In addition, the maximum corrosion rate without the LinerVent™ was 0.49 mm/y, compared to 0.36 mm/y with the LinerVent™ over the vent (Figure 7-11).

Control Sample and Test Electrode Pair 1 (*with* LinerVent™)

It was decided to connect only the control sample in the tank and test electrode pair 1, directly under the vent, to the LPR measuring equipment to monitor the corrosion rate. This arrangement gave more data points required to observe changes occurring beneath the liner, with the LinerVent™ over the vent and when it is not in place. The results from these tests (control sample and test electrode pair 1), with and without the LinerVent™, are shown in Figure 7-12 and Figure 6-2 (Chapter 6) respectively.

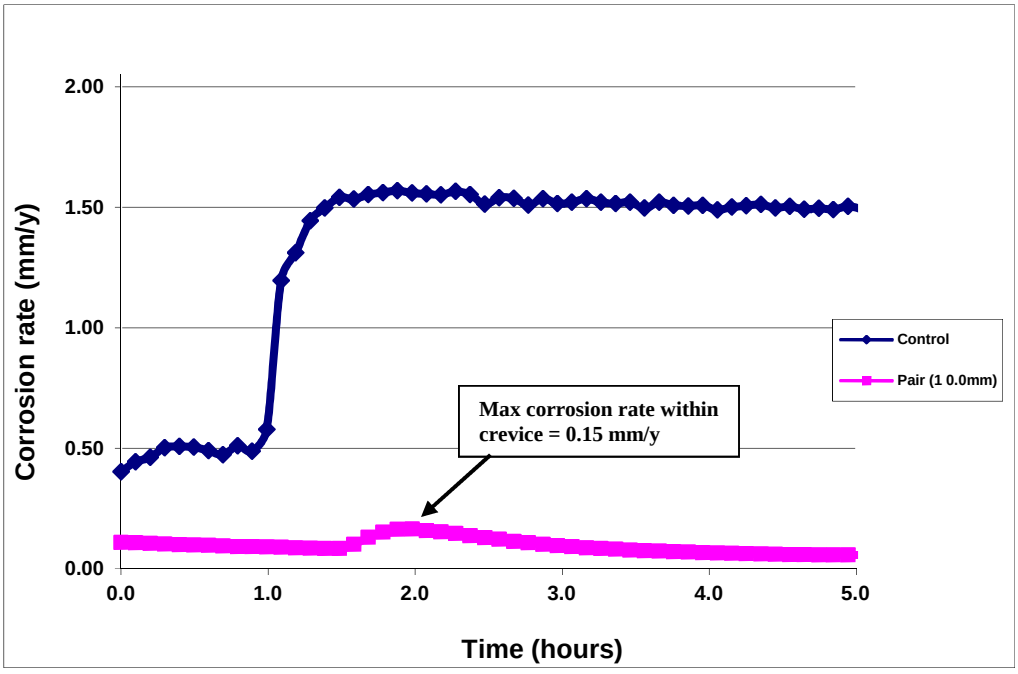

Figure 7-12: Corrosion rate against time *with* LinerVent™ over the plastic liner vent

Figure 7-12 is the graph obtained when only the control sample and one test electrode were used in the experiment to test the effectiveness of the LinerVent™. Like the previous experiments, the corrosion rate of the control sample increased rapidly with the introduction of CO_2 into the bulk solution. After some time the surface of the control sample changed to grey/black due to the formation of corrosion products followed by a drop in the corrosion rate to an average value of 1.50 mm/y. The corrosion rate of the test electrode (pair 1) under the vent increased slightly (0.15 mm/y) because of the LinerVent™.

Control Sample and Test Electrode Pair 1 *(without* LinerVent™)

The result of the test without the LinerVent™ over the vent opening is presented in Figure 6-2. The corrosion rate of the control sample increased suddenly to a maximum value of 1.60 mm/y when CO_2 was bubbled into the solution. Unlike Figure 7-12 where the corrosion rate of electrode pair 1 within the annular space increased to 0.15 mm/y, the corrosion rate of electrode pair 1 increased to a value of 0.20 mm/y. The breakthrough time was 33 minutes.

7.5.3 Applying Diffusion Model to Swagelining LinerVent™

In Chapter 6, a mathematical model was described for transport of CO_2 through the liner vent. The model was based on a one-dimensional diffusion equation through a plane sheet (the electrolyte within the vent).

Applying Model to Result of Test Electrode Pair 1 *with* and *without* LinerVent™

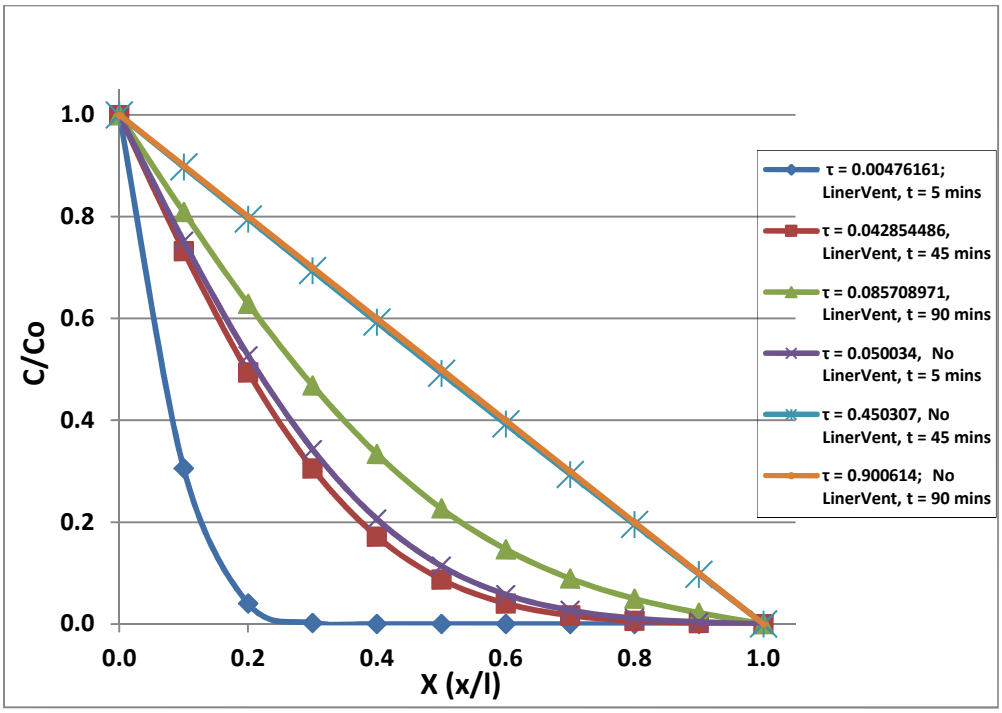

Figure 7-13: Concentration profile for test electrode pair 1 *with* and *without* LinerVent™ (comparing diffusion rates using τ values for various times)

Figure 7-13 is the concentration profile generated from the results of figures 7-12 and 6-2. The different sets of curves represent the concentration of CO_2 along the length of the vent with the LinerVent™ installed over the vent and when the vent is open, for different times. The graph shows a constant concentration ($C/C_o = 1$) at the top of the vent and zero concentration ($C/C_o = 0$) at the bottom of the vent. Each of the plots represents different values of the non-dimensional term $\tau = (Dt/l^2)$ (*Equation 6-11*) discussed in Chapter 6. $\tau = 0.06$ defines the breakthrough time (t_b) which is when the diffusing CO_2 just reaches the far end of the vent (electrolyte medium) to corrode the metal surface in the annular space.

The curves in the transient state show the gradual process of diffusion of CO_2 within the time interval specified. Five minutes after the test, the experiment without the LinerVent™ was already attaining breakthrough while for the test with the LinerVent™, the CO_2 was just about 30% through the vent. After about 45 minutes, the

experiment without the vent was almost attaining steady state while the experiment with the LinerVent™ had not yet reached breakthrough condition.

The diffusion model demonstrated that the corrosive species diffuse faster through the vent and attain steady state in the absence of the LinerVent™. This implied a quicker and higher corrosion rate within the annular space. The model also demonstrates that the corrosive species are delayed through the vent and the time to attain steady state was much longer with the LinerVent™.

7.5.4 Diffusion Coefficient of Carbon Dioxide with LinerVent™ over Vent

It follows that if the breakthrough time was determined by experiment from the time taken for the first signs of CO_2 to diffuse through the vent and corrode the steel beneath, then the diffusion coefficient D could be calculated from the expression $\tau\ (Dt/l^2) = 0.06$. A mean breakthrough time of 29 minutes was obtained from the experiments performed without the LinerVent™ and a coefficient of diffusion D for CO_2 in brine of $5.6 \times 10^{-5} cm^2 s^{-1}$ at 25°C obtained.

A longer mean breakthrough time of 54 minutes (75 minutes + 33 minutes) was obtained from the experiments for a vent with the LinerVent™. An effective CO_2 diffusion coefficient of $3.0 \times 10^{-5} cm^2 s^{-1}$ at 25°C was obtained for this breakthrough situation with $\tau = 0.06$, $t_b = 3240$ s (54 minutes) and $l = 1.27$ cm. Clearly, this value reflects the combined behaviour of diffusion through the LinerVent™ and the brine solution within the vent.

7.6 Use of the LinerVent™ to Control the effect of Vigorous Mixing

Referring to Figure 5-9, vigorous agitation of the solution in the tank reduced the time for the onset of corrosion in the annular space. The result was for a liner without a LinerVent™ over the vent. Three points where the corrosion rates increased suddenly are clearly identified. The first peak is the normal initial increase due to diffusion of CO_2 into the annular space. The second and third peaks of electrode pair 1 shown by points **y** (0.540 mm/y) and **z** (0.399 mm/y) are as a result of increased mass transport of CO_2 into the annular space due to vigorous mixing within the bulk solution.

The same experiment was performed with the LinerVent™ placed over the vent and the bulk solution vigorously mixed. Figures 7-14 (a) and (b) are the results showing the corrosion rates of the control sample and test electrodes.

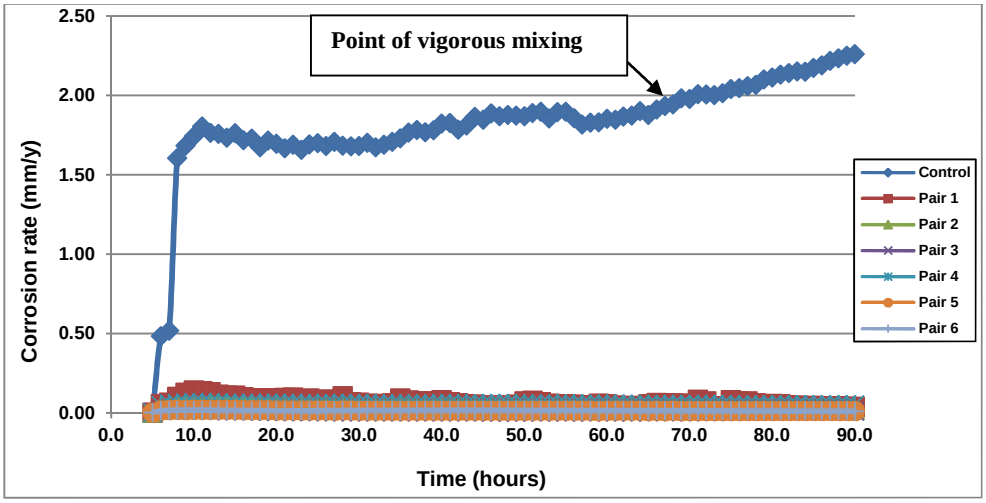

Figure 7-14(a): Effect of LinerVent™ on corrosion rate during vigorous mixing (control sample and test electrodes)

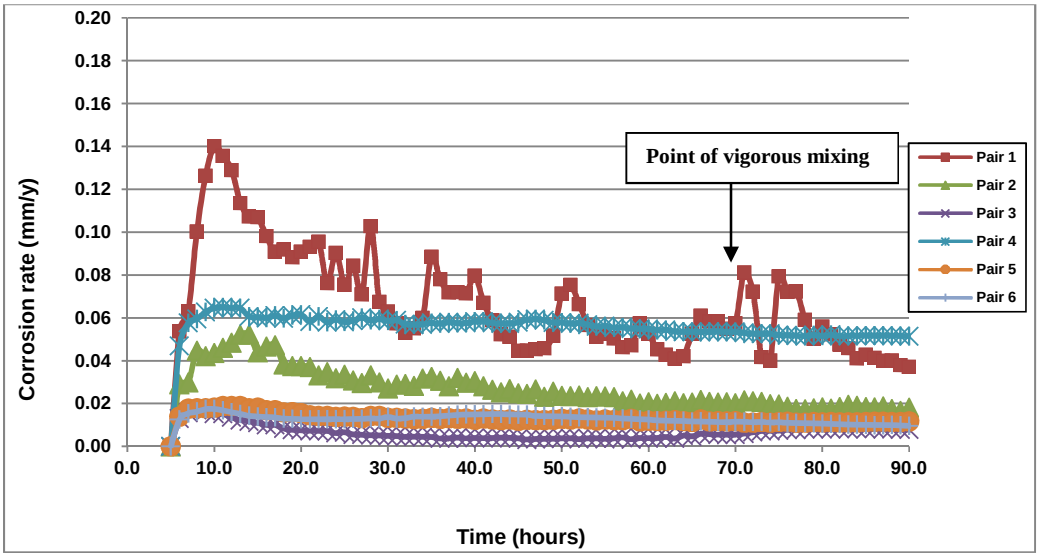

Figure 7-14 (b): Effect of LinerVent™ on corrosion rate during vigorous mixing (test electrodes within annular space)

Figure 7.14 (a) shows the corrosion rate of the control sample in the bulk solution where mixing took place while Figure 7-14 (b) shows the test electrodes within the annular space. It can be seen that despite the mixing within the bulk solution, the corrosion rate

within the annular space was not affected. Despite some scattering of the data points, the general corrosion rate was on the decrease. The absence of sudden corrosion peaks within the annular space is attributed to the effect of the LinerVent™.

7.7 Summary of Discussion

The physical presence of the LinerVent™ installed over the vent reduced the effect of turbulence in the pipeline within the annular space and delayed the rate of mass transport of corrosive species because of the configuration of the pores.

Diffusion of CO_2 into Annular Space *with* and *without* LinerVent™ over Vent

The corrosion rates of the test electrodes under the vented liner covered with the LinerVent™ increased to a maximum value of 0.36 mm/y. When there was no LinerVent™ over the vent, the maximum corrosion rate was 0.49 mm/y. It took about 15 hours for the corrosion rate to increase to 0.36 mm/y while only about 2 hours for it to increase to 0.49 mm/y. This implied a very long breakthrough time (t_b) and slower CO_2 diffusion rate for the former and the reverse is the case for the latter. Also the average corrosion rate with the LinerVent™ is approximately 0.15 mm/y. These observations are attributed to the effect of the LinerVent™ installed over the vent because it delayed the diffusion process.

In the experiment with only the unlined control sample and one electrode, the corrosion rate of the test electrode under the vent with the LinerVent™ over the vent did not even witness any increase during the test period. On the other hand, the corrosion rate of the test electrode without the LinerVent™ witnessed an increase in the corrosion rate within some hours; which again supports the effectiveness of the LinerVent™.

Swagelining LinerVent™

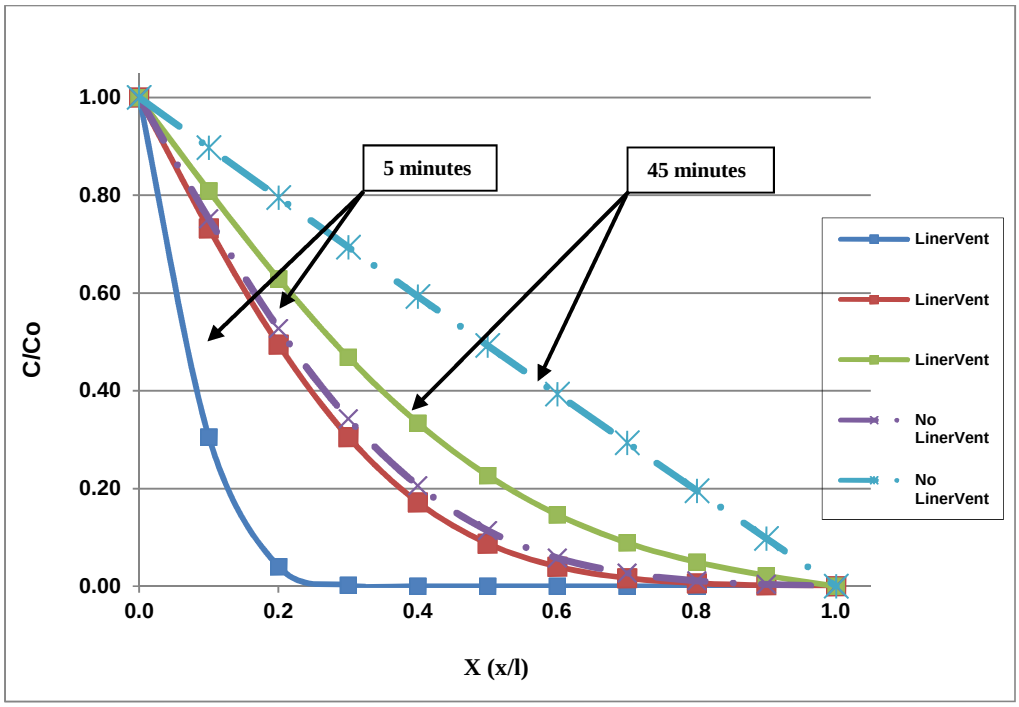

Figure 7-15: Concentration profile with and without LinerVent™ over defined time scales

Figure 7-15 is a comparison of the concentration profiles of CO_2 in the vent showing the effectiveness of the LinerVent™. It can be seen that after 5 minutes; the corrosive species had travelled only 25% through the vent because of the LinerVent™ while it had travelled over 85% when there was no LinerVent™. When we consider the 45 minutes scale, steady state was attained in the case where there was no LinerVent™ while only a breakthrough was experienced when the LinerVent™ was in place.

It can therefore be concluded that the LinerVent™ is very beneficial in reducing the mass transport of corrosive species and so reduces the corrosion rates beneath plastic liner. The diffusion model demonstrated that the corrosive species diffuse faster through the vent and attain steady state when the LinerVent™ was not in place.

Diffusion Coefficient and Metal Loss with the LinerVent™

A mean breakthrough time of 29 minutes was obtained from the experiments performed without a LinerVent™ over the vent and gave a coefficient of diffusion D for CO_2 in

brine as 5.6 x $10^{-5}cm^2s^{-1}$ at 25°C. The longer mean breakthrough time of 54 minutes for a vent with the LinerVent™ gave an effective CO_2 diffusion coefficient of 3.0 x $10^{-5}cm^2s^{-1}$. Clearly, this value reflects the combined behaviour of diffusion through the LinerVent™ and the brine solution within the vent.

Possible Sources of Error in the Experiment

As discussed in the previous chapter, convection, from slight mixing, and variation in temperature of the corrosion cell increases the D (coefficient of diffusion) value. However, the assumption of a zero concentration at the bottom of the vent was another source of error because if C > 0 at the vent bottom, ΔC across is reduced and D decreases.

LinerVent™ over Plastic Liner vent Vigorous Mixing

Vigorous agitation of the solution in the tank reduced the time for the onset of corrosion in the annular space and increased the mass transport of CO_2 into the annular space. With the LinerVent™ over the vent, there was no effect within the annular space whenever the bulk solution was vigorously mixed.

It is true that the corrosion rate, metal loss and the coefficient of diffusion showed the benefits of the LinerVent™. It is pertinent to note that the main benefit of the LinerVent™ is in the reduction of the corrosion rate when there was vigorous mixing or turbulence within the pipeline.

CHAPTER 8
FLOW WITHIN ANNULAR SPACE

8.1 Introduction

This chapter is aimed at investigating the effect of fluid flow through the annular space of vented plastic liner. The objective is to investigate the effect of CO_2 corrosion on carbon steel in the event that a liner is not tightly fitted to the pipe wall or due to design error.

Therefore this section presents findings of the investigation of the influence of brine containing CO_2 flowing through the annular space. The effect of flow will be considered only in a qualitative sense; thus flow rates are not considered.

8.2 Material Preparation and Assembly of Corrosion Cell for Flow Experiment

Prior to each test the steel plate with all the inserted test electrodes and the control sample on the Perspex tank were ground to remove rust and other impurities. The steel plate, Perspex tank, gasket and all components were cleaned with iso-propanol before assembly. Two different experiments were carried out to investigate the effect of flow within the annular space. One of the experiments would investigate the effect around the vent area and so only test electrode pairs 1, 3 and 5 were connected to the LPR equipment. The second experiment was designed to measure the corrosion rate along the whole length of the carbon steel plate during brine flow. In this particular experiment, the six channels of the LPR equipment were connected to cover the full length of the steel at test electrodes 1, 3, 8, 16 and 17. The remaining two channels of the LPR equipment were connected to the control sample and reference electrode.

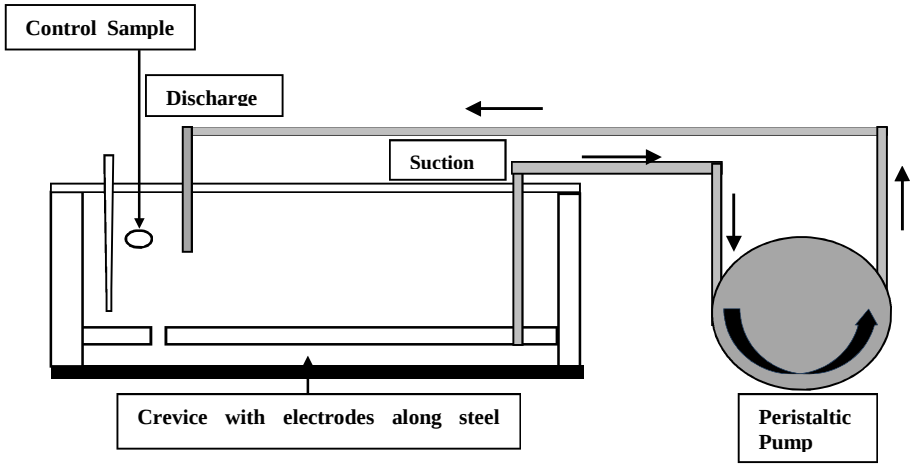

Figure 8-1: Schematic of corrosion cell for flow experiment

Figure 8-1 is a schematic of the corrosion cell for the flow experiment. A peristaltic pump for the test was connected with clips to two lengths of hose; one at the inlet side and the other at the return side. The two lengths of rubber hoses were flushed with deaerated brine solution to remove oxygen as much as possible before connection to the corrosion cell and pump. The hose on the inlet side of the pump was connected to the suction tube which is at the far end of the cell and gives access to the solution within the annular space. This was to ensure that the suction pressure created by the pump causes the fluid in the annular space to flow into the pump. As expected, the electrolyte within the bulk solution flows through the vent to replace the annular space solution.

On the other hand the hose on the return line of the pump returns the fluid from the annular space back into the tank through the discharge tube secured on the tank cover. This circuit results in a continuous flow of electrolyte from the tank into the annular space and back into the tank. Three experiments in flowing conditions were performed and after each experiment, the metal plate with the test electrodes was reground and cleaned before assembly.

8.3 Deaeration Process and Simulation of CO_2 Corrosion

Immediately after assembling the corrosion cell and pump, nitrogen gas was supplied to the unit to keep it free from oxygen. Four litres of deaerated electrolyte was siphoned into the corrosion cell and the LPR equipment was switched on. The pump was also switched on and delivered the brine solution at a flow rate of 635.0 ml/minute and the nitrogen gas was left to bubble in the corrosion cell for 1 hour to completely deaerate the unit. It was then replaced with carbon dioxide (CO_2) gas which was maintained throughout the duration of the experiment to simulate sweet corrosion. Figures 8-2 is a pictorial view of the corrosion cell and pump unit.

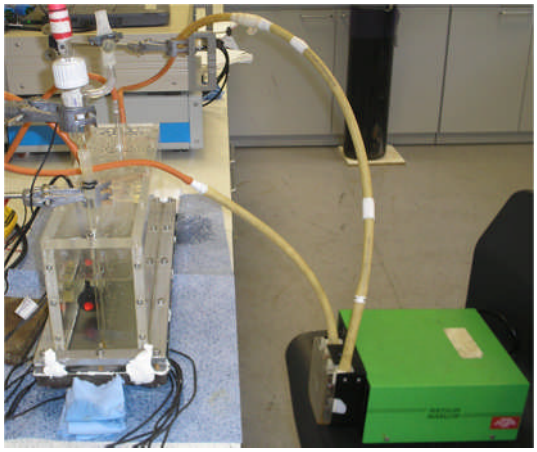

Figure 8-2: Pictorial view of flow experiment apparatus

8.4 Results and Discussion

The results are recorded and presented in graphical forms and analysed below. The results are also followed by a discussion section.

8.4.1 Effect of Flow on Control Sample and Test Electrodes near Vent Area

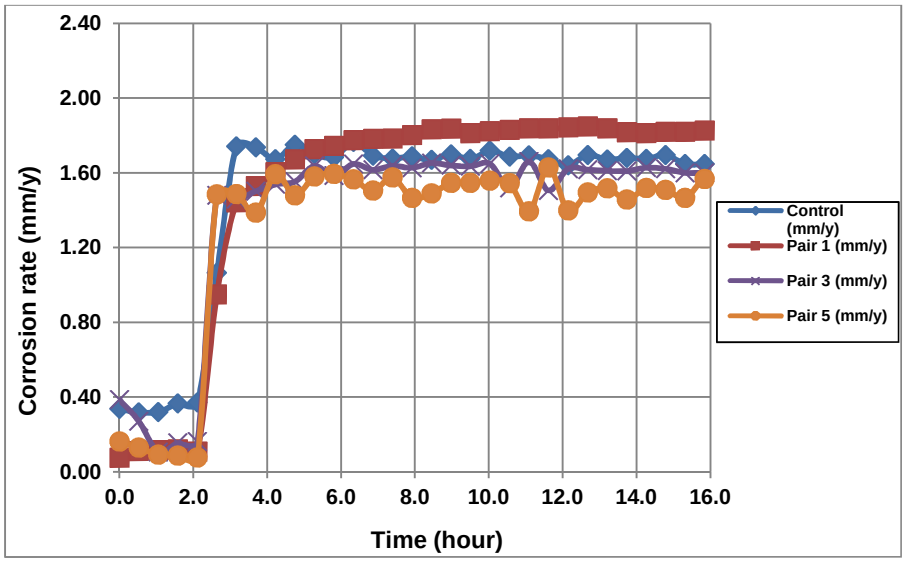

Figure 8-3: Graph of corrosion rate for control sample and test electrodes near the vent with flow through the annular space

From Figure 8-3 it is observed that the corrosion rate of the control sample and test electrodes within the annular space experienced a high corrosion rate. This is evident by the value of approximately 1.60 mm/y. The corrosion rates of electrodes pair 1, 3 and 5 were about 1.80 mm/y, 1.60 mm/y and 1.55 mm/y respectively. Apart from electrode pair 1 that was slightly higher, the corrosion rates of all the test electrodes including the control sample had almost the same corrosion rate. This almost uniform corrosion rate demonstrates the fact that the same concentration of CO_2 in the bulk solution also flowed into the annular space. However, the high corrosion rate of electrode pair 1, directly beneath the vent, could be attributed to impact of the brine saturated with CO_2 as it flows out of the peristaltic pump into the tank and through the vent into the annular space.

It is important to note that when the electrolyte was saturated with N_2 the corrosion rate did not increase even when there was flow within the annular space. Therefore the result also demonstrated the fact that the corrosion was as a result of the carbonic acid.

8.4.2 Effect of Flow along the full length of Steel Plate

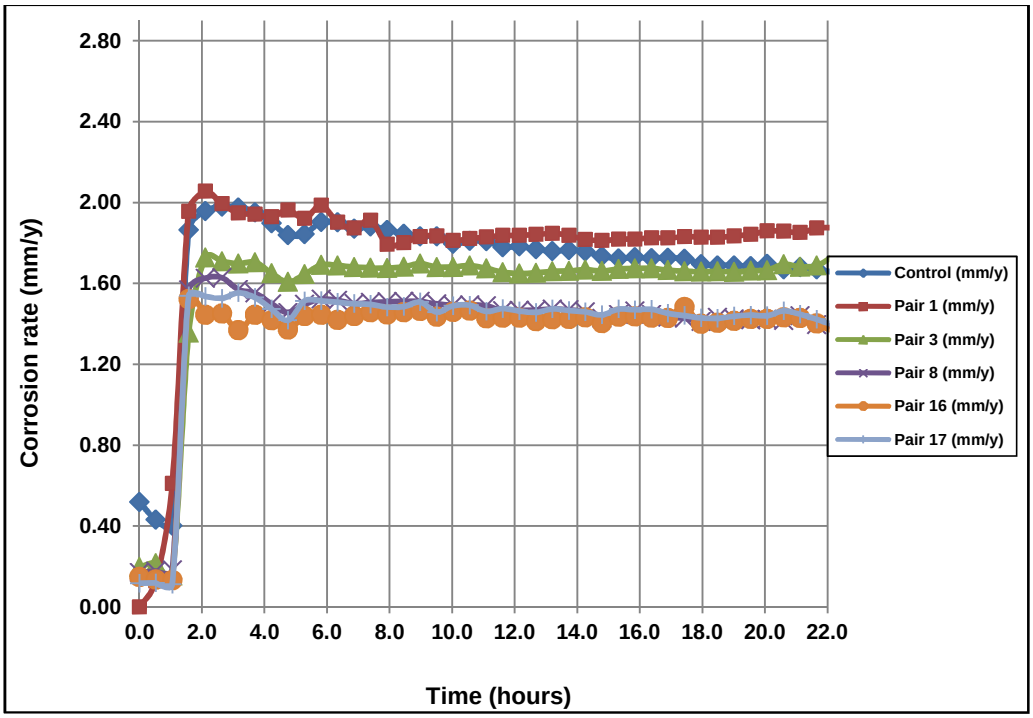

Figure 8-4: Graph of corrosion rate for control sample and test electrodes covering full length of plate with flow through the annular space

Figure 8-4 is the result obtained from measuring the corrosion rate along the whole length of the plate with brine flowing through the annular space. From the curves, it can be seen that the test electrodes like the control sample witnessed sudden and high corrosion rates. The corrosion rate of the control sample increased from 0.16 mm/y to an average value of 1.80 mm/y. The corrosion rates of electrode pairs 3, 8, 16 and 17 increased from about 0.18 mm/y to an average value of between 1.50 mm/y and 1.70 mm/y.

These sudden and high corrosion rates observed could only be attributed to the flow of the brine saturated with CO_2 through the annular space. Like the result in Figure 8-3, only electrode pair 1 had a higher corrosion rate compared to the control sample and the other test electrodes possibly because of the pumping action of the peristaltic pump. The uniform corrosion rate in this case can also be attributed to the fact that the

concentration of CO_2 in the bulk solution and within the annular space is the same because of the constant flow of the electrolyte.

8.5 Summary of Discussion

The corrosion rate of the test electrodes within the annular space showed a very high corrosion rate all along the length of the steel plate. If the corrosion rate of electrode pair 1 in Figure 8-3 is compared to the result of the static test in Figure 5-4, it can be seen that the maximum corrosion rate in the static test is 0.54 mm/y compared to 1.80 mm/y for the flow test, over 230% increase. Using the result obtained from Figure 8-4, the difference in the maximum corrosion rate compared to electrode pair 1 in Figure 5-4 is 1.16 mm/y (1.70 mm/y - 0.54 mm/y); over 210% increase.

As discussed in the literature review, mass transport influences the corrosion process in flowing fluid environments. Fluid flow can result in high mass transfer (Meng and Jovancicevic, 2008) and therefore the increased flux of CO_2 into the annular space is responsible for the high corrosion rate observed. Hara et al. (2000) also demonstrated that the corrosion rates of carbon and low carbon steels increases with increasing fluid flow.

From a practical point of view, any form of increase of mass transport of corrosive species into the annular space of the vented liner could lead to greater presence of corrosive species which will generally increase the corrosion rate. Consequently serious corrosion problems could occur that will affect the structural integrity of the pipeline.

CHAPTER 9
ANNULAR SPACE GAP

9.1 Introduction

Crevice geometry such as the crevice gap affects crevice corrosion. It was therefore decided to investigate the effect of annular space gap on vented plastic lined pipelines. This chapter aims to investigate the effect of the size of the micro-annulus (created between the carbon steel pipeline and the vented plastic liner) on the corrosion rate within the annular space. As discussed in Chapter 4, the annular space created in the corrosion cell served as the micro-annulus for the simulation of CO_2 corrosion.

Gaskets of various thicknesses were cut to shape and used to vary the annular space and the corrosion rates measured under CO_2 environment.

9.2 Gasket Material Design

The thicknesses of the gaskets used for the experiments were 1.60 mm, 1.00 mm, 0.75 mm, 0.30 mm and 0.15 mm. The last experiment was performed without a gasket in place (0.00 mm). The length and width of the gasket materials were 500 mm and 150 mm respectively. They were then cut to fit the corrosion cell and a gasket punch used to create the holes around the circumference. Figure 9-1 is a schematic of a typical gasket used for creating the annular space.

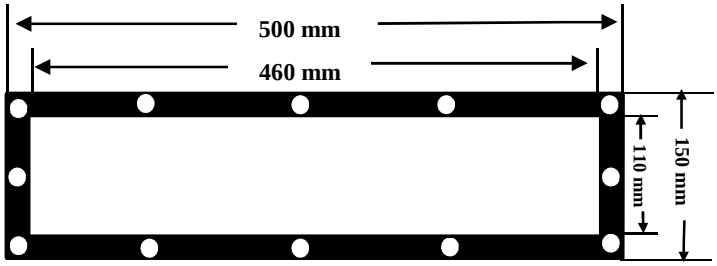

Figure 9-1: Schematic of a typical gasket design

9.3 Installation of Gaskets

The rectangular shaped gasket was placed around the outer edges of the steel plate. On mounting the tank on the gasket already positioned on the plate, the assembly was complete with a annular space created between the Perspex tank and the steel plate. Figure 9-2 shows the positioning of the gasket before coupling.

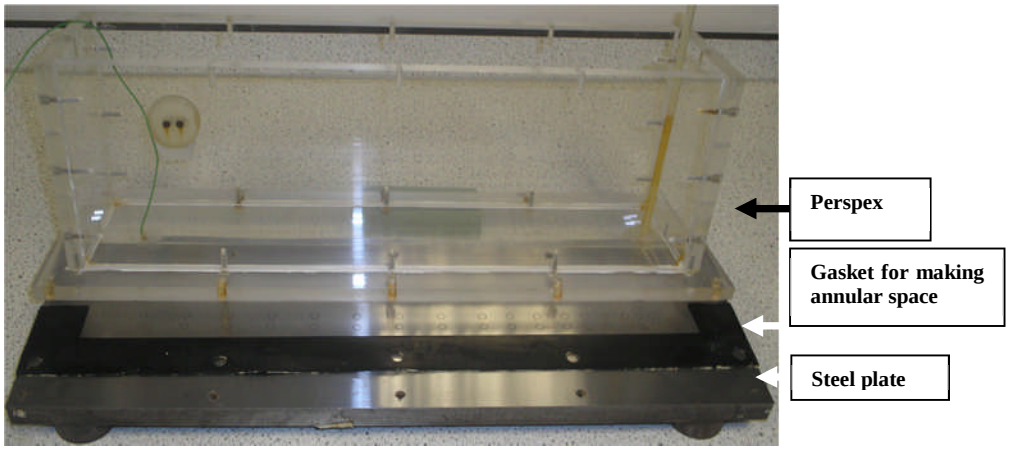

Figure 9-2: Picture showing Perspex, gasket and steel plate before coupling

9.3.1 Material Preparation

Before each test the steel plate with the test electrodes and the control sample installed on the Perspex tank were cleaned with iso-propanol. The test electrodes (pairs 1, 2, 3, 4, 5 and 6) and control sample were then connected to the Solartron LPR measuring equipment and programmed for the test.

9.3.2 Simulation of CO_2 Corrosion

After filling the corrosion cell with 4 litres of deaerated NaCl and purging with nitrogen for 1.5 hours, CO_2 corrosion was simulated by bubbling CO_2 gas. Different gasket types were then tested and the results recorded. Eight of these experiments were performed and after each experiment, the metal plate with the test electrodes and the control sample was reground and cleaned before assembly.

9.4 Results and Discussion

The results will focus only on the control sample and the first three test electrodes (35.0 mm from the vent) or where the corrosion rate was greater than 0.05 mm/y. As discussed previously (Chapter 5) corrosion is local to the vent area, therefore the results were recorded and analysed for this region in particular. The results and discussion are presented in the subsections below.

9.4.1 Corrosion Distribution for Different Annular Space Gaps

Annular space gap – 1.60 mm

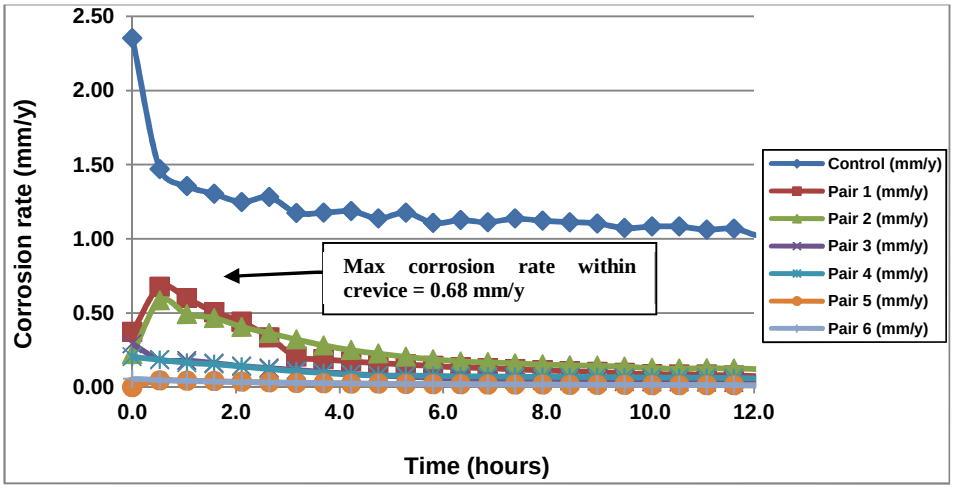

Figure 9-3: Graph of corrosion rate against time for annular space gap 1.60 mm

From Figure 9-3 it is observed that the average corrosion rate of the control sample is about 1.00 mm/y while the corrosion rates of the test electrodes within the annular space are presented below:

- Maximum corrosion rate of pair 1 = 0.68 mm/y
- Maximum corrosion rate of pair 2 = 0.59 mm/y
- Maximum corrosion rate of pair 3 = 0.18 mm/y
- Maximum corrosion rate of pair 4 = 0.10 mm/y

Annular space gap – 1.00 mm

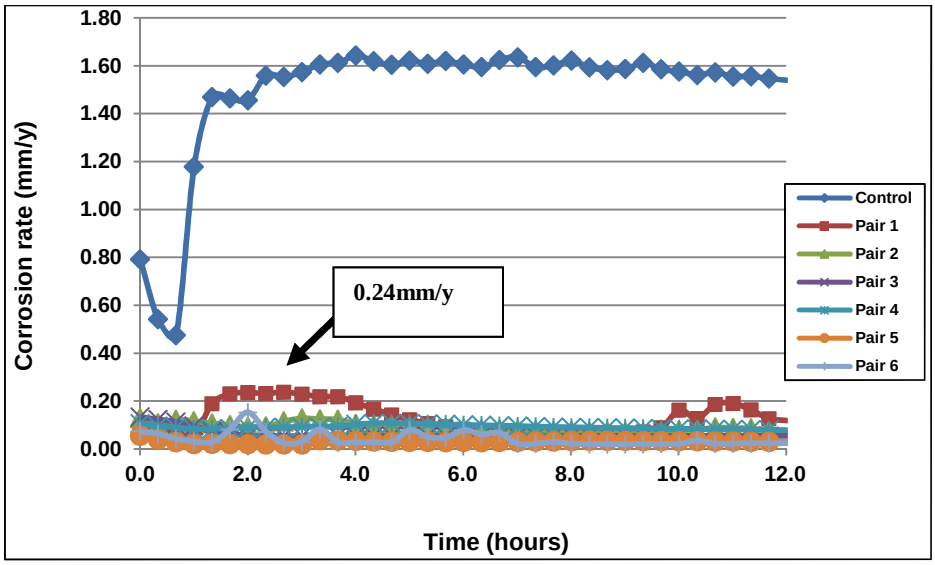

Figure 9-4: Graph of corrosion rate against time for annular space gap 1.00 mm

From Figure 9-4, the average corrosion rate of the control sample is about 1.60 mm/y. The corrosion rates of the test electrodes within the annular space are:

- Maximum corrosion rate of pair 1 = 0.24mm/y
- Maximum corrosion rate of pair 2 = 0.13mm/y
- Maximum corrosion rate of pair 3 = 0.10mm/y

Annular space gap – 0.75 mm

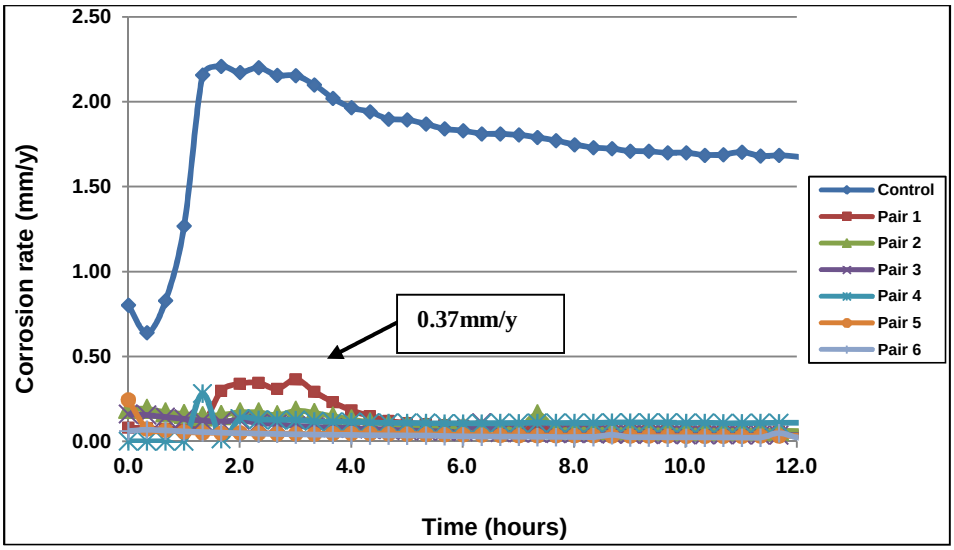

Figure 9-5: Graph of corrosion rate against time for annular space gap 0.75mm

From Figure 9-5, the average corrosion rate of the control sample is about 1.60mm/y while the corrosion rates of the test electrodes within the annular space are:

- Maximum corrosion rate of pair 1 = 0.37mm/y
- Maximum corrosion rate of pair 2 = 0.18mm/y
- Maximum corrosion rate of pair 3 = 0.16 mm/y

Annular space gap – 0.30 mm

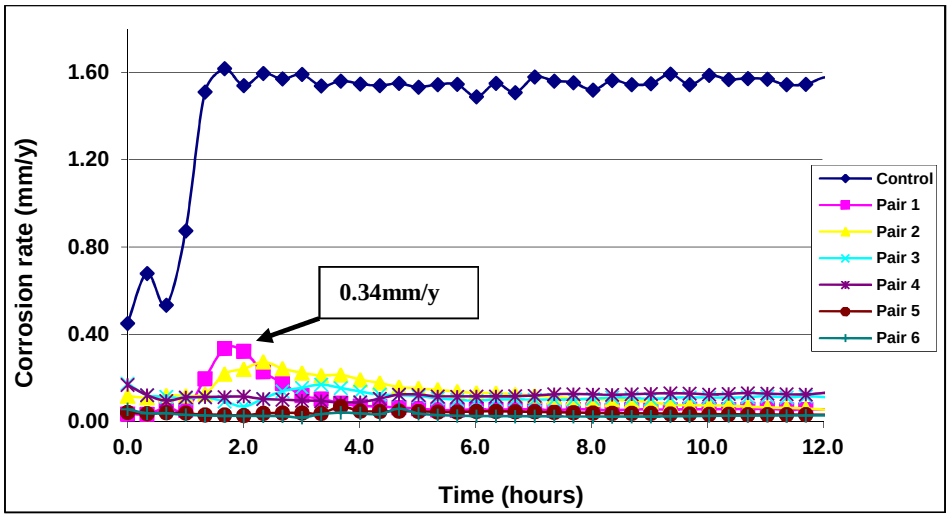

Figure 9-6: Graph of corrosion rate against time for annular space gap 0.30 mm

It can be seen from Figures 9-6 that the corrosion rate of the control sample is about 1.60mm/y while the corrosion rates of the test electrodes within the annular space are:

- Maximum corrosion rate of pair 1 = 0.34mm/y
- Maximum corrosion rate of pair 2 = 0.27mm/y
- Maximum corrosion rate of pair 3 = 0.17mm/y

Annular space gaps – 0.15 mm

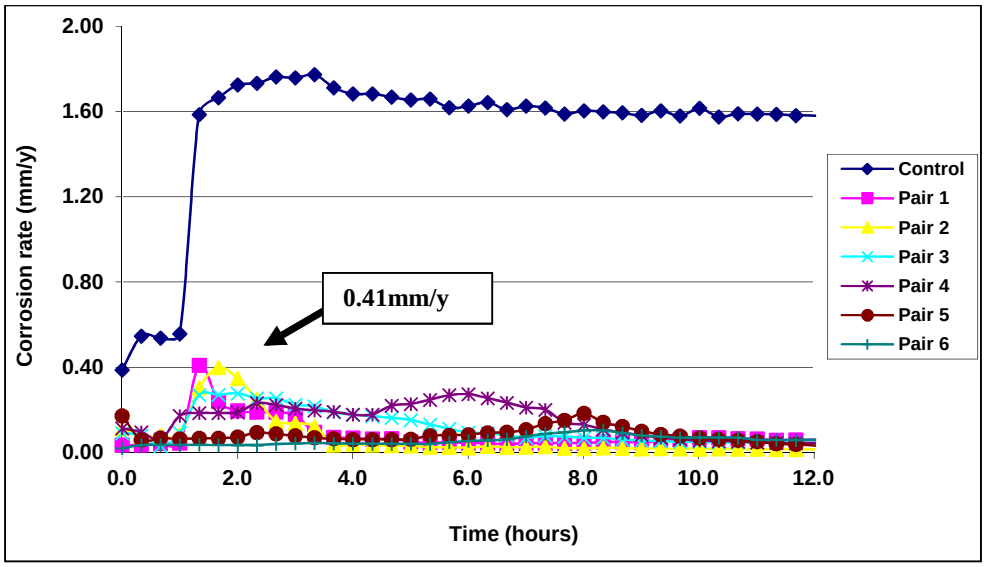

Figure 9-7: Graph of corrosion rate against time for annular space gap 0.15 mm

Figure 9-7 shows that the corrosion rate of the control sample in the bulk solution is about 1.60 mm/y while that of the electrodes within the annular space are presented below.

- Maximum corrosion rate of pair 1 = 0.41mm/y
- Maximum corrosion rate of pair 2 = 0.40mm/y
- Maximum corrosion rate of pair 3 = 0.28mm/y

Annular space gaps – 0.00mm (No gasket)

Three experiments were conducted without a gasket (zero annular space gap). This was because the first two results obtained were not reliable as some of the test electrodes within the annular space did not have any readings. This challenge was likely due to the limited quantity of electrolyte that had access into some part of the annular space. Since the electrochemical process requires an electrolyte medium, it was therefore difficult (due to limited quantity of electrolyte) to get any result.

After observing the problems with the two tests, the third test was conducted by slightly loosening the Allen bolts holding the Perspex tank and steel plate together. This action

allowed some quantity of the electrolyte to wet the surface of the steel plate to ensure conductivity for the corrosion process to take place.

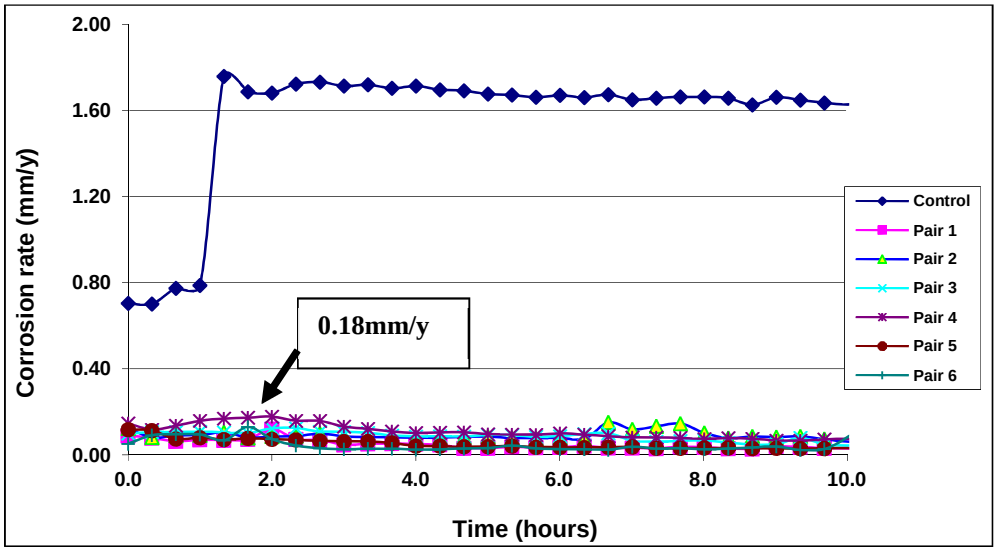

Figure 9-8: Graph of corrosion rate against time for annular space gap 0.00mm

Figure 9-8 shows the average corrosion rate of the control sample as 1.60mm/y while the maximum corrosion rate within the annular space as 0.18mm/y. This is quite good taking into consideration the fact that the installation technique for plastic lined pipelines is a tight fit, that is, a no gasket situation.

9.4.2 Relationship between Corrosion Rate and Annular Space Gap

Figure 9-9 shows the relationship between the annular space gap and the corrosion rate within the annular space. The corrosion rate within the annular space is seen to drop from a maximum value of 0.68 mm/y when the annular space gap is 1.60 mm to a minimum value of 0.18 mm/y when the annular space gap is 0.00 mm, except for annular space gap 1.00 mm. When the distance from the vent is 10.00 mm, the corrosion rate dropped from 0.27 mm/y when the annular space gap is 1.60 mm to 0.13 mm/y when the annular space gap is 1.00 mm. It then increased to 0.18 mm/y for annular space gap 0.30 mm and then 0.27 mm/y for annular space gap 0.30 mm before

increasing to 0.41 mm/y and later to 0.15 mm/y for annular space gaps 0.15 mm and 0.00 mm respectively.

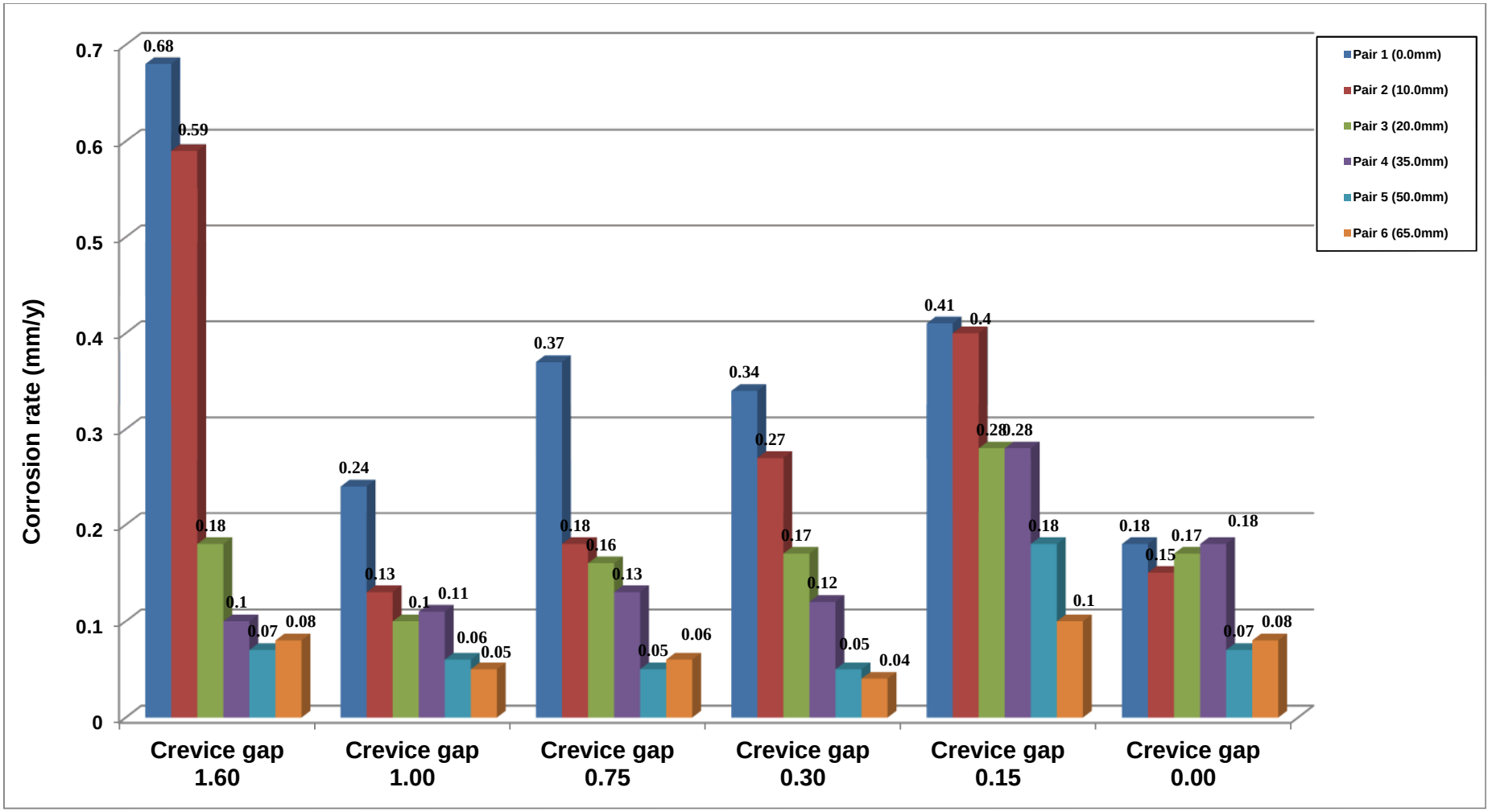

Figure 9-9: Graphical representation of relationship between corrosion rate and annular space gap

9.5 Summary of Discussion

The result showing the relationship between the corrosion rate and the annular space gap depicted in Figure 9-9 show a direct relationship for electrode pair 1. That is, as the annular space gap decreased the corrosion rate decreased. For the other test electrodes, a relationship could not be defined as for electrode pair 1.

The lowest corrosion rates of 0.18 mm/y and 0.15 mm/y were measured when the annular space gap was 0.00 mm (no gasket situation) for electrode pairs 1 and 2 respectively, except for annular space gap 1.00 mm where the corrosion rate of electrode pair 2 was lower (0.13 mm/y). This drop in the corrosion rate for annular space gap 0.00 mm is attributed to decrease in the quantity of CO_2 available within the annular space to cause corrosion of the steel surface.

The work of Degerbeck and Gille (1979) also demonstrated the fact that varying crevice geometry can cause serious corrosion in some crevices. Walton (1990) went further to state that if all other conditions within a crevice are equal, larger crevices are expected to develop a stronger corrosive environment compared to smaller crevices. As such the larger crevices with the more corrosive crevice solution will have a higher corrosion rate compared to smaller crevices with less corrosive environments. Li et al. (2002) concluded that if the crevice width is increased, the potential gradient decreases and the current density increase within the crevice.

Practical Application

The case of no gasket (zero annular space gaps) is a more likely situation to be encountered in the construction of plastic lined pipelines. This is because vented plastic lined pipeline designed by Swagelining Limited are designed with the liner fitting tightly around the pipeline (Swagelining). The design concept is having a plastic liner with an outer diameter slightly larger than the internal diameter of the pipe to be lined and so fits tightly against the inside wall of the pipe with zero annular space gap (Swagelining, 2010). Therefore the corrosion rate expected within the annular space of a tightly fitted plastic lined pipeline is likely that for no gasket situation which has the

lowest corrosion rate. Therefore the tight fitting liner combined with the vent design helps in mitigating against internal corrosion of the lined pipeline.

CHAPTER 10
CATHODIC PROTECTION

10.1 Introduction

In Chapter 5, it was concluded that the corrosion of the steel beneath the plastic liner was mainly localised around the vent area. Therefore any action to prevent this localised corrosion would be a positive development for the application of cost effective vented plastic liner designs for carbon steel pipelines. Researches have shown that applied potential is a key factor in cathodic protection of coated steel pipes (Chin and Sabde, 1999). Therefore its principle can be applied for the case of localised corrosion in the annular space created by the vented plastic liner. Toncre (1984) and Orton (1985) in their different researches cited by Li et al. (2002) demonstrated that it was possible to achieve cathodic protection (CP) on the steel surface within a crevice as long as it contains an electrolyte of low resistivity.

This chapter investigates the feasibility of controlling the corrosion within the annular space of the vented plastic lined carbon steel pipeline by CP using a sacrificial zinc anode, which preferentially corrode in place of the steel (Trethewey and Chamberlain, 1995). Two types of CP design, namely disc and long strip sacrificial zinc anode, were applied within the annular space and tested. In addition, a novel Luggin capillary tube was designed to measure the potential distribution within the small annular space area during the deaeration process and when CO_2 was introduced.

10.2 Sacrificial Anode Design

A piece of zinc sheet was cut to make a disc-shaped zinc anode with internal and external diameters of 4.2 mm and 23.8 mm respectively. Another piece was cut into a rectangular shape to form a long-strip zinc anode with a length of 41.40 cm and width of 0.9 cm. Figure 11-1 is a schematic diagram of the two sacrificial zinc anode designs.

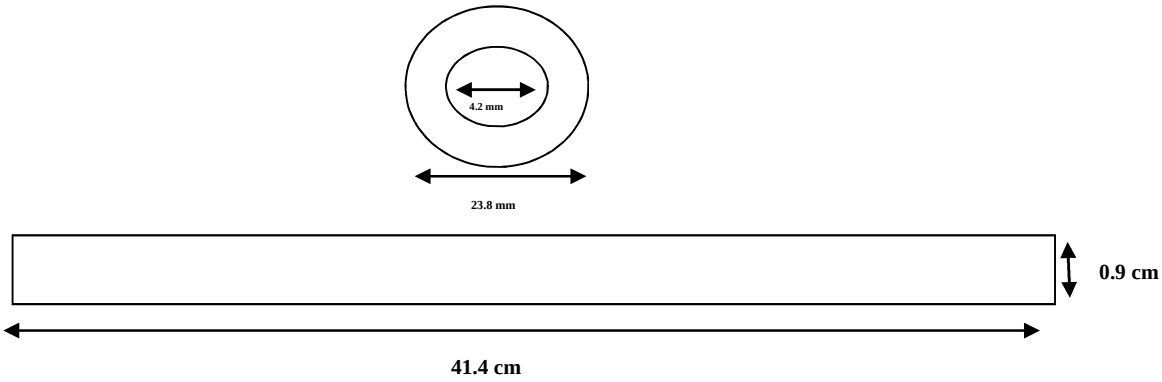

Figure 10-1: Schematic diagram of sacrificial zinc anode designs (a) disc anode; (b) long strip sacrificial anode

The disc shaped zinc sacrificial anode was designed to fit perfectly around the vent of the Perspex tank without obstruction. It was secured under the bottom surface using glue. A wire cable was secured to the zinc in order to connect it to the steel plate to complete the electrical circuit for the cathodic protection. Figure 11-2 is the schematic diagram showing the disc zinc sacrificial anode connected beneath the liner in the corrosion cell.

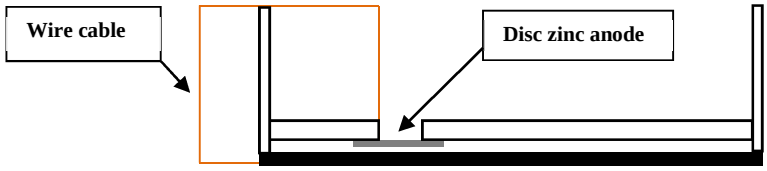

Figure 10-2: Schematic diagram showing disc zinc sacrificial anode

10.2.1 Long Strip Zinc Sacrificial Anode Design

The long strip was designed to fit under the space of the annular space between the Perspex and steel plate, starting from the vent area to the end of the plate. The strip zinc anode was made into an “S” shape before gluing to the bottom of the Perspex tank. A good connection between the zinc anode and the steel plate was made when the Perspex tank was assembled on the plate such that it compressed the zinc against the steel plate. This is demonstrated in the schematic diagram in Figure 10-3.

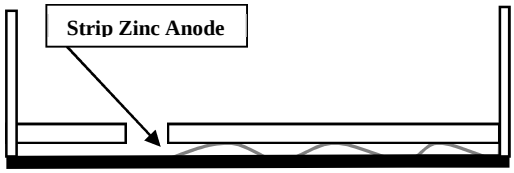

Figure 10-3: Schematic diagram showing long strip zinc anode

10.3 Design and Installation of Potential Measuring Luggin Probe

To effectively measure the actual potential in the annular space without the effect of ohmic resistance a specially designed novel Luggin capillary was made from a small wire cable and placed close to the test electrodes. The Luggin capillary was placed in between two heat shrink sleeve to ensure free movement within the small annular space. The two lengths of heat shrink sleeve were cut and heated to size to encase the Luggin capillary cable and served as the glands at the exit points from the corrosion cell.

The Luggin capillary was made from an empty wire cable of 0.12 cm diameter and an approximate length of 90.00 cm. The wire threads within the cable were removed to form a hollow tube. Along the length of the wire cable a small hole was inserted, with an identification mark, to serve as the opening for Luggin capillary. The voltages measured at the opening corresponded to the potential of the steel adjacent to it. This unit is presented in Figure 10-4.

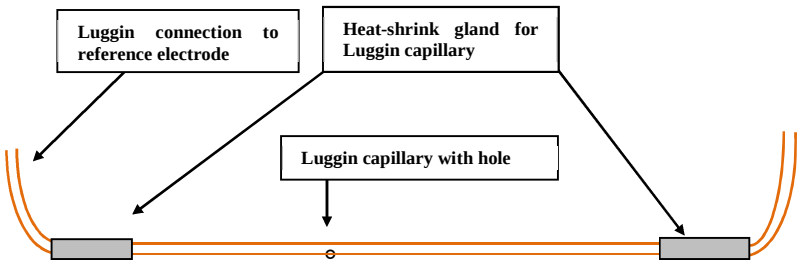

Figure 10-4: Schematic diagram of Lugging capillary tube and heat shrink for potential measurement within annular space

It is pertinent to note that the gasket used for creating the annular space gap was cut at the ends to give access to the heat shrink and Luggin capillary unit. The heat shrinks were secured to the gasket and corrosion cell and sealant applied to prevent leakages. This design was necessitated by the need to prevent leakage during the process of moving the Luggin capillary tube along the annular space in the course of potential measurements.

In essence, the Luggin capillary ran through the heat shrink sleeves, gasket and between the steel plate and Perspex tank. One end of the Luggin capillary was coupled to a reference electrode and multimeter for monitoring the potential. The other end of the heat shrink/Luggin capillary unit was secured to a clamp at a position slightly higher than the height of the electrolyte in the Perspex tank to prevent leakage.

10.4 Corrosion Cell Set-up

10.4.1 Material Preparation

Before setting up the corrosion cell, the zinc anodes were abraded with carbide paper of grades 240 and 800 to remove surface impurities and expose the clean shiny zinc surface. It was then cleaned with iso-propanol before been glued to the bottom of the Perspex tank. The other components including the Luggin capillary and heat shrink sleeves were also cleaned with iso-propanol before assembly and the complete corrosion cell coupled.

10.4.2 Simulation of CO_2 Corrosion

After the set-up, deaerated electrolyte was siphoned into the corrosion cell and then nitrogen gas bubbled to further deaerate it for another 1.5 hours. It was later replaced with the carbon dioxide (CO_2) gas, for both tests, throughout the duration of the experiment to simulate sweet corrosion. The Luggin capillary was moved from the left to the right and the potential of the point adjacent to the hole was accurately measured and recorded. Figure 10-5 is a schematic showing part of the corrosion cell used for

measuring the potential distribution within the annular space, without and with the cathodic protection. Ten experiments were performed and after each experiment, the metal plate with the test electrodes and the control electrodes was reground and cleaned before assembly.

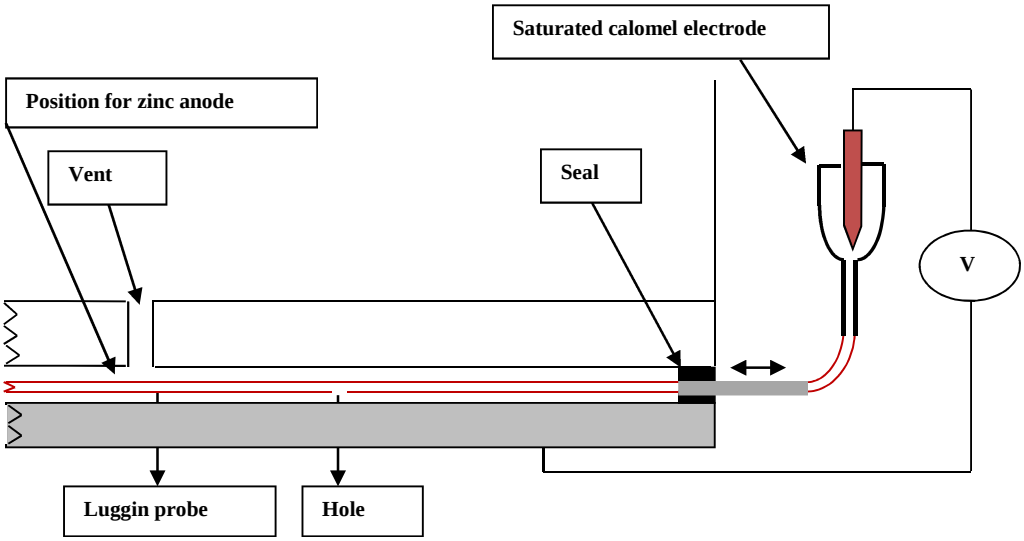

Figure 10-5: Schematic diagram showing part of the corrosion cell for cathodic protection measurement

The Luggin capillary was designed and used to manually measure the potential of the test electrodes within the annular space. It is also important to mention that this design is necessary for the CP experiment. This was because the corrosion rate cannot be determined using the LPR technique when the CP is in operation because the LPR technique works by measuring the gradient ($\Delta E/\Delta i$) of the linear portion of the LPR scan around the free corrosion potential, far above the CP potential. It is also important to note that the potential is a good indicator of the effectiveness of CP. Therefore to determine if the CP system was operating effectively, the potential within the annular space must be measured to ensure that it falls within the immunity region of the iron-water system.

10.4.3 Potential Distribution within Annular Space

This sub-section is dedicated to the measurement of the potential distribution along the annular space during the process of deaeration and sweet corrosion simulation. The potentials are measured using the specially designed Luggin capillary from the annular space mouth down into the annular space. According to Walton (1990), electrochemical reaction at the metal-solution interface within a crevice is related to the corrosion potential of the metal. Generally the occurrence of crevice corrosion can be monitored by potential measurements (Ijsseling, 2000) and therefore the potential distribution can be used as an investigative technique for the determination of onset of corrosion within the annular space.

During the period of deaeration with the nitrogen gas, the Luggin capillary tube was moved from electrode pair 1 (under the vent) through to electrode pair 6 (65.0 mm from the vent) and the readings on the voltmeter were noted and recorded (Figure 10-5). This was done throughout the period that nitrogen was bubbled into the tank. It is pertinent to note that this movement from one electrode position to another was made possible because of the indicator mark at the hole and because the Perspex tank is transparent.

After this period, nitrogen purging was stopped and the solution was bubbled with carbon dioxide, which marked the start of the sweet corrosion test. The Luggin probe was again moved from electrode pair 1 to pair 6 as described above. The potential distribution along the annular space during sweet corrosion was monitored and recorded.

10.4.4 Potential Measurement along Annular Space with Cathodic Protection

During cathodic protection, a negative potential was applied to the metal surface inside the using the zinc anode to bring it to the immunity region (Chin and Sabde, 2000b). Like the previous test, the potential distribution with the annular space was also measured under cathodic protection. The same experimental set-up shown in Figure 10-5 was used. During the period of nitrogen purging, the Luggin capillary tube was moved

from under the vent position (electrode pair 1) and the reading on the voltmeter noted and recorded. The Luggin capillary was successively moved to pairs 2, 3 and 6 and the corresponding potential readings recorded accordingly. This was done throughout the period that nitrogen gas was bubbled into the tank.

The nitrogen supply was replaced with the CO_2 gas supply to simulate sweet corrosion. The Luggin probe was again moved from one electrode pair position to another as described above. The potential distribution along the annular space during sweet corrosion was monitored and recorded over the duration of the test. The experiment was left for some hours before starting other sets of measuring and recording.

10.5 Results and Discussion

10.5.1 Result of Potential Distribution within the Annular Space

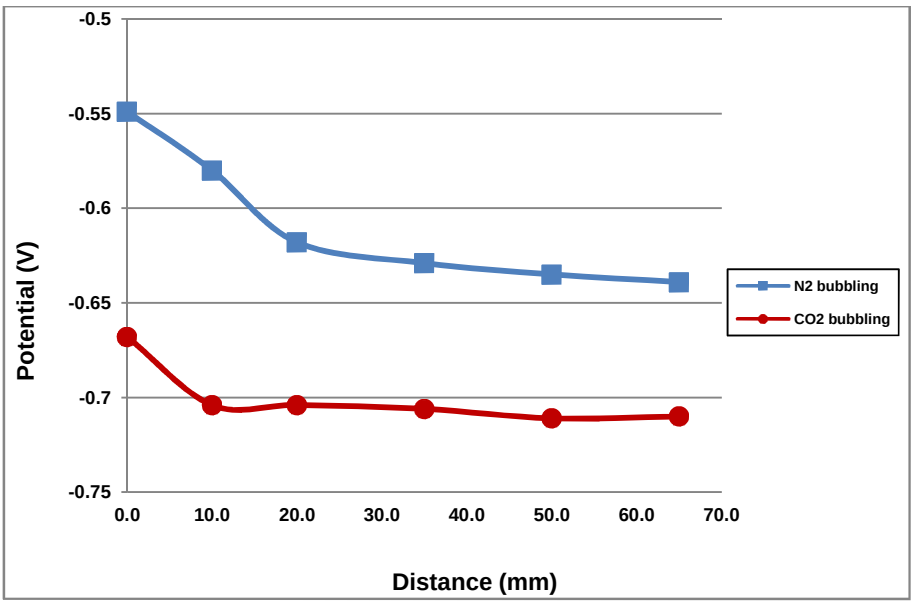

Figure 10-6: Potential distribution within annular space measured manually

Figure 10-6 shows the potential distribution within the annular space from beneath the vent (electrode pair 1) to electrode pair 6 (65.0 mm from the vent). During the period of deaeration, the potential dropped from -0.550 V from under the vent to -0.580 V, 10.0 mm into the annular space (electrode pair 2) and -0.618 V, 20.0 mm further into the

annular space. Further into the annular space the potential dropped and remained low around an average value of -0.639 V up to 65.0 mm from the vent.

The introduction of CO_2 caused an active shift in the potential within the annular space. The potential of electrode pair 1 dropped from –0.550 V to -0.668 V. Likewise the potential of electrode pairs 2 to 6 dropped to lower values. This drop in the potential is attributed to the corrosive effect of the CO_2 gas that diffused through the vent into the annular space.

10.5.2 Cathodic Protection using Disc Zinc Sacrificial Anode

Figure 10-7 is a pictorial view of a running test with the disc zinc sacrificial anode and Luggin capillary in place.

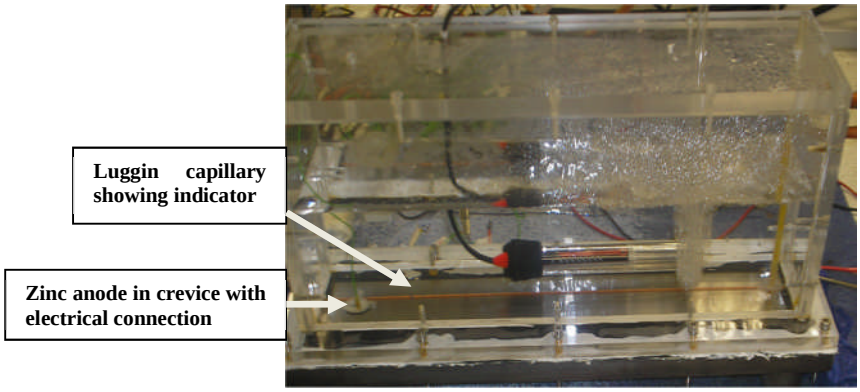

Figure 10-7: Pictorial view of experiment with zinc anode and Lugging capillary in position

The effectiveness of a disc anode in protecting the steel from corrosion around the liner vent area is demonstrated in Figure 10-8. The potential at the bottom of the vent, adjacent to the anode, was close to the expected value for zinc [-1,040 mV (SCE)] and the level of protection then decreased with distance. The blue curve [**a**] shows the potential distribution within the annular space throughout the period when the bulk solution was purged with nitrogen gas. It can be observed that the potential increased as we move further into the annular space. This observation is discussed further in the summary of discussion sub-section. During this period of deaeration the potential was

below the commonly accepted design protection potential of -850 mV (SCE) (Baboian, 2002) and this was achieved up to 185.0 mm from the vent area.

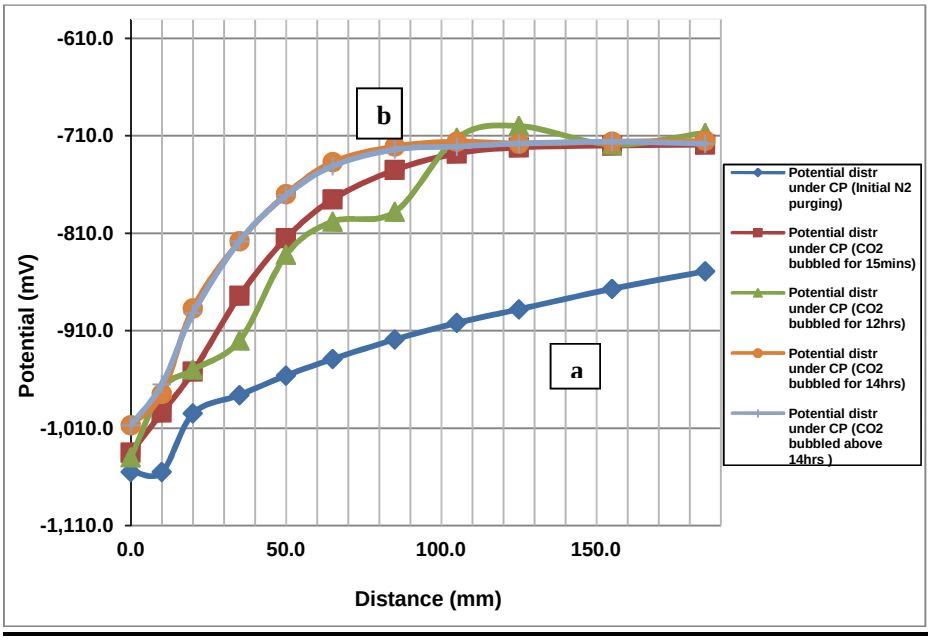

Figure 10-8: Potential distribution in annular space under cathodic protection using disc zinc anode

After bubbling the solution with carbon dioxide, the potentials became more noble and full protection was reduced to the region within approximately 40.0 mm of the vent. The curves labelled [**b**] represent the set of results obtained during the period when CO_2 was bubbled into the corrosion cell. It can be seen that the potentials generally increased along the plate from -1,040 mV to about -850 mV, around the 40.0 mm point. Visual observation showed that the surface of the steel within 40.0 mm of the vent area appeared bright, but beyond this point small patches of light grey/black films were seen (slight corrosion). These corrosion patches increased as one goes further away from the position where the CP was installed (vent area). In general, the curves demonstrate that complete protection could not be obtained beyond the 40.0 mm point as the potential is above -850 mV.

The protection is therefore limited by the low CP voltage beyond this point. This observation is supported by the work of Chin and Sabde (1999) which confirms that low

CP voltage would not permit penetration of electrical current further into a crevice to polarize the carbon steel surface to a sufficiently negative potential (Chin and Sabde, 2000a). Also Li et al. (2002) demonstrated in their work that only steel surfaces in the vicinity of the zinc anode come under the direct cathodic protection and that corrosion will still occur in the deeper area of the crevice.

It is interesting to note that the extent of the area protected (40.0 mm) by the disc anode CP is further compared to the distance affected by corrosion (35.0 mm), as was seen in Figure 5-9. It can therefore be concluded that, provided there is no flow of liquid beneath the liner, a simple disc anode located beneath the vent would offer the benefit of controlling corrosion in the region where it is most likely to occur.

10.5.3 "*Throwing Power*" Limitation of Disc Sacrificial Anode

From Figure 10-8(a), it is clear that the "throwing power" of the zinc anode CP system could not cover the whole length of the steel plate. "Throwing power" limitation implied that the protection given by the disc zinc anode is affected by the distance from the metal been protected (Trethewey and Chamberlain, 1995). This protection did not extend further than approximately 40.0 mm from the vent where the zinc anode was installed, due to the confined geometry of the annular space. The limited "throwing power" depicted by the current coverage is shown schematically in Figure 10.9 (a).

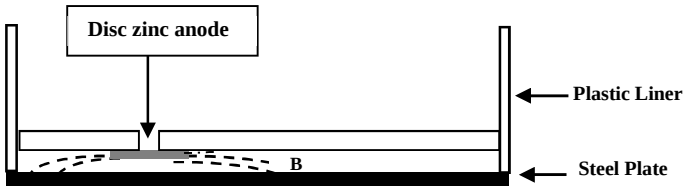

Figure 10-9(a): Schematic diagram showing "throwing power" limitation of disc zinc anode

The Evan's diagram in Figure 10-9(b) explains why the protection of the steel plate decreased as one moves further away from the plate, that is, the reduction in the "throwing power".

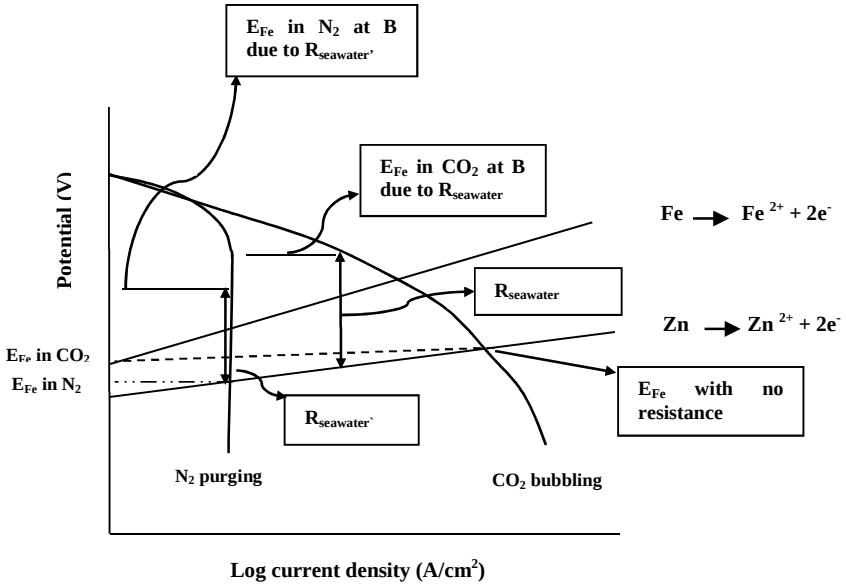

Figure 10-9(b): Evans diagram showing changes in resistance and the effect on the potential

The Evans diagram shows the changes in the solution resistance and the corresponding changes in the system potential. It is pertinent to note that this change in system potential called ohmic potential drop (iR) is due to the electrolyte resistance and is required to move the ions through the electrolyte. One of the major effects of ohmic potential drop (iR) is the decrease in the magnitude of the cathodic current, resulting in limited protection.

The reduction in the 'throwing power' is attributed to the increase in the resistance of the seawater ($R_{seawater}$ and $R_{seawater`}$) as the distance moved further away from the zinc anode. Close to the zinc anode, the potentials measured for the N_2 and CO_2 environments are E_{Fe} in N_2 and E_{Fe} in CO_2 respectively. These values are low and give protection to the carbon steel plate because of the short distance. On the other hand, increase in the distance from the sacrificial zinc anode resulted in increase in the seawater resistance. Consequently, the resultant resistances in the two test environments ($R_{seawater`}$ in N_2 and $R_{seawater}$ in CO_2) increased, leading to higher potentials [E_{Fe} (iR_{Fe}) in N_2 and E_{Fe} (iR_{Fe}) in CO_2] and therefore a limited level of protection.

10.5.4 Cathodic Protection using long Strip Zinc Sacrificial Anode

Because of "throwing power" limitation and in the event of some form of fluid flow through the annular space, additional transport of carbon dioxide would extend the region at risk of corrosion. Therefore an alternative method of providing protection would be required. This is the reason for the long strip sacrificial zinc anode design which runs through the length of the annular space.

According to Chin and Sabde (2000a), to fully protect a carbon steel pipe against corrosion, electrical current must penetrate into the annular space to polarise the steel surface.

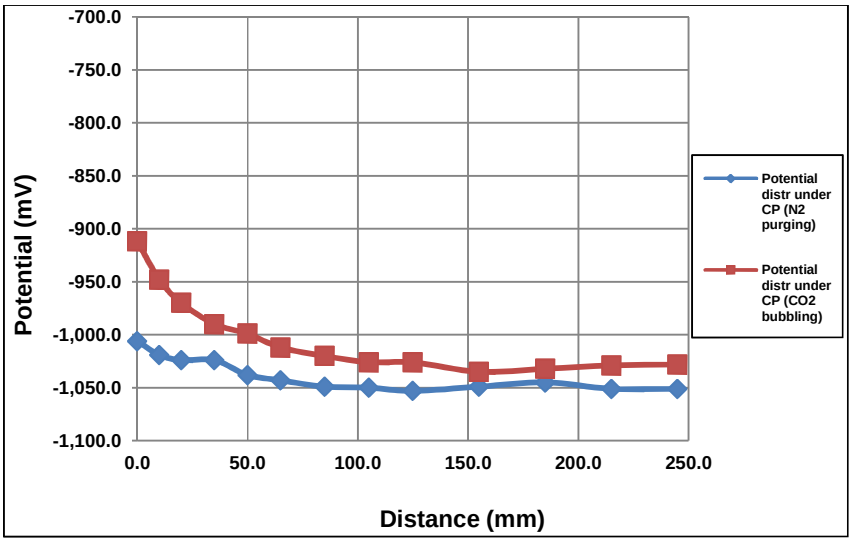

Figure 10-10: Potential distribution in annular space under cathodic protection using strip zinc anode

Figure 10-10 is the graphical presentation of the result of the strip zinc anode design. During the process of deaeration with nitrogen gas, the carbon steel had a fairly uniform potential ranging from -1,005 mV to -1,050 mV (close to the electrode potential of zinc). When carbon dioxide was bubbled into the tank, the potentials near the vent became progressively nobler but remained below -850 mV, the value required for full protection of the steel. Again, the increase in potential was due to carbon dioxide diffusing into the annular space.

It was observed that the whole length of the carbon steel plate was bright after the test which indicated no corrosion as a result of the long strip CP system. Figure 10-11(a) shows the fully protected steel plate which is still shiny after the test. This figure can be compared to the unprotected steel plate with corrosion seen over its surface as shown in Figure 10-11(b). Clearly, the incorporation of a zinc anode strip to the underside of the flexible liner would be a safer method of combating corrosion in the annular space and would provide protection over a wider range of operating conditions.

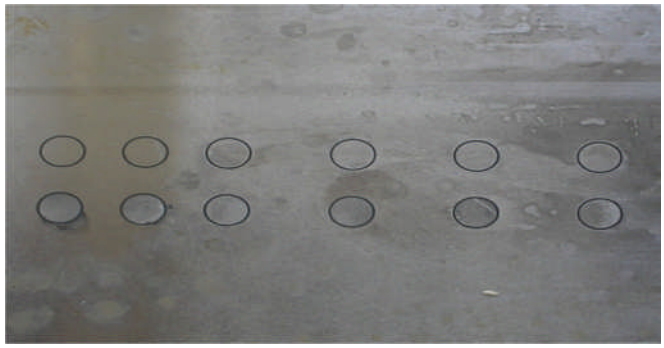

Figure 10-11(a): Pictorial view of fully protected steel plate under cathodic protection

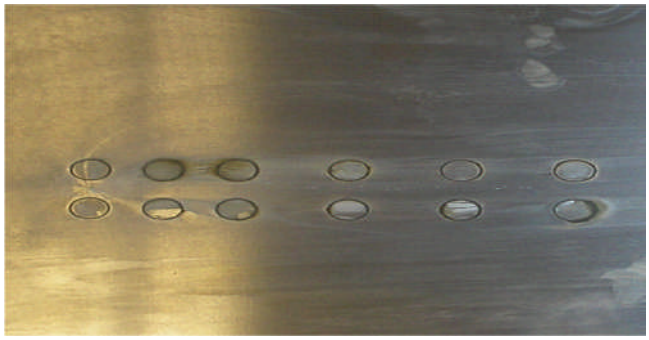

Figure 10-11(b): Pictorial view of corroded steel plate without cathodic protection

10.5.5 Potentiodynamic Scan

The corrosion behaviour of steel in brine containing dissolved corrosive species such as CO_2 has been obtained from surface analysis and potentiodynamic experiments (Filbo and Orazem, 2001). Therefore potentiodynamic scans were performed to better understand and explain the observations of the results in figures 10-8(a) and 10-10. It

can be seen from these curves that the potential became nobler whenever the nitrogen gas was replaced with CO_2 gas. As expected the corrosion rate increased because of the corrosive effect of the CO_2. These observations will be discussed next using an Evan's diagram derived from a simple potentiodynamic scan.

A simple corrosion cell (Figure 10-12) consisting of a working electrode, counter electrode, gas bubbler and reference electrode was assembled and connected to the Solartron equipment for the experiment. The gas bubbler was to supply a stream of air (for aeration), nitrogen (for deaeration) or carbon dioxide (for simulating CO_2 corrosion) depending on the experiment.

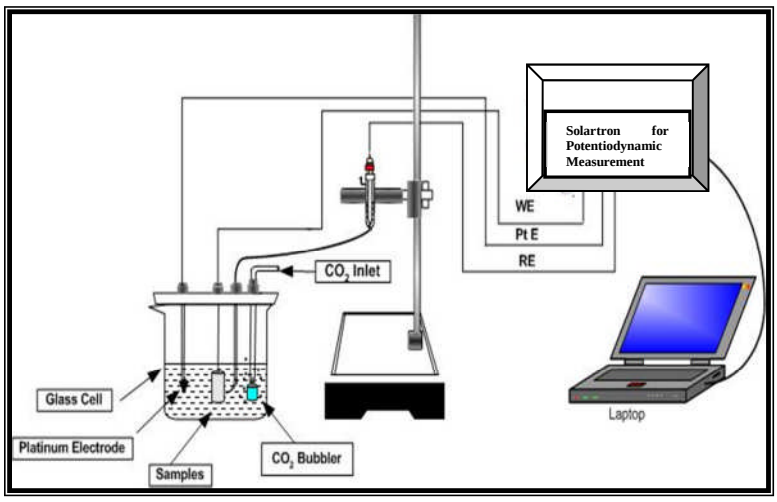

Figure 10-12: Schematic diagram showing cell for potentiodynamic measurement

Cathodic Scan

A cathodic scan was carried out in which the potential was varied from the free corrosion potential to a final potential of 0.300 V below the free corrosion potential. The current density was recorded and a graph of logarithms of the current density (log i) against potential (Evans diagram) was plotted and presented as Figure 10-13.

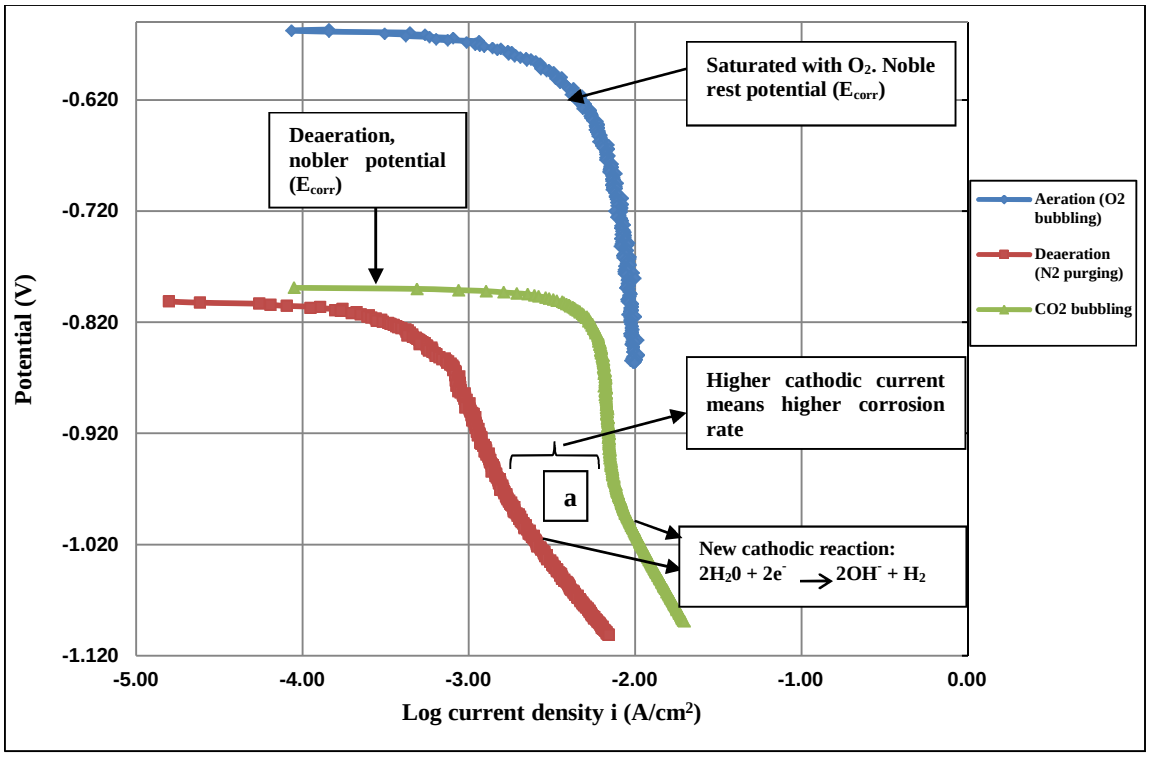

Figure 10-13: Cathodic scan showing effects of aeration, nitrogen purging and CO_2 bubbling

It can be seen from the cathodic scan that when the cell was aerated with air, the potential became more nobler and the current density was highest. Bubbling the solution with nitrogen gas resulted in a reduction in the potential of the steel plate and also the corrosion rate. On the other hand the addition of CO_2 resulted in a rapid increase in the current density (corrosion rate) and a slight increase in steel potential. This simple test confirmed that the carbonic acid was responsible for the potential becoming nobler as seen in figures 10-8(a) and 10-10.

Further decrease in the potential, down to -0.950 V, resulted in a slight change in the current density. However, at point [**a]**, the applied potential became adequately negative for another cathodic reaction to occur with a rapid increase in the current density (Li et al., 2002). This new reaction is the reduction of water as shown below:

$$2H_2O + 2e^- \longrightarrow 2HO^- + H_2\uparrow$$ **Equation 10-1**

This experiment also demonstrates the negative effect of high CP voltage which can result in hydrogen embrittlement as a result of absorption of the hydrogen generated due to water reduction (Robinson and Kilgallon, 1994).

Anodic Scan

Anodic scans were carried out in which the potential was varied from the free corrosion potential to a final potential of 0.300 V above the free corrosion potential. The current density was recorded and a graph of the log current density (log i) against potential (Evans diagram) was plotted and presented as Figure 10-14.

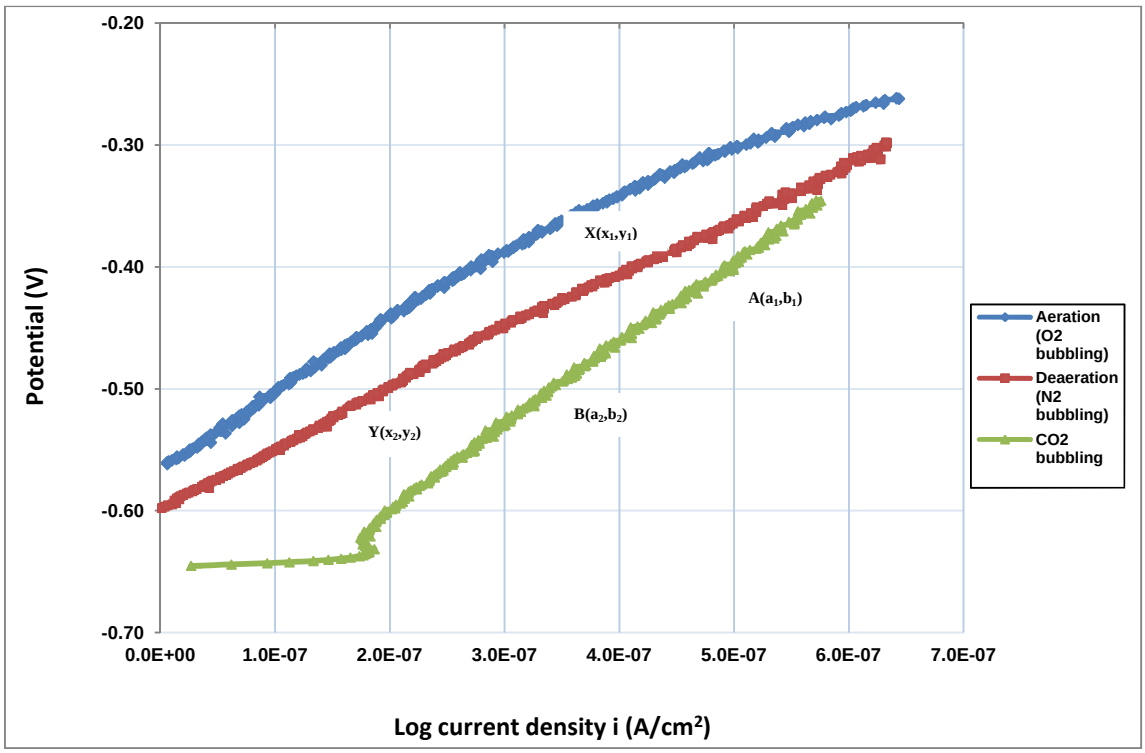

Figure 10-14: Anodic scan showing effects of aeration, nitrogen purging and CO_2 bubbling

The anodic curves show the effects of bubbling air, nitrogen gas and carbon dioxide on the carbon steel rod. The important point in the curves is the gradient of the anodic curve when CO_2 was bubbled into the solution. The addition of CO_2 resulted in a slight increase in steel potential with the formation of corrosion product on the metal surface

and a reduction in the corrosion rate. The steepness of the curve can be determined by calculating the gradient; and a higher gradient value indicated a steeper incline.

The slope is defined as the ratio of the $\Delta E/\Delta i$ where E is the potential and i, the current density between two points on the curve. Taking the points A(a_1,b_1) and B(a_2,b_2) on the CO_2 bubbling curve (green), the gradient is given as 588,235. Taking points X(x_1,y_1) and Y(x_2,y_2), on the N_2 bubbling curve, the gradient is given as 500,000. Therefore since the gradient of the CO_2 bubbling curve is higher, it is steeper than the N_2 bubbling curve. This test like the cathodic test confirms that the carbonic acid was responsible for the potential becoming nobler as seen in figures 10-8(a) and 10-10.

10.6 Summary of Discussion

Potential distribution measurements are another method of assessing corrosion behaviour of materials because regions of high corrosion activity can be identified as they show characteristically low potentials.

With CO_2 corrosion localised around the vent area of the plastic lined pipeline, zinc anode CP system was employed to protect the carbon steel plate underneath the liner. In theory, complete cathodic protection can be achieved if the protection potential is below the reversible potential of the carbon steel (Kim, 2001).

This protection potential was established around the vent area using a disc type sacrificial anode CP design. Unfortunately, the protection was limited to just 40.0 mm around the vent area due to the limitation of “throwing power” resulting from the crevice geometry. However, the area under cathodic protection covered the region (35.0 mm) of threat, provided no fluid flow occurs through the vent to transport more CO_2 into the annular space.

To overcome the “throwing power” limitation encountered with the disc zinc anode design and to cover the full length of the steel plate, the long strip zinc anode CP system was designed and gave an almost uniform cathodic current along the entire length of the plate. Despite CO_2 diffusing into the annular space, the potential within the annular

space was within the protective range (≤ -0.900 V). The carbon steel plate had no signs of corrosion attack as a result of the long strip CP system. Therefore incorporating a zinc anode strip to the underside of the flexible liner would be a safer method of combating corrosion in the annular space and would provide protection over a wider range of operating conditions.

Effect of Deaeration with Nitrogen gas under Cathodic Protection

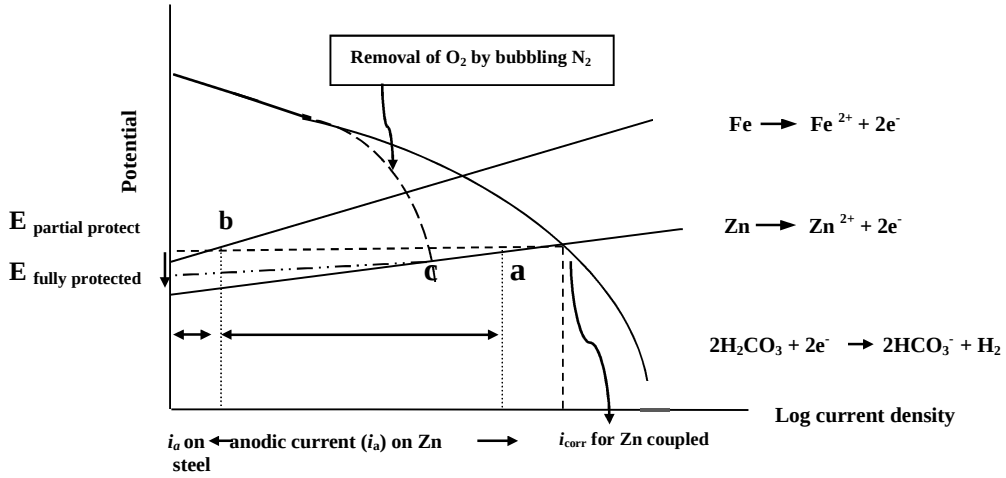

Figure 10-15: Evans diagram showing the principle of cathodic protection and the effect of purging with nitrogen gas

It was observed that during the deaeration process the potential always decreases to the region of immunity. This observation is explained using the Evans diagram in Figure 10-15. The figure shows the cathodic curve intersecting the zinc anodic curve at point [**a]**, which signifies the start of the experiment. Unfortunately, at this point [**b]** there is still some level of corrosion of the steel plate (partial protection). This occurs because there is an anodic current from the steel which implies little corrosion equivalent to i_a (current density).

With the bubbling of nitrogen gas, some of the oxygen still in solution were removed (deaeration) thereby moving the cathodic curve towards the left. The cathodic curve then intersects the zinc anodic curve at a lower point [**c]** which results in full protection

of the steel and also a reduced rate of corrosion even for the zinc anode. The potential dropped from $E_{partially\ protected}$ to $E_{fully\ protected}$ (complete protection of the steel plate).

The results obtained showed that corrosion rate decreases as the CP current or i_{cp} increases, i.e., the steel potential moved from the free corrosion potential towards the equilibrium.

Limitation of Zinc Anode Cathodic Protection

The main limitation of the cathodic protection is that the zinc anode will be consumed at which point protection will be lost. The rate of dissolution of the zinc anode in carbonic acid would be another factor and this would need to be investigated separately as information does not seem to be available in the literature.

CHAPTER 11
CORROSION INHIBITOR

11.1 Introduction

Addition of corrosion inhibitor with the aim of controlling internal corrosion of carbon steel structures is a standard practice in oil and gas production systems (Villamizar et al., 2007). Corrosion inhibitors are extensively used to reduce the rate of sweet corrosion in the oil and gas industry, and they have been shown to be very effective. The basic principle of operation of oilfield inhibitors is that they form a film on the metal surface, preventing corrosive agents from having direct contact with the metal as reviewed in Chapter 2 (Palmer-Jones and Paisley, 2000; Nesic, 2007; Bentiss et al., 1999). It was therefore important to investigate the effect of corrosion inhibitors on vented plastic lined pipelines as most operators use inhibitors. In addition, the investigation looked into whether the amount of inhibitor that enters the annular space is beneficial.

In this section, investigation and evaluation of the behaviour of CORRTREAT 05-193 as a corrosion inhibitor in seawater saturated with CO_2 are presented. Tests were carried out in order to determine the level of protection the inhibitor can provide for vented plastic lined carbon steel in a static condition. The test results are presented in graphical forms and compared with results obtained in previous chapters.

11.2 CORRTREAT 10-569 Corrosion Inhibitor

CORRTREAT 05-193 is an oilfield corrosion inhibitor supplied by *Clariant Oil Services*. The inhibitor is made from a combination of neutralising amines in a water/glycol based solvent package. The inhibitor is a clear liquid with amber colour and the main chemical components included 2-Butoxyethanol, Acetic Acid, Imidazoline, Imidazoline ethoxylate and Thioglycolic acid.

11.2.1 Preparation of Corrosion Inhibitor

In the oil and gas industry, it is a common practice to apply corrosion inhibitors at parts-per-million (ppm) (Meng and Jovancicevic, 2008). For all experiments conducted, the CORRTREAT 05-193 inhibitor concentration used was 30 ppm by volume, typical of industry accepted levels (Gulbrandsen and Dugstad, 2005).

The quantity of inhibitor required to make a concentration of 30 ppm is 30×10^{-6} or 0.03 ml per litre. Therefore for a 4 litre solution of brine in the corrosion cell, 0.12 ml of inhibitor was required to make up a concentration of 30 ppm for the test. In the interests of health and safety, this quantity of the inhibitor was drawn from its container with a syringe in a fume cupboard and safely stored.

11.2.2 Simulation of CO_2 Corrosion and Applying Corrosion Inhibitor

The corrosion cell was assembled after cleaning with iso-propanol to remove impurities. The cell was then connected to the Solartron corrosion monitoring equipment while being deaerated with nitrogen gas. Four litres of previously deaerated NaCl (3.5%) was slowly transferred into the corrosion cell and the process of deaeration continued for another 4 hours. The nitrogen gas supply was then replaced with the CO_2 gas line to simulate CO_2 corrosion.

After running the test for 2 hours, the 0.12 ml of inhibitor drawn in the syringe was slowly injected into the Perspex tank of the corrosion cell containing brine saturated with CO_2 to produce a 30 ppm concentration. The addition having been completed, the experiment was allowed to run with the CO_2 being bubbled continuously for about 20 hours. This was done to observe the effect of the inhibitor on the control sample and then on the test electrodes within the annular space in the presence of CO_2 corrosion. Two experiments were performed and after each experiment, the metal plate with the test electrodes was reground and cleaned before assembly.

11.3 Results and Discussion

11.3.1 Comparison of Corrosion Rate in Reservoir and Annular Space

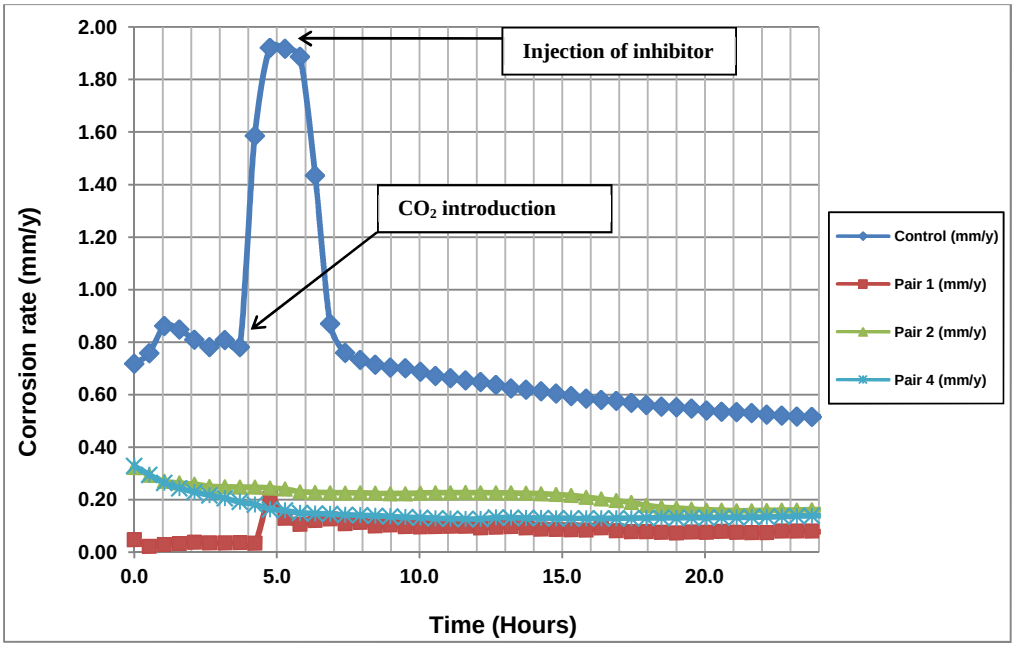

Figure 11-1: Effect of inhibitor on corrosion rate of control sample and test electrodes

Figure 11-1 is the graph showing the effect of the inhibitor on the control sample, in the Perspex tank, and some of the test electrodes within the annular space. It can be seen that there was a slight decrease in the corrosion rate of the control sample during the period of deaeration, which took 4 hours. The corrosion rate however increased suddenly from 0.80 mm/y to 1.90 mm/y when CO_2 was bubbled into the corrosion cell.

The addition of the corrosion inhibitor caused the sudden drop in the corrosion rate of the control sample from about 1.90 mm/y to a value of 0.8 mm/y within an hour and then gradually to about 0.56 mm/y after about 14 hours. The corrosion rates of the test electrodes within the annular space showed a general decrease and will be discussed in the next sub-section. This result agrees with other results of the corrosion reduction ability of oil field inhibitor (López et al., 2005; Dave et al., 2008).

11.3.2 Effect of Inhibitor within Annular Space

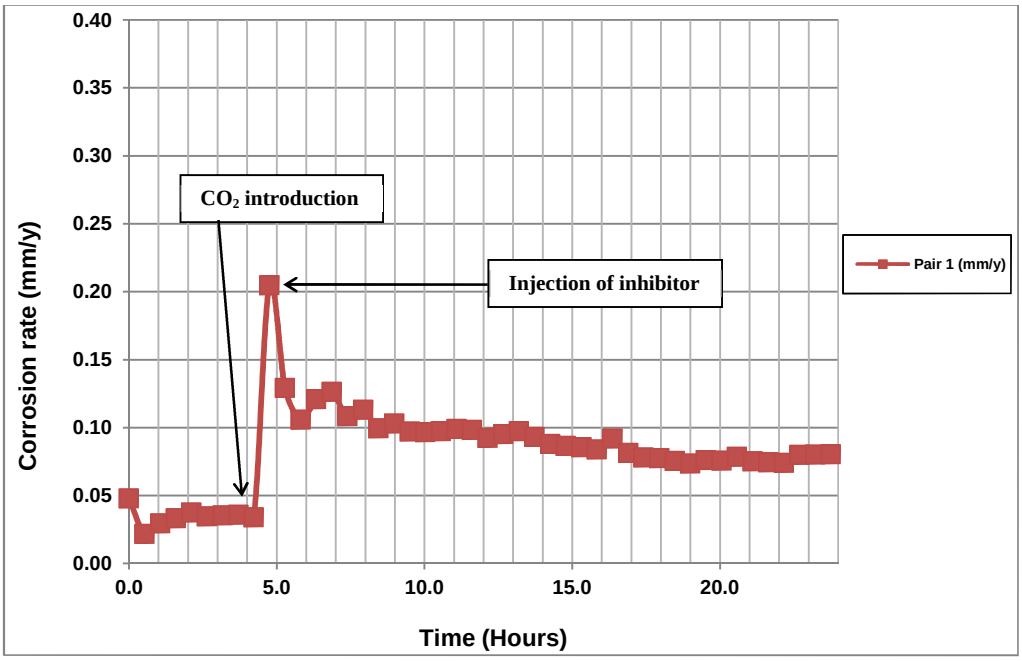

Figure 11-2: Effect of inhibitor on corrosion rate within annular space

Figure 11-2 shows the corrosion rates of test electrode pair 1 within the annular space. Like in other experiments, it can be seen that the corrosion rate of electrode pair 1, directly under the vent, showed an increase from about 0.04 mm/y to 0.22 mm/y after CO_2 had diffused into the annular space. After an hour, the corrosion inhibitor was added and almost immediately the corrosion rate started dropping from 0.22 mm/y to 0.13 mm/y within the hour and then gradually to an average value of 0.07 mm/y in about 14 hours.

Comparing the graph with that obtained without inhibitor in Figure 5-5 (b), it is clearly seen that the corrosion rate remained at an average value of 0.11 mm/y. This rapid decrease in the corrosion rate within the hour was also reported by Martinez et al. (2011). They attributed this action to the fact that the CORRTREAT05-193 corrosion inhibitor formed an inhibitor film on the surfaces of the electrodes. They concluded that the inhibitor has a remarkable influence on the corrosion behaviour of carbon steel pipelines.

These results imply that oilfield inhibitors when present in transported hydrocarbons will be effective in providing additional protection for the carbon steel surface within the vented plastic liner. According to Nesic (2007), the inhibitor absorbs onto the carbon steel surface and thereby slows down one or more of the electrochemical reactions. He also mentioned that the degree of protection was a function of the carbon steel surface covered by the inhibitor.

11.4 Summary of Discussion

The results obtained shows that the CORRTREAT 05-193 inhibitor is effective not only for normal unprotected pipelines but also for vented plastic lined pipelines. CORRTREAT 05-193 is a good corrosion inhibitor at the recommended concentration of 30 ppm. Regardless of the diffusion of CO_2 into the annular space, the corrosion rate was decreased with the addition of the inhibitor.

Comparing inhibited with uninhibited tests

Figure 5-5(b) in Chapter 5 shows the result obtained for electrode pair 1, directly under the vent, without any corrosion inhibitor. Comparing this result with that obtained with the application of the corrosion inhibitor, the effect of the CORRTREAT 05-193 can be clearly seen. For the uninhibited case [Figure 5-5(b)], the corrosion rate dropped from a maximum value of about 0.21 mm/y to 0.10 mm/y after over 4 hours. For the inhibited case (Figure 11-2), the corrosion rate of electrode pair 1 dropped from about 0.21 mm/y to 0.10 mm/y in less than 1 hour. This relatively fast drop in the corrosion rate is due to the diffusion of the corrosion inhibitor (CORRTREAT 05-193) through the vent into the annular space. Despite the presence of carbonic acid, the corrosion rate within the annular space was reduced to a very low value. Therefore the presence of oilfield corrosion inhibitor in transported hydrocarbon will also reduce the corrosion rate within the annular space of vented plastic lined pipelines.

Also the corrosion peaks observed on the test electrodes due to the diffusion of CO_2 into the annular space in the uninhibited experiments were not seen on the test electrodes of the inhibited experiments. Olsen et al. (2005) defined the inhibited corrosion rate based

on field experience to be within the range 0.1 – 0.3 mm/y which is in good agreement with the results obtained.

CHAPTER 12
GENERAL DISCUSSION

12.1 Introduction

According to Tems and Zahrani (2006) most of the conventional corrosion mitigation techniques have not proven to be cost-effective, long term corrosion protection strategies because of sudden failures of construction materials. Therefore the drive for the use of flexible plastic liners to protect the internal surface of carbon steel pipelines cannot be over-emphasised as over 24% of pipeline leakages are due to internal corrosion.

However, the use of these liners has been faced with the major challenge of permeation through the liner of associated gases such as CO_2 and H_2S. These gases are contained in the hydrocarbon being transported and accumulate in the micro-annulus and eventually expand and cause the liner to collapse (Boot and Naqvi, 2000). As a result of this problem, the COREL Joint Industry Project in partnership with Atkin-Boreas took the challenge to investigate possible solutions to liner collapse.

Grooved and perforated (vented) liner designs were developed as solutions for liner collapse but the perforated liner was preferred for subsea application because of its self-contained venting mechanism (Baker, 2005).

Preliminary tests conducted by the COREL team on the vented liner design were promising but inconclusive. There was also the concern that the vent design concept would lead to excessive corrosion of the carbon steel beneath the vent because of transport of corrosive species into the micro-annulus.

The extent and gravity of this corrosion in a CO_2 environment showed localised corrosion around the vent area. The limited corrosion was the effect of the carefully designed vent. In addition the effectiveness of the LinerVent^{TM} developed by Atkin-Boreas to cover the vent and further reduce mass transport needed to be investigated.

12.2 CO_2 Corrosion Mechanism

The presence of CO_2 in hydrocarbons causes severe internal corrosion problems (Schmitt and Horstemeier, 2006) made possible by the formation of carbonic acid (H_2CO_3). The corrosion mechanism consists of the anodic dissolution of steel and the cathodic reduction of carbonic acid as described in the following reactions:

Formation of carbonic acid	$H_2O + CO_2 \rightarrow H_2CO_3$
Reduction of carbonic acid	$2H_2CO_3 + 2e^- \rightarrow H_2 + 2HCO_3^-$ (cathode)
Acid regeneration	$HCO_3^- + H^+ \rightarrow H_2CO_3$
Overall cathodic reaction	$2H^+ + 2e^- \rightarrow H_2$
Metal dissolution	$Fe \rightarrow Fe^{2+} + 2e^-$ (anode)
Overall reaction	$Fe^{2+} + CO_3^{2-} \rightarrow FeCO_3$

12.3 Static Test

The static tests were conducted with the aim of studying the rate of the transport of the carbon dioxide through the vent into the annular space without intentionally mixing the electrolyte. As discussed in the literature review, transport of corrosive species could be due to diffusion or convection (Ahmad, 2006). However, it was assumed that since the electrolyte was static and there was no mixing, transport of corrosive species through the vent would only be by diffusion. This was necessary to describe the transport of CO_2 through the vent using a mathematical model.

The corrosion cell was deaerated with nitrogen gas to remove any dissolved oxygen to avoid any form of oxygen corrosion when investigating the effect of CO_2 corrosion. Complete deaeration was demonstrated by a reduction of the potentials to between -0.680 V and - 0.702 V. Introduction of CO_2 into the corrosion cell resulted in a sudden increase in the corrosion rate of the control sample to above 1.60 mm/y, in the bulk solution and later dropped to an average value of about 1.60 mm/y. After a time delay, a gradual increase in the corrosion rate beneath the vent increased suddenly to 0.49 mm/y

and then dropped almost immediately to about 0.15 mm/y. The carbon steel surface became grey/black as the corrosion rate began to drop due to corrosion product film. Beyond the 35.0 mm point onwards, there was no appreciable increase in the corrosion rates and remained around 0.02 mm/y (Figure 5-11).

The Evans diagram in Figure 12-1 shows the effect of CO_2 gas introduced into the corrosion cell on the anodic curve.

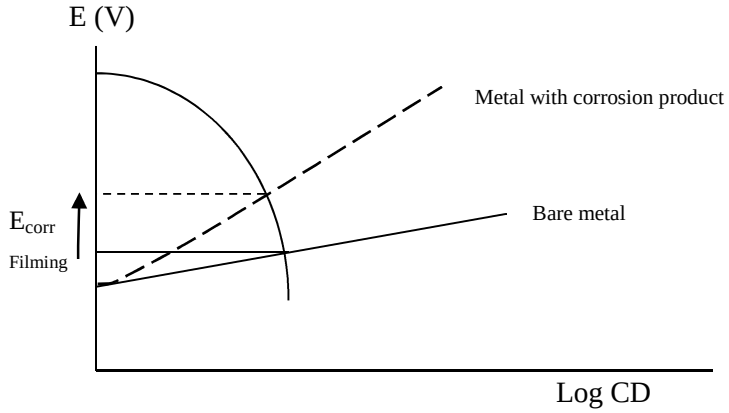

Figure 12-1: Movement of the anodic curve upward showing the effect of corrosion product film on the test electrode

The anodic curve moved upward due to the effect of filming of the electrode with corrosion product. As a result, the potential increased with a corresponding reduction in the current density/corrosion rate [point **d** on Figure 5-2(a)]. This is expected because of the assumed formation of a corrosion film as discussed in the literature review (Schmitt and Horstemeier, 2006; Hong et al., 2000; Martinez et al., 2011; Alawadhi, 2009).

Another interesting point in the static test was when the bulk solution was vigorously mixed. There were sudden increases in the corrosion rates because of the introduction of more CO_2 that were transported into the annular space.

Effect of Mass Transport of CO_2 within the Annular Space due to Mixing

The increase affected electrode pair 1 (directly under the vent) up to electrode pair 3 (20.0 mm from the vent). These sudden increases were over 250% above the normal

corrosion rates and are attributed to more transport of CO_2 through the vent, aided by flow and diffusion. There was no effect beyond the 35.0 mm point and the corrosion rate generally decreased after forming a corrosion film. The practical implication of these results is that vigorous mixing or turbulence in pipelines with vented plastic liners could lead to greater mass transport of corrosive species through the liner vent and greatly affect the extent of corrosion occurring beneath.

The results on the corrosion distribution (corrosion rate against distance) demonstrated the fact that the corrosion rates decreased with distance despite the diffusion of CO_2 into the annular space. There was a progressive reduction in corrosion rate over time, accompanied by the formation of a surface film. The corrosion did not extend significantly more than 35.0 mm from the liner vent and beyond this point, the corrosion rate was generally low (0.02 mm/y). This is attributed to the fact that the CO_2 that diffused into the annular space was depleted due to corrosion reaction with the carbon steel around the vent area.

Generally the results demonstrated the fact that the vent design restricted the mass transport of CO_2 into the annular space. Provided no flow occurred beneath the liner, corrosion only took place locally and its rate was limited by the slow transport of carbon dioxide through the liner vent. The corrosion rates were typically 20% of those of the control (unlined pipe) and diminished with distance from the vent. However, the main challenge was the issue of mixing which always suddenly increased the corrosion rates.

The high corrosion rate of the control sample (1.60 mm/y) compared to low corrosion rates within the annular space (between 0.10 mm/y and 0.20 mm/y) demonstrated that the vent actually reduced the corrosion rate under the liner to acceptable levels necessary to apply the technology.

12.4 Mathematical Modelling

The delay before the onset of corrosion of the test electrodes [Figure 5-5(b)] within the annular space supported a diffusion mechanism for the transport of CO_2 through the

vent due to the concentration gradient of the CO_2. The results of the static test were used to describe a mathematical model for its transport based on Fick's laws of diffusion. Figure 6-3 shows the plane sheet formed by the liner surfaces $x = 0$ (top), and $x = l$ (bottom). The model was intended to serve as a guide for the determination of the corrosion rate under a plastic liner in CO_2 environment and was obtained by plotting the concentration profile of the CO_2 through the electrolyte medium in the vent shown in Figure 6-5.

From some of the static tests performed, an average breakthrough time of 29 minutes was obtained and used to calculate the coefficient of diffusion of dissolved CO_2 through the vent containing brine. From the concentration profile, breakthrough was achieved at a τ value of 0.06. With the mean breakthrough time of 29 minutes for an open vent, the coefficient diffusion for CO_2 in brine was calculated to be **$5.6 \times 10^{-5} cm^2 s^{-1}$** at 25°C, which compares quite favourably with a value of $1.96 \times 10^{-5} cm^2 s^{-1}$ at 25°C. It is important to mention that despite the precautions taken a limited amount of mixing did occur and temperature fluctuations occurred during the tests; thus, there is some scatter of the D value.

12.5 Swagelining LinerVent™

Diffusion of CO_2 into Annular Space with and without LinerVent™ over Vent

In the experiment with only the control sample and electrode pair 1, the corrosion rate of the test electrode in the annular space with the LinerVent™ over the vent did not witness any increase during the test period. On the other hand, the corrosion rate of test electrode pair 1, without the LinerVent™ over the vent, increased within some hours. Figure 12-2 is a graph showing the comparison of the corrosion rates of pair 1, with and without the LinerVent™ installed over the vent.

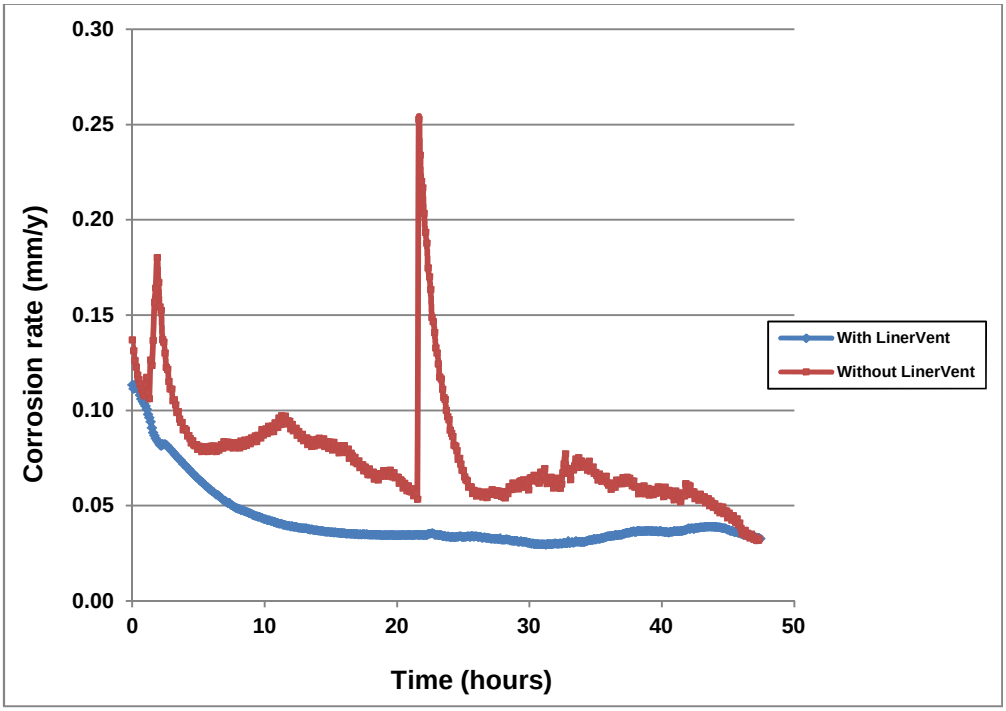

Figure 12-2: Corrosion rate of electrode pair 1, with and without LinerVent™ over vent

In addition when there was no LinerVent™ over liner vent, the breakthrough time (t_b) was shorter compared to when there was LinerVent™ over the vent. This implied that the rate of diffusion of corrosive species through the vent into the annular space was faster without the LinerVent™ and therefore the LinerVent™ delayed the diffusion of CO_2 into the annular space.

Vigorous Mixing within bulk solution with and without LinerVentTM

During the static test experiments, vigorous mixing was performed to observe the effect of the corrosion rate of the test electrode within the annular space. An increase in the corrosion rate of the test electrodes within the annular space, would have served as a basis for investigating whether the LinerVent™ designed by Atkins-Boreas could be beneficial when installed over the liner (Figure 7-3).

Vigorous mixing was therefore performed in some of the static tests. There were sudden increases in the corrosion rates in the annular space from the bottom of the vent to about 20.0 mm into the annular space. The test demonstrated the reduced time for the onset of corrosion and increase in the mass transport of CO_2 into the annular space.

When the LinerVent^{TM} was installed over the vent and the bulk solution stirred vigorously, there was little or no effect within the annular space. The device therefore provided additional reduction of transport of corrosive species into the annular space and prevented the high corrosion rates caused by turbulence within the pipeline. Despite the mixing, the LinerVent^{TM} reduced the mass transport of corrosive species into the annular space which resulted in reduction of the maximum corrosion rate and absence of corrosion peaks within the annular space as shown in Figure 12-3. This effect could be attributed to the configuration of the pores. Overall, the main benefit of the LinerVent^{TM} is in the reduction of the corrosion rate whenever there was vigorous mixing or turbulence within the pipeline.

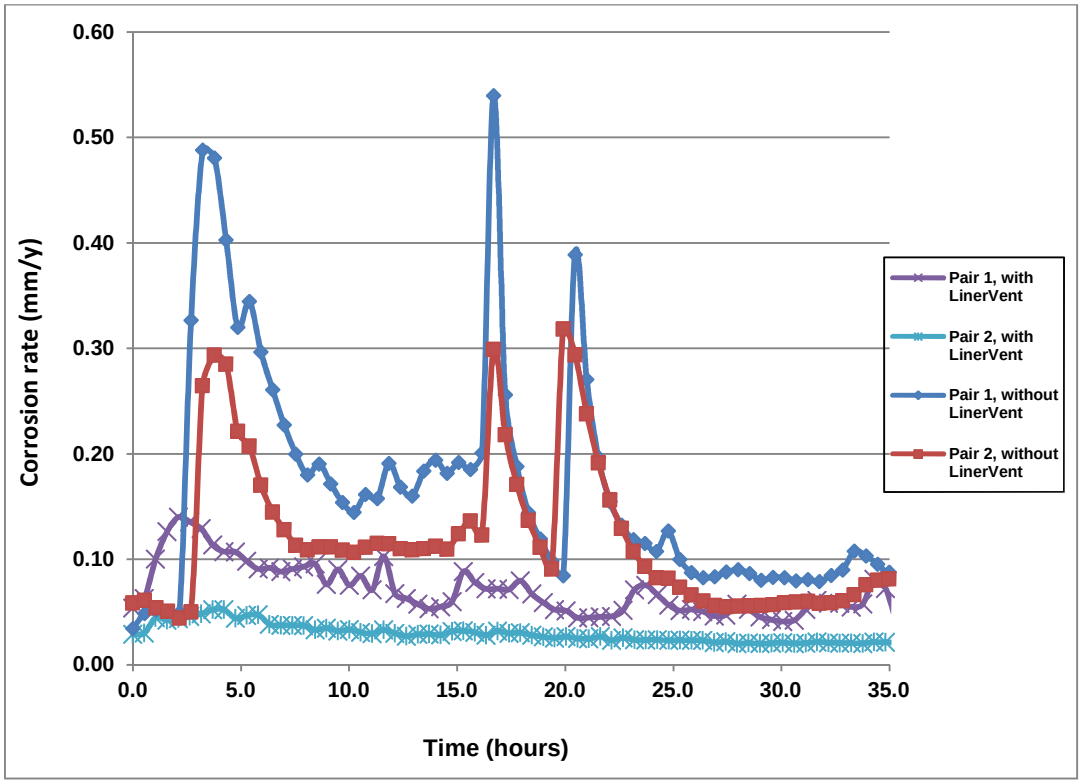

Figure 12-3: Effect of LinerVent^{TM} in reducing turbulence within the annular space

Modelling the effect of the Swagelining LinerVent^{TM}

The diffusion model demonstrated that the corrosive species diffuse faster through the vent and almost attain steady state when the LinerVent^{TM} was not in place. On the other

hand, the corrosive species were delayed through the vent and steady state could only be attained at a much longer period due to the LinerVent™.

Diffusion Coefficient of CO_2 with the LinerVent™

A longer mean breakthrough time of 54 minutes was obtained for a vent with the LinerVent™ and gave an effective CO_2 diffusion coefficient of $3.0 \times 10^{-5} cm^2 s^{-1}$. This reduced diffusion coefficient is attributed to the effect of the LinerVent™. The value reflects the combined behaviour of diffusion through the LinerVent™ and the brine solution within the vent. The effectiveness of the LinerVent™ to reduce mass transport of CO_2 when installed over the vent was demonstrated by a lower coefficient of diffusion of the CO_2 in the brine.

12.6 Flow within Annular Space

One of the areas covered in the research was to investigate the effect of fluid flow through the annular space; that is from one vent opening into the annular space and out through another vent. The corrosion rate of the test electrodes within the annular space showed a very high corrosion rate along the length of the steel plate. The corrosion rate increased by over 200% when there was flow through the annular space compared to the static case, where there was no flow through the annular space. This increase is attributed to the increased mass transport of CO_2 into the annular space. Fluid flow can result in high mass transfer (Meng and Jovancicevic, 2008) and therefore the increased flux of CO_2 into the annular space is responsible for the high corrosion rate observed.

Flow of corrosive species between vents lead to increase in mass transport of corrosive species into the annular space of the vented liner and will lead to serious corrosion problem. Therefore the suggestion by Frost et al. (Frost et al., 2000) for the vents to be spaced at 90° interval around the circumference as the most appropriate hole distribution is therefore supported.

12.7 Annular Space

Another area investigated in this research was to investigate the effect of the size of the annular space (created between the carbon steel pipeline and the vented plastic liner) on the corrosion rate within the. The relationship between the corrosion rate and the annular space gap showed a direct relationship for electrode pair 1.

The lowest corrosion rates were obtained when the annular space gap was 0.00 mm (no gasket situation) for electrode pair 1. This drop in the corrosion rate for annular space gap 0.00 mm is attributed to decrease in the quantity of CO_2 available within the annular space to cause corrosion of the steel surface. If all other conditions are equal, smaller crevices are expected to experience a lower corrosion rate compared to larger crevices (Walton, 1990; Li et al., 2002). This is attributed to the fact that fewer species diffused into smaller crevices to form a less corrosive environment.

From a practical point of view, the case of no gasket (zero annular space gap) is most likely the situation to be encountered in the construction of plastic lined pipelines since the pipelines are designed with the liner fitting tightly within the pipeline (Swagelining). Therefore the corrosion rate expected within the annular space of a tightly fitted plastic lined pipeline will be very low.

12.8 Corrosion Protection Strategy for Perforated Liner

Provided other factors that influence the crevice are taken into account, the potential distribution can be used to provide a reasonable indication of the corrosion state within the annular space created by a plastic lined pipeline. The potential-time graph was used to study the onset of corrosion (Trethewey and Chamberlain, 1995), or the formation corrosion product film or its breakdown. It was observed that under static conditions within the corrosion cell, corrosion of the plastic lined carbon steel pipeline was localised around the vent.

12.8.1 Cathodic Protection

Cathodic protection ensures the protection of the carbon steel pipeline by providing a sufficiently negative potential using a zinc sacrificial anode (Chin and Sabde, 2000a). Two types of design were used: disc and the long strip zinc sacrificial anode.

Disc-type zinc anode

The disc-type zinc anode was designed to be fitted beneath the liner vent to cathodically protect the corroding portion of the carbon steel around the vent where corrosion is more pronounced (figures 10-2 and 10-3). During deaeration of the corrosion cell, the potential within the annular space dropped below the NACE approved corrosion protection potential of -0.850 V (Baboian, 2002). The potential of unprotected steel became nobler due to changes to the anodic and cathodic curves. However, the protection with disc-type anode was limited to 40.0 mm due to IR drop effect discussed later.

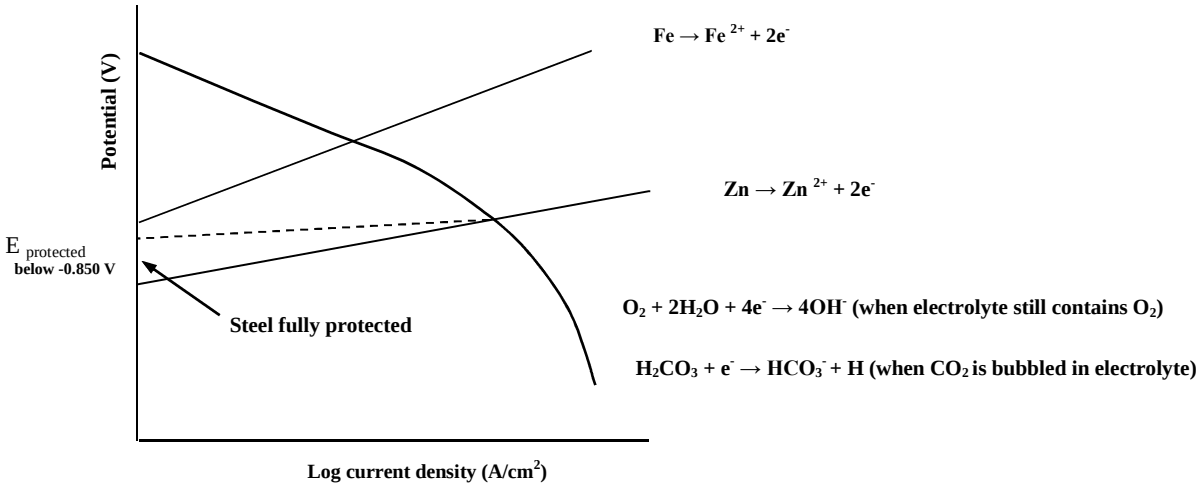

Figure 12-4: Evans diagram showing the principle of cathodic protection of steel plate

The Evans diagram (Figure 12-4) shows the reduction of the potential of the carbon steel from the equilibrium potential by the zinc anode. The zinc anode reduced the potential from the corrosion potential to a potential within the immunity region (below -

0.850 V) where the carbon steel beneath the liner is fully protected as observed within the vent area (40.0 mm).

Beyond this point, the potential increased above -0.850 V and black/grey discolouration indicating corrosion was observed on the steel surface. The Evans diagram in Figure 12-5 shows the effect of the cathodic curve during the deaeration process and when sweet corrosion was simulated. With the zinc anode in place and the solution was bubbled with N_2, there was full protection with the potential well below – 0.850 V. When CO_2 was bubbled into the solution, the cathodic curve moves to the right leading to a resultant increase in the potential, above the recommended protection potential (Baboian, 2002), and increase in the corrosion rate of the zinc anode.

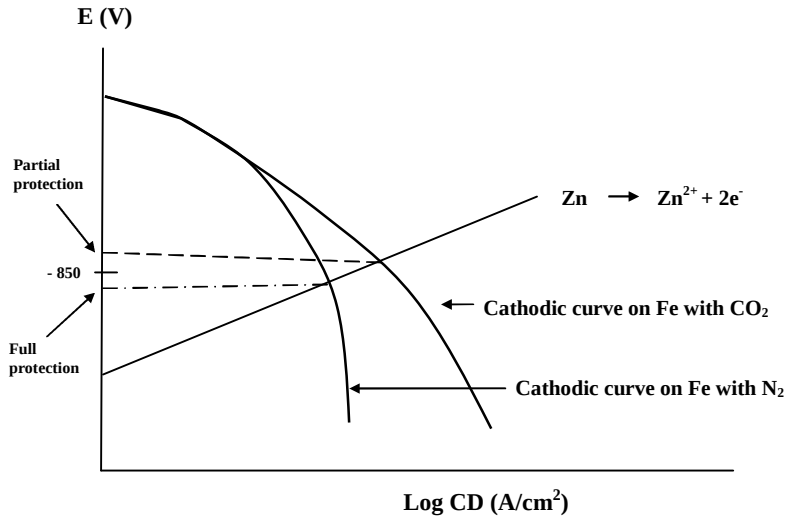

Figure 12-5: Evans diagram showing the cathodic effect

Therefore the disc anode located beneath the vent would offer the benefit of controlling corrosion, in the region where it is most likely to occur provided there is no condition that will increase the mass transport of corrosive species into the crevice. It is clear that "throwing power" limitation of the disc zinc anode CP could not protect carbon steel beyond 40.0 mm due to the confined geometry of the crevice (Oldfield and Sutton, 1978b).

Figure 12-6 is an Evans diagram showing the "throwing power" limitation which is attributed to the effect of the solution resistance as we move further away from the disc CP at the vent. In both situations (deaeration and sweet corrosion simulation), it can be seen that the effect of the solution resistance (IR) caused an increase in the potential leading to less protection and poorer throwing power. For the case of CO_2 corrosion, full protection was limited to just 40.0 mm from the vent.

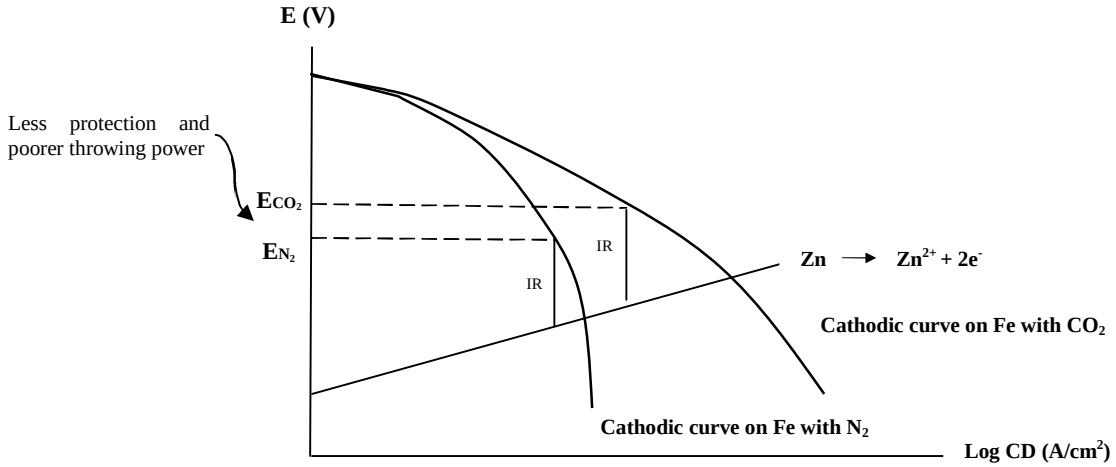

Figure 12-6: Evans diagram showing the effect of solution resistance

Long Strip Zinc Sacrificial Anode Cathodic Protection Design

"Throwing power" limitation of the disc zinc anode design was overcome with the long strip zinc anode CP design which runs through the full length of the steel plate. The long strip zinc anode CP design gave an almost uniform protection potential along the entire length of the plate. Despite CO_2 diffusing into the crevice, the potential within the crevice was within the protective range ($\leq$ -0.900 V) with no signs of corrosion attack. However, it is pertinent to note that further decrease in the potential, down to -0.950 V could result in the reduction of water and generation of hydrogen (Robinson and Kilgallon, 1994).

Therefore incorporating a zinc anode strip to the underside of the flexible liner would be a safer method of combating corrosion in the crevice and would provide protection over

a wider range of operating conditions. The long strip zinc anode can be applied as a spiral cable around the liner so that it makes contact with the carbon steel plate on insertion. This design is shown schematically in Figure 12-7.

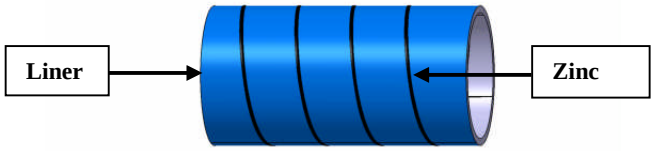

Figure 12-7: Schematic diagram of zinc anode spirally wound round liner

12.8.2 Corrosion Inhibitor

The CORRTREAT 05-193 oilfield inhibitor reduced the corrosion rates of both the control sample (unprotected pipeline) and most especially the test electrodes (carbon steel under the vented plastic liner) were reduced. Despite the continuous diffusion of CO_2 into the crevice, the corrosion rates decreased and remained low with the presence of the inhibitor.

Comparing Inhibited with Uninhibited Tests

When the result of the uninhibited condition (Figure 5-4) was compared with the inhibited (Figure 11-1), it can be observed that the corrosion rate of the control sample dropped immediately the inhibitor was introduced. The corrosion rate of the control sample dropped from 1.60 mm/y to 0.60 mm/y, a 167% drop. Also the corrosion rate of the test electrodes under the vented plastic liner dropped from 0.20 mm/y to 0.075 mm/y, a 167% drop.

Another point that needs mention is the ease with which the inhibitor can diffuse through the LinerVent^{TM} installed over the vent. It is not possible to determine the diffusion coefficient of the inhibitor at this point but it could be similar to that of CO_2. If it compares favourably with the carbonic acid, then it can be assumed that sufficient

concentration of the inhibitor will diffuse through the vent/LinerVent™ and quickly inhibit corrosion attack within the crevice.

As discussed in section 12.8.1, protection with the disk anode was limited to 40.0 mm from the vent area due to IR drop effect. With the encouraging results obtained from the test with the inhibitor, operators that would prefer the disk anode design for cost reduction or design reasons. They can be sure of protection beyond this point as demonstrated in Figure 12-8 which shows the inhibitor overcoming the throwing power limitation of the disk anode CP system and complete protection. Overall, whether the disk anode or the long strip; the inhibitor will serve as a backup or additional protection measure that will ensure complete protection in case of failure of the CP system due to failure of the system or error in design.

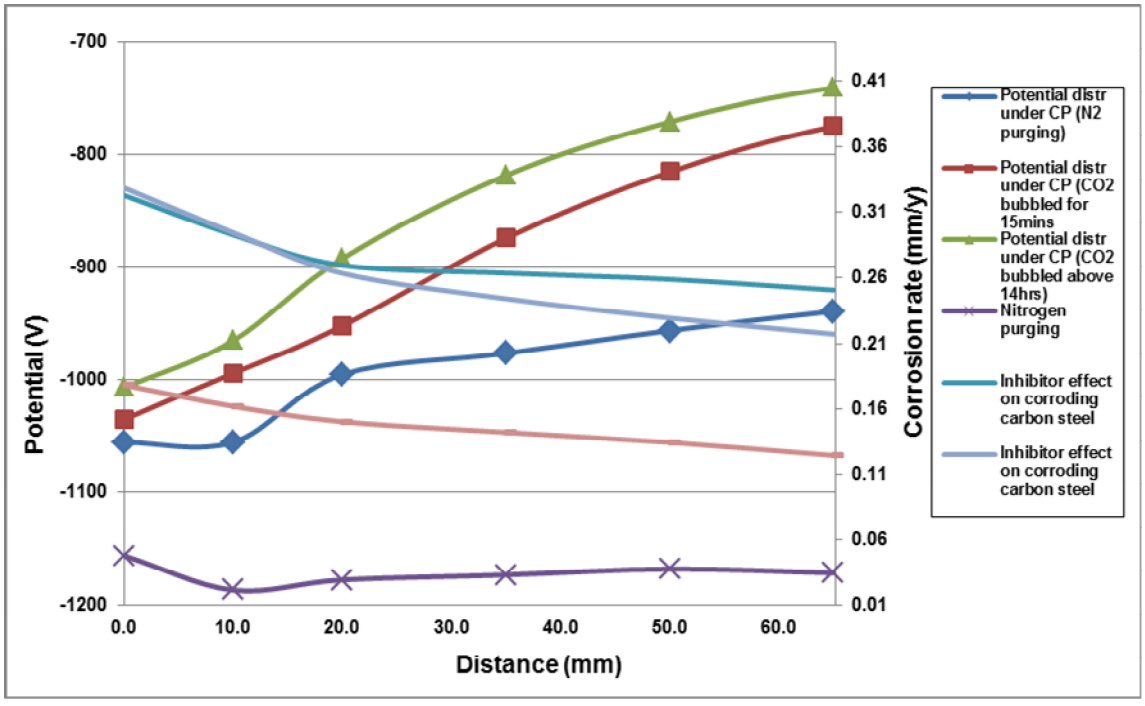

Figure 12-8: Effect of inhibitor in overcoming throwing power limitation of the disk anode CP system

In addition to the reduction in the corrosion rates, the corrosion peaks observed on the test electrodes due to the diffusion of CO_2 into the crevice in the uninhibited tests were not seen on the test electrodes of the inhibited tests. Therefore the presence of oilfield

corrosion inhibitor as the CORRTREAT 05-193 in transported hydrocarbon will be beneficial in further reducing the corrosion rate within the crevice of plastic lined pipelines.

CHAPTER 13
CONCLUSIONS AND RECOMMENDATIONS FOR FURURE WORK

13.1 Introduction

This chapter is aimed at discussing the key research findings of the research and recommendations for further work. It is pertinent to note that due to time limitation, some of the desired experiments could not be performed.

13.2 Conclusion

[1] The effect of installing a gas-escape vent in the wall of a flexible liner on the corrosion behaviour of the underlying pipe was investigated using a crevice corrosion cell. Provided there was no flow within the bulk solution, the vent design restricted the mass transport of CO_2 through the vent of the liner into the annular space. The corrosion rates recorded directly beneath the liner vent were within acceptable limit (average value of about 0.15 mm/y) and typically 20% of those of an unlined pipe.

[2] There was a progressive reduction in corrosion rate over time, accompanied by the formation of a surface film. During the period of the experiment, corrosion had not extended significantly more than 35.0 mm from the vent area. Beyond this point, the corrosion rate was generally low (0.02 mm/y). Provided no flow occurs beneath the liner, corrosion only takes place locally and its rate is limited by the slow transport of carbon dioxide through the liner vent.

[3] There was sudden increase in the corrosion rates within the annular space whenever there were mixing in the tank (bulk solution). The practical implication of this result is that vigorous mixing or turbulence will lead to greater mass transport of corrosive species through the liner vent and increase the corrosion rate of carbon steel beneath the plastic liner.

[4] A mathematical modelling to predict the transport of CO_2 through the liner vent into the annular space was described. The model was used to calculate the coefficient of diffusion D for carbon dioxide in static 3.5% NaCl solution as 5.6 **x 10^{-5}cm^{2}s^{-1}** at 25°C. It is worthy of note that this value of D compares quite favourably with a value of 1.96 x 10^{-5}cm^{2}s^{-1} at 25°C reported in the literature (Song, 2010).

[5] The mathematical model proposed was used to estimate the metal loss within the annular space of a vented plastic lined pipeline. The estimated total metal loss during a 27.7 hours test obtained using the model, was 0.94 mg while that obtained from direct calculation using the measured corrosion rate under the liner was 2.78 mg. The difference is attributed to the assumptions made in modelling CO_2 transport in the vent and the distribution of carbonic acid over the surface of the plate.

[6] The LinerVent™ produced a small reduction in the diffusion of CO_2 in the vent. The effective diffusion coefficient D for carbon dioxide in brine at ambient temperature and pressure was 3.0 x 10^{-5}cm^{2}s^{-1}. However, the main benefit of the LinerVent™ is in the reduction of the corrosion rate when there was vigorous mixing or turbulence within the pipeline. The physical presence of the LinerVent™ installed over the vent reduced the effect of turbulence within the pipeline in the annular space. In addition, it delayed the rate of mass transport of corrosive species because of the configuration of the pores.

[7] It was demonstrated that the steel in the annular space could be cathodically protected by a sacrificial anode. A disc of zinc protected the steel up to a distance of 40.0 mm from the vent, in the region that was most susceptible to corrosion attack. The "throwing power" limitation of the disc zinc anode design was overcome with a long strip zinc anode, aligned along the pipe. This design gave a better potential distribution and would be more suitable in the event of corrosion further into the vent. Therefore incorporating a zinc anode strip to the underside of the flexible liner would be a safer method of combating corrosion in the annular space and would provide protection over a wider range of operating conditions.

[8] It was also demonstrated that despite the presence of carbonic acid, the corrosion rate within the annular space was reduced to very low values with the CORRTREAT 05-193 oilfield corrosion inhibitor. Therefore the presence of an oilfield corrosion inhibitor in transported hydrocarbons will be beneficial and would further reduce the corrosion rate within the annular space beneath vented plastic lined pipelines.

13.3 Recommendations for Future Work

In the course of the research, there was need to carry out some other experiments. However, due to time constraint, the following areas are recommended for further work:

- Apart from CO_2 gas, H_2S is one of the associated gases present in hydrocarbons and hydrogen sulphide corrosion has been found in production wells, flowlines, and pipelines. It is therefore important to investigate the effect of H_2S in a vented plastic lined pipeline.

- Micro-organisms such as sulphate reducing bacteria (SRB) could attack metallic structures in anaerobic conditions by reducing sulphate ions into sulphide ions which can lead to microbiologically induced corrosion. Therefore it will be necessary to investigate their effect on vented plastic lined pipelines.

- More work to investigate the effect of cathodic protection and corrosion inhibitor when there is fluid flow within the annular space.

- More work to investigate the effect of annular space gap and vent size. Annular space gaps of 1.0 mm and below, and different vent sizes below and above the one used in this project (3.8 mm) should be tested.

- Further work will be necessary to investigate the corrosion rate and corrosion distribution within the annular space at temperatures above room temperature.

LIST OF PUBLICATIONS

Allison, C. and Robinson, M. (2011), "Assessment of Vented Flexible Liners for Corrosion Protection of Pipelines" NACE Corrosion Conference, March 13-17, Houston, Texas.

Allison, C. and Robinson, M. (2010), "Assessment of Vented Flexible Liners for Corrosion Protection of Pipelines" 51st Corrosion Science Symposium, 1-3 September, Southampton. [*Oral Presentation*].

Allison, C. and Robinson, M. (2009), "Assessment of Vented Flexible Liners for Corrosion Protection of Pipelines" 50th Corrosion Science Symposium (Electrochem 09), Manchester. [*Poster Presentation*].

REFERENCES

Abayarathna, D. and Naraghi, A. (2001), "Evaluation of Corrosion Inhibitors for CO_2 Corrosion using Electrochemical and Non-electrochemical Techniques", *Corrosion*.

Abdulsalam, M. I. and Pickering, H. W. (1998), "Effect of the Applied Potential on the Potential and Current Distributions within Crevices in Pure Nickel", *Corrosion Science,* vol. 41, no. 2, pp. 351-372.

Ahmad, Z. (2006), "Principles of Corrosion Engineering and Corrosion Control", 1st ed, Butterworth-Heinemann, London.

Alavi, A. and Cottis, R. A. (1987), "The Determination of pH, Potential and Chloride Concentration in Corroding Crevices on 304 Stainless Steel and 7475 Aluminium Alloy", *Corrosion Science,* vol. 27, no. 5, pp. 443-451.

Alawadhi, K. (2009), "Inhibition of Weld Corrosion in Flowing Brines Containing Carbon Dioxide" *(PhD thesis)*, Cranfield University.

Allison, C. (2004), "Hydrogen Embrittlement of Steel Reinforcement in Prestressed Concrete" *(MSc thesis)*, Cranfield University.

Archer, M. D. and Grant, N. C. (1984), "Achievable Boundary Conditions in Potentiostatic and Galvanostatic Hydrogen Permeation through Palladium and Nickel Foils", *Proceedings of the Royal Society of London. Series A, Mathematical and Physical Sciences,* Royal Society of London, pp. 165.

ASTM (1999), "Standard Practice for Conducting Potentiodynamic Polarisation Resistance Measurements", *ASTM Standards G-59, American Society for Testing and Material International,* West Conshohocken, United States.

Baboian, R. (ed.) (2002), "Nace Corrosion Engineer's Reference Book", 3rd Edition ed, NACE International, Houston, Tx.

Badr, G. E. (2009), "The Role of Some Thiosemicarbazide Derivatives as Corrosion Inhibitors for C-steel in acidic media", *Corrosion Science,* vol. 51, no. 11, pp. 2529-2536.

Baker, J. (2005), "A Programme for Proving Perforated Liners", *A Technical Note for Potential JIP Participants,* BR05058/BOR-01-A/Rev A, BOREAS Consultants Ltd, Aberdeen.

Baker, J. and McIntyre, S. (2003), "A Cost-Effective Corrosion Barrier for Welded Joints in Plastic-lined Pipelines", BOREAS Consultants Ltd, Aberdeen.

Baptista, W. and Pimenta, G. (1995), "Cathodic Protection against Crevice Corrosion of high-alloy steel in seawater", *Materials Performance,* vol. 34, pp. 29-32.

Bentiss, F., Lagrenee, M., Traisnel, M. and Hornez, J. C. (1999), "The corrosion Inhibition of Mild Steel in Acidic Media by a New Triazole Derivative", *Corrosion Science*, vol. 41, no. 4, pp. 789-803.

Beunier, M., Pionetti, F., Ardavanis, K., Gourdoux, E., Mauriès, B., Verdeil, J. and Lachheb, K. (2009), "Latest Concepts of Plastic-lined Water Injection Flowlines for Deepwater Field Developments", *SPE Projects, Facilities and Construction*, vol. 4, no. 2, pp. 13-18.

Biezma, M. V. and San Cristóbal, J. R. (2005), "Methodology to Study Cost of Corrosion", *Corrosion Engineering Science and Technology*, vol. 40, no. 4, pp. 344-352.

Boot, J. C. and Naqvi, M. M. (2000), "The Structural Characterisation of Corrosion-Resistant Linings for Hydrocarbon Pipelines", .

Bouklah, M., Hammouti, B., Lagrenée, M. and Bentiss, F. (2006), "Thermodynamic Properties of 2,5-bis(4-methoxyphenyl)-1,3,4-oxadiazole as a Corrosion Inhibitor for MildSteel in Normal Sulfuric AcidMedium", *Corrosion Science*, vol. 48, no. 9, pp. 2831-2842.

Cavassi, P. and Cornago, M. (1999), "The Cost of Corrosion in the Oil & Gas Industry", *Journal of Protective Coatings and Linings*, vol. 16, no. 5, pp. 30-40.

Chen, K. J. and Rizvi, S. S. H. (2006), "Measurement and Prediction of Solubilities and Diffusion Coefficients of Carbon Dioxide in Starch-water Mixtures at Elevated Pressures", *Journal of Polymer Science Part B: Polymer Physics*, vol. 44, no. 3, pp. 607-621.

Chin, D. T. and Sabde, G. M. (1999), "Current Distributon and Electrochemical Environment in a Cathodically Protected Crevice", vol. 55, no. 3.

Chin, D. T. and Sabde, G. M. (2000a), "Modeling Transport Process and Current Distribution in a Cathodically Protected Crevice", *Corrosion*, vol. 56, no. 8, pp. 783-793.

Chin, D. T. and Sabde, G. M. (2000b), "Modeling Transport Process and Current Distribution in a Cathodically Protected Crevice", *Corrosion*, vol. 56, no. 8, pp. 783-793.

Clark, J. C., Bui, T. D., Harris, G. D. and Cloke, K. M. (2007), "Differentiation of Corrosion Inhibitors for the Prevention of Localized Corrosion", *NACE Corrosion Conference*, March 11 - 15, Nashville, Tennessee, NACE International.

Congram, G. E. (2009), *HDPE Liner saves cost in Brent South Project*, available at: http://findarticles.com/p/articles/mi_m3251/is_/ai_n25023050 (accessed October 2008).

Crank, J. (1968), Diffusion in polymers, Academic Press, London.

Crank, J. (1975), The Mathematics of Diffusion, 2nd ed, Clarendon Press, Oxford.

Crolet, J. L. and Bonis M.R. (1986), "A Tentative Method for Predicting the Corrosivity of Wells in New CO_2 Fields", *Materials Performance,* vol. 25, no. 3, pp. 41-49.

Cruz, J., Martínez, R., Genesca, J. and García-Ochoa, E. (2004), "Experimental and Theoretical Study of 1-(2-ethylamino)-2-methylimidazoline as an Inhibitor of Carbon Steel Corrosion in Acid Media", *Journal of Electroanalytical Chemistry,* vol. 566, no. 1, pp. 111-121.

Curtis, M., Sally, M. B. and Lawrence (2002), "CO_2 Injection for Enhanced Gas Production and Carbon Sequestration".

Dave, K., Shadley, J. R., Rybicki, E. F., Roberts, K. P., Ramachandran, S. and Jovancicevic, V. (2008), "Effect of a Corrosion Inhibitor for Oil and Gas Wells when Sand is Produced".

Dayalan, E., De Moraes, F. D., Shadley, J. R., Shirazi, S. A. and Rybicki, E. F. (1998a), "CO_2 Corrosion Prediction in Pipe Flow under FeCO3 Scale-Forming Conditions", *Corrosion,* Vol. Paper 51, Houston, Texas, USA, National Association of Corrosion Engineers.

Dayalan, E., De Moraes, F. D., Shadley, J. R., Shirazi, S. A. and Rybicki, E. F. (1998b), "CO_2 Corrosion Prediction in Pipe Flow Under $FeCO_3$ Scale-Forming Conditions".

De Mul, L. M., Gerretsen, J. H. and Van de Haterd, A. W. (2000), "Experiences with Polyethylene Lined Pipeline Systems in Oman".

De Waard, C. and Milliams, D. E. (1975), "Carbonic Acid Corrosion of Steel", *Corrosion,* vol. 31, no. 5.

De Waard, C. and Lotz, U. (1993), "Prediction of CO_2 Corrosion of Carbon Steel", *National Association of Corrosion Engineers,* Vol. Paper 69, Orleans, USA., Institute of Materials, London, UK.

De Waard, C., Lotz, U. and Milliams, D. E. (1991), "Predictive Model for CO_2 Corrosion Engineering in Wet Natural Gas Pipelines", *Corrosion/91,* Vol. 47, Cincinnati, Ohio; USA, NACE International, Houston, TX, USA, pp. 976.

Degerbeck, J. and Gille, I. (1979), "Crevice Corrosion-A New Crevice Former", *Corrosion Science,* vol. 19, no. 7, pp. 1113-1115.

Duan, J., Wu, S., Zhang, X., Huang, G., Du, M. and Hou, B. (2008), "Corrosion of Carbon Steel Influenced by Anaerobic Biofilm in Natural Seawater", *Electrochimica Acta,* vol. 54, no. 1, pp. 22-28.

Enos, D. G. and Scribner, L. L. (1997), *The Potentiodynamic Polarization Scan - Solartron Analytical,* 33, Solartron Instruments, Hampshire, UK.

Fessler, R. F., Markworth, A. J. and Parkins, R. N. (1983), "Cathodic Protection Levels under Disbonded Coatings", *Corrosion*, vol. 39, no. 1, pp. 20-25.

Filbo, J. C. C. and Orazem, M. E. (2001), "Application of a Submerged Impinging Jet to Investigate the Influence of Temperature, Dissolved CO_2, and Fluid Velocity on Corrosion of Pipeline-Grade Steel In Brine".

Fontana, M. G. (1986), *Corrosion Engineering*, 3rd ed, McGraw-Hill Book Company, New York.

Fosbol, P. L., Thomsen, K. and Stenby, E. H. (2009), "Improving Mechanistic Model CO_2 Corrosion Models".

Fouda, A. S., Elewady, G. Y. and El-Haddad, M. N. (2011), "Corrosion Inhibition of Carbon Steel in Acidic Solution using some Azodyes", *Canadian Journal on Scientific and Industrial Research*, vol. 2, no. No. 1.

Frost, S. R., Cambers-Smith.J., Savadis, Y., Illison, T., Ashworth, R. and Heath, S. (2000), "COREL (Corrosion Resistant Liners) Joint Industry Project (JIP)".

Gan, F., Sun, Z. W., Sabde, G. and Chin, D. T. (1994), "Cathodic Protection to Mitigate External Corrosion of Underground Steel Pipe Beneath Disbonded Coating", *Corrosion*, vol. 50.

Gao, M., Pang, X. and Gao, K. (2011), "The Growth Mechanism of CO2 Corrosion Product Films", *Corrosion Science*, vol. 53, no. 2, pp. 557-568.

Groves, S., Mehta, S. and de Mul, L. M. (2004), "Corrosion Resisting Liners-The Results of an Investigation into Plastic Lining of Pipelines for Corrosive Hydrocarbon Service".

Gulbrandsen, E. and Dugstad, A. (2005), “Corrosion Loop Studies of Preferential Weld Corrosion and its Inhibition in CO_2 Environments", *Corrosion*.

Guo, B., Song, S., Chacko, J. and Ghalambor, A. (2005), "Offshore Pipelines", Elsevier Incorporated, Oxford.

Hara, T., Asahi, H., Suehiro, Y. and Sabde, G. M. (2000), "Effect of Flow Velocity on Carbon Dioxide Corrosion Behaviour in Oil and Gas Environments", .

Heppner, K. L., Evitts, R. W. and Postlethwaite, J. (2004), "Effect of the Crevice Gap on theInitiation of Crevice Corrosion in Passive Metals", *Corrosion*, vol. 60, no. 8, pp. 718-728.

Hong, T., Shi, H., Wang, H., Gopal, M. and Jepson, W. P. (2000), "EIS Study of Corrosion Product Film in Pipelines" .

Ijesseling, F. P. (2000), "Survey of Literature on Crevice Corrosion *(1979-1998)*", IOM Communications.

John C., W. (1990), "Mathematical Modeling of Mass Transport and Chemical Reaction in Crevice and Pitting Corrosion", *Corrosion Science*, vol. 30, no. 8-9, pp. 915-928.

Kapusta, S. D. and Pots, B. F. M. (2004), "The Application of Corrosion Prediction Models to the Design and Operation of Pipelines", .

Kennell, G. F., Evitts, R. W. and Heppner, K. L. (2008), "A Critical Crevice Solution and IR Drop Crevice Corrosion Codel", *Corrosion Science*, vol. 50, no. 6, pp. 1716-1725.

Kermani, M. B. and Morshed, A. (2003), "Carbon Dioxide Corrosion in Oil and Gas Production - A Compendium", *Corrosion*, vol. 59, no. 8, pp. 659-683.

Kermani, M. B. and Smith, L. M. (eds.) (1997), "CO_2 Corrosion Control in Oil and Gas Production - Design Considerations: (EFC 23)", Maney Publishing.

Kim, J. and Kim, Y. (2001), "Cathodic Protection Criteria of Thermally Iinsulated Pipeline Buried in Soil", *Corrosion Science*, vol. 43, no. 11, pp. 2011-2021.

Kouril, M., Novak, P. and Bojko, M. (2006), "Limitations of the Linear Polarisation Method to Determine Stainless Steel Corrosion Rate in Concrete Environment", *Cement and Concrete Composites*, vol. 28, no. 3, pp. 220-225.

Kvarekval, J. and Dugstad, A. (2005)," Pitting Corrosion in CO_2/H_2S Containing Glycol Solutions under Flowing Conditions", *NACE Corrosion Conference*, April 3 - 7, Houston, Tx, NACE International.

Lee, T. S., Kain, R. M. and Oldfield, J. W. (1984), "The Effect of Environmental Variables on Crevice Corrosion of Stainless Steels in Seawater", *Materials Performance*, vol. 23, no. 7.

Leffler, W., Pattarozzi, R. and Sterling, G. (2003), "Deepwater Petroleum Exploration and Production", *A Non-Technical Guide*, Penn Well Corporation, Tulsa,Oklahoma.

Li, Z., Gan, F. and Mao, X. (2002), "A study on Cathodic Protection Against Crevice Corrosion in Dilute NaCl Solutions", *Corrosion Science*, vol. 44, no. 4, pp. 689-701.

Lopez, D. A., Simison, S. N. and de Sanchez, S. R. (2003), "The Influence of Steel Microstructure on CO_2 Corrosion. EIS Studies on the Inhibition Efficiency of Benzimidazole", *Electrochimica Acta*, vol. 48, no. 7, pp. 845-854.

López, D. A., Pérez, T. and Simison, S. N. (2003), "The Influence of Microstructure and Chemical Composition ofCarbon and Low Alloy Steels in CO_2 Corrosion. A State-of-the-Art Appraisal", *Materials and Design*, vol. 24, no. 8, pp. 561-575.

López, D. A., Simison, S. N. and de Sánchez, S. R. (2005), "Inhibitors Performance in CO_2 Corrosion: EIS Studies on the Interaction Between their Molecular Structure and Steel Microstructure", *Corrosion Science*, vol. 47, no. 3, pp. 735-755.

Maclachlan, A. (1996), "Plastic Liners for Hydrocarbon Service".

Marais, S., Saiter, J. M., Devallencourt, C., Nguyen, Q. T. and Métayer, M. (2002), "Study of Transport of Small Molecules through Ethylene-co-vinyl Acetate Copolymers Films. Part B: CO_2 and O_2 Gases", *Polymer Testing*, vol. 21, no. 4, pp. 425-431.

Martinez, M., Alawadhi, K., Robinson, M., Nelson, G. and MacDonald, A., (2011), "Control of Preferential Weld Corrosion of X65 Pipeline Steel in Flowing Brines Containing Carbon Dioxide".

McIntyre, S. (2006) *Lined Pipeline Vent.* BOREAS Consultants Limited (Aberdeen, GB). Patent no. WO02/33298.

McIntyre, S. *Plastic Linavent*, available at: http://www.boreasconsultants.com/site.php?page=44 (accessed September 2008).

McIntyre, S. (2000) "Venting of Plastic Lined Pipelines". Anonymous Patent no. WO/2000/008368.

McIntyre, S. (2002), "Plastic Lining Subsea Pipelines", BOREAS Consultants Ltd, Aberdeen.

Melchers, R. E. (2003), "Mathematical Modelling of the Diffusion Controlled Phase in Marine Immersion Corrosion of Mild Steel", *Corrosion Science*, vol. 45, no. 5, pp. 923-940.

Meng, Q. and Jovancicevic, V. (2008), "Electrochemical Evaluation of CO_2 Corrosion Inhibitors in High Turbulence Multiphase Fluid Flow", NACE International, pp. 086251.

Mohammed, I. A. (2005), "Behaviour of Crevice Corrosion in Iron", *Corrosion Science*, vol. 47, no. 6, pp. 1336-1351.

Morgan, J. (1993), *Cathodic protection*, 2nd ed, National Association of Corrosion Engineers, Houston, Texas.

Nesic, S. (2007), "Key Issues Related to Modelling of Internal Corrosion of Oil and Gas Pipelines - A Review", *Corrosion Science*, vol. 49, pp. 4308-4338.

Okafor, P. C., Liu, C. B., Zhu, Y. J. and Zheng, Y. G. (2011), "Corrosion and Corrosion Inhibition Behavior of N80 and P110 Carbon Steels in CO_2-Saturated Simulated Formation Water by Rosin Amide Imidazoline".

Oldfield, J. W. (1996), "Prediction of Initiation and Propagation of Crevice Corrosion on aluminium Alloys in Seawater by Mathematical Modelling", *NACE Corrosion Conference*, March 24 - 29, Denver, NACE International.

Oldfield, J. W. and Sutton, W. H. (1978a), "Crevice Corrosion of Stainless Steels II. Experimental Studies", *Corrosion*, vol. 13, no. 3, pp. 104-110.

Oldfield, J. W. and Sutton, W. H. (1978b), "Crevice Corrosion of Stainless Steels I. Mathematical Model", *Corrosion*, vol. 13, no. 1, pp. 13-22.

Olsen, S., Halvorsen, A. M., Lunde, P. G. and Nyborg, R. (2005), "CO_2 Corrosion Prediction Model - Basic Principles", *Corrosion; 3-7 Apr. 2005*, vol. 05551, 13 pp. *Houston, TX, USA*, NACE International.

Palmer-Jones, R. and Paisley, D. (2000), "Repairing Internal Corrosion Defects in Pipelines" .

Papavinasam, S., Wally, F. R., Revie, W. and Doiron, A. (2005), "Predicting Internal Pitting Corrosion of Oil and Gas Pipelines: A Corroson Engineering Approach", .

Parjus, T., Champagne, E. C. and Vecchio, J. M. (1996), "Deepwater production", *Offshore*, vol. Vol. 56, no. No. 9.

Payton, S. (2011), Abu Dhabi Renovates Old Gas Pipe for Water Transport by Swagelining, available at: http://images.pennnet.com/articles/wwi/cap/cap_116278.gif (accessed November).

Pedeferri, P. (1996), "Cathodic Protection and Cathodic Prevention", *Construction and Building Materials*, vol. 10, no. 5, pp. 391-402.

Postlethwaite, J. and Nesic, S. (2000), "Erosion-Corrosion in Single and Multiphase Flow", in Revie, W. (ed.) *Ulig's Corrosion Handbook*, 2nd Edition ed, John Wiley & Sons, Inc.

Revie, R. W. (ed.) (2011), "Uhlig's Corrosion Handbook", 3rd edition ed, John Wileys & Sons.

Robinson, M. J. and Kilgallon, P. J. (1994), "Hydrogen Embrittlement of Cathodically Protected High-Strength, Low-Alloy Steels Exposed to Sulfate-Reducing Bacteria", .

Rothwell, N. and Tullmin, M. (2000), "The Corrosion Monitoring Handbook", First edition ed, Coxmoor Publishing Company, Oxford, UK.

Sharland, S.M. (1992), "A Mathematical Model of the Initiation of Crevice Corrosion in Metals", *Corrosion Science*, vol. 33, no. 2, pp. 183-201.

Sato, Y., Fujiwara, K., Takikawa, T., Sumarno, Takishima, S. and Masuoka, H. (1999), "Solubilities and Diffusion Coefficients of Carbon Dioxide and Nitrogen in Polypropylene, High-density Polyethylene, and Polystyrene under High Pressures and Temperatures", *Fluid Phase Equilibria*, vol. 162, no. 1-2, pp. 261-276.

Schmitt, G. and Horstemeier, M. (2006), "Fundamental Aspects of CO_2 Metal Loss Corrosion - Part II: Influence of Different Parameters on CO_2 Corrosion Mechanisms", vol. 06112, National Association of Corrosion Engineers, Houston, Texas, USA.

Shayegani, M., Afshar, A., Ghorbani, M. and Rahmaniyan, M. (2008), "Mild Steel Carbon Dioxide Corrosion Modelling in Aqueous Solutions", *Corrosion Engineering Science and Technology,* vol. 43, no. 4, pp. 290-296.

Shreir, L. L., Jarman, R. A. and Burstein, G. T. (eds.) (1994), *Corrosion,* 3rd ed, Butterworth Heinemann.

Siegmund, G., Schmitt, G., Noga, J. and Sadlowsky, B. (2002), "Lining Pipelines with PE - A Solution for Wet Gas Transport?".

Song, F. M. (2010), "A Comprehensive Model for Predicting CO_2 Corrosion Rate in Oil and Gas Production and Transportation Systems", *Electrochimica Acta,* vol. 55, no. 3, pp. 689-700.

Song, F. M., Jones, D. A. and Kirk, D. W. (2005), "Modeling Pipeline Corrosion within a Disc-Shaped Crevice for Various Cathodic Protection Levels at the Holiday and the Effect of Crevice Geometry", *NACE Corrosion Conference,* April 3 - 7, Houston, Tx, NACE International.

Song, F. M., Kirk, D. W., Graydon, J. W. and Afshar, A. (2004), "Predicting Carbon Dioxide Corrosion of Bare Steel Under an Aqueous Boundary Layer".

Song, F. M., Kirk, D. W., Graydon, J. W. and Cormack, D. E. (2003a), "A New Pipeline Crevice Corrosion Model with O_2 and CP", *Corrosion Science*.

Song, F. M., Kirk, D. W., Graydon, J. W. and Cormack, D. E. (2003b), "Steel Corrosion under a Disbonded Coating with a HolidayPart 2: Corrosion Behavior", *Corrosion*, vol. 59, no. No. 01.

Song, H. W., Saraswathy, V., Muralidharan, S., Lee, C. H. and Thangavel, K. (2009), "Corrosion Performance of Steel in Composite Concrete System Admixed with Chloride and various Alkaline Nitrites ", *Corrosion Engineering, Science and Technology*, vol. 44, no. 6, pp. 408-415.

Stefan, R. and Anders, M. (eds.) (2010), "Corrosion Monitoring in Nuclear Systems - Research and Applications", *(EFC 56),* Maney Publishing.

Swagelining (a), How Does Swagelining™ Work, available at: http://swagelining.com/01002-how-does-swagelining-work.html (accessed July 2011).

Swagelining (b), Life Extending Technology for New and Existing Pipelines - Venting, available at: http://swagelining.com/06004-venting.html (accessed 2008).

Swagelining(2010), "Major Savings Highlighted in Polymer lined Pipe Study", Swagelining Limited, Glasgow.

Tan, Y., Bailey, S. and Kinsella, B. (2001), "Mapping Non-Uniform Corrosion Using the Wire Beam ElectrodeMethod. II. Crevice Corrosion and Crevice Corrosion Exemption", *Corrosion Science,* vol. 43, no. 10, pp. 1919-1929.

Tao, Z., Zhang, S., Li, W. and Hou, B. (2009), "Corrosion Inhibition of Mild Steel in Acidic Solution by Some Oxo-triazole Derivatives", *Corrosion Science,* vol. 51, no. 11, pp. 2588-2595.

Teevens, P. J. and Sand, K. W. (2008), "Application of Internal Corrosion Predictive Modelling (ICPM) in 2 or 3 -Phase Petroleum Pipelines: Model Validation".

Tems, R. and Al Zahrani, A. M. (2006), "Cost of Corrosion in Oil Production and Refining", *Saudi Aramco Journal of Technology,* no. Summer, pp. 2-14.

Thompson, N. G. (2006), "Gas and Liquid Transmission Pipelines", CC Technologies, Dublin, Ohio.

Thompson, N. G. and Patrick, H. V. (2003), "Corrosion Costs US Transmission Pipelines as Much as $8.6 Billion/Year", *Pipeline and Gas Journal* .

Toncre, A.C. and Ahmad, N. (1980), “Cathodic Protection in Crevices under Disbonded Coatings", Materials Performance Journal, vol. 19, no. 5.

Treseder, R. S. (1980), Baboian, R. and Munger, C. G. (eds.) "NACE Corrosion Engineer's Reference Book", 2nd ed, NACE International.

Trethewey, K. R. and Chamberlain, J. (1995), "Corrosion for Science and Engineering", 2nd ed, NACE International, Houston, Tx.

Van Hunnik, E. W. J., Pot, B. F. M. and Hendriksen, E. L. J. A. (1996), "The Formation of Protective $FeCO_3$ Corrosion Product Layers in CO_2 Corrosion", *Corrosion 96,* Vol. Paper 6, Houston, Texas, USA, NACE International.

Villamizar, W., Casales, M., Gonzalez-Rodriguez, J. G. and Martinez, L. (2007), "CO_2 corrosion inhibition by hydroxyethyl, aminoethyl, and amidoethyl imidazolines in water–oil mixtures".

Walton, J. C. (1990), "Mathematical Modeling of Mass Transport and Chemical Reaction in Crevice and Pitting Corrosion", *Corrosion Science,* vol. 30, no. 8-9, pp. 915-928.

Walton and J.C. (1990), "Mathematical Modeling of Mass Transport and Chemical Reaction in Crevice and Pitting Corrosion", *Corrosion Science,* vol. 30, no. 8-9, pp. 915-928.

Wang, F. and Postlethwaite, J. (2001), "Modelling of Aqueous CO_2 Corrosion of Iron in Turbulent Pipe Flow ".

Wranglen, G. (1985), “An introduction to Corrosion and Protection of Metals", 1st ed, Chapman and Hall, London.

Wright, S. (2006), "Flexible Liners for Corrosion Protection of Pipelines", *(MSc thesis)*, Cranfield University, Bedfordshire, UK.

APPENDIX

Appendix A :

Calculation of Metal Loss from Corrosion Rate and Corroding Area under Liner

$$CR = 87.6 \times (W/DAT) \qquad \text{(Equation 6-14)}$$

Where,

- CR – Corrosion rate (in mm/y)
- W – weight loss (in mg)
- D – density (in g/cm^3)
- A – area of sample (in cm^2)
- T – time of exposure of the metal sample (in hours)

Therefore, metal loss $W = \frac{CR \times DAT}{87.6}$

Metal loss over area $A_1 = \frac{0.261 \times 7.84 \times 0.85 \times 27.7}{87.6} = 0.550$ mg

Metal loss over area $A_2 = \frac{0.144 \times 7.84 \times 0.85 \times 27.7}{87.6} = 0.303$ mg

Metal loss over area $A_3 = \frac{0.048 \times 7.84 \times 10.63 \times 27.7}{87.6} = 1.264$ mg

Metal loss over area $A_4 = \frac{0.021 \times 7.84 \times 12.75 \times 27.7}{87.6} = 0.664$ mg

Therefore total metal loss = 0.550 + 0. 303 + 1.264 + 0.664 = **2.781 mg**

This page is intentionally left blank